GTO debris mitigation using natural perturbations

Aleix Pinardell Pons

Technische Universiteit Delft

TU Delft Delft University of Technology

Challenge the future

GTO DEBRIS MITIGATION USING NATURAL PERTURBATIONS

by

Aleix Pinardell Pons

October 9, 2017

in partial fulfilment of the requirements for the degree of

Master of Science
in Aerospace Engineering

at Delft University of Technology,
to be defended publicly on Wednesday October 25, 2017 at 14:00

Student number:	4520777	
Project duration:	November 7, 2016 – June 30, 2017	
Supervisor:	ir. R. Noomen	
Thesis committee:	Dr. D.M. D. Stam,	TU Delft
	ir. R. Noomen,	TU Delft
	Dr. ir. Q. P. Chu,	TU Delft

An electronic version of this thesis is available at http://repository.tudelft.nl/.

Cover image: artist's rendition of Ariane 6 launch vehicle. Credit: ESA and Le Scienze.
http://digiorgio-lescienze.blogautore.espresso.repubblica.it/2014/12/03/dopo-lussemburgo/

Preface

My passion for space arose when I was six years old. At that age I carried out the conceptual design, development and testing of a space-based amusement system (yes, I drew and played a space-themed board game). Twelve years later, I started my BSc in Aerospace Engineering in València, in which I had plenty of courses on aeroplanes, and a campus with plenty of space, hence the name. Then, I started my MSc in Aerospace Engineering at TU Delft, and this time –yes!– I had plenty of space courses during my first year. After my internship at Leiden (from which I will highlight the profound words of a senior: "You are on the way to becoming an engineer"), I started my Master thesis. And now here I am: writing the lines that put an end to this period.

Before concluding this chapter of my life there are several people I would like to thank for helping me in bringing this thesis to a good end. I would like to thank Ron, for guiding me throughout my research and for providing feedback that helped me analyse my previous steps and plan my next moves critically, and for bringing me down to earth whenever I reached Low Enlightenment Orbit.

I would also like to thank Dominic, for helping me cope with Tudat throughout the thesis: from the beginning, when just getting the code to compile was an achievement, to the end, when getting the code to compile was just an achievement. I also want to thank all the people who have put effort into developing Tudat; without their contribution this thesis would not have been possible.

Finally, I would like to thank those who helped me with the integration of the equations of welfare. I am talking about my parents, who provided the right initial conditions, and the fellows in the student room, who provided the right amusement-to-concentration ratio. I want to thank especially Tim, Hanneke and Evelyne, who made me want to go back to Delft even when I was enjoying the lovely Spanish weather. And I want to thank my parents again for being those two exceptional persons I am proud of and I will try my best to make this feeling always stay reciprocal.

Aleix Pinardell Pons
Delft, 30 June 2017

Abstract

Objects in geostationary transfer orbit (GTO) can collide with operative satellites in low Earth orbit (LEO) and geostationary orbit (GEO). Various organisations have laid down debris-mitigation guidelines that will be enforced by law for future launchers. One of the guidelines entails proving that the generated debris will re-enter in less than 25 years with a 90% probability. Natural perturbations can be exploited to meet this requirement without the use of extra propellant or complex de-orbiting systems, which is especially attractive from an economic point of view.

Objects in GTO can undergo a resonance triggered by an interplay between perturbations caused by the Suns gravity and the irregularities in Earths gravity field, leading to a sudden re-entry or making the object stay in orbit for decades. This effect is very sensitive to initial conditions because it depends on the relative positions of the perigee and the Sun when the semi-major axis is close to 15 000 km. By simulating the orbital evolution of a representative GTO object –ballistic coefficient of 0.011 m^2/kg, initial orbital inclination of 10 degrees and initial perigee altitude of 200 km– for several initial epochs, it was found that favourable launch conditions take place twice per day during most part of the year, while for epochs close to the equinoxes of March and September they only happen once per day or not at all.

Given the high sensitivity to initial conditions, the problem was studied from a statistical perspective, taking into account the uncertainties in the values of the relevant parameters. Semi-analytical techniques were used to propagate the mean equinoctial elements instead of the osculating Cartesian elements, which reduced computation times by a factor of 45 while still keeping proper levels of accuracy. It was found that the launch time leading to the highest probability of compliance with debris-mitigation guidelines for GEO launches from the European spaceport in Kourou is approximately 9 AM/PM local time, regardless of the day of the year. However, the value of the optimal lifetime does vary slightly throughout the year. Current practice for GTO launches from Kourou is to launch at around 6-7 PM, so a change in procedures would be required in order to reach a higher degree of compliance with debris-mitigation guidelines, which was below 10% for GTO launches carried out with Ariane 5 from in the period 2004-2012.

CONTENTS

LIST OF ABBREVIATIONS

AN	Ascending node
API	Application programming interface
AU	Astronomical unit [149 597 870 700 m] [1]
CNES	Centre national d'études spatiales (French Space Agency)
DC	District of Columbia
DLTP	Date and local time of perigee
DoY	Day of year
ECI	Earth-centred inertial
ECP	Earth-centred perifocal
ECR	Earth-centred rotational
ESA	European Space Agency
GEO	Geostationary orbit
GRACE	Gravity Recovery and Climate Experiment
GST	Greenwich Sidereal Time
GTO	Geostationary transfer orbit
HEO	Highly elliptical orbit
IADC	Inter-Agency Space Debris Coordination Committee
ISS	International Space Station
JD	Julian day
LEO	Low Earth orbit
LP	Long period
MDP	Mean drift of perigee
MEO	Medium Earth orbit
NORAD	North American Aerospace Defense Command
PDF	Probability density function
RAAN	Right ascension of the ascending node
RK	Runge-Kutta
RK4	Fourth-order Runge-Kutta method
RMS	Root mean square

S	Secular
SP	Short period
SRP	Solar radiation pressure
SSP	Sub-satellite point
SST	Semi-analytical satellite theory
TESP	Tudat Earth Satellite Propagator
TLE	Two-line element
TT	Terrestrial time
Tudat	TU Delft Astrodynamics Toolbox
TU Delft	Technische Universiteit Delft (Delft University of Technology)
URL	Uniform resource locator
US	United States
UT	Universal time
UV	Ultraviolet
VE	Vernal equinox
VOP	Variation of parameters

List of symbols

All vectors (e.g. $\vec{r}$) are indicated in bold ($\boldsymbol{r}$) and their magnitudes are written using normal weight font (r).

Latin symbols

A	Cross-sectional area $[\mathrm{m}^2]$
A	SST's first parameter $[\mathrm{m}^2\,\mathrm{s}^{-1}]$
A_i	Mean rate function for orbital element i $[-]$
A_p	Geomagnetic index $[\mathrm{T}]$
a	Semi-major axis $[\mathrm{m}]$
$\boldsymbol{a_D}$	Acceleration due to atmospheric drag $[\mathrm{m\,s}^{-2}]$
a_i	i^{th} orbital element $[-]$
$\boldsymbol{a_{SRP}}$	Acceleration due to solar radiation pressure $[\mathrm{m\,s}^{-2}]$
B	Ballistic coefficient $[\mathrm{m}^2\,\mathrm{kg}^{-1}]$
B	SST's second parameter $[-]$
C	SST's third parameter $[-]$
C_D	Drag coefficient $[-]$
C_i^j	Cosine part of the short-period terms $[-]$
$C_{n,m}$	Cosine term associated to the tesseral term of the geopotential of degree n and order m $[-]$
C_R	Radiation pressure coefficient $[-]$
c	Speed of light $[299\,792\,458\,\mathrm{m\,s}^{-1}]$ [2]
D_{ap}	Days since last time that Earth was at aphelion $[\mathrm{day}]$
E	Eccentric anomaly $[\mathrm{rad}]$
e	Eccentricity $[-]$
$\boldsymbol{e}$	Eccentricity vector $[-]$
$\boldsymbol{e_S}$	Unit vector from the orbiting body to the Sun $[-]$
$F_{10.7}$	Radiation flux index at 10.7 cm wavelength $[\mathrm{W\,m}^{-2}\,\mathrm{Hz}^{-1}]$
F	Eccentric longitude $[\mathrm{rad}]$
$\boldsymbol{f}$	Perturbing acceleration $[\mathrm{m\,s}^{-2}]$
$\overline{f}$	True anomaly limit for neglecting drag $[\mathrm{rad}]$
$\boldsymbol{f}$	First axis of the equinoctial reference frame $[-]$
f	True anomaly $[\mathrm{rad}]$
f_d	Disturbing acceleration $[\mathrm{m\,s}^{-2}]$
f_E	Central acceleration due to Earth $[\mathrm{m\,s}^{-2}]$
$\boldsymbol{f_t}$	Total acceleration $[\mathrm{m\,s}^{-2}]$
G	Universal gravitational constant $[6.67408\times10^{-11}\,\mathrm{m}^3\,\mathrm{kg}^{-1}\,\mathrm{s}^{-2}]$ [3]
$\boldsymbol{g}$	Second axis of the equinoctial reference frame $[-]$
H_0	Density scale height $[\mathrm{m}]$
$\overline{h}$	Altitude limit above which drag is neglected $[\mathrm{m}]$
h_0	Reference altitude $[\mathrm{m}]$
h	Component of the eccentricity vector along the $\boldsymbol{g}$ axis of the equinoctial reference frame $[-]$
h_a	Apoapsis altitude $[\mathrm{m}]$
h_p	Periapsis altitude $[\mathrm{m}]$
I	Retrograde factor $[-]$
I_j	Modified Bessel function of order j $[-]$
i	Inclination $[\mathrm{rad}]$
J_n	Zonal term of the geopotential of degree n $[-]$
$J_{n,m}$	Tesseral term of the geopotential of degree n and order m $[-]$
k	Component of the eccentricity vector along the $\boldsymbol{f}$ axis of the equinoctial reference frame $[-]$
L	True longitude $[\mathrm{rad}]$

M Mass of the central body [kg]

M Mean anomaly [rad]

M_d Mass of the disturbing body [kg]

M_E Earth's mass [5.97219×10^{24} kg] [4]

m Mass [m]

m Order of the geopotential expansion [−]

N Number of terms in the series expansions of SST [−]

N_3 Number of terms in the series expansions of third-body gravity in SST [−]

N_{drag} Number of nodes in the Gaussian quadrature of the averaging integral of drag [−]

N_{Moon} Number of terms in the series expansions of lunar gravity in SST [−]

N_{SRP} Number of terms in the series expansions of SRP in SST [−]

N_{Sun} Number of terms in the series expansions of solar gravity in SST [−]

n Degree of the geopotential expansion [−]

n Mean motion [rad s^{-1}]

O Order of [−]

O Origin [−]

P_n Legendre polynomial of degree n [−]

$P_{n,m}$ Associated Legendre function of the first kind of degree n and order m [−]

p Component of the ascending node vector along the $\boldsymbol{g}$ axis of the equinoctial reference frame [−]

p Semi-latus rectum [m]

q Component of the ascending node vector along the $\boldsymbol{f}$ axis of the equinoctial reference frame [−]

q Encke parameter [−]

R_3 Mean radius of a third body [m]

R Radius [m]

R Rotation matrix [−]

R_E Earth's radius [m]

R_X Rotation matrix that rotates a vector about the X-axis [−]

R_Y Rotation matrix that rotates a vector about the Y-axis [−]

R_Z Rotation matrix that rotates a vector about the Z-axis [−]

$\tilde{R}$ Perturbing potential [m^2 s^{-2}]

$\tilde{R}_{SH}$ Perturbing potential due to Earth's irregular gravity field [m^2 s^{-2}]

$\tilde{R}_{3B}$ Perturbing potential due to third-body gravitational attraction [m^2 s^{-2}]

$\boldsymbol{r}$ Position vector [m]

r Radial distance [m]

r_a Apoapsis radius [m]

$\boldsymbol{r_d}$ Position vector of the disturbing body [m]

r_p Periapsis radius [m]

r_S Distance from Earth to the Sun [m]

S Sailing coefficient [m^2 kg^{-1}]

S_i^j Sine part of the short-period terms [−]

$S_{n,m}$ Sine term associated to the tesseral term of the geopotential of degree n and order m [−]

T Orbital period [s]

T_L Lifetime [s]

$T_L^{(90\%)}$ Lifetime for which an orbit will have decayed with a 90% probability [s]

$\tilde{T}$ Minimum period of the perturbations [s]

t Time [s]

U Gravitational potential [m^2 s^{-2}]

$U_{,\alpha\beta}$ Cross-derivative operator [−]

u Argument of latitude [rad]

$\boldsymbol{V_r}$ Relative velocity with respect to the rotating atmosphere [m s^{-1}]

W_S Energy flux of the Sun at 1 AU [W m^{-2}]

$\boldsymbol{w}$ Angular momentum vector [m^2 s^{-1}]

$\boldsymbol{w}$ Third axis of the equinoctial reference frame [−]

w	Gaussian weight factor [–]
X	First axis of a Cartesian reference frame [–]
x	Distance along the X-axis [m]
x_d	X component of a disturbing body [m]
x_S	First coordinate of the Sun in an Earth-centred perifocal reference frame [m]
Y	Second axis of a Cartesian reference frame [–]
y	Distance along the Y-axis [m]
y_d	Y component of a disturbing body [m]
y_S	Second coordinate of the Sun in an Earth-centred perifocal reference frame [m]
Z	Third axis of a Cartesian reference frame [–]
z	Distance along the Z-axis [m]
$\boldsymbol{z_B}$	Perturbing body unit vector [–]
z_d	Z component of a disturbing body [m]
z_S	Third coordinate of the Sun in an Earth-centred perifocal reference frame [m]

GREEK SYMBOLS

α	First direction cosine [–]
β	Second direction cosine [–]
Γ	Gamma function [–]
γ	Third direction cosine [–]
δ_{i6}	Kronecker delta [–]
ε	Small parameter [–]
η_i	Short-periodic terms for orbital element i [–]
θ	Perturbing-body phase angle [rad]
κ	Step-size [s]
Λ	Geographic longitude [rad]
Λ	Sun azimuth angle [rad]
$\Lambda_{n,m}$	Angle associated to the tesseral term of the geopotential of degree n and order m [rad]
λ	Mean longitude [rad]
λ	Sun declination angle [rad]
μ	Standard gravitational parameter
μ_d	Standard gravitational parameter of the disturbing body [$\mathrm{m^3\,s^{-2}}$]
μ_3	Standard gravitational parameter of a third body [$\mathrm{m^3\,s^{-2}}$]
μ_E	Earth's standard gravitational parameter [$3.98600441\times10^{14}\,\mathrm{m^3\,s^{-2}}$] [5]
ξ	Gaussian abscissa or node [–]
$\boldsymbol{\rho}$	Position vector body in an unperturbed reference orbit [m]
ρ_0	Reference density [$\mathrm{kg\,m^{-3}}$]
ρ	Atmospheric density [$\mathrm{kg\,m^{-3}}$]
ρ	Reflectivity [–]
τ	Time of last periapsis passage [s]
ϕ	Geocentric latitude [rad]
χ	Reciprocal of SST's second parameter [–]
Ω	Right ascension of the ascending node [rad]
ω	Argument of perigee [rad]
$\boldsymbol{\omega_E}$	Earth's rotational velocity [$\mathrm{rad\,s^{-1}}$]
ω_S	Rate of rotation of the Sun about Earth in an Earth-centred reference frame [$\mathrm{rad\,s^{-1}}$]

OTHER SYMBOLS

$\mathbb{E}$	Standard direct equinoctial elements set [–]
$\boldsymbol{\nabla}$	Gradient operator [–]

1

Introduction

Low Earth orbit and geostationary orbit are two regions of near-Earth space that are very popular for space missions. As a consequence, they also show a high probability of collisions between man-made objects and debris generation due to their high density of Earth-orbiting bodies [6]. Objects such as depleted rocket stages used to bring spacecraft to GEO altitude usually follow a type of highly elliptical orbit (HEO) known as geostationary transfer orbit, which crosses the LEO and GEO regions. The perigee altitude of GTOs is normally between 170 and 650 km, whilst their apogee is near geostationary altitude, i.e. 35 786 km [7]. GTO objects can take years to decay naturally and re-enter Earth's atmosphere [8], which increases the risk of space-debris generation, near the GEO region initially, and within the LEO region almost during their entire lifetime.

Previous studies have shown that orbital perturbations such as those due to Earth's irregular gravity field, luni-solar attraction, atmospheric drag and solar radiation pressure can significantly reduce the natural decay time of GTO objects if wisely exploited, meaning that slightly different launch conditions can lead to significantly different lifetimes [8–10]. However, the accurate long-term propagation of GTOs poses some challenges, mainly due to the existence of resonances caused by the interplay between different perturbations at different parts of the orbit, which can lead to a high sensitivity of the lifetime to initial conditions and environment-related parameters [8, 9, 11, 12]. This problem has led some authors to propose alternative formulations in which the problem is analysed from a statistical point of view and approached using semi-analytical techniques [11, 13, 14].

In this Master thesis, the focus will be put on determining whether the high sensitivity of the orbital evolution of objects in GTO to initial conditions and body characteristics can be exploited in order to achieve faster re-entry for debris generated during actual GEO launches, without the use of additional propellant. By developing new and improving existing software tools capable of propagating the orbital state of GTO debris quickly and accurately, it will be possible to determine whether these lifetime predictions can be used to show compliance with debris-mitigation guidelines for future GEO launches, and what the optimal conditions leading to maximum probability of compliance with those guidelines are.

1.1. Research questions and objective

The main research question to be answered during the development of this Master thesis can be stated as follows:

> *How can orbital perturbations be used to comply with debris-mitigation guidelines for future geostationary transfer orbit objects?*

This main question can be divided into two subquestions, each of which containing further subquestions, which will be answered during the development of this Master thesis:

1. How can the orbital evolution and lifetime of GTO objects be reliably predicted?
    (a) What is the best way to model orbital perturbations to enable fast, yet accurate, long-term propagations?
    (b) What is the accuracy of the lifetime predictions for GTO objects?

2. How do orbital perturbations affect the evolution of GTO objects?
   (a) Which are the most relevant perturbations and which can be neglected?
   (b) How can these perturbations affect the lifetime of GTO objects?
   (c) What is the influence of initial launch conditions, body characteristics and environment-related parameters on the orbital evolution of objects in GTO?
   (d) What are the main sources of uncertainty in the lifetime predictions?
   (e) What are the launch conditions that lead to the shortest lifetimes?

By answering these research questions, it will be possible to reach the research objective, which is formulated as follows:

> *To minimise the lifetime of debris in geostationary transfer orbits by exploiting the effects of orbital perturbations.*

1.2. STRUCTURE

This report is structured in several chapters. First, the context in which the need for minimising the lifetime of GTOs is framed will be given in Chapter 2. The risks of GTO objects for active satellites will be identified, and the main disposal options will be introduced. Proposed debris-mitigation guidelines and the compliance of current GEO launchers will be discussed. Finally, a review of the orbital and body characteristics of debris in GTO will be provided.

Then, in Chapter 3, the principal coordinate systems and reference frames that will be used for modelling the propagation of GTOs will be described. An analysis of the main perturbations affecting GTOs will follow. These perturbations include the geopotential, third-body attraction, atmospheric drag and solar radiation pressure. After that, the interplay between these perturbations in GTOs, which can lead to solar resonances, will be explained.

Once the main concepts and orbital perturbations have been introduced, the numerical approach followed during the first part of the thesis will be discussed in Chapter 4. This approach is based on the propagation of the osculating Cartesian elements with small integrator step-sizes. Preliminary results will be provided, and a feasibility study will be carried out to determine whether the research objective can be reached with this method.

Then, in Chapter 5, a different approach based on semi-analytical satellite theory will be introduced, and the main aspects regarding its implementation into existing software tools and subsequent verification and validation will be covered. This approach is based on the propagation of the mean equinoctial elements with large integrator step-sizes, which enables faster orbital propagations than the numerical approach.

After having assessed the accuracy and performance of the propagator based on the semi-analytical satellite theory, the main results obtained to answer the research questions and reach the research objective will be given in Chapter 6. The application of these results to real cases will follow in Chapter 7, where a case study regarding the launch of a GEO satellite from the Euroepan spaceport in Kourou will be provided.

Finally, the main conclusions of this Master thesis will be summarised in Chapter 8, and recommendations for future research on this topic will be given. The bibliography and appendices including astrodynamics-related equations (Appendix A) and additional plots (Appendix B) will be provided at the end of this document.

2

CONTEXT

The optimisation of the lifetime of objects in GTO can be framed within the context of passive space debris mitigation techniques. In this chapter, the current state of the space debris population will be presented briefly in Section 2.1. The identification of regions with high spatial densities of debris that are crossed by GTO objects and the relatively large number of rocket-related debris that are currently in orbit justify the need to minimise the lifetime of GTO objects. Then, in Section 2.2, a short review of the characteristics of GTOs will provide insight on the disposal options that exist for this type of orbits, the current status of compliance with debris-mitigation guidelines and the orbital and body characteristics of debris in GTO generated during the last years.

2.1. SPACE DEBRIS

Space debris, or orbital debris, represent a hazard for current and future manned and unmanned space missions. Because of the high relative velocities that Earth-orbiting objects can achieve, even small pieces of 1 mm size could render a satellite's subsystem inoperative or perforate an astronaut's spacesuit [15]. Although collisions between large objects are very infrequent (only one accidental collision between two satellites has occurred thus far [16]), the likelihood of a collision between small yet hazardous objects is significantly higher. For instance, in 1999 the International Academy of Astronautics predicted that a collision between trackable objects (i.e. larger than 10 cm [15]) in the altitude region ranging from 800 to 1 000 km would happen in the following 10 to 15 years with a likelihood greater than 50% [17], and the International Space Station (ISS) has to perform orbital manoeuvres about once a year to prevent collisions with trackable debris [18].

The problem of space debris gained public relevance after D. J. Kessler predicted in 1978 that the population of orbital debris would rise exponentially as a result of a run-away effect in which fragments from orbital collisions would increase the likelihood of further collisions and thus the generation of additional fragments, even if no additional satellites were launched in the future [19]. This effect is now known as the Kessler syndrome, and is usually used as justification for the need of active debris removal, also known as debris remediation, i.e. the launch of satellites whose mission would be to remove large inoperative spacecraft either by forcing them to re-enter (and burn up) in Earth's atmosphere (de-orbiting) or by moving them to a graveyard orbit in which the risks of collisions are lower (re-orbiting). However, as of 2016, no active debris removal spacecraft has been launched because capturing a non-cooperative satellite without risk of generating more debris represents a technological challenge that still needs to be overcome [20].

Because of the difficulties associated with the concept of debris remediation, most effort is currently being put into passive debris removal, also known as debris mitigation. The main disadvantage of this approach is that it cannot be applied to satellites that have already been launched. However, it has the potential to reduce the pace at which the orbital debris are generated and prevent the debris population from becoming unmanageably large while technological advances are made in the context of debris remediation. In this case, the disposal options of de-orbiting and re-orbiting exist as well. For satellites in the LEO region (i.e. with apogee altitude lower than 2 000 km), the atmospheric re-entry option is customary, whilst for higher orbits a graveyard orbit is usually chosen due to economic reasons [17]. Some organisations, such as the European Space Agency (ESA) [21], the United States (US) Government [22] and the United Nations [23], have proposed guidelines for passive debris removal in the last decade. Although these guidelines are not enforced by law, it is widely accepted that spacecraft should not remain in near-Earth regions more than 25 years after their end of life [21, 22]. As proposed in [21, 24], the sensitive orbital regions that have to be protected are the LEO region and the zone in the vicinity of the GEO ring.

The need for protecting only the LEO and GEO regions from orbital debris can be justified by the uneven distribution of orbiting objects in near-Earth space. Due to the unique features that LEOs and GEOs can offer, these are the two regions of near-Earth space with the highest density of orbiting bodies (cf. Figure 2.1). Consequently, they are also the regions with highest density of space debris and highest risk of collisions [25].

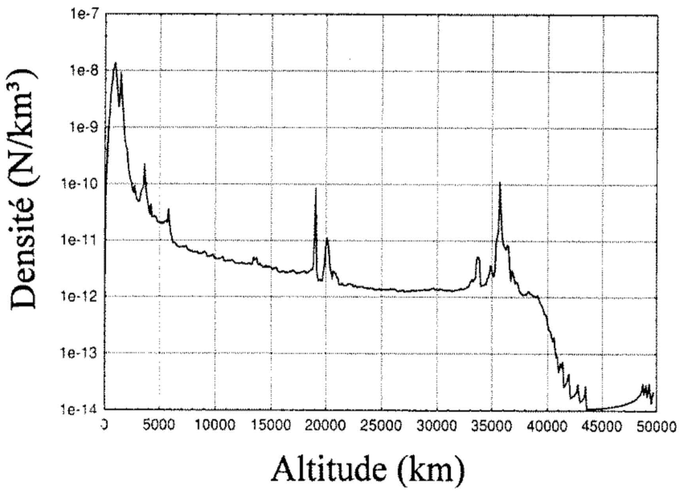

Figure 2.1: Spatial density of objects as a function of orbiting altitude [21]. Note the peaks near LEO (altitudes lower than 2 000 km) and GEO (altitude of 35 786 km) regions.

As of June 2017, the total on-orbit catalogued debris population amounts to almost 17 000 objects [26]. This only includes objects larger than 10 cm, while millions of smaller objects may exist [17]. The debris population can be classified into several categories. Depending on their function, they can be either payloads or rocket bodies used to insert payloads into orbit. For each of these categories, a distinction can be made between objects that remain structurally intact but have reached their end of life, mission-related objects that have separated from the main body, and debris in the strict sense, generated during on-orbit explosions or collisions. In Figure 2.2, it can be seen that, historically, about half of the debris population is or originates from rocket bodies, the other half being or originating from payloads. However, due to China's anti-satellite test in 2007 and the Iridium-Kosmos collision in 2009 [16], a high increase of the payload-related debris has been experienced in the last decade, almost doubling the overall debris population.

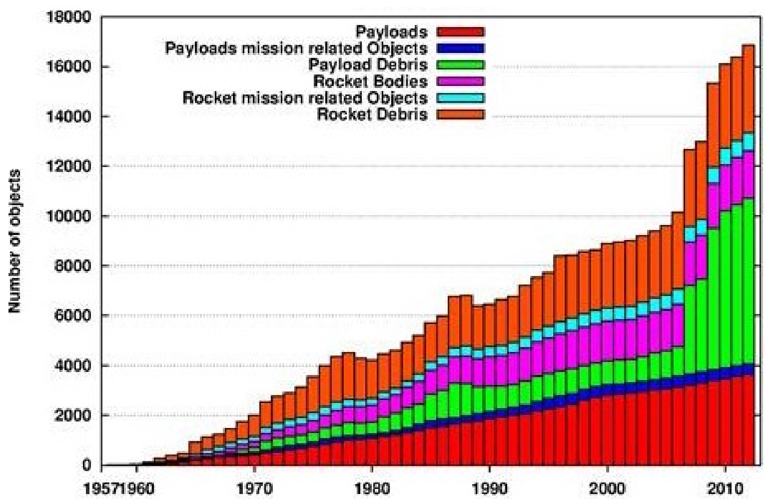

Figure 2.2: Composition of debris object classes in space as of October 2012 [27].

From Figure 2.2 it can be deduced that implementing passive removal strategies is equally important for rocket bodies and payloads, given the historical 50-50% distribution. It is true that at this moment the number of payload-related debris is higher, but this is due to two recent events involving payloads, in which rocket bodies could have been involved as well. Moreover, some studies that have simulated the long-term evolution of the orbital debris population also point out that de-orbiting upper stages is key to maintain a stable space debris environment. A prediction for the year 2200 revealed that the number of total orbital debris larger than 1 mm, 1 cm and 10 cm could be reduced by about 62, 57 and 43%, respectively, just by implementing de-orbiting strategies for all upper stages launched after 2010 with perigee altitude below 2 000 km [28]. Thus, the development of strategies for efficiently removing upper stages and mission-related objects from protected regions is deemed to be sufficiently justified from a practical point of view, and will be the core of this Master thesis.

2.2. GEOSTATIONARY TRANSFER ORBITS

There is no agreement on how to define a highly elliptical orbit quantitatively. Some sources define it in terms of perigee (usually below 1 000 km altitude) and apogee (usually at or above GEO altitude) [29], while others prefer to define it in terms of a minimum value of the eccentricity, typically 0.5 [30]. Some sources refuse to make a distinction between elliptical and highly elliptical orbits [31], thus including in this category any Earth-orbiting object in which the difference between apogee and perigee altitudes is purposely chosen for its advantages from an operational point of view.

Independently of the chosen definition, there are certain types of orbits that are universally considered to be highly elliptical. Some examples are Molnya, Tundra, Loopus and Archimedes orbits [32]. Molnya orbits have perigee altitudes between 450 and 600 km and apogee altitudes around 40 000 km, with an orbital period of half a sidereal day. Tundra orbits have perigee and apogee distances of 17 951 and 53 622 km, respectively, completing one orbital revolution every sidereal day (i.e. 23 h 56 min 4 s). Both orbits have an inclination of 63.4 degrees (also known as critical inclination) to avoid the precession of the line of apsides [33]. Keeping the line of apsides fixed is fundamental for both Molnya and Tundra orbits, as they have been historically used by Russia for communication purposes and thus it is required that their apogee, where the satellite's velocity is smallest, be located above high-latitude regions in order to provide continuous coverage with a low number of satellites. Satellites in Loopus and Archimedes orbits complete three orbital revolutions every sidereal day, and are conceptually similar to Molnya and Tundra orbits, although their apogee and perigee distances differ. Other highly elliptical orbits that do not form a subcategory on their own have been used by scientific missions [30].

In addition to the aforementioned types of HEOs, which are mainly used by satellites during their nominal mission segment, there exist other HEOs that are typically used during transfer of satellites from parking orbits to nominal mission orbits, or to reach the final orbits in a direct ascent from Earth's surface, and that are populated with depleted upper stages from rocket bodies and other mission-related objects. One of the most critical subcategories is the GTO, because bodies following these orbits cross the LEO and GEO protected regions (cf. Figure 2.3). GTOs have a perigee altitude typically below 2 000 km and an apogee near GEO [34]. Their eccentricity is thus about 0.7.

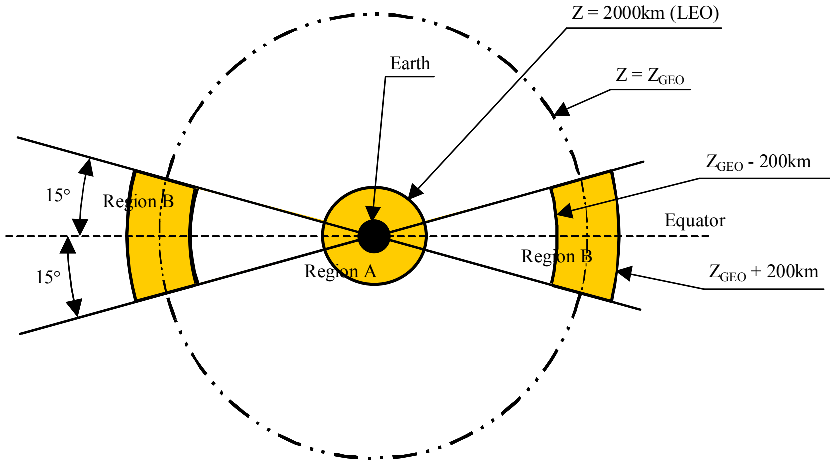

Figure 2.3: Definition of near-Earth space protected regions proposed by IADC [24].

The number of satellites that use elliptical orbits for their nominal mission segment is quite limited. As of December 2015, there were only 37 operative satellites in elliptical orbits, which represents less than 2.7% of the operative satellite population [31]. In contrast, on average about 33 new upper stages and mission-related objects are being left every year in GTOs around Earth [34]. Only about 31% of these objects are currently compliant with debris-mitigation guidelines, i.e. have left or are expected to leave the protected regions in less than 25 years after their end of life, which for GTO objects is usually reached when the payload is separated from the upper stage (i.e. relatively soon after launch). This means that, on average, every two years the population of GTO objects that are not compliant with debris-mitigation guidelines is increased by a number larger than the overall population of operative HEO satellites. These computations only account for objects that are purposely put into orbit according to the planned mission, and not for those that may originate from explosions or collisions.

2.2.1. DISPOSAL OPTIONS

Three mitigatory orbits for GTOs that would comply with the debris-mitigation guidelines defined in [24] by the Inter-Agency Space Debris Coordination Committee (IADC) are identified in [34]. These are: (1) a low-perigee orbit (less than 200 km altitude), which would likely decay in less than 25 years; (2) an orbit between LEO and GEO, with perigee altitude above 2 000 km and apogee altitude below 35 351 km or inclination of more than 15 degrees; and (3) a super-synchronous orbit with perigee and apogee altitudes above 36 221 km. The last option is rarely chosen because it would require large amounts of propellant. According to the same source, only 2 of the 294 GTO objects generated in the period 2004-2012 chose this option. In contrast, 47 objects have chosen mitigatory orbit 1, while 41 objects have chosen mitigatory orbit 2. More than 90% of the objects that were put in low perigee orbits had already re-entered by 2014. The remaining 204 GTO objects, i.e. almost 70%, were left in orbits that are not compliant with IADC guidelines.

From the data of past missions, it could be deduced that the disposal strategies of atmospheric re-entry and disposal in medium Earth graveyard orbits have similar implementation shares. However, a more detailed analysis can lead to a different conclusion. For instance, the fact that some of the GTO objects that were placed in mitigatory orbit 2 had initial perigee altitudes as high as 14 676 km [34] may suggest that option 2 is not that common amongst regular GTOs, i.e. with perigee altitudes lower than 2 000 km. On the other hand, some of the objects that re-entered Earth atmosphere did not even complete one orbital revolution after their end of life, as their initial perigee altitudes were as low as 110 km [34].

In any case, independently of what has been customary in the last decade, some authors claim that a low perigee altitude leading to a re-entry in less than 25 years is preferable in most scenarios [30, 35], although it may not be always feasible depending on the chosen initial perigee altitude. Some of the advantages of a de-orbiting disposal are:

- **Natural decay**. As the evolution of the orbit is driven by orbital perturbations, there is no need for carrying additional propellant on-board that would be needed if re-orbiting was chosen. Moreover, the disposal into a graveyard orbit can potentially fail, while choosing an initial perigee altitude below 200 km would remove this risk as the decay would happen naturally.

- **Definitive measure**. Re-orbiting objects to graveyard orbits is a palliative measure that can be acceptable at this time for the current definition of protected regions. However, in the future it is possible that additional protected regions between LEO and GEO will be proposed (the protection of Global Navigation Satellite Systems regions is currently being studied [36]) and thus it is not guaranteed that these objects in graveyard orbits will never interfere with any other missions. Consequently, de-orbiting is always preferable in the long-term.

For these reasons, the focus is put on the natural decay of geostationary transfer orbits in this document. However, although de-orbiting is always preferable from the point of view of guaranteeing the viability of future spaceflight, it also poses some risks and challenges. The uncontrolled re-entry of large objects, such as depleted rocket stages, may eventually result in catastrophic damage for humans on Earth if the objects do not fully disintegrate in the atmosphere and fall on inhabited areas. Thus, regulations require the total casualty risk to be no larger than 10^{-4} in case of uncontrolled re-entry [37]. This constrains the size and materials of GTO objects that can be de-orbited, as their re-entry is typically uncontrolled, especially when the orbit takes several months or years to decay.

Another challenge in the context of passive de-orbiting of GTO objects is related to the difficulties found during orbit propagation and estimation of the re-entry time. GTOs interface with regions in which the main perturbations are drag and Earth's irregular gravity field, and regions where third-body perturbations are predominant. This can produce an effect known as Sun-synchronous resonance, which can lead to very different orbital evolutions for slightly different initial conditions [8, 9, 11, 34]. This effect and the main characteristics of the dynamic evolution of GTOs are covered in Section 3.3.

2.2.2. COMPLIANCE WITH DEBRIS-MITIGATION GUIDELINES

An exhaustive study of the GTOs that were used for the launch of 185 GEO satellites in the period 2004–2012 is provided in [34]. The most relevant findings of this study, regarding the chosen disposal options and compliance with debris-mitigation guidelines, are summarised in this section.

Three types of orbits that would comply with debris-mitigation guidelines are defined:

- **Compliant orbit 1: low-perigee orbit**. The perigee altitude is sufficiently low so as to guarantee a re-entry in less than 25 years.
- **Compliant orbit 2: medium-Earth orbit**. The orbit stays between LEO and GEO, outside the protected regions.
- **Compliant orbit 3: super-synchronous orbit**. The LEO and GEO protected regions are avoided by choosing and altitude higher than that of GEO.

On the other hand, the non-compliant orbits can be subdivided in three categories: LEO-crossing only, GEO-crossing only, and LEO- and GEO-crossing.

In Figure 2.4, the percentage of the orbits that corresponds to each of these categories can be visualised broken down by launcher. As can be seen, most launchers are not complying with debris-mitigation guidelines.

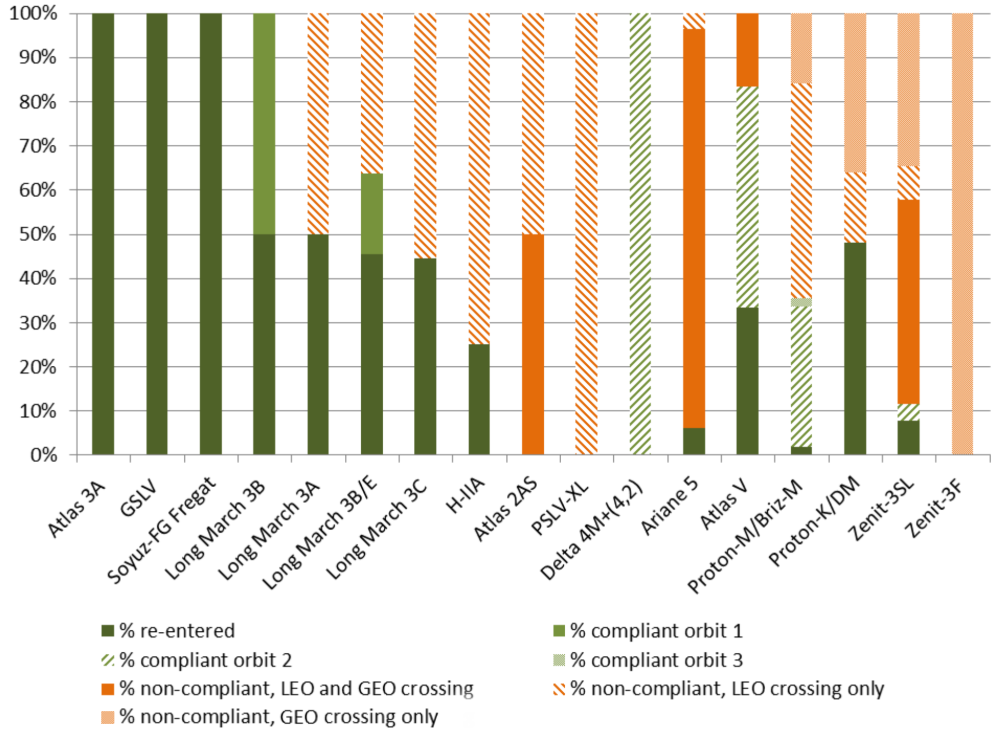

Figure 2.4: Orbits of upper stages and mission related debris from GEO launches in the period 2004-2012 [34].

However, to get an idea on what the contribution of each of these launchers is to the non-compliant debris population it is necessary to analyse the absolute number of launches. The major contributor is Ariane 5, as this launcher was used in 23% of the studied cases and almost none of them adopted a compliant orbit for the upper stages and mission-related debris, leaving them in GTO. Ariane 5 is mainly used by European countries and is launched from Kourou, close to the equator, which allows for launches with low inclinations, which is attractive for GEO missions.

Another big contributor is Proton-M, representing about 29% of the GEO launches, although in this case none of the generated debris was both LEO- and GEO-crossing. This launcher is mainly used by Russia. In this case, two impulsive shots are performed to reach GTO, resulting in an intermediate transfer orbit with an apogee at about 15 000 km, leading to debris that will not interfere with the GEO protected region.

Finally, the United States of America used the Atlas and Delta families of launchers for GEO payloads. However, those only account for about 5% of the GEO launches in the studied period, so their contribution to the debris population is quite limited. Additionally, most of the resulting debris ended up in compliant orbits or have already re-entered.

In conclusion, the major generator of debris crossing protected regions has been Ariane 5 in the last years. Thus, later in this Master thesis the focus will be put especially on studying the applicability of the developed theory and the obtained results to the case in which the launch is performed from the Europan spaceport in Kourou, in order to determine whether the initial launch conditions can be chosen such that the orbits of the resulting debris have a lifetime shorter than 25 years.

2.2.3. CHARACTERISATION OF OBJECTS IN GTO

In order to generate relevant results, it will be necessary to propagate the orbits of several objects in different GTOs. Some of the parameters will have to be fixed during the propagation, and thus it is convenient to know what the usual values of these parameters are for objects in GTO. This was achieved by studying the two-line elements (TLE) of GTO objects tracked by the US Strategic Command [38] (cf. Section 5.2.2 for a description of the TLE format specification). The last TLEs of all the objects tracked since the 1st of January of 2010 until the 28th of April of 2017, with perigee altitude up to 1 000 km and apogee altitude between 34 800 and 36 800 km, were requested. The characteristics of a total of 673 unique objects were obtained.

The distribution of the values of the Keplerian elements for these 673 orbits are provided in the following paragraphs. The definition of the Keplerian orbital elements is provided in Section 3.1.2.

From Figures 2.5 and 2.6 it can be seen that the values of the perigee and apogee altitudes of the studied objects are considerably spread across the specified ranges of 0–1 000 km and 34 800–36 800 km, respectively. In the case of the apogee, the largest frequencies are obtained around the altitude of 35 700 km (GEO altitude is 35 786 km). In the case of the perigee, many of the tracked objects have values of about 600 km. However, objects in these orbits would take very long to re-enter (several decades under most circumstances), so a smaller initial perigee altitude (around 200 km) will be chosen later in order to obtain results that can be used to comply with guidelines, which set a lifetime of 25 years as a reasonable limit.

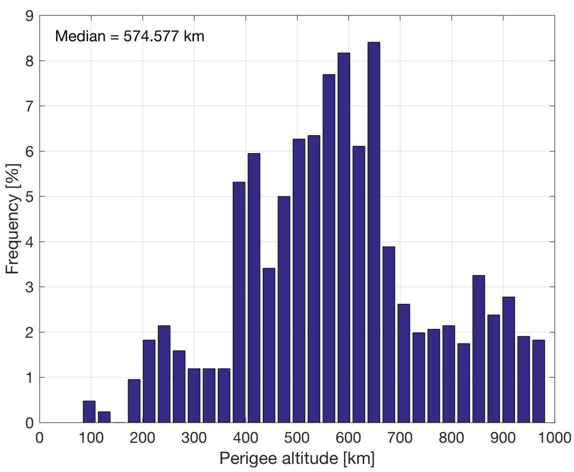

Figure 2.5: Distribution of the perigee altitudes of GTO objects tracked since January 2010.

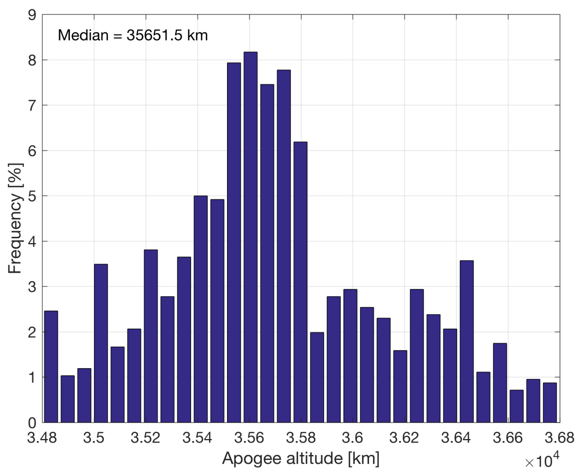

Figure 2.6: Distribution of the apogee altitudes of GTO objects tracked since January 2010.

Regarding the orbital inclination, two peaks at about 7 and 22 degrees are observed in Figure 2.7. Very likely the first peak corresponds to launches from Kourou, which cannot launch directly at inclinations lower than 5 degrees, while the second peak may correspond to launches from Cape Canaveral with inclinations close to 30 degrees for objects that have undergone correcting manoeuvres leading to slightly smaller inclinations. Thus, a value of 10 degrees for the inclination seems reasonable for studying the evolution of objects in GTO, while other inclinations (closer to 20-30 degrees) should also be studied in order to get the whole picture.

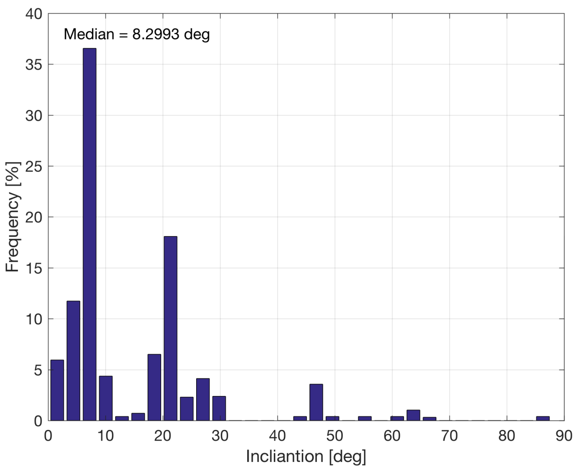

Figure 2.7: Distribution of the inclinations of GTO objects tracked since January 2010.

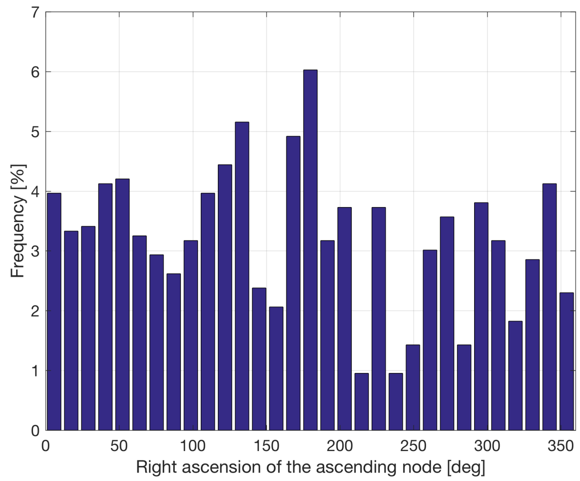

Figure 2.8: Distribution of the right ascensions of the ascending node of GTO objects tracked since January 2010.

The values of the right ascension of the ascending node are distributed relatively evenly throughout the range 0–360 degrees, as seen in Figure 2.8. This suggests that this parameter may have to be chosen as one of the optimisation variables. A similar distribution is observed for the argument of perigee in Figure 2.9. However, as will be discussed later in this report, the initial argument of perigee will have to be set at either 0 or 180 degrees in order to be within the GEO ring when GEO altitude is reached. Thus, the widespread distribution observed in Figure 2.9 can be explained by the fact that these values do not correspond to initial arguments of perigee but to the value after an arbitrary period of time. Taking into account that some perturbations can introduce secular variations in the value of the argument of perigee, it is reasonable to expect this kind of distribution.

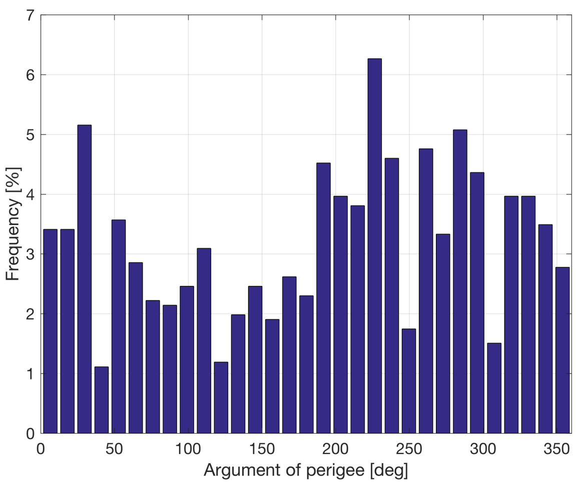

Figure 2.9: Distribution of the arguments of perigee of GTO objects tracked since January 2010.

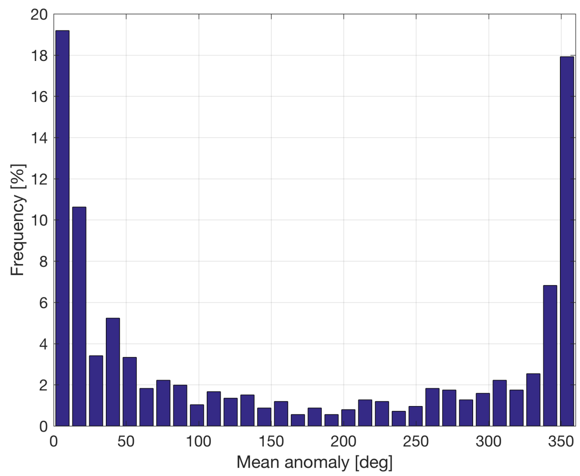

Figure 2.10: Distribution of the mean anomalies of GTO objects tracked since January 2010.

The mean anomaly has a peak around the value of 0 degrees, as can be seen in Figure 2.10. The mean anomaly is a fast variable that changes throughout each orbital revolution from 0 to 360 degrees, so any value in that range could be expected. However, the fact that most of the TLEs correspond to mean anomalies close to 0 degrees can have two possible explanations. Since the obtained data correspond to the last available TLEs of the considered objects, it is possible that some of these TLEs would correspond to the final epoch just before re-entry. Since re-entry happens at (or close to) perigee, a larger number of mean anomalies close to 0 can be expected. Another possible explanation is that, given the high eccentricity of GTOs, it is easier to track the objects when they are close to Earth (at perigee and thus with mean anomalies close to 0 degrees) than when they are further away at GEO altitude.

Finally, the ballistic coefficient (cf. Eq. (4.7)) of the tracked objects was studied. As seen in Figure 2.11, most of the objects had values below 0.01 m^2/kg. A few objects had ballistic coefficients as large as 8 m^2/kg, but these have been left out of the plot so that the region where the most objects are located can be better seen. Previous studies on the evolution of GTOs have recommended to use a mass of about 2 900 kg and a cross-sectional area of about 14.5 m^2 as characteristic values for debris in GTO [34]. For a drag coefficient of 2.2 (cf. Section 3.2.3), these values lead to a ballistic coefficient of 0.011 m^2/kg, which coincides with the median ballistic coefficient obtained from the 673 studied GTO objects.

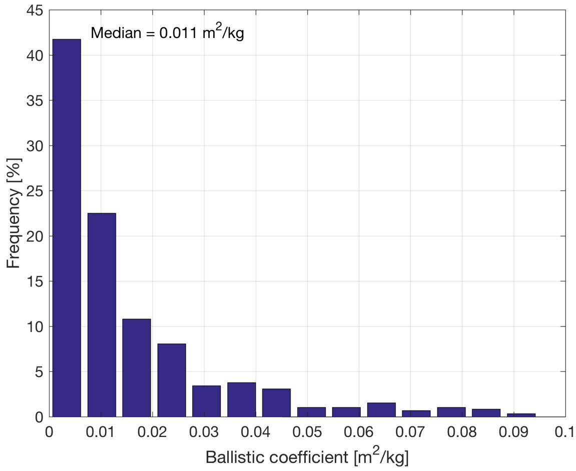

Figure 2.11: Distribution of the ballistic coefficients of GTO objects tracked since January 2010.

3

THEORETICAL BASIS

In this chapter, the main physical concepts and mathematical tools necessary to understand and model the temporal evolution of objects in GTO will be presented. First, a few widely used coordinate systems, namely Cartesian, Keplerian and equinoctial elements, will be described in Section 3.1. Then, the main orbital perturbations that affect the evolution of objects in GTO will be introduced in Section 3.2. These perturbations are caused by Earth's irregular gravity field, luni-solar attraction, atmospheric drag and solar radiation pressure. Finally, the complex orbital dynamics of GTOs will be described in Section 3.3, with especial emphasis on the solar resonance effect.

3.1. REFERENCE FRAMES AND COORDINATE SYSTEMS

A necessary step before beginning a mathematically consistent analysis and modelling of orbital perturbations is to define the frame(s) of reference and coordinate system(s) that will be used. In the field of astrodynamics, it is customary to use either geocentric (i.e. centred at Earth's centre of mass) or heliocentric (i.e. centred at the solar system's barycentre) reference frames, the former being mostly used for describing the motion of Earth satellites and the latter for interplanetary spaceflight [39]. In the case of GTOs, the motion takes place always within the sphere of influence of Earth, and thus it is preferable to use a geocentric reference frame and consider the Sun, the Moon and other planets as third bodies. Indeed, a geocentric reference frame has been widely used in previous analyses of the dynamics of GTO objects [8, 9, 11, 12, 30, 34]. For this reason, heliocentric reference frames will not be considered in this report.

On the other hand, there is no consensus amongst the scientific community on the coordinate system that is most suitable for modelling the dynamics of GTOs. Keplerian elements provide direct insight on the characteristics and the evolution of the orbit, so it may be suitable for simple analytical studies. On the other hand, Cartesian components are more suitable for integration and mathematical manipulation as they do not present singularities. Equinoctial elements can provide the best of these two options, as they are non-singular for GTOs. Given their relevance, all these options are explained in more detail in the following subsections.

3.1.1. CARTESIAN COMPONENTS

In a Cartesian coordinate system, a point is specified by its signed distances from fixed perpendicular axes [40]. In Figure 3.1a, a sketch of a three-dimensional coordinate system is given, in which the coordinates of a point are called x, y and z, and the reference frame has origin O and axes X, Y and Z.

In the field of astrodynamics, several geocentric Cartesian coordinate systems have been used historically. Probably, the most common ones are Earth-centred rotational (ECR) and Earth-centred inertial (ECI) [39]. In the former, the X-axis is aligned with the International Reference Meridian, also known as prime meridian or Greenwich meridian. The Z-axis is aligned with the International North Pole, which does not coincide exactly with the axis of rotation of Earth. The Y-axis is perpendicular to both X and Z. This reference frame is not inertial, as it rotates with Earth (once every sidereal day), meaning that any point on the surface of Earth has fixed components. For this reason, this system is suitable for describing the location of objects on Earth, but in order to describe the motion of Earth-orbiting bodies, a (pseudo-)inertial reference frame such as ECI is typically preferable, as the equations of motion become simpler.

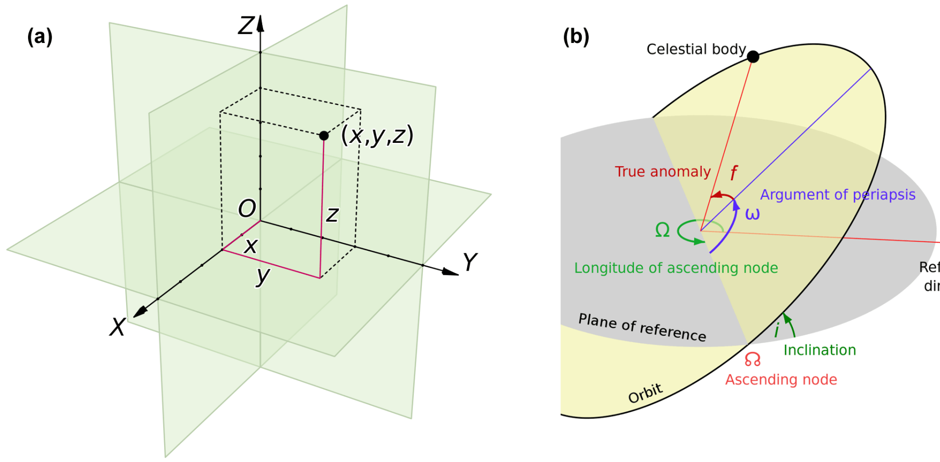

Figure 3.1: **(a)** Three dimensional Cartesian coordinate system [40]. **(b)** Definition of some of the Keplerian elements [41].

The Earth-centred inertial reference frame also has its origin at the centre of mass of Earth, but the orientation of its axes is fixed with respect to inertial space. It is common to define the X-axis pointing towards the location of the vernal equinox [39], also known as the first point of Aries. This direction is defined by the relative position of the Sun with respect to Earth at the vernal equinox, i.e. around March 20/21, when the Sun crosses the equatorial plane, leading to day and night being equally long everywhere on Earth. The Z-axis, on the other hand, is aligned with Earth's rotational axis, and the Y-axis is perpendicular to both X and Z. The first point of Aries and Earth's rotational axis are not actually fixed with respect to distant stars, but undergo slow oscillations known as luni-solar precession and nutation. For this reason, ECI is actually pseudo-inertial, and it has to be defined with respect to a certain epoch in order to be able to accurately describe the location of orbiting objects. The most common system definition is called J2000, with Earth's mean equator and equinox at 12:00 TT on 1 January 2000 [39].

It has been mentioned previously (and it will be discussed later in more detail) that, in the context of modelling of GTOs, some authors use Keplerian components to describe the temporal evolution of the orbit. However, in [9, 11], a Cartesian geocentric reference frame with the X-axis pointing in the direction of the GTO perigee is chosen for describing the position of third bodies (mainly the Sun). In this reference frame, the Z-axis has the same direction as the orbital angular momentum, and the Y-axis is perpendicular to X and Z. It is noteworthy to say that this frame of reference cannot be considered inertial, as the line of apsides (and thus the perigee) can precess relatively fast. In fact, for semi-major axes of about 15 000 km, the perigee location drifts at a rate similar to Earth's mean motion (close to 1 degree per day), giving rise to the Sun-synchronous resonance that will be discussed in Section 3.3.1. Very insightful expressions relating the rate of change of orbital parameters to the disturbing body's x_d, y_d and z_d components defined in this reference frame are given in [9, 11]. This reference frame will appear again later in this report, referred to as the Earth-centred perifocal (ECP) reference frame.

3.1.2. KEPLERIAN ELEMENTS

Keplerian elements, also known as orbital elements, are a set of parameters that can be used to uniquely identify an orbit [41]. The parameters that define the orbital plane with respect to a plane of reference are the inclination i and the longitude or right ascension of the ascending node (RAAN) Ω, depicted in Figure 3.1b. With these two parameters, and a plane of reference (for Earth-orbiting objects, typically the equatorial plane) and a reference direction (typically the first point of Aries), the orbital plane is fully defined. However, within one orbital plane, there exist infinitely many orbits, and thus additional parameters are required to uniquely identify a particular orbit. Two of these parameters define the size and shape of the orbit, namely the semi-major axis a and the eccentricity e. Both of them are related to the minimum (i.e. periapsis, r_p) and maximum (i.e. apoapsis, r_a) distances from the centre of mass of the central body to the orbiting body:

$$a = \frac{r_a + r_p}{2}; \qquad e = \frac{r_a - r_p}{r_a + r_p} \tag{3.1}$$

The only remaining parameter required to fully define an orbit is the argument of perigee ω. This angle is measured in the orbital plane, from the ascending node to the periapsis (cf. Figure 3.1b). For circular orbits

($e = 0$), this parameter is undefined, or in other words, the orbit can be fully determined without specifying a value for ω. Similarly, when the orbital plane coincides with the reference plane ($i = 0$), there is no need to provide a value for Ω.

In addition to these five parameters (a, e, i, Ω and ω), which are known as orbital elements, it is possible to describe the state (i.e. location and velocity) of an orbiting body by providing one additional parameter. This parameter is typically related to the time elapsed or the angle travelled by the body since a specific epoch. It is common to find sources in which all the sixth parameters are referred to as orbital elements, although some authors have noted that this is not correct as one of them depends on the motion of the body, and thus should be considered as a parameter but not as an orbital element [39]. However, in this document, the terms orbital elements and orbital parameters will be used interchangeably.

Several definitions for the sixth orbital parameter exist. One of them is the time of last periapsis passage τ. Another common parameter that also varies linearly but is defined as an angle is the mean anomaly M, which is simply the mean motion ($n = 2\pi/T$) times ($t-\tau$), with t the current time. Since a body in an elliptical orbit moves faster at periapsis than at apoapsis, the mean anomaly does not coincide with the actual angle swept by the body (except for circular orbits), which is called the true anomaly f (cf. Figure 3.1b). This angle, as well as the eccentric anomaly E, are also widely used in astrodynamics. In some cases, the mean motion or the true anomaly at a certain epoch (M_0 or f_0) are used as the sixth parameter.

3.1.3. EQUINOCTIAL ELEMENTS

The set of parameters (a, e, i, Ω, ω and M) is used by several authors for describing orbital perturbations generically [39, 42] and also for analysing the dynamics of GTOs in particular [9, 11]. However, in [11, 14] these parameters are not directly used as a set of orbital elements, but instead a dedicated set of orbital elements is proposed, which is obtained by combining the basic six parameters. This set of parameters is suitable for orbits with high eccentricities and inclinations other than 180 degrees (GTOs typically have low inclinations as the final orbit of the payload needs to have zero inclination). The set, called equinoctial elements, is defined as follows [14]:

$$\mathbb{E} = \begin{pmatrix} a \\ h \\ k \\ p \\ q \\ \lambda \end{pmatrix} = \begin{pmatrix} a \\ e \sin(\omega + \Omega) \\ e \cos(\omega + \Omega) \\ \tan i/2 \sin\Omega \\ \tan i/2 \cos\Omega \\ M + \omega + \Omega \end{pmatrix} \tag{3.2}$$

although some authors replace the terms $\tan i/2$ by $\sin i/2$ [11].

Actually, there are two possible definitions of equinoctial elements: direct and retrograde. The equations given in [14] for long-term semi-analytical propagations are generic, meaning that they can be used with any of the two sets. The authors use the parameter I in their equations, which has to be substituted by 1 when direct equinoctial elements are being used or by -1 for retrograde equinoctial elements. Since direct equinoctial elements work better for prograde orbits, as they are singular for inclinations of 180 degrees while retrograde elements are singular for inclinations of 0 degrees, and given that most GTOs are near-equatorial and prograde, in this report only the direct set will be used.

The axes of the direct equinoctial reference frame, $\boldsymbol{f}$, $\boldsymbol{g}$ and $\boldsymbol{w}$, depicted in Figure 3.2, are defined as follows:

1. $\boldsymbol{f}$ and $\boldsymbol{g}$ lie both in the orbital plane.
2. $\boldsymbol{w}$ is parallel to the angular momentum vector of the satellite.
3. The angle between $\boldsymbol{f}$ and and the ascending node is equal to the value of the right ascension of the ascending node.

As can be seen in Eq. (3.2), equinoctial elements contain five slow parameters: a, the semi-major axis; h and k, the $\boldsymbol{g}$ and $\boldsymbol{f}$ components of the eccentricity vector; and p and q, the $\boldsymbol{g}$ and $\boldsymbol{f}$ components of the ascending node vector. Additionally, they contain one fast parameter: λ, the mean longitude. The eccentricity vector has a magnitude equal to the value of the eccentricity and points towards the perigee, whilst the ascending node vector has a magnitude of $\tan i/2$ and points towards the ascending node [14].

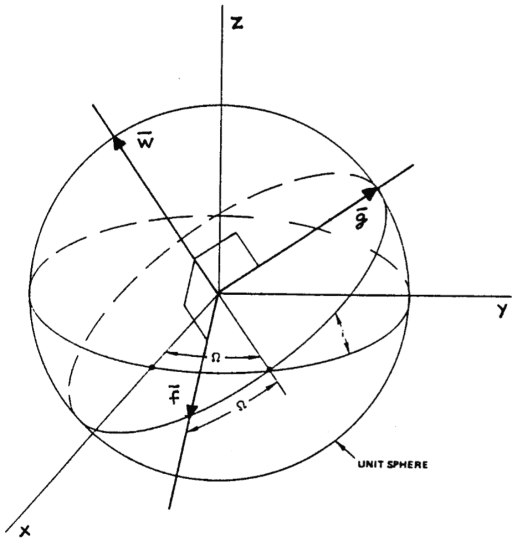

Figure 3.2: Direct equinoctial reference frame [14].

At this point, the Cartesian components and Keplerian elements coordinate systems have been described. As mentioned earlier, it is possible that both of them will have to be used in different phases of the Master thesis, as each provides advantages and disadvantages. For instance, integration of the equations of motion may be simpler and more reliable using Cartesian components, but once integrated the orbital elements of the orbit may be of interest for interpreting these integration results. Thus, transformations between the discussed systems are required. In Section A.1.2, the equations and steps required to perform such transformations are reported. Frame transformations involving equinoctial elements can be found in Sections A.1.3 and A.1.4.

3.1.4. LOCAL TIME OF LAUNCH

Many authors have identified the influence that the epoch of launch has on the evolution of GTOs [8, 9, 11]. Some of them have provided graphs in which the expected lifetime is plotted as a function of launch time (cf. Figure 3.3), while others have provided the evolution of the perigee altitude (or the lifetime) as a function of day of year and local time of the ascending node (or local time of perigee) at the beginning of the propagation (cf. Figure 3.4).

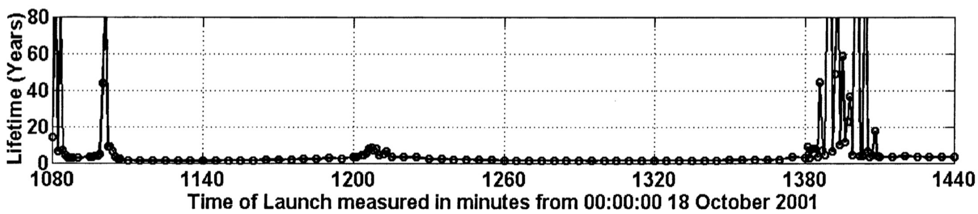

Figure 3.3: Evolution of the orbital lifetime of a GTO object as a function of the time of launch [8].

If the period of time since launch until injection into GTO is neglected, the initial epoch is just the launch epoch (which is universal and does not depend on the launch site). Most of the components of the initial Keplerian state can also be directly inferred or are chosen during mission design: the perigee and apogee altitudes (and thus the semi-major axis and eccentricity) can be chosen depending on the ascent profile and/or the performed impulsive shots; the inclination can be chosen with some restrictions (depending on the latitude of the launch site); the argument of perigee has to be chosen equal to 0 or 180 in order to guarantee that the satellite will reach the GEO altitude when it is in the equatorial plane (and not when it is e.g. over one of Earth's poles); and the true anomaly varies as the body orbits about Earth, so it can be set to 0 to initialise the propagation at perigee. However, the initial RAAN cannot be chosen freely, and is given by the launch time and launch location. Given the relevance of the initial local time of launch, it is convenient to introduce a procedure to determine the initial RAAN from the local time of launch (and launch site).

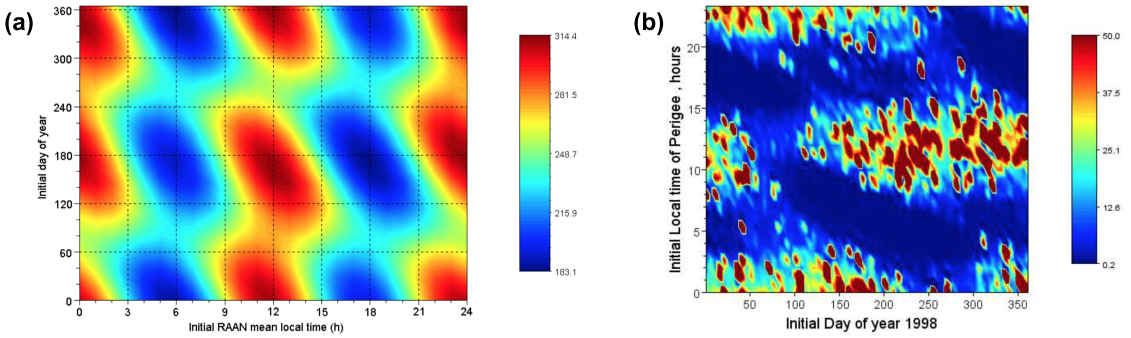

Figure 3.4: **(a)** Mean altitude of perigee over 4 years (initial perigee altitude is 250 km) as a function of initial day of year and mean local time of the ascending node for a GTO with 7 degree inclination and considering only perturbations due to J_2 and luni-solar attraction [9]. **(b)** Lifetime variations with respect to initial date and local time of perigee for a GTO with 23 degree inclination [11].

The RAAN is the angle measured from the first point of Aries or vernal equinox to the ascending node on the equatorial plane. Assuming a spherical Earth, this is equivalent to measuring the difference in longitude between the projections of the ascending node and the vernal equinox on Earth's surface (both points will lie on the equator).

The longitude of the vernal equinox can be obtained from the Greenwich Sidereal Time (GST), which is the angle from the vernal equinox to the Greenwich meridian expressed in hours. Its value in degrees can be obtained from the following equation [33]:

$$GST = 99.690983° + 36000.768925° T + 0.000387° T^2 + \frac{360°}{24} UT \tag{3.3}$$

where T is the number of Julian centuries of 365.25 days which have elapsed since noon on January 0 1900:

$$T = \frac{JD_{J2000} + \frac{t}{86400} - JD_{J1900}}{36\,525} \tag{3.4}$$

where the Julian days of J2000 and J1900 are, respectively, 2 451 545 and 2 415 020, and t is the epoch of interest in seconds since J2000.

The universal time UT in hours is given by:

$$UT = \left[12 + \frac{t}{3\,600}\right] mod_{24} \tag{3.5}$$

From the definition of GST, it is clear that the longitude of the vernal equinox will be:

$$\Lambda_{VE} = 360° - GST \tag{3.6}$$

Then, the RAAN can be expressed as:

$$\Omega = \Lambda_{AN} - \Lambda_{VE} = [\Lambda_{AN} + GST]\, mod_{360} \tag{3.7}$$

The longitude of the ascending node Λ_{AN} can be determined from a spherical trigonometric construction using the geocentric latitude ϕ and geographic longitude Λ of the launch site and the initial orbital inclination i. Assuming a launch in an eastward direction (i.e. $i < 90$ deg), it can be shown that [33]:

$$\Lambda_{AN} = \Lambda - \arcsin \frac{\tan\phi}{\tan i} \tag{3.8}$$

Note that Eq. (3.8) is only valid for $i \geq \phi$. Indeed, launches from a latitude of e.g. 5 degrees to an orbit with an inclination smaller than 5 degrees are not possible unless an inclination-correction manoeuvre is conducted. These corrections are typically performed at high altitudes (at GEO altitude or even higher), where they are less expensive in terms of delta-V (and thus in terms of propellant expenditure) [39].

Using Eq. (3.7), the initial RAAN can be determined given the launch site, launch epoch and initial orbital inclination. However, the launch epoch cannot be directly determined from the RAAN due to the non-invertibility of the "modulo day" (a certain epoch corresponds to a unique RAAN, but a certain RAAN corresponds to infinite epochs). However, if the range of possible epochs is limited to one day, then it *is* possible to obtain the launch epoch from the RAAN using an iterative procedure.

3.2. ORBITAL PERTURBATIONS

The motion of a satellite in a non-rotating reference frame is described by [39]:

$$\frac{\mathrm{d}^2\boldsymbol{r}}{\mathrm{d}t^2} + \frac{\mu}{r^3}\boldsymbol{r} = -\nabla\tilde{R} + \boldsymbol{f} \tag{3.9}$$

where $\boldsymbol{r}$ is the position vector of the satellite with respect to the system barycentre, μ is the standard gravitational parameter of the central body, $\tilde{R}$ is the disturbing potential and $\boldsymbol{f}$ is the disturbing acceleration. Under the only influence of a point-like gravitational attraction, the right-hand side becomes 0 and the motion of a body is described by a so-called Keplerian orbit [39]. The main characteristic of its motion is that the first five orbital elements remain constant, while the time derivative of the mean anomaly equals the mean motion. Thus, it is possible to know the state of the orbiting body at any time in the future (and in the past) immediately, with the same computational effort regardless of the epoch of interest.

However, this situation is rarely encountered in practice. Planet-orbiting bodies are influenced by the attraction of the planet's primary(ies) and moons, and by other close planets. Moon-orbiting bodies also experience strong third-body perturbations. When these bodies have an atmosphere, drag can also influence their orbits significantly. Stellar flux also perturbs the orbits of these bodies, so even a satellite orbiting an isolated star would not follow a Keplerian orbit. Moreover, celestial bodies typically do not have perfectly spherical mass distributions, leading to different gravitational attraction throughout the orbit. Finally, other perturbations, such as tides and relativistic effects, can also cause significant effects over long periods of time [39].

In order to accurately predict the state of an Earth-orbiting body, some of these perturbations cannot be neglected. For certain types of HEOs, such as GTOs, the minimum dynamical model that yields reliable results includes the expansion and usage of Earth's spherical harmonic gravity field model up to degree and order 7, solar and lunar gravity, atmospheric drag and solar radiation pressure (including Earth's shadow) [11, 13]. The modelling of these perturbations is discussed in the following subsections. As will be shown in Section 3.2.5, other perturbations can be neglected, so they will not be discussed in detail in this report.

When the relevant perturbations are included in the acceleration model, the disturbing potential in Eq. (3.9) will be given by $\tilde{R} = \tilde{R}_{SH} + \tilde{R}_{3B}$, i.e. the sum of the disturbing potentials due to the geopotential (expressed as a spherical harmonics expansion) and to gravitational attraction by third bodies, which will be provided later in Eqs. (3.11) and (3.13), respectively. On the other hand, the disturbing acceleration will be given by $\boldsymbol{f} = \boldsymbol{a_D} + \boldsymbol{a_{SRP}}$, i.e. the sum of the disturbing accelerations due to atmospheric drag and solar radiation pressure, which will be provided later in Eqs. (3.15) and (3.19), respectively.

When these perturbations are considered, the analytical integration of the equations of motion is not possible anymore [39]. This means that the propagation of the orbit must rely on numerical methods, in which the orbit for a certain epoch can only be accurately known if it is known at a prior close-in-time epoch, i.e. if a sufficiently small integration step-size is used, which increases computational times. However, some authors have derived analytical expressions up to a certain order describing the temporal evolution of Keplerian elements [43] and some others have used a semi-analytical approach [44], which enables a faster orbit propagation (using large step-sizes in the order of one day) through the removal of short-period terms. This technique, which has been applied successfully to the long-term propagation of GTOs, reducing computation times by several orders of magnitude, will be discussed in more detail in Chapter 5.

3.2.1. GEOPOTENTIAL

The gravitational potential of a point mass and that of a spherical body with a radially-symmetric mass density distribution can be shown to be equivalent and equal to [39]:

$$U = -\frac{\mu}{r} \tag{3.10}$$

with $\mu = GM$ the gravitational parameter of the body and r the distance to the centre of mass of the body. For a spherical body, this equation is only valid for $r \geq R$, with R the radius of the body.

Earth is not a perfect sphere with a radially symmetric mass distribution, and thus Eq. (3.10) cannot be used when high accuracy is desired. To account for this fact, Earth's gravitational potential, or geopotential, can be written as [39]:

$$U = -\frac{\mu_E}{r} + \tilde{R}_{SH} = -\frac{\mu_E}{r}\left[1 - \sum_{n=2}^{\infty} J_n \left(\frac{R_E}{r}\right)^n P_n(\sin\phi) + \sum_{n=2}^{\infty}\sum_{m=1}^{n} J_{n,m}\left(\frac{R_E}{r}\right)^n P_{n,m}(\sin\phi)\cos m(\Lambda - \Lambda_{n,m})\right] \tag{3.11}$$

where $\tilde{R}_{SH}$ is the disturbing potential, ϕ the geocentric latitude, Λ the geographic longitude, and $J_{n,m}$ and $\Lambda_{n,m}$ dimensionless parameters and angles, respectively, of degree n and order m that are found empirically. $P_n(\sin\phi)$ are Legendre polynomials and $P_{n,m}(\sin\phi)$ are associated Legendre functions of the first kind that can be obtained from recurrence relations given in [39].

Eq. (3.11) can be written is several ways. Another possibility is to use the coefficients $C_{n,m}$ and $S_{n,m}$. When these values are provided, $J_{n,m}$ and $\Lambda_{n,m}$ can be found using the following relations:

$$J_{n,m} = \sqrt{C_{n,m}^2 + S_{n,m}^2} \quad ; \qquad \Lambda_{n,m} = \frac{1}{m} \arctan \frac{S_{n,m}}{C_{n,m}} \tag{3.12}$$

The coefficients $J_{n,m}$, also known as J-terms, are currently known at least up to degree and order 2 150, thanks to the analysis of orbital data and missions such as the Gravity Recovery and Climate Experiment (GRACE), which has been used to define the so-called GGM02C geopotential model, which is a combination of the GGM01 model developed prior to GRACE and the GGM02S model obtained exclusively from GRACE orbital data [45]. Additionally, weekly updates of the values of $C_{n,m}$ and $S_{n,m}$ coefficients up to degree and order 5, as they become more accurate with the acquisition of new data, are provided in [46].

Depending on the values of the degree n and order m, the different harmonic terms represent deviations of the geopotential in a certain direction and receive different names. When $n \neq 0$ and $m = 0$, the terms are referred to as zonal harmonics and they represent deviations of the shape and mass distribution in the north-south direction. If $n = m \neq 0$, the terms are called sectorial harmonics and account for deviations in the east-west direction. The terms in which $n \neq m \neq 0$ are called tesseral harmonics, although sometimes all the terms with $m \neq 0$ are referred to as tesseral harmonics. A sketch of the different types of harmonics is provided in Figure 3.5.

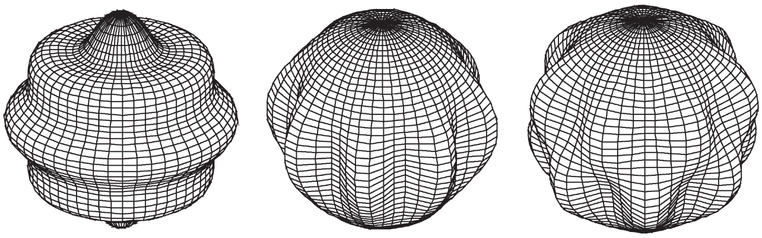

Figure 3.5: Examples of zonal (left), sectorial (centre) and tesseral (right) harmonics [47].

By convention, $J_n \equiv J_{n,0} = -C_{n,0}$ [39], in order to make the J_2-term positive, which is the largest one. While the zonal J-terms can be positive or negative, all the tesseral (and sectorial) harmonics terms are positive by definition. In order to have a complete geopotential model, it can be seen from Eq. (3.11) that values for Earth's gravitational parameter μ_E and reference radius R_E have to be provided. For instance, in the GGM02C model, the values of these constants are $\mu_E = 398\,600.4415\ \mathrm{km^3/s^2}$ and $R_E = 6378.1363$ km [45].

The effects that some of the most relevant J-terms have on orbits have been studied by several authors, leading to analytical expressions that relate the temporal variations of orbital elements to the values of the J-terms and other orbital parameters. For instance, expressions for the secular (i.e. non-periodic) and long-period variations due to J_2, J_3 and J_4 derived in [48] are summarised in [43], while secular, long-period and short-period effects are studied in [39] for the J_2- and $J_{2,2}$-terms. Long-period variations are those that are related (typically by a sinusoidal function) to a slowly-changing angular orbital element, such as i, ω or Ω, whilst short-period variations depend on (sinusoidal functions of) fast-changing parameters, such as f, M or the argument of latitude $u = \omega + f$.

The terms J_2, J_3, $J_{2,2}$ and J_4 are four of the five J-terms with the largest magnitude, and thus the study of their effects alone can provide insight on the general effect that the geopotential has on orbital evolution. Expressions for the effects of these J-terms on some of the orbital parameters can be found in Section A.2.1. However, as previously mentioned, for the propagation of an object in GTO, given the high sensitivity to initial conditions and the appearance of solar resonances, more terms may be necessary to get an accurate description.

A summary of the effects of J_2, J_3, J_4 and $J_{2,2}$ on the evolution of orbital elements is provided in Table 3.1. The results presented there regarding the semi-major axis can be generalised to conclude that Earth's gravitational model does not cause long-period or secular effects on this parameter [39].

Table 3.1: Effects of some J-terms on the orbital elements. Short-period variations have not been considered. Only the presence of long-period (LP) and/or secular (S) variations is reported. [39, 43, 48]

J-term	a	e	i	Ω	ω
J_2	–	–	–	LP + S	LP + S
J_3	–	LP	LP	LP	LP
J_4	–	LP	–	LP + S	LP + S
$J_{2,2}$	–	–	LP	LP	LP

More terms will have to be included in the propagation model, up to degree and order 7 according to [11, 13]. The individual study of each of these terms is beyond the scope of this thesis. Some authors have obtained expressions for the mean rates of change of orbital elements due to these terms [14], although the expressions are given in terms of equinoctial elements and are used in the context of semi-analytical propagation. This topic is covered in Section 5.1.

3.2.2. THIRD-BODY ATTRACTION

An Earth-orbiting body is affected by the gravitational attraction of celestial bodies other than Earth. The perturbing potential due to the gravitational attraction of a third body is given by [9]:

$$\tilde{R}_{3B} = \mu_d \left(\frac{1}{|\boldsymbol{r} - \boldsymbol{r_d}|} - \frac{\boldsymbol{r} \cdot \boldsymbol{r_d}}{r_d^3} \right) \tag{3.13}$$

where μ_d is the gravitational parameter of the disturbing body and $\boldsymbol{r}$ and $\boldsymbol{r_d}$ are, respectively, the position vectors of the satellite and the disturbing body with respect to Earth's centre of mass.

For objects inside the sphere of influence of Earth, the two disturbing bodies with the largest contribution are the Sun (because of its mass) and the Moon (because of its proximity). This can be readily deduced from the following relation [39]:

$$\left(\frac{f_d}{f_E} \right)_{max} \approx 2 \frac{M_d}{M_E} \left(\frac{r}{r_d} \right)^3 \tag{3.14}$$

where f_d and f_E are the magnitudes of the accelerations experienced by the satellite due to the gravitational attraction of the perturbing body and Earth, respectively. For a geostationary satellite, this ratio is equal to 3.9×10^{-5} in the case of the Moon and 1.5×10^{-5} for the Sun. For all other celestial bodies, it is smaller than 2×10^{-10} [39], and thus can be neglected in the analysis of GTOs [11].

The magnitude of the disturbing potential is not constant: it depends on the geometry as can be deduced from the vectorial operations in Eq. (3.13). This means that, even for a circular orbit with constant magnitudes of r and r_d, the value of $\tilde{R}_{3B}$ changes with time.

Several authors have obtained analytical expressions for the rate of change of orbital elements due to third-body perturbations in terms of orbital elements (cf. Section A.2.2). Other authors have used the expressions for the rate of change of the orbital elements in terms of Earth-centred perifocal components (cf. Section 3.1.1), as they can provide more insight on the solar resonance that can affect the dynamics of GTOs [9, 11, 43] (cf. Section 3.3.1).

3.2.3. ATMOSPHERIC DRAG

Drag is the only orbital perturbation that introduces significant secular variations in the semi-major axis [43]. This means that, without drag, a satellite could only be de-orbited (naturally) if the eccentricity of its orbit became large enough so that the value of its perigee distance fell below the value of Earth's radius, resulting in an Earth-intersecting trajectory and potentially in a hazardous crash. Drag is mainly caused by the presence of gases in the Earth's atmosphere, which at the same time is responsible for the burn-up of satellites during re-entry, significantly reducing the likelihood of large objects eventually hitting Earth's surface.

Below approximately 120 km altitude, a satellite can be considered to be re-entering, as it will decay very rapidly and burn up partially or totally in the atmosphere [33]. On the other hand, for orbits with perigee altitudes above 600 km, the effect of atmospheric drag is limited and can result in orbit lifetimes of decades or even longer. In the case of GTOs, two regimes in which the effects of drag on the orbital parameters differ can be identified. Initially, when the perigee is at LEO altitude and the apogee is at GEO altitude, atmospheric drag circularises the orbit, making the apogee altitude decrease while the perigee altitude remains roughly constant. Then, when the eccentricity of the orbit approaches zero, atmospheric drag at apogee is not negligible anymore, and thus the orbit spirals in until re-entry, with both the perigee and apogee altitudes decreasing at similar rates. In both cases, the effect of atmospheric drag on the semi-major axis is always a secular decrease. However, depending on the effects of other orbital perturbations, re-entry can happen for very low eccentricities (close to 0) or for still relatively large values (around 0.5).

Atmospheric drag is one of the most important perturbations for the evolution of GTOs in the context of passive de-orbiting. However, it is also the main source of uncertainty for the determination of the re-entry time or orbit lifetime. This is not due to lack of advanced models describing this perturbation, but to the dependence of these models on changing parameters whose values are difficult to predict [42]. Even for LEOs, which are not affected by the Sun-synchronous resonance discussed in Section 3.3.1, the changing solar activity levels can lead to lifetime durations differing two orders of magnitude [39]. However solar flux levels are not the only source of uncertainty, as the cross-sectional area of the orbiting object is typically difficult to know when it is tumbling, which is typically the case for upper stages of rocket bodies.

The acceleration undergone by the satellite due to atmospheric drag is given by [42]:

$$\boldsymbol{a_D} = -\frac{1}{2}\rho\frac{C_D A}{m}V_r^2\frac{\boldsymbol{V_r}}{V_r} \tag{3.15}$$

where ρ is the atmospheric density, C_D, A and m are respectively the drag coefficient, cross-sectional area and mass of the orbiting body and $\boldsymbol{V_r}$ is its relative velocity with respect to the rotating atmosphere. The term $B = C_D A/m$ is known as the ballistic coefficient. Analytical expressions for the evolution of the mean elements due to atmospheric drag can be found in Section A.2.3.

Looking at Eq. (3.15), three sources of uncertainty can be identified: the atmospheric density, the external shape and attitude of the body (which affect the value of the ballistic coefficient) and the relative velocity. These factors are discussed in more detail hereafter.

RELATIVE VELOCITY

The intertial velocity of the satellite can be known accurately in most cases, but the velocity of the atmosphere with respect to Earth's surface is typically not. The wind velocities are difficult to determine at high altitudes, and are even more difficult –if not impossible– to predict in the long term. Thus, it is customary to assume that the atmosphere is co-rotating with Earth, so that [43]:

$$\boldsymbol{V_r} = \dot{\boldsymbol{r}} - \boldsymbol{\omega_E} \times \boldsymbol{r} \tag{3.16}$$

with $\boldsymbol{\omega_E}$ Earth's rotational velocity, which can be assumed to be constant and equal to $[0, 0, \omega_E]^T$, with $\omega_E = 7.292115 \times 10^{-5} \pm 1.5 \times 10^{-12}$ rad/s [43].

BALLISTIC COEFFICIENT

The ballistic coefficient of the body is an important source of uncertainty in the determination of the effects of atmospheric drag on the evolution of orbital elements. Although the mass m is known accurately in most cases, the drag coefficient C_D and the cross-sectional area A are more difficult to determine.

The drag coefficient is obtained from combinations of different interactions between gas particles and the satellite, namely specular reflection (modelled through $C_D^{(S)}$), diffuse reflection ($C_D^{(D)}$) and absorption ($C_D^{(A)}$) [33]:

$$C_D = \alpha C_D^{(S)} + \beta C_D^{(D)} + \gamma C_D^{(A)} \tag{3.17}$$

These three coefficients can typically be computed if the shape and attitude of the body are known, but their relative weights α, β and γ can only be determined empirically [33]. However, some authors have developed semi-empirical relations for the drag coefficient [49], which is given as a function of wall temperature, atmospheric temperature and mean molecular mass, local time, solar activity and satellite's velocity. The value of C_D is not very sensitive to many of these parameters, so in some cases resorting to Figure 3.6 is accurate enough for orbit propagation. Although this model was developed for the propagation of LEOs, some authors are using the results presented in [49] regarding the determination of C_D for the propagation of GTOs as well [9, 11]. Some software tools allow the user to provide a configuration file with values for the drag coefficient as a function of altitude, which is accessed during the propagation [13]. They also allow to specify an equivalent constant C_D; when no information is available, a value of 2.2 is recommended.

The other parameter that affects the value of the ballistic coefficient is the cross-sectional area. Spacecraft and rocket bodies that have reached the end of their useful life are typically uncontrolled in attitude and

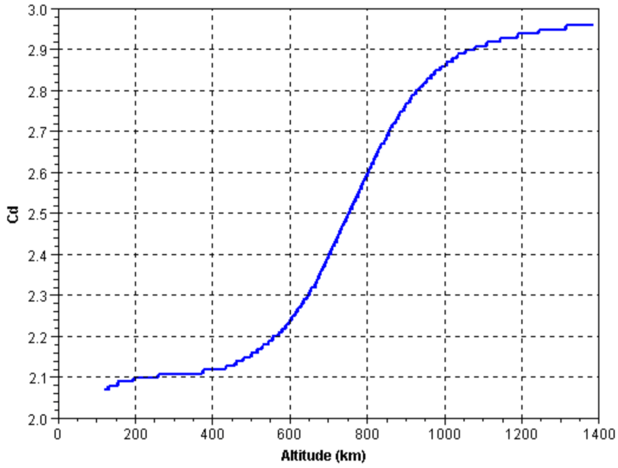

Figure 3.6: Mean drag coefficient of a sphere or tumbling plate as a function of altitude [49]. Below 120 km, the satellite is assumed to have re-entered. Above 1 320 km, the mean drag coefficient remains constant.

thus their cross-sectional area changes with time and is difficult to predict. In the case of satellites with large deployable solar panels, the value of the cross-sectional area can change up to one order of magnitude depending on the angle formed by the normal vector of the panels and the velocity vector [33]. The shape of a rocket body also differs significantly from that of a perfect sphere (which has a constant cross-sectional area independent of its attitude). Thus, it seems obvious that the cross-sectional area is a parameter that will remain a source of uncertainty in the propagation of orbits.

The approach proposed by CNES (for the propagation of both LEOs and GTOs) is to use an equivalent constant value for the cross-sectional area obtained as an average of the cross-sectional areas observed from any direction [11, 13, 49]. This only applies when it is not possible to show that the object will remain at a fixed attitude and thus it is assumed to be tumbling. If some passive de-tumbling technique such as aerodynamic equilibrium or gravity gradient stabilisation is used, then a more accurate value of the cross-sectional area may be available.

ATMOSPHERIC DENSITY

The density of Earth's atmosphere depends on many factors, but the one with the highest influence is altitude. Thus, a very rough estimate of the atmospheric density can be obtained using the following exponential law [42]:

$$\rho = \rho_0 e^{-\frac{h-h_0}{H_0}} \tag{3.18}$$

where ρ_0 is the atmospheric density at the reference altitude h_0, and H_0 is the density scale height, which at sea level is 7.9 km [42] but at satellite altitudes ranges typically from 50 to 100 km [33].

The atmosphere density is neither spatially homogeneous nor independent of time at one and the same location. More complex models have been developed in order to allow for more accurate orbit propagations. Some authors have used the NRLMSISE-00 atmosphere model for the propagation of GTOs [9, 11, 13]. This model can provide the temperature, mass density and even partial densities of different gases for any date in the past since 1960, and for any location over Earth's surface up to altitudes of 1 000 km [50]. However, the Community Coordinated Modeling Center recommends to use now the IRI-2007 model, an enhanced version which allows a wider altitude range, between 60 and 2 000 km [51].

Although there are models describing the characteristics of the atmosphere in the past very accurately, the prediction of the atmospheric density for propagation of orbits in the future is highly uncertain. The main reason is that solar activity levels, which are difficult to predict, can change the atmospheric density for a given altitude by up to two orders of magnitude [33]. Even for orbits lacking complex third-body resonance effects, such as LEOs, this can result in orbital lifetimes differing one order of magnitude, as shown in Figure 3.7. It can be seen that orbits decay faster when solar activity is higher. This is due to an expansion of the atmosphere when heated by solar flux. Although this may seem counterintuitive, as an expansion of a gas typically leads to lower densities, what is actually happening is that the atmosphere rises as it expands, pushing denser layers up towards higher altitudes [33]. The result is that, for a given altitude, the density (and thus the drag) is higher during solar maxima. However, solar activity levels are difficult to predict. Despite the fact

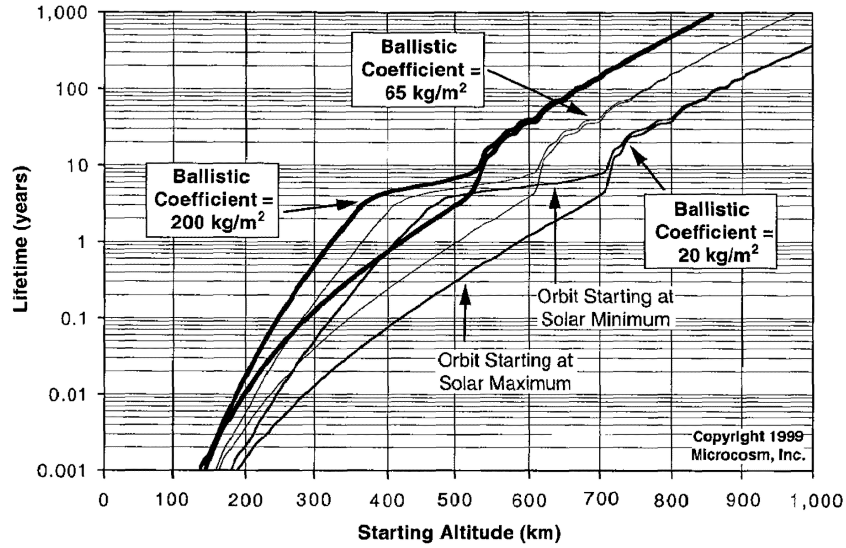

Figure 3.7: Maximal satellite lifetime as a function of altitude for different ballistic coefficients at solar minima (upper curve for each of the ballistic coefficients) and solar maxima (lower curves) [33].

that it is well-known that solar maxima are undergone roughly every 11 years, the flux levels at these maxima vary from cycle to cycle, as seen in Figure 3.8. Two parameters that can be measured on Earth and that are correlated to the solar activity levels are [39]:

- **Solar 10.7-cm radiation flux,** $F_{10.7}$. This parameter represents a measure of the UV and X-ray radiation entering Earth's atmosphere, and is specified in units of 10^{-22} W m^{-2} Hz^{-1}, also known as solar flux units (sfu). Typical values are between 75 sfu for solar minima and 250 sfu for solar maxima, although it can get significantly higher at specific dates (cf. Figure 3.8a). The current cycle is being especially low (cf. Figure 3.8b).

- **Three-hour geomagnetic index,** A_p. This parameter provides a measure of the corpuscular radiation entering Earth's atmosphere, and is given in units of nanotesla (i.e. 10^{-9} N A^{-1} m^{-1}). Its value is typically below 20 nT, but it can get higher than 200 nT at specific dates.

These two parameters can be measured on Earth, but nowadays there exist more complex models that include other parameters that have to be measured by satellites outside the atmosphere [39]. However, these additional parameters are not discussed here, since they are not typically included in the existing methods developed for the propagation of GTOs [9, 13, 49].

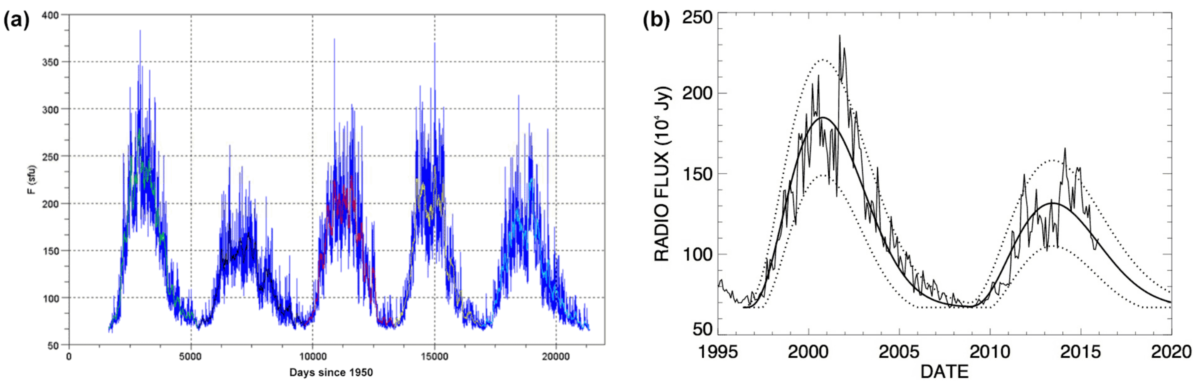

Figure 3.8: **(a)** Observed daily mean solar radio flux at 10.7 cm between 1954 and 2008 [49]. **(b)** Observed solar radio flux at 10.7 cm between 1995 and 2016, together with the predicted maximum, average and minimum levels until 2020 [52].

3.2.4. SOLAR RADIATION PRESSURE

An Earth-orbiting body experiences several forces caused by radiation coming from the Sun, sunlight reflected by Earth (albedo) and Earth infrared radiation. The most relevant of these forces is the one due to the direct solar flux [39], known as solar radiation pressure (SRP), and thus is the only radiation force considered in this report and in the majority of models for propagation of GTOs [9, 13].

The acceleration undergone by an Earth-orbiting body due to solar radiation is given by [39]:

$$\boldsymbol{a_{SRP}} = -C_R \frac{W_S A}{mc} \boldsymbol{e_S} \tag{3.19}$$

where W_S is the energy flux of the Sun at 1 AU, C_R is the radiation pressure coefficient, c is the speed of light, and A and m are, as before, the cross-sectional area and mass of the orbiting body. The $\boldsymbol{e_S}$ unit vector points from the satellite to the Sun. Thus, the acceleration due to solar radiation acts always in the Sun-satellite direction. This expression only holds when the satellite is not in eclipse; otherwise, $\boldsymbol{a_{SRP}} = \boldsymbol{0}$.

The main sources of uncertainty in Eq. (3.19) are the radiation pressure coefficient C_R, the energy flux W_S and the cross-sectional area A. The latter can be computed in the same way as has been discussed for atmospheric drag, i.e. using a mean surface area if the attitude of the body is unknown [13].

The radiation pressure coefficient can be found from [42]:

$$C_R \approx \rho + 1 \tag{3.20}$$

where ρ is the reflectivity, a property of the material. It is clear that the effective reflectivity will depend on the attitude of the orbiting body. Typically the value of C_R can only be determined empirically, i.e. obtained from Eq. (3.19) when all the other parameters are known [42].

Finally, for the energy flux of the Sun at 1 AU, the value of 1 366 $\mathrm{W/m^2}$ has been historically used [42]. However, recent observations have shown that a yearly mean value of 1 361 $\mathrm{W/m^2}$ is more realistic [39]. This value is not constant and changes mainly due to the fact that Earth's orbit about the Sun is not perfectly circular. A more accurate value can be obtained from [39]:

$$W_S = \frac{1361}{1 + 0.0334 \cos \frac{2\pi D_{ap}}{365}} \tag{3.21}$$

where W_S is given in $\mathrm{W/m^2}$ and D_{ap} is the time since Earth was last at aphelion, measured in days.

In order to model occultations of the solar flux by Earth's shadow, also known as eclipses, it is customary to assume a cylindrical Earth shadow for the propagation of GTOs [13]. Expressions for a first-order approximation of the rate of change of the orbital elements due to solar radiation pressure can be found in Section A.2.4.

Of all the disturbing forces discussed so far, SRP is the one with the smallest effect on the evolution of objects in GTO [11]. In Figure 3.9, the effects of the solar radiation pressure can be observed. Since they are small, the radiation force has been artificially multiplied by a factor of 10 in the right-hand side plot. Having to use a multiplier factor in order to be able to visualise the effects of SRP shows that this is not the main perturbing force affecting GTOs, but if accurate predictions are wanted it cannot be neglected.

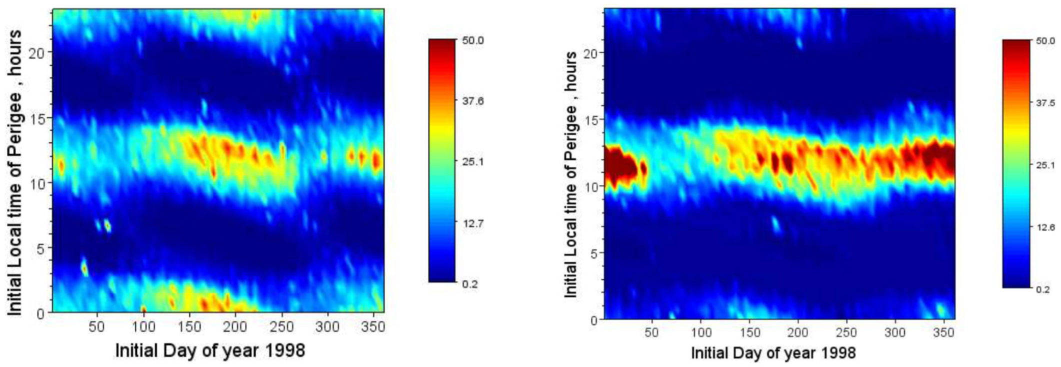

Figure 3.9: Lifetime variations with respect to initial date and local time of perigee for an orbit with a 2 degree inclination. In the plot on the right, the solar radiation pressure has been artificially multiplied by a factor of 10 [11].

3.2.5. COMPARISON

Once that the main perturbations that will affect the evolution of objects in GTO have been described, it is convenient to quantify their relative effects as a function of altitude (or distance to Earth's centre of mass) in order to have an idea of the orbital perturbations that are most relevant at different parts of the orbit. In the case of GTOs, the most relevant perturbation near perigee (altitudes of less than 2 000 km) is Earth's irregular gravity field, with the J_2-term having the largest effect, as can be seen in Figure 3.10a. However, when the altitude becomes lower than about 120 km, drag becomes the main perturbation. Above 500 km, drag has the smallest effect, whilst below 500 km SRP is the least relevant perturbation (of the four perturbations that have been discussed in previous subsections).

The apogee altitude of GTOs changes significantly as drag tends to circularise the orbit. Initially, when it is close to GEO altitude, third-body perturbations caused by the Moon and the Sun and the effect of the J_2-term are of the same order of magnitude, as seen in Figure 3.10b. As the apogee altitude decreases, the effects of the J-terms increase and third-body attraction and SRP become less relevant. During the Sun-synchronous condition (apogee distances of about 24 000 km), J_2 has become predominant at apogee, but luni-solar attraction still plays a significant role.

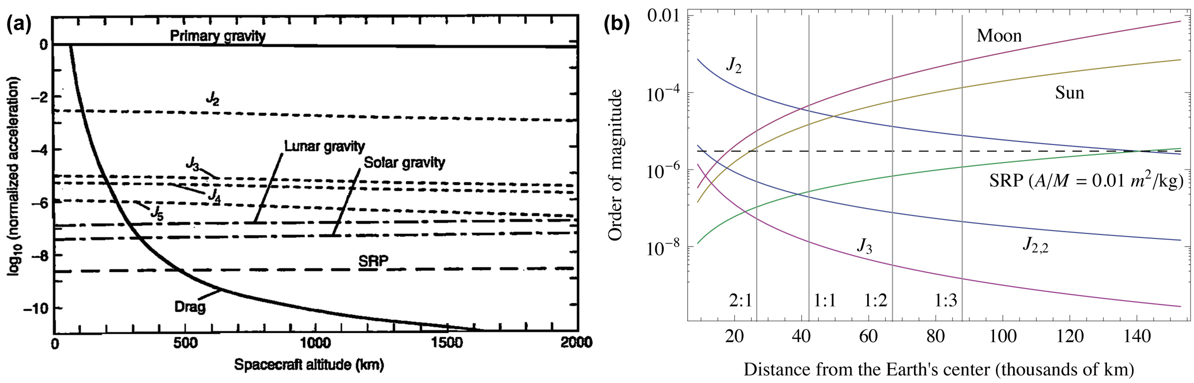

Figure 3.10: Order of magnitude of several perturbations relative to Keplerian attraction (primary gravity) near LEO altitudes **(a)** [53] and for distances to Earth's centre ranging from R_E to about 150 000 km **(b)** [44]. An area-to-mass ratio of 0.005 m^2/kg has been assumed in (a), while in (b) a value of 0.01 m^2/kg has been used. Vertical lines in (b) denote semi-major axes for which the sidereal day over the orbital period is the ratio of two small integers. The vertical line labelled 1:1 corresponds to GEO distance.

The perturbations that have been left out are those caused by third bodies other than the Sun or the Moon, ocean tides caused by third bodies, and relativistic effects. Before concluding this section on orbital perturbations, it is necessary to corroborate that these perturbations can be neglected.

Regarding the gravitational attraction of third bodies, it was already mentioned in Section 3.2.2 that the maximum acceleration caused by the Moon and the Sun (relative to the central acceleration caused by Earth) is in the order of 10^{-5} for GEO satellites. For other planets in the Solar System, this relative acceleration is at least four orders of magnitude smaller, while for the closest star it is 18 orders of magnitude smaller [39]. Thus, it can be said that the perturbation caused by third bodies other than the Sun or the Moon can be safely neglected.

The Moon causes significant tides on Earth oceans, leading to a redistribution of Earth's mass that causes an acceleration on orbiting satellites. However, this acceleration is relatively small. Studies concerning the effects of tidal deformation of Earth on the motion of close artificial satellites have found that the effects can be expressed as a deviation in the value of J_2. This deviation is not constant, but its amplitude is generally not larger than $8 \times 10^{-7} J_2$ [54]. The magnitude of the J_8 term is about 1.8×10^{-4} that of J_2, so if that term can be neglected, as will be shown in Section 4.1.2, then the effects of tides on artificial satellites can too.

Relativistic effects can introduce a precession in the argument of perigee of the orbit. For an Earth satellite with perigee and apogee altitudes of 800 and 1 000 km, this precession is about 0.34 degrees per century [39]. Thus, this perturbation can also be neglected without introducing significant errors in propagations lasting generally less than 25 years.

3.3. DYNAMICS OF GEOSTATIONARY TRANSFER ORBITS

The lifetime of objects in GTOs is very sensitive to several factors that cannot be known with sufficient accuracy. Some of these factors are the solar activity levels, the area-to-mass ratio and some initial orbital conditions, especially the date and local time of perigee [11]. Several researchers have found that a small deviation in the values of these parameters, which would have negligible effects for the propagation of LEOs and GEOs, can change the lifetime of GTOs by an order of magnitude in some cases [8, 11] (cf. Figure 3.11). This is due to an interplay between several orbital perturbations affecting GTOs. Due to their high eccentricity, GTO objects are mainly influenced by atmospheric drag and Earth's irregular gravity field when they are close to perigee, while third-body perturbations, mainly the Sun's and the Moon's, are dominant close to apogee.

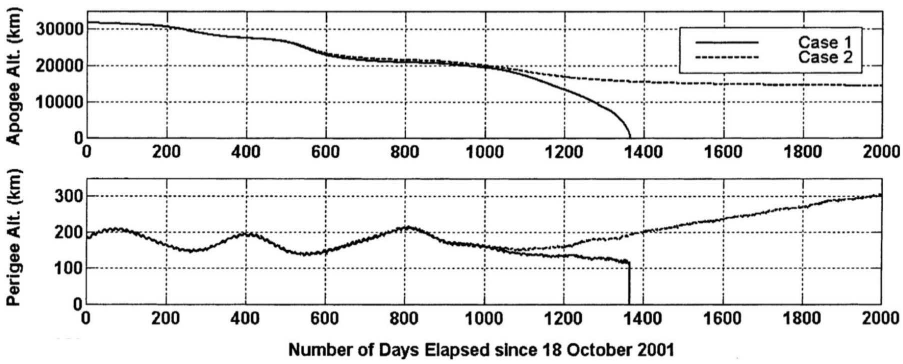

Figure 3.11: Simulation of the evolution of the perigee and apogee altitudes of two objects in the same GTO orbit launched with a time difference of one minute [8].

In the context of orbital propagation of objects in GTO, it has been proposed that the minimum acceleration model that can provide acceptable results needs to take into account Earth's irregular gravity field (zonal harmonics and some dedicated tesseral harmonics), luni-solar attraction, atmospheric drag and solar radiation pressure (including Earth's shadow) [11], all of which have been described in Section 3.2. The solar resonance identified in previous studies is covered in detail in the following subsections.

3.3.1. SOLAR RESONANCE

The coupling between orbital perturbations, sometimes referred to as Sun-synchronous resonance [34], or simply solar resonance, makes it difficult to comply with space debris-mitigation guidelines, as re-entry in less than 25 years cannot be guaranteed for all possible conditions slightly deviating from the nominal case. For instance, for orbital inclinations of 0 and 30 degrees, resonance typically occurs for apogee altitudes of 16 000 and 12 000 km, respectively [8]. Under those conditions, the Sun azimuth angle, i.e. the angle between the line of apsides and the Sun vector measured in the orbital plane (cf. Figure 3.12a), remains roughly constant for a very long time. This can result in an increase in perigee altitude, reducing the atmospheric drag and thus increasing lifetime. However, depending on the geometry, the resonance can also have a positive effect and lower the perigee to an altitude where the atmosphere is denser, making the decay much faster. In Figure 3.12b it can be seen that when the Sun is in the first or third quadrants, an increase of the perigee altitude is undergone, while the perigee altitude decreases when the Sun is in the second or fourth quadrants. The magnitude of the effect is largest when the orbital plane coincides with the ecliptic (i.e. when $\lambda = 0$).

The changes in eccentricity, and thus in perigee altitude, are deemed to be of high relevance, since atmospheric drag changes exponentially with altitude, having a big impact on the lifetime of the GTO object. The averaged effect of a third-body's gravity on the eccentricity is given by [11]:

$$\frac{\mathrm{d}e}{\mathrm{d}t} = -\frac{15}{2}\frac{\mu_E}{r_d^3} e\sqrt{1-e^2}\, x_d y_d \tag{3.22}$$

where x_d and y_d denote the position of the disturbing body in the Earth-centred perifocal reference frame defined in Figure 3.12b.

From Eqs. (A.39) and (3.22) it is clear that the sign of the rate of change of the perigee altitude will coincide with that of the product $x_d y_d$. This means that, when the third body is in the first or third quadrants, where x_d and y_d have same sign, the perigee altitude of the spacecraft will increase with each orbital revolution, whilst the opposite effect will be experienced when the perturbing body lies on the second or fourth quadrants. Moreover, if the projection of the third body is on the X- or Y-axis (i.e. $y_d = 0$ or $x_d = 0$), the eccentricity, and thus the perigee altitude, will not experience secular variations [9].

Even though the changes in perigee altitude can have a large impact on the orbital lifetime, the Sun-synchronous resonance governing the complex dynamics of GTOs is triggered by changes in other orbital

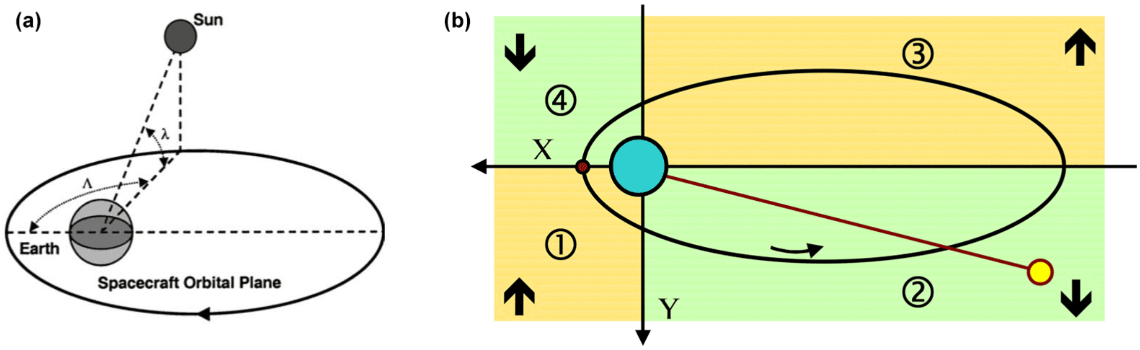

Figure 3.12: **(a)** Definition of the relevant angles for the modelling of Sun-synchronous resonances. Λ is the Sun azimuth angle and λ is the Sun declination angle [8]. **(b)** Definition of the X and Y axes in the Earth-centred perifocal reference frame. Arrows pointing up denote quadrants in which the perigee altitude increases due to the effect of Sun attraction, whilst those pointing down correspond to quadrants where the perigee altitude decreases [9].

elements, namely Ω and ω. From the geometry depicted in Figure 3.12b, it is clear that, each year, the Sun will spend roughly half of the year in quadrants 1 and 3 and the other half in quadrants 2 and 4, if it is assumed that the perifocal reference frame XYZ does not rotate. This would lead to alternating periods in which the value of the perigee altitude oscillates throughout the year (cf. Figure 3.11). However, the location of the perigee with respect to Earth is not fixed, but changes with time due to the long-period and secular variations in Ω and ω (cf. Table 3.1 and Eqs. (A.37-4) and (A.37-5)). Due to the drift of the perigee, the orientation of the perifocal reference frame in inertial space also changes. The Sun-synchronous resonance appears when the rate of rotation of the perifocal reference frame (also known as mean drift of perigee) coincides with (or is close to) that of Earth about the Sun [9], i.e. 0.986 deg/day. The mean drift of perigee (MDP) is equal to $\dot{\Omega}+\dot{\omega}$ [9], where $\dot{\Omega}$ and $\dot{\omega}$ are determined by the orbital perturbations that are included in the model.

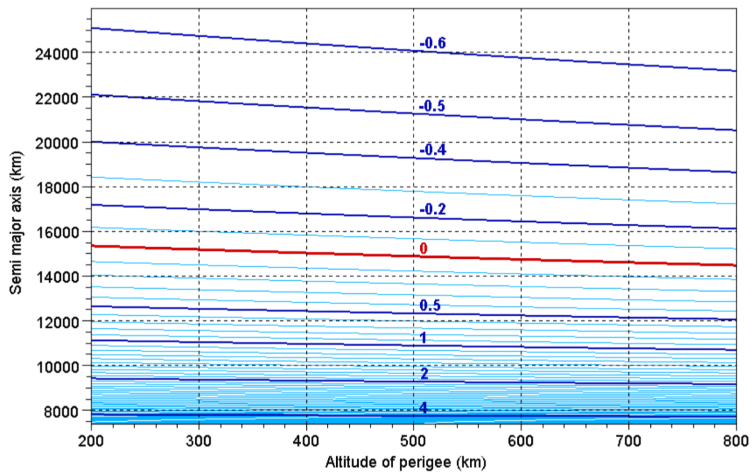

Figure 3.13: Mean drift of perigee with respect to Sun's rate of rotation about Earth (in degrees per day), for a GTO with 7 degree inclination and considering only perturbations due to the J_2-term [9].

In Figure 3.13, the MDP with respect to the Sun's rate of rotation about Earth, i.e. $MDP-\omega_S$, is plotted for a GTO orbit in which only the perturbations by the J_2-term are considered. Taking into account that for a GTO with initial perigee altitude of 800 km, the semi-major axis will change from about 24 660 km at the beginning to slightly over R_E at re-entry, it is clear that at some point of its lifetime it will encounter the condition $MDP-\omega_S \approx 0$, as this typically happens for values of the semi-major axis around 15 000 km. This condition leads to the so-called Sun-synchronous resonance, in which the Sun remains for long periods of time in the same quadrant, i.e. $\dot{\Lambda} \approx 0$ (cf. Figure 3.12a for the proper definition of Λ). This means that, for very long periods of time, the effect of the Sun's gravitational attraction on the evolution of the eccentricity and thus on the perigee altitude has the same sign, with variations building up over time (cf. Figure 3.11), since x_d and y_d (and thus $x_d y_d$) do not change sign.

The consequences of this Sun-synchronous resonance are obvious: if it happens when the Sun is at the first or third quadrants, the perigee rises, drag decreases significantly and consequently the lifetime increases. Since the only perturbation that has significant secular effects on the evolution of the semi-major axis is atmospheric drag [43], when the perigee rises to an altitude in which drag is significantly lower, the lifetime can increase by one order of magnitude, or even more, with respect to the value that would have been obtained if the Sun-synchronous resonance would not have been experienced [11]. On the other hand, if the Sun-synchronous resonance happens when the Sun is at the second or fourth quadrants, the opposite effect can be potentially exploited in the context of passive de-orbiting.

From Eqs. (3.22) and (A.39) it is possible to obtain an expression for the mean rate of change of the perigee altitude due to the Sun's gravity perturbation in terms of the Sun azimuth and declination angles:

$$\frac{\mathrm{d}h_p}{\mathrm{d}t} = \frac{15}{2}\frac{\mu_E}{r_d} ae\sqrt{1-e^2}\frac{x_d}{r_d}\frac{y_d}{r_d} = \frac{15}{4}\frac{\mu_E}{r_d} ae\cos^2\lambda\sin 2\Lambda \tag{3.23}$$

where it has been used that $x_d/r_d = \cos\lambda\cos\Lambda$ and $y_d/r_d = \cos\lambda\sin\Lambda$. Indeed, as mentioned previously, this expression becomes zero when the Sun declination angle is ± 90 deg and/or when the Sun azimuth angle is a multiple of 90 deg. This expression has been validated by propagating a GTO following the experimental set-up described in Section 4.1, and corroborating that there is a 100% correlation between the derivative of the perigee altitude and the quantity $\cos^2\lambda\sin 2\Lambda$ when only the perturbation caused by the Sun's gravity is included in the acceleration model (thus neglecting all other perturbations). The results of this validation can be found in Figure B.1.

When all the relevant perturbations are included in the acceleration model (J-terms up to degree and order 7, Sun's and Moon's gravity, atmospheric drag and SRP), there are other perturbations other than the Sun's gravity affecting the evolution of the perigee altitude, so the correlation is not perfect. However, it is still very strong, as can be seen in Figure 3.14 for a representative GTO in which no significant resonances are experienced (i.e. the Sun azimuth angle does not remain constant for long periods of time). This big correlation, even when all perturbations are considered, suggests that the evolution of the perigee altitude for GTO orbits is mainly driven by the Sun's gravity, at least for this altitude regime (perigee altitude of about 300 km).

An orbit with slightly different initial conditions was propagated, leading to the evolution depicted in Figure 3.15. In this case, the orbit begins to precess at a rate close to 1 deg/day close to year 2001 (mainly due to the effects of zonal terms of the geopotential). The Sun azimuth angle stays relatively stable at 60 to 90 degrees from 2001 to 2005, and in the range 90 to 120 degrees for the next 7 years. This leads to the effect of the Sun's gravity building up over time and thus to a long period of increasing perigee altitude first (when $\Lambda < 90$ degrees) followed by a long period of decreasing perigee altitude (when $\Lambda > 90$ degrees). Note that this is in agreement both with Figure 3.12b and Eq. (3.23).

3.3.2. COUNTERINTUITIVE EFFECTS

As mentioned in Section 3.2.3, atmospheric drag is the only perturbation causing a secular variation of the semi-major axis, and thus it is responsible for the eventual re-entry of the orbiting body. From Figure 3.14 it can be seen that when the perigee altitude remains at a relatively stable value (e.g. between 250 and 350 km), the apogee altitude decreases at a more or less constant rate. However, when the perigee changes significantly (e.g. in the range 150 to 500 km), so does the rate at which the apogee altitude decreases, as can be seen in Figure 3.15. This means that the existence of solar resonance can have a big impact on the orbital lifetime.

However, the interplay between orbital perturbations causing solar resonances does not only lead to very different lifetimes for slightly changing conditions, but is also the cause of some counterintuitive effects that can potentially take place during orbital evolution. For instance, an example in which an increase of drag (either by considering larger atmospheric densities or area-to-mass ratios) leads to longer lifetimes is given in [8]. This is due to the fact that an increase in drag causes the semi-major axis to decay initially at a faster rate, and thus the Sun-synchronous resonance is reached at a different epoch. From Figure 3.12b it is clear that the moment (and thus the geometry) at which the resonance is experienced influences the perigee evolution and can have drastic consequences for the lifetime. Thus, it is not valid to claim that a GTO object will re-enter for sure in less than e.g. 25 years, based on simulations showing that for the most unfavourable conditions of low drag it would decay in 25 years.

Using the experimental set-up described in Section 4.1, it was possible to identify two cases with very different evolutions, despite the fact that the orbit and initial conditions are the same, while the only parameter that has been changed is the drag coefficient. It is clear that a change in the value of the drag coefficient will

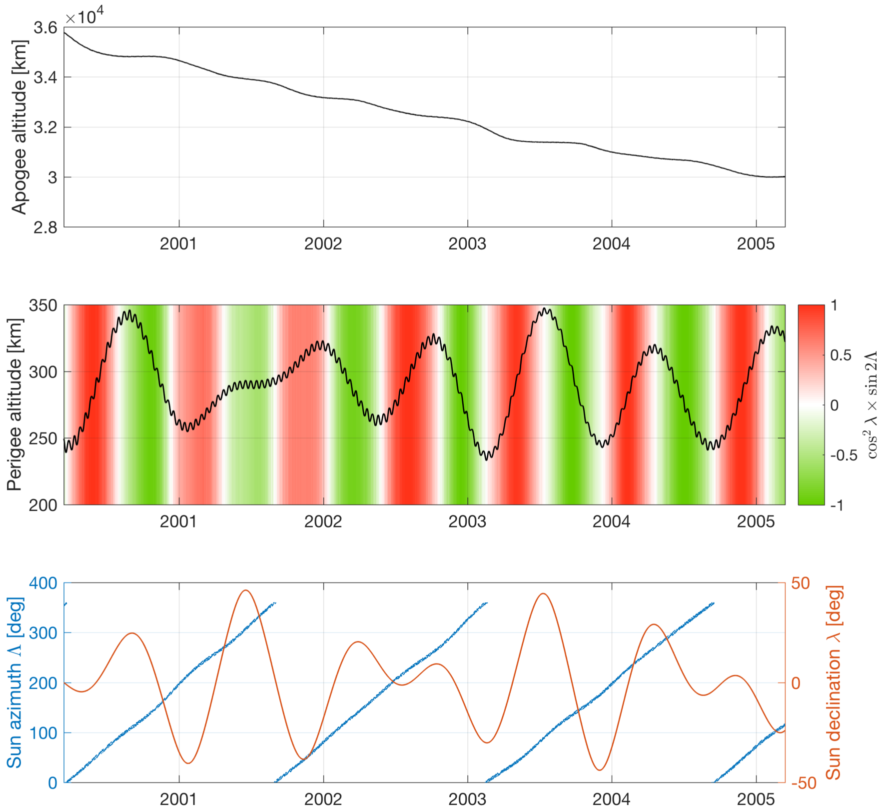

Figure 3.14: Temporal evolution of the perigee and apogee altitudes and Sun azimuth and declination angles for a representative GTO in which no significant solar resonance are undergone.

lead to a different orbital evolution; however, one may not expect the lifetime to get significantly longer when the drag coefficient is increased. Because of the solar resonance, this effect can be undergone for certain GTOs, as depicted in Figure 3.16.

3.3.3. STATISTICAL APPROACH

The effects of the Sun-synchronous resonance (its magnitude and whether it will be perigee-raising or perigee-lowering) are very sensitive to initial conditions, because these initial conditions will determine the geometry when the solar-resonance conditions are reached. The key parameter is the position of the Sun in the Earth-centred perifocal reference frame when $MDP - \omega_S \approx 0$, a condition that most GTO objects will encounter at some point in their lifespan before re-entry. The signs of x_d and y_d (or equivalently, the angle Λ) at that moment will determine the magnitude and sign of the Sun-synchronous effect. However, knowing the geometry at that point in time requires both an accurate modelling of perturbations and an accurate knowledge of the initial conditions (typically the mean local time of perigee of the GTO when the payload is injected into GEO [55]). This is difficult to know in early stages of design, and in some cases even when the rocket has already been launched. Other aspects, such as the GTO object's mass, area and drag coefficient, and solar activity levels, are also sources of uncertainty that complicate the prediction of the orientation of the orbit with respect to the Sun at Sun-synchronous conditions. Thus, a statistical approach, in which the different parameters that are considered sources of uncertainty are varied and several propagations are performed, is necessary in order to obtain reliable predictions about the lifetime of GTOs [11].

Given the complexity of accurate orbital propagation of GTOs and its extreme sensitivity to several parameters that in most cases cannot be known with sufficient accuracy, some organisations have proposed a dedicated debris mitigation guideline for GTOs slightly different from the one defined for LEOs [11]. The proposal consists in redefining the requirement of re-entry in less than 25 years to re-entry in less than 25 years with a probability of 90%. This means that, for a given GTO object, its orbit will not be propagated only once, but several times for different combinations of slightly changing conditions, and at least 90% of these propagations should lead to a re-entry in less than 25 years. It is clear that statistics will play an important

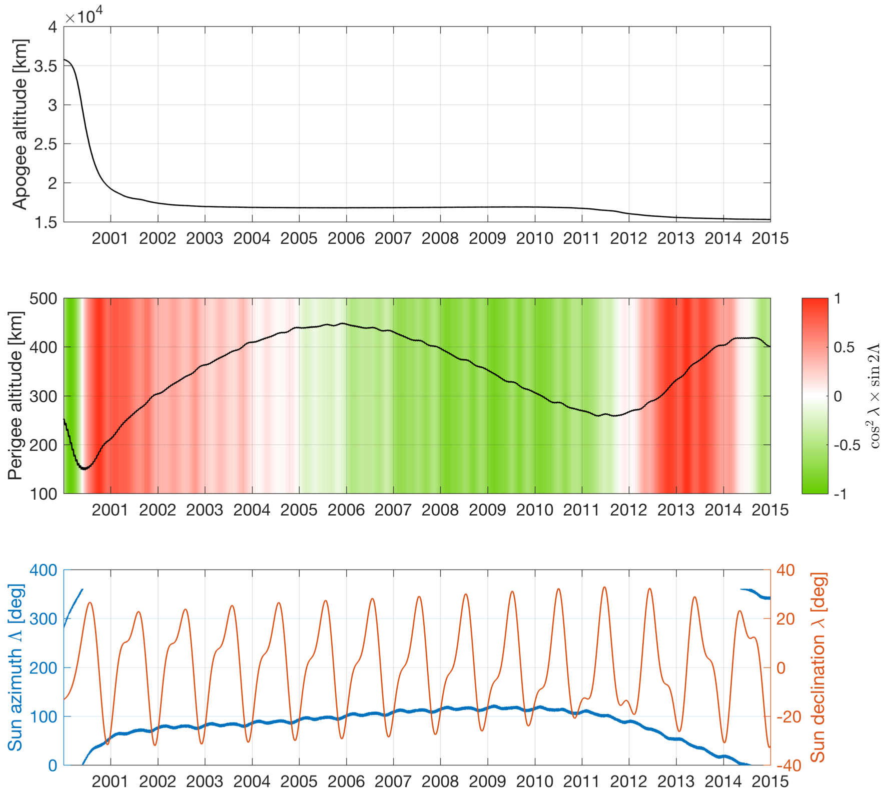

Figure 3.15: Temporal evolution of the perigee and apogee altitudes and Sun azimuth and declination angles for a representative GTO in which a solar resonance is undergone.

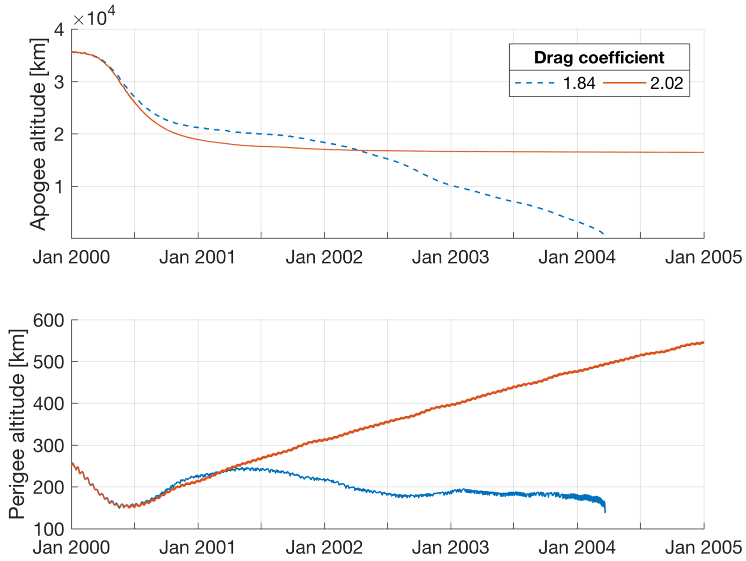

Figure 3.16: Temporal evolution of two objects in a GTO with identical initial conditions, except for the use of a different drag coefficient. Note that, counterintuitively, increasing the drag coefficient can lead to a longer lifetime.

role in the study of long-term evolution of GTOs.

Several definitions and procedures that may be useful during the development of the thesis are introduced in [11] and summarised here. The first concept is called $T_L^{(90\%)}$, which is defined as the period of time (or lifetime) after which a given GTO object has a 90% probability of having re-entered. The disposal perigee altitude is defined as the perigee altitude that guarantees a re-entry in less than 25 years with a 90% probability. Another concept is the date and local time of perigee (DLTP), which corresponds to the moment at which the object reaches the end of its operational life and thus the natural, uncontrolled orbital propagation begins. Given that this parameter is difficult to know in early stages of design, the concept of domain is introduced, defined as the range of possible dates of perigee and local times of perigee. For instance, two possible domains could be: (1) variable day (from 1 to 365) and local time fixed at 16 h; and (2) fixed day at summer solstice and variable local time from 21 to 24 h. Then, the reference provides two approaches that can be used to show fulfilment of the requirement $T_L^{(90\%)} < 25$ years for a given domain:

- **Local approach**. All the possible combinations of date and local time within the domain (in practice a limited number due to the use of a finite step-size) have a 90% probability of decaying in less than 25 years. The value of DLTP is fixed for each propagation, i.e. it is assumed to be known with no uncertainties.

- **Global approach**. There may be certain combinations of date and local time with a lower than 90% probability of decaying in 25 years, but on average the requirement is satisfied for the whole domain because of the counterbalance effect of the combinations that decay more rapidly. The value of DLTP is not fixed for each propagation, but included in the statistical analysis as a source of uncertainty.

The local approach has the advantage of guaranteeing the fulfilment of re-entry in less than 25 years with at least 90% probability under any foreseeable scenario. However, it can be computationally more demanding, since a statistical analysis including uncertainties in drag, area-to-mass ratio, etc., and consequently a large number of orbital propagations, are required for each combination of date and local time. Additionally, it requires lower disposal perigee altitudes in order to guarantee re-entry (about 35 km lower [11]) than the global approach.

The reference does not recommend one approach over the other, as both have advantages and drawbacks. However, it is deemed convenient for researchers to be aware of both of them, since eventually what currently are only guidelines may become regulations enforced by law, and, from that moment on, following one of the approaches presented here (or an approach defined in a similar way) may become mandatory as well. In this Master thesis, the local approach will be followed, i.e. the DLTP has been chosen as an optimisation variable rather than setting it as an uncertain parameter.

4

NUMERICAL APPROACH

A necessary step towards being able to generate the results of interest for this Master thesis consists in identifying and/or developing a tool capable of propagating the orbits of objects in GTO for long periods of time (in the order of years or decades) with proper accuracy and in feasible computation times. Given the complexity of the problem at hand, a numerical approach has to be followed in order to integrate the equations of motion, as no analytical solution exists when the relevant perturbations are included in the acceleration model.

This chapter covers the description of the fully numerical approach, in which the contribution of each orbital perturbation to the total acceleration has to be assessed several times every orbital revolution. In Section 4.1, the experimental set-up to obtain the relevant results is discussed, including the choice of software and determination of the best propagator and integrator settings for the case of GTOs. A study of the sensitivity to changes in the values of some of the parameters, such as initial state and body properties, will follow in Section 4.2. Then, the optimisation problem will be properly defined in Section 4.3. Finally, some of the results obtained with the experimental set-up described in this chapter will be provided in Section 4.4, as well as a feasibility study on whether the research objective of the Master thesis can be reached by following the fully numerical approach.

4.1. EXPERIMENTAL SET-UP AND TUNING

In order to know the lifetime of an orbiting body, it is necessary to establish a condition in terms of re-entry altitude. During re-entry, non-linear effects will dominate and the problem may not be described as a simple perturbed orbital motion, requiring the use of more advanced models to obtain an accurate description. This period, from the beginning of re-entry until an eventual burn-up or crash onto Earth's surface, has not been studied in this thesis, as it is typically in the order of hours [33]. Compared to a lifetime of e.g. 25 years, as some guidelines suggest (cf. Section 2.2.1), it is obviously negligible. Thus, determining the lifetime consists in finding the epoch at which the orbiting body will reach an altitude of 100 km.

As mentioned in Section 3.2, the equations of motion cannot be solved analytically when all the relevant perturbations are included in the acceleration model. Thus, the epoch leading to an altitude of 100 km cannot be computed directly, and the motion of the body has to be propagated using numerical integration. The choice of the software to perform this propagation and the development of further functionality will be discussed in Section 4.1.1. The obtained tool will be used in the first place to determine the minimum acceleration model leading to reliable results for the problem of propagation of GTOs in Section 4.1.2. Then, the tuning of the propagator and integrator will be discussed in Sections 4.1.3 and 4.1.4, respectively.

4.1.1. TUDAT EARTH SATELLITE PROPAGATOR

The TU Delft Astrodynamics Toolbox (Tudat) is a C++ library that provides support for simulating various astrodynamics problems [56]. Most of the features needed for performing numerical orbital propagations were already included in the latest version at the beginning of the thesis.

In addition to Tudat's core library, a few example applications are provided by the project administrators. One relevant example is the single perturbed satellite propagator application, which can be used to propagate a single satellite while including several perturbations in the acceleration model. The initial conditions and characteristics of the body, as well as which perturbations to include, can be chosen, but this can only be done by modifying the code and re-compiling before running the app again with the new conditions. Given that many propagations will have to be performed in order to find the conditions leading to shortest orbital lifetimes, this approach, in which the code has to be manually modified and the app re-compiled for every case, seemed unfeasible and unpractical.

Thus, a new application based on the single perturbed satellite propagator example application was created. This application reads the input settings from a text file, translates them to C++ objects, and then those settings are used to set up the propagation accordingly. Then, when the propagation is done, the information of interest (specified in the input file) is exported to an output text file. In this way, the application only needs to be compiled once and then it can be run with many different input files leading to different results.

This application has been called Tudat Earth Satellite Propagator (TESP), since currently, given the settings that can be changed through the input file, it enables the propagation of the orbit of any satellite about Earth including the most relevant orbital perturbations, namely geopotential, Sun's and Moon's third-body attraction, atmospheric drag and SRP. Although Tudat is not optimised for parallel processing (i.e. using several cores at the same time), mainly because the propagation of the orbit of a body is a sequential procedure, in which step i cannot be started until step $i-1$ has been completed, TESP *can* take advantage of the availability of multiple cores, as it has been designed so that each propagation is independent of each other, by using different input and output files to prevent problems that may occur if one would try to modify the same file from different cores at the same time. This means that many instances of TESP can be run concurrently with different settings, potentially reducing computation times significantly on systems with multiple CPUs.

In fact, most of the propagations were run on the Eudoxos server of the Aerospace Engineering Faculty, which has 56 CPUs. A maximum of 14 TESP processes were run concurrently to leave sufficient computational power available for other users. Once the propagations had been completed, the output files were downloaded to a local computer and analysed with other tools, mainly MATLAB [57].

When many input files had to be generated, rather than generating them one by one manually, MATLAB was used to generate them automatically by reading an optimisation-setup file in which it would be specified, for instance, that the inclination should range from 0 to 45 degrees, with steps of 5 degrees, and the mass from 2 000 to 3 000 kg, with steps of 50 kg, leading to a total of 210 different files in this case. This is done locally, as this is not computationally expensive, but then, these files are uploaded to the sever, where the propagations are performed. This whole process is summarised in the work-flow diagram in Figure 4.1.

For running several propagations in parallel on the sever, the GNU Parallel software [58] was used. This software allows the user to specify a set of input arguments for a program (e.g. all the input files in a given directory) and it runs each case in parallel up to a specified limit of concurrent jobs (14 for the Eudoxos server). Then, as soon as one of the processes finishes, the next case (i.e. with the path to a different input file as input argument) is automatically started, and this process is repeated until all the cases have been run.

Although Tudat is a validated tool, it was necessary to check that Tudat apps developed for this Master thesis were providing valid results. This was done by propagating several orbits with different perturbations turned on and off, and observing the appearance of the expected effects on the orbital elements. Additionally, the software to compute the sub-satellite point using the equations described in Section 3.1.4 was validated by checking that, for a GEO satellite, if all perturbations are turned off: (1) the longitude of the SSP remains constant; (2) the longitude of the SSP oscillates around a constant value if the inclination is not exactly 0; (3) the longitude of the SSP experiences an increasing secular variation if the altitude is set 100 km below GEO (i.e. the SSP moves eastwards). This is in accordance with expected behaviour. When the relevant perturbations are turned off, there is a secular variation of the longitude of the SSP (for a *pure* GEO satellite) of about 0.57 degrees per month, which is in accordance with observations indicating that this precession has a period of 53 years (or 0.566 deg/month) [59]. This serves also as validation of Tudat and TESP, as the function to compute the longitude of the SSP has been applied to data obtained from orbital propagations set up through TESP and run by Tudat. The results of this validation can be found in Figure B.2.

4.1.2. ACCELERATION MODEL

Before finding out which are the most suitable propagator and integrator (in terms of accuracy and computation times) for GTOs, it is necessary to determine which are the relevant perturbations that cannot be neglected, as the choice of the propagator and the integrator will very likely depend on the perturbations that are included in the acceleration model.

In this phase, thus, accuracy will rule over efficiency. A very accurate integrator (a Runge-Kutta 4 integrator with a step-size of just one second) will be used to perform the propagations, and a propagator based on

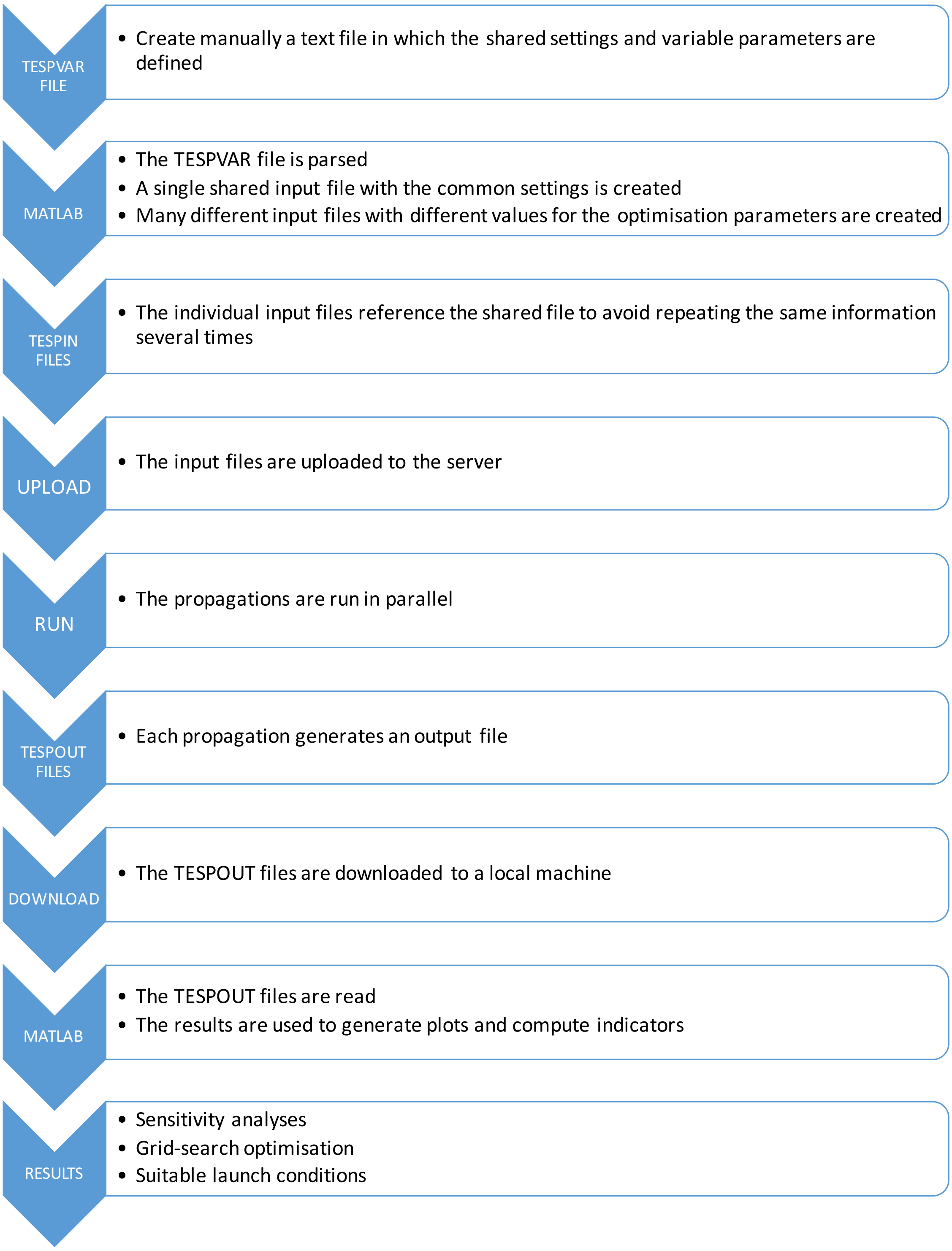

Figure 4.1: Main work-flow diagram for the generation of results.

the Cowell method will be used. For more information on this integrator and propagator, see Sections 4.1.4 and 4.1.3, respectively.

According to previous studies on the propagation of objects in GTO, the perturbations that have to be included in order to yield reliable results are the geopotential (a spherical harmonics expansion up to degree and order 7), the Sun's and Moon's central gravity, atmospheric drag and SRP [11]. By propagating the same object in the same orbit with each of these perturbations turned on and off, it has been determined that, in fact, they cannot be neglected, and additionally the minimum degree and order of the geopotential expansion have been obtained.

The characteristics of the object and the initial orbit that has been propagated with different perturbations neglected or included in the acceleration model are:

- Initial epoch: J2000.
- Initial perigee altitude: 175, 200 or 250 km (can be inferred in each case from the perigee altitude plots provided in the following subsections).
- Initial apogee altitude: 35 780 km.
- Initial inclination: 10 deg.
- Initial argument of perigee, RAAN and true anomaly: 0 deg.
- Constant body mass: 3 000 kg.
- Constant body cross-sectional area: 15 m^2.
- Constant drag coefficient: 2.2.
- Constant radiation pressure coefficient: 1.5.

GEOPOTENTIAL

From Figure 4.2 it is clear that the geopotential can play an important role on the evolution of the orbit. The line labelled 1 (i.e. degree and order 1) corresponds to the case in which only Earth's central gravity is considered, and all the J-terms are neglected. This approximation is clearly not accurate enough. It is also clear that an expansion up to degree and order 2 is not enough. The rest of the curves are closer, although when zooming in significant gaps are found between the curves labelled 3, 5 and 7/10. Finally, it was decided that using degree and order 7 was accurate enough, as including a higher expansion (which is computationally more expensive) does not provide significantly different results.

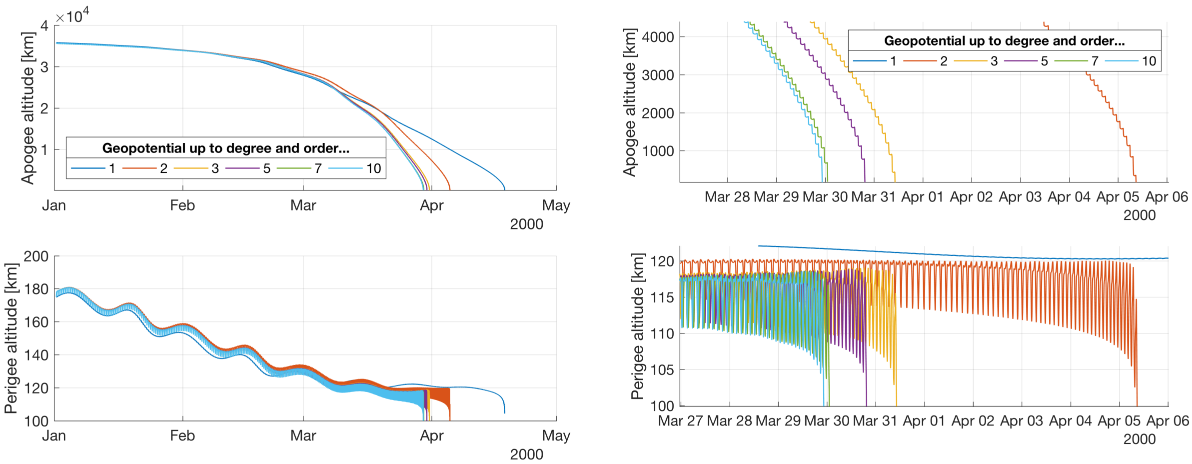

Figure 4.2: Evolution of the apogee and perigee altitudes of a GTO as a function of the degree and order of the spherical harmonics expansion of the geopotential (left) and zoom-in around the final epochs (right).

In the zoom-in plot in Figure 4.2 (right) it can be seen that the lifetime can change by several days if a degree lower than 7 is used. For instance, choosing a degree and order of 2, compared to a degree and order of 7, yields a lifetime 7 days longer, or 12.7% in relative terms, which is deemed to be too inaccurate.

However, although the degree has been fixed to 7, this does not necessarily mean that all the terms of the 7x7 expansion need to be included. In fact, the inclusion of the zonal terms alone is sufficient, as can be seen in Figure 4.3, which means that the order of the geopotential expansion can be set to 0. The evolution

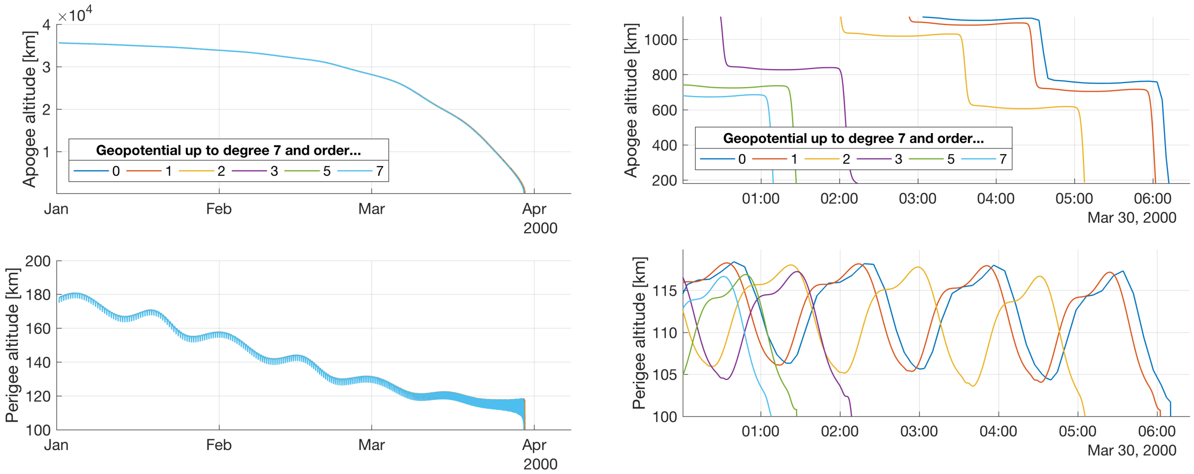

Figure 4.3: Evolution of the apogee and perigee altitudes of a GTO as a function of the order of a 7th-degree spherical harmonics expansion of the geopotential (left) and zoom-in around the final epochs (right).

of the orbit is virtually the same regardless of the chosen order, as long as the zonal terms up to degree 7 are included.

In the zoom-in plot in Figure 4.3 (right) it can be seen that the lifetime only changes by a few hours when changing the order of the geopotential expansion. For instance, choosing an order of 0 (i.e. neglecting all tesseral terms), compared to an order of 7, yields a lifetime about 7 hours longer, or 0.5% in relative terms, which is deemed to be acceptable.

Thus, from now on all the results will correspond to propagations in which the geopotential is expanded up to degree 7 and order 0, unless otherwise specified.

SUN'S GRAVITY

From Figure 4.4 it is clear that the Sun's gravity cannot be neglected. This result was already expected, as the Sun-synchronous resonance, which can affect the lifetime of objects in GTO drastically, is triggered by an interplay between several orbital perturbations, including the Sun's gravity, as explained in Section 3.3.1.

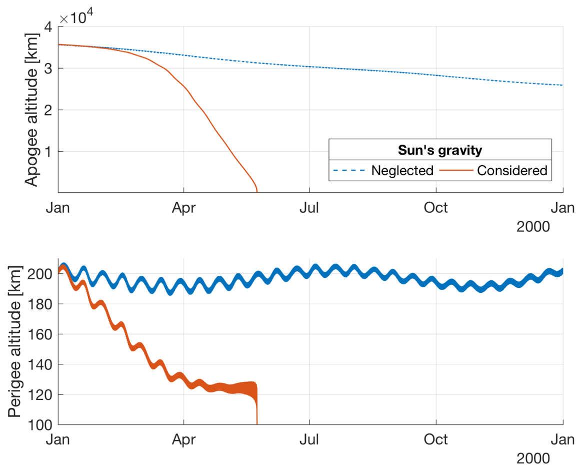

Figure 4.4: Evolution of the apogee and perigee altitudes of a GTO depending on whether the Sun's gravitational attraction is included in the acceleration model.

MOON'S GRAVITY

From Figure 4.5 (left) one could think that the effect of the Moon is not very important for the evolution of the orbit. However, it would be imprudent to conclude that this is always the case just by propagating a single orbit. Thus, another sample orbit was propagated, with a slightly higher initial perigee altitude (200 km instead of 175 km). In this case, as seen in Figure 4.5 (right), the no-inclusion of the Moon's gravity in the acceleration model does have an important effect on the evolution of the orbit. Thus, it can be concluded that the Moon's gravity cannot be neglected during the propagation of objects in GTO, as doing so could cause errors of about 13%, as in Figure 4.5 (right) for example, or perhaps even more in some cases.

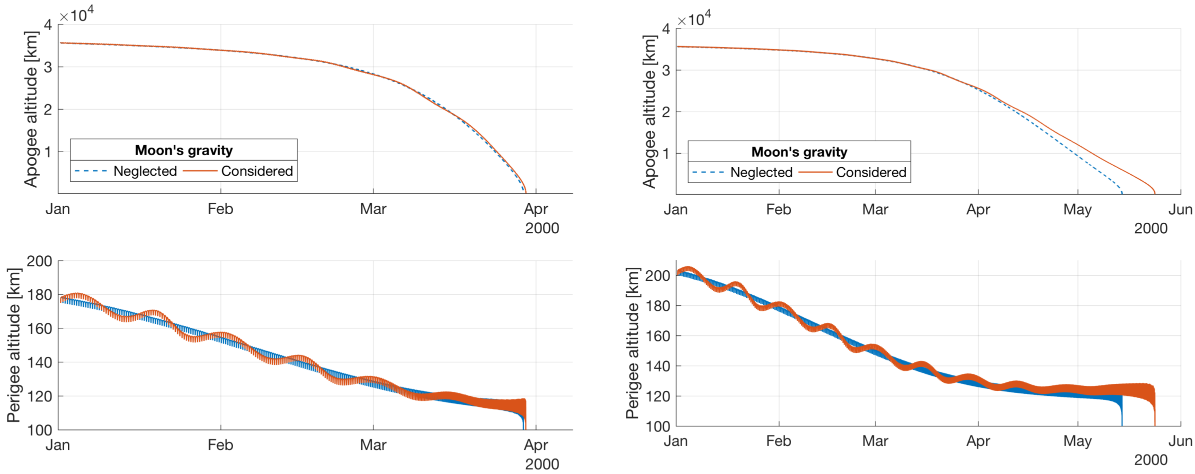

Figure 4.5: Evolution of the apogee and perigee altitudes of a GTO depending on whether the Moon's gravitational attraction is included in the acceleration model and with initial perigee altitude at 175 km (left) and 200 km (right).

ATMOSPHERIC DRAG

Since atmospheric drag is the only perturbation that causes secular effects on the semi-major axis [44] it is clear that it cannot be neglected, otherwise the object could only have been assumed to have re-entered when its perigee altitude had become negative. This is confirmed by Figure 4.6, in which it can be seen that when drag is considered, the object re-enters in about half year, but if it is neglected, it would never re-enter as the amplitude of the other perturbations is not sufficiently large so as to bring the perigee altitude to a value of 0 (if there is no atmosphere, it does not make sense to set a re-entry altitude). Indeed, the apogee altitude remains almost constant during the propagation if drag is neglected.

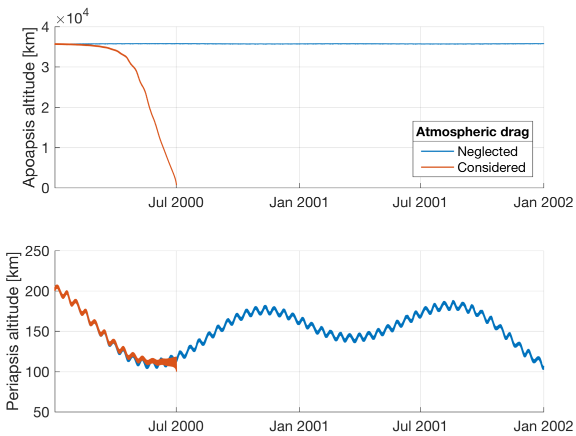

Figure 4.6: Evolution of the apogee and perigee altitudes of a GTO depending on whether atmospheric drag is included in the acceleration model.

The model being used for the propagations is the NRLMSISE-00 atmosphere model. This model provides estimates for the density of the atmosphere as a function of location (longitude, latitude and altitude) and time, based on historical data. Originally, Tudat did not support using this model when performing propagations in the future, as this model requires data about the solar activity levels, which are read from a file generated from past measurements. For that reason, Tudat's functionality has been extended in order to be able to provide the values for the predicted solar activity levels (which have significant levels of uncertainty, especially if the predictions are for distant times in the future). Although it is now possible to generate space weather files for future epochs from predictions, this functionality has not been used in the generation of results, in which all the perturbations have been performed starting at an epoch sufficiently back in time so that the propagation does not extend beyond 2017.

However, even for propagations in the past, when the model uses data coming from actual measurements, there is a significant level of uncertainty in the estimated value for the atmospheric density, which is related to the availability of measurements, both spatially and temporarily. For mean activity conditions, the estimated uncertainty of the densities provided by the NRLMSISE-00 atmospheric model is 15% [60]. This value decreases to about 5% for lower altitudes (below 90 km, although the body can be assumed to be re-entering at this point).

Since the NRLMSISE-00 model has a significant uncertainty, it was considered convenient to test another model: the exponential atmospheric density model, which is the simplest model (and thus also expected to be the one with highest uncertainty). If propagating with this model introduces an error that is within the range of uncertainty introduced by NRLMSISE-00, then the use of NRLMSISE-00 may be overkill, as it is expected to be computationally more expensive. Although using the exponential model reduces computation times to about 50%, the introduced error is too high, as can be seen in Figure 4.7. Even for a regular orbit with no Sun-synchronous resonances, using this atmospheric model leads to a lifetime that is almost 30% shorter. This model is clearly insufficient for the propagation of GTOs.

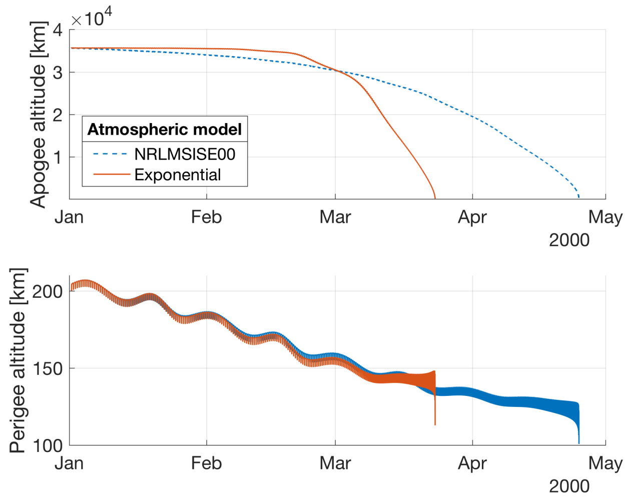

Figure 4.7: Evolution of the apogee and perigee altitudes of a GTO for two different atmospheric models.

The 30% error in the lifetime introduced by the exponential model is significantly larger than the error that would be introduced due to the uncertainties of the NRLMSISE-00 model, as in this case the 15% uncertainty in the atmospheric density scales down to a smaller error in the value of the lifetime. Although the density cannot be modified manually in Tudat, which would be ideal if one would want to determine the introduced error in the value of the lifetime when the density is changed by 15% with respect to the nominal value, there is a way around this limitation: since the atmospheric density and C_D only appear in one equation and appear multiplying each other (cf. Eq. (3.15)), a change by 15% in the value of C_D should lead to identical results as the same change in the value of the density. For instance, in Figure 4.11, two cases with $C_D = 2.0$ and $C_D = 2.2$ (10% increase) are compared. In this case, the 10% change in the value of C_D is scaled down to 1.8% when it comes to lifetime, i.e. about 5.5 times smaller. When C_D is increased from 1.0 to 2.0 (100% increase), the lifetime decreases by 17%, giving again the same 5–6 error scaling factor. Thus, it can be expected that the errors of about 15% in the value of the density introduced by the atmospher model will lead to errors in the value of the lifetime of about 2.5–3%.

SOLAR RADIATION PRESSURE

From Figure 4.8 it is clear that the effect of SRP cannot be neglected if reliable results are desired. Additionally, it was studied wether occultations of the rocket body (i.e. when Earth is located between the rocket and the Sun, blocking the radiative flux) have a big influence on the orbital evolution. If they can be neglected, the propagation would be a bit faster, as the geometric condition for occultation would not have to be tested at every integration step.

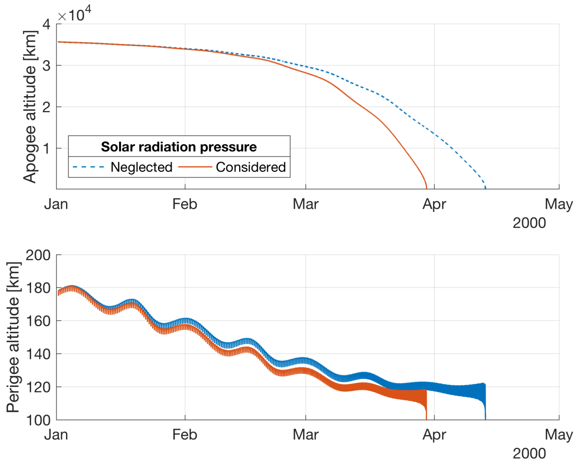

Figure 4.8: Evolution of the apogee and perigee altitudes of a GTO depending on whether SRP is included in the acceleration model.

Initially, a generic orbit, which does not undergo Sun-synchronous resonances, was tested. In this case, as seen in Figure 4.9, eclipses can be neglected, since the introduced error in the value of the lifetime is just a few hours (less than 0.2%), as can be seen in Figure 4.9 (right). In this case, the estimated lifetime is slightly shorter when eclipses are neglected, although this does not always hold; SRP can either slow down or speed up the body, depending on the position of the Sun relative to the spacecraft.

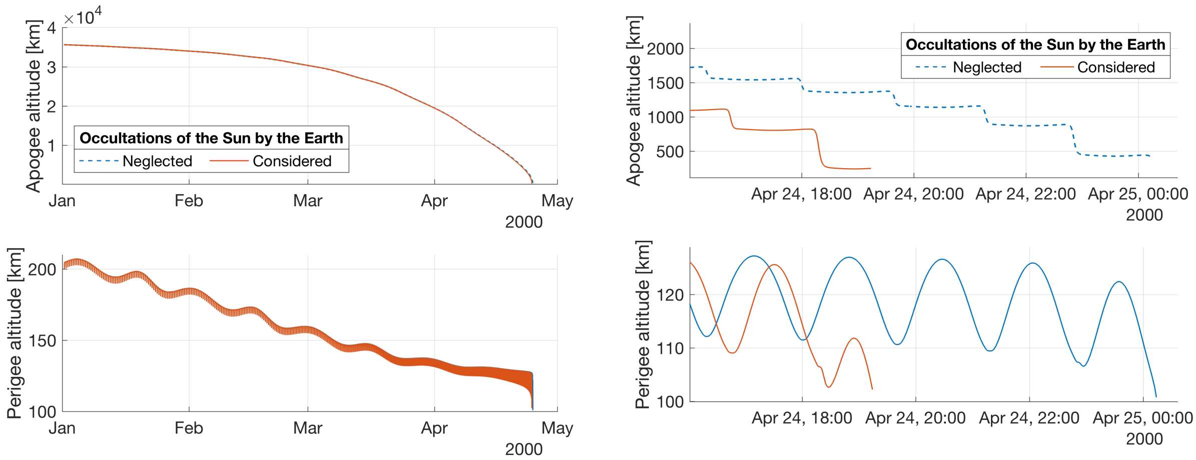

Figure 4.9: Evolution of the apogee and perigee altitudes of a GTO depending on whether eclipses are considered in the acceleration model (left) and zoom-in around the final epochs (right).

Another orbit, one in which a Sun-synchronous resonance takes place, was propagated with eclipses turned on and off, leading to the results provided in Figure 4.10. In this case, the introduced error in the value of the lifetime, which is more than 7%, is not negligible. For this specific case, neglecting eclipses makes the orbit decay slightly faster prior to Sun-synchronous conditions (not noticeable in the plot) and significantly slower afterwards.

In conclusion, eclipses cannot be neglected when the propagated body is (near conditions leading to) experiencing Sun-synchronous resonance, and thus will have to be considered when an accurate description of its evolution under those conditions is desired.

4.1.3. PROPAGATOR

Tudat includes two numerical propagators implementing, respectively, the Cowell and Encke methods. Before choosing one propagator over the other for the propagation of GTOs, a brief review of the characteristics of these two propagators is provided.

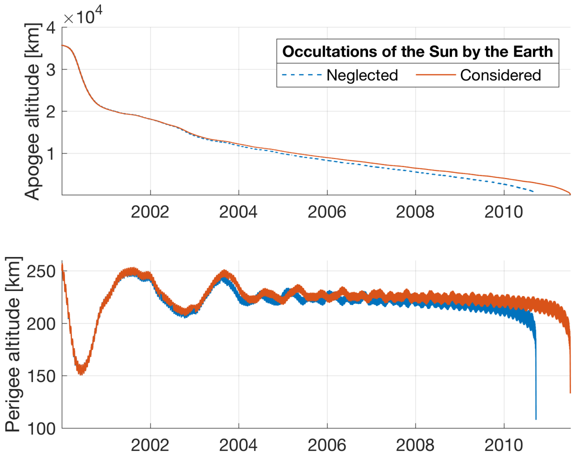

Figure 4.10: Evolution of the apogee and perigee altitudes of a GTO experiencing Sun-synchronous resonance depending on whether eclipses are considered in the acceleration model.

METHOD OF COWELL

This is the simplest method for the propagation of perturbed orbits. The following equation is solved numerically [39]:

$$\frac{\mathrm{d}^2\boldsymbol{r}}{\mathrm{d}t^2} = \boldsymbol{f_t} \tag{4.1}$$

where the total acceleration is given by $\boldsymbol{f_t} = -\frac{\mu}{r^3}\boldsymbol{r} - \nabla\tilde{R} + \boldsymbol{f}$. As can be seen, this is a direct numerical integration of Eq. (3.9). Small integrations steps are thus needed, leading to long computation times and integration errors building up over time.

METHOD OF ENCKE

This method uses the concept of a reference orbit, commonly a Keplerian orbit. The first step is to solve the following equation analytically [39]:

$$\frac{\mathrm{d}^2\boldsymbol{\rho}}{\mathrm{d}t^2} + \frac{\mu}{\rho^3}\boldsymbol{\rho} = 0 \tag{4.2}$$

where $\boldsymbol{\rho}$ is the position vector that the satellite would have if it followed an unperturbed reference orbit. Then, only the deviations in position and velocity with respect to this reference orbit are computed numerically, using the following expression:

$$\frac{\mathrm{d}^2\boldsymbol{\Delta r}}{\mathrm{d}t^2} = \frac{\mu}{\rho^3}\left[(\boldsymbol{\rho} + \boldsymbol{\Delta r})\mathbb{F}(q) - \boldsymbol{\Delta r}\right] - \nabla\tilde{R} + \boldsymbol{f} \tag{4.3}$$

where $\mathbb{F}(q) = \frac{2q}{1+2q}\left[1 + \frac{1}{1+2q+\sqrt{1+2q}}\right]$, and $q = \frac{\boldsymbol{\Delta r}\cdot(\boldsymbol{\rho}+\frac{1}{2}\boldsymbol{\Delta r})}{\rho^2}$. Finally, the perturbed position is obtained from $\boldsymbol{r} = \boldsymbol{\rho} + \boldsymbol{\Delta r}$, while the perturbed velocity can be obtained from $\frac{\mathrm{d}\boldsymbol{r}}{\mathrm{d}t} = \frac{\mathrm{d}\boldsymbol{\rho}}{\mathrm{d}t} + \frac{\mathrm{d}\boldsymbol{\Delta r}}{\mathrm{d}t}$.

The parameter q provides a measure of how much the perturbed orbit is differing from the reference one. As more integration steps are completed, the perturbed orbit usually starts to differ significantly from the reference orbit and thus the reference orbit has to be rectified, i.e. computed again from Eq. (4.2). This should be done whenever the value of q rises above 0.01. This method typically yields better performance than Cowell's method for small but strongly varying perturbing forces, since the integration step can be chosen larger [39].

When propagating the same orbit using different propagators, it was observed that the accuracy remains fixed, as it is determined by the integrator (step-size and/or error tolerance) rather than by the choice of the propagator. However, the two propagators did perform differently, as the Encke propagator took slightly longer than the Cowell propagator for a few representative orbits on which both were tested. On average, the computation time was about 10% larger when the Encke propagator was used, both when using a fixed-step-size and a variable step-size integrator. Thus, all the future propagations were performed using the Cowell propagator, unless otherwise specified.

4.1.4. INTEGRATOR

Tudat includes several numerical integrators. Before choosing one integrator over the rest for the propagation of GTOs, a brief review of the Runge-Kutta methods is provided.

STANDARD RUNGE-KUTTA METHOD

The use of the standard fourth-order Runge-Kutta integrator (RK4) is proposed in [14] for the integration of the averaged equations of motion, and is also the most widely used integrator for solving engineering problems [61]. According to this method, Eq. (3.9) can be solved recursively using [14]:

$$\begin{aligned} \boldsymbol{x_{i+1}} &= \boldsymbol{x_i} + \frac{\kappa}{6}(\boldsymbol{k_1} + 2\boldsymbol{k_2} + 2\boldsymbol{k_3} + \boldsymbol{k_4}) \\ \boldsymbol{k_1} &= \boldsymbol{f}(\boldsymbol{x_i}, t_i) \\ \boldsymbol{k_2} &= \boldsymbol{f}(\boldsymbol{x_i} + \frac{\kappa}{2}\boldsymbol{k_1}, t_i + \frac{\kappa}{2}) \\ \boldsymbol{k_3} &= \boldsymbol{f}(\boldsymbol{x_i} + \frac{\kappa}{2}\boldsymbol{k_2}, t_i + \frac{\kappa}{2}) \\ \boldsymbol{k_4} &= \boldsymbol{f}(\boldsymbol{x_i} + \kappa\boldsymbol{k_3}, t_i + \kappa) \end{aligned} \tag{4.4}$$

with κ the integration step-size and $t_i = t_0 + i\kappa$.

This method is computationally more expensive than the Euler method, as four function evaluations per integration step are required. However, it is also more accurate and thus larger integration steps can be used, generally leading to better efficiency for most astrodynamics problems.

This method is called a fourth-order method because its global error is of order $O(\kappa^4)$ [14]. In contrast, the global error of Euler's method is of order $O(\kappa)$ [62]. There exist Runge-Kutta methods of higher order, some of which have been used for the long-term propagation of HEOs. Some of these methods are discussed below.

HIGHER-ORDER RUNGE-KUTTA METHODS

In addition to the standard Runge-Kutta (RK) method described above, there exist many other Runge-Kutta methods that can provide better performance for certain applications. Any Runge-Kutta method can be expressed in a general way through [63]:

$$\begin{aligned} y_{n+1} &= y_n + \kappa \sum_{i=1}^{s} b_i k_i \\ k_i &= f\left(y_n + \kappa \sum_{j=1}^{i-1} a_{ij} k_j, t_n + c_i \kappa\right) \end{aligned} \tag{4.5}$$

Then a Runge-Kutta method is completely defined by providing the values of c_i, b_i and a_{ij}, which can be done using a so-called Butcher tableau:

$$\begin{array}{c|cccc} c_1 & a_{11} & a_{12} & \dots & a_{1s} \\ c_2 & a_{21} & a_{22} & \dots & a_{2s} \\ \vdots & \vdots & \vdots & \ddots & \vdots \\ c_s & a_{s1} & a_{s2} & \dots & a_{ss} \\ \hline & b_1 & b_2 & \dots & b_s \end{array} \tag{4.6}$$

The semi-analytical propagation tool developed by CNES uses a sixth-order Runge-Kutta method [13], although in the documentation it is not specified which specific algorithm is being used, as many sixth-order RK methods exist. For instance, an RK6 method is derived in [64], but in this case only five function evaluations per step are needed in comparison to conventional RK6 methods which require the computation of $k_1, k_2, \dots, k_6$. This is achieved by considering evaluation of higher-order derivatives.

Some studies suggest that the use of a high-order RK-Nyström (RKN12) method is the best option for numerical integration of super-geostationary disposal orbits when non-singular (e.g. equinoctial) orbital elements are used [65]. Butcher tableaus for RK-Nyström methods of order 8 and 12 can be found in [66], although the algorithms derived there are more suitable for (systems of) second-order differential equations. The problem of orbital propagation can be formulated in this way in Cartesian components, but when orbital elements are used, it becomes a system of first-order differential equations, so the methods presented there may not be suitable when integrating the orbital elements.

There are many integrators available in Tudat, from the simple yet powerful RK4 integrator to more advanced variable step-size integrators. Since GTOs have large eccentricities (about 0.7), their dynamics are much faster close to perigee that when at apogee, so a variable step-size integrator should be suitable for this kind of orbit, as small steps would have to be taken at perigee but larger steps could be taken near apogee. It was found that the most efficient integrator was the one based on the Runge-Kutta-Fehlberg's 7(8) method (RK78), which computes the suitable integration step-size based on a specified error tolerance. The default error tolerance for this integrator is 10^{-12}. With this tolerance, the integrator was compared to a very accurate (but slow) RK4 with step-size of one second. Both integrators provided virtually the same results (relative error of less than 0.01%), although the RK78 was hundreds of times faster.

It was also checked whether this accuracy was maintained when propagating orbits in which a Sun-synchronous resonance arises. When comparing an RK4 with step-size of 10 seconds to an RK78 with tolerance of 10^{-12}, it was found that, despite the Sun-synchronous resonance and the larger propagation period, the results of the two propagations were virtually identical, although the RK78 integrator was again several times faster. For this case, the step-size for the RK4 integrator was increased to 10 seconds because the propagation period was significantly longer (leading to very long computation times if 1 s was used), after checking that the RK4 integrator provides virtually the same results for step-sizes of 1 and 10 seconds.

After deciding that the RK78 integrator would be used for further propagations, an analysis to determine a reasonable error tolerance was carried out. The orbit undergoing solar resonance was propagated with the RK78 integrator using four different error tolerances, namely 10^{-8}, 10^{-9}, 10^{-10} and 10^{-12}. Although all of them provided reasonably similar results, it was found that the integrator with a tolerance of 10^{-8} could lead to significant errors in the perigee altitude (more than 10 km). Since the re-entry condition is defined in terms of perigee altitude, it is necessary to know this parameter with sufficient accuracy in order to get reliable estimates of the lifetime. Thus, it can be concluded that an error tolerance of 10^{-9} is sufficient, which is about twice as fast as the same integrator with a tolerance of 10^{-12}.

From now on, all the presented results will correspond to propagations using an RK78 variable step-size integrator with an error tolerance of 10^{-9}.

4.2. SENSITIVITY ANALYSIS

After having decided upon the perturbations to include in the acceleration model (zonal terms up to degree 7, Sun's and Moon's gravity, atmospheric drag and SRP with eclipses), the propagator (based on the Cowell method) and the integrator (RK78 with variable step-size and error tolerance of 10^{-9}), it is possible to use TESP with those settings to propagate different orbits in order to study the characteristics of GTOs in more detail. Since the evolution of GTOs can be very sensitive to many parameters, the problem of optimising (minimising) the lifetime of a GTO could become unfeasible if the number of optimisation variables is too large. Thus, it is key to identify which are the parameters GTOs are most sensitive to, and which can be assumed to be fixed, at least in a first iteration of the optimisation process.

In this section, several sensitivity analyses will be provided for changing values of the body properties (drag and radiation pressure coefficients) in Section 4.2.1 and to the change of the initial conditions (epoch and state) in Section 4.2.2.

4.2.1. BODY PROPERTIES

There are four relevant properties of the propagated body, namely its mass, cross-sectional area, drag coefficient and radiation pressure coefficient. The values of these four parameters can be changed independently, although in practice they could be combined into two variables. For the computation of drag, the ballistic coefficient appears in the equations of motion:

$$B = \frac{C_D A}{m} \tag{4.7}$$

On the other hand, for the computation of SRP, the following parameter, which will be called the sailing coefficient in this document, appears:

$$S = \frac{C_R A}{m} \tag{4.8}$$

Thus, in order to perform a sensitivity analysis about the body properties, it is not necessary to study the response to changes in the value of the four parameters; varying C_D and C_R (which is equivalent to varying B and S, respectively) will suffice. For instance, in Figure 4.11, the effect of varying the value of the drag coefficient is shown.

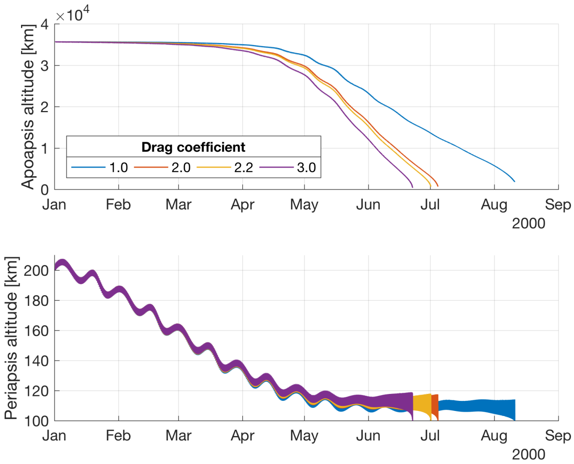

Figure 4.11: Evolution of the apogee and perigee altitudes of a GTO for different values of the body's drag coefficient.

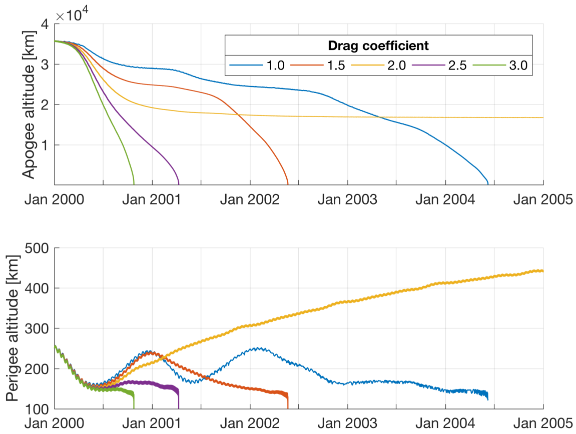

Figure 4.12: Evolution of the apogee and perigee altitudes of a GTO for different values of the body's drag coefficient, in which the case $C_D = 2$ leads to a Sun-synchronous resonance.

Although apparently the lifetime changes linearly with the drag coefficient, resulting in shorter lifetimes for larger drag coefficients, this does not always hold. For instance, in Figure 4.12 the initial perigee altitude is slightly higher, leading to a different evolution and to a Sun-synchronous resonance for the case $C_D = 2$. This means that the relation between lifetime and drag coefficient (or, equivalently, ballistic coefficient) can be strongly non-linear. Knowing the lifetime for $C_D = 1.5$ and $C_D = 2.5$ does not allow one to say anything about the lifetime for $C_D = 2.0$.

A similar sensitivity study was conducted for the radiation pressure coefficient. The results of propagating three objects with different C_R can be found in Figure 4.13. The value of C_R was varied from 1 (body that absorbs all solar radiation) to 2 (body that reflects all solar radiation). From there it can be seen that the sensitivity to C_R is small. However, after propagating more cases and identifying a few that undergo Sun-synchronous resonances (cf. Figure 4.14), it was observed that the lifetime can also be significantly sensitive to the value of the radiation pressure coefficient. This confirms again that the effects of SRP have to be included in the acceleration model.

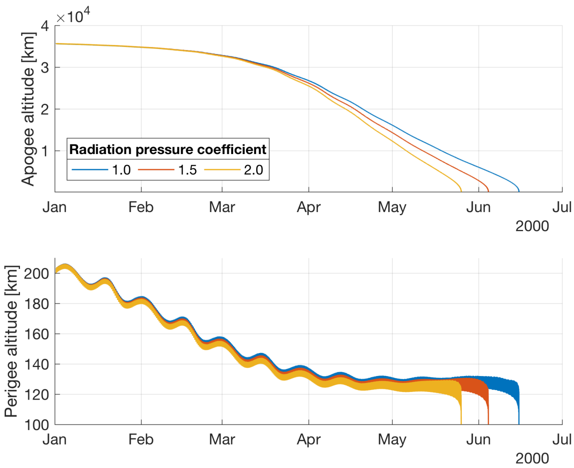

Figure 4.13: Evolution of the apogee and perigee altitudes of a GTO for different values of the body's radiation pressure coefficient.

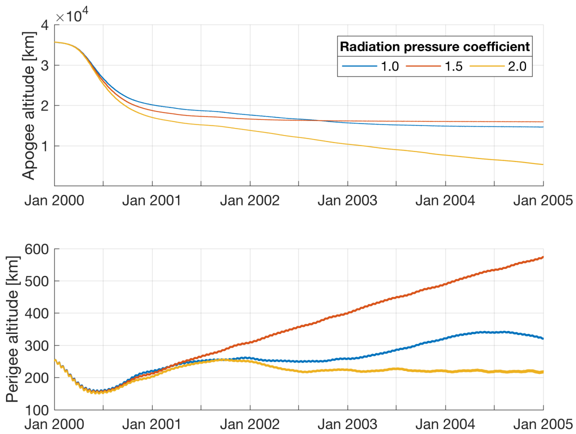

Figure 4.14: Evolution of the apogee and perigee altitudes of an object in a higher GTO for different values of the body's radiation pressure coefficient, in which the case $C_R = 1.5$ leads to a Sun-synchronous resonance.

4.2.2. INITIAL CONDITIONS

INITIAL EPOCH

The initial epoch can play a significant role on the evolution of the orbit. Depending on the moment at which the propagation begins, the Sun and the Moon will be positioned differently, and the solar activity levels will be different, which will affect atmospheric density.

As can be seen in Figure 4.15, the orbital evolution differs less when the propagation is postponed one year than when it is postponed a few months. This is due to the fact that the Sun will be located approximately at the same relative position after one year, so the only differences would be caused by the Moon (which has a less relevant effect) and solar activity levels (which change with a period of about 11 years).

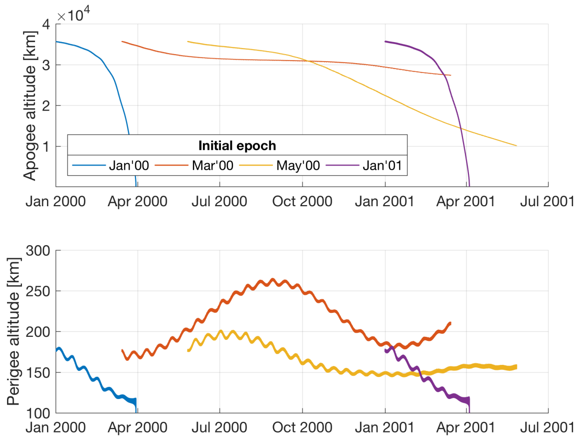

Figure 4.15: Evolution of the apogee and perigee altitudes of a GTO as a function of the initial epoch.

Previous research has shown that the effect of the Sun on the evolution of the perigee (and consequently on the lifetime, as the perigee is typically at altitudes where atmospheric drag is significant) depends on the position of the Sun in an Earth-centred perifocal reference frame. The key parameter is the Sun azimuth angle Λ, i.e. the angle between the Earth-pericenter line and the Earth-Sun line measured in the spacecraft orbital plane. When this angle is a multiple of 90 degrees, the Sun has no effect on the perigee altitude. On the other hand, when this angle is $45+90k$ degrees, with k an integer, its effect is maximum (causing the fastest increase or decrease of the perigee altitude, depending on the quadrant), as explained in Section 3.3.1. This means that, in two orbits for which the Sun azimuth angle is e.g. 45 and 135 degrees, the effect of the Sun on the lifetime will be the opposite. This can be seen in Figure 4.15, in which the two orbits whose evolution differs the most are those whose initial epoch differs by a value close to 0.25 years (or equivalently $\Delta\Lambda = 90$ degrees), i.e. those starting on January and March 2000.

INITIAL STATE

The initial perigee and apogee altitudes play an important role on the orbital evolution and lifetime. Changing the perigee altitude in the altitude range in which atmospheric drag is significant has a drastic effect on the lifetime, as can be seen in Figure 4.16. On the other hand, the effect of changing the apogee altitude is less noticeable, as seen in Figure 4.17. For instance, changing the apogee altitude by 2 000 km is less relevant than changing the perigee altitude by 75 km. Moreover, for this orbit a counter-intuitive effect is observed, since starting with higher apogee altitudes (while keeping the initial perigee altitude constant) leads to shorter lifetimes.

The initial inclination and RAAN determine the orientation of the orbit, and thus the relative position of the perigee with respect to the Sun. Thus, changing their values has a big impact on the lifetime of the orbit, as can be seen in Figures 4.18 and 4.19. Moreover, the relation is not linear: see for instance the curve for $i = 40$ degrees from Figure 4.18. One may expect it to lie between the curves for 23.4 and 60 degrees, but it does not. On the other hand, regarding the RAAN, looking at Figure 4.19 it seems that the orbital evolution is similar for those orbits whose initial RAAN differs by (a multiple of) 180 degrees.

The initial argument of perigee is also relevant for determining the initial geometry (i.e. the position of the Sun in the Earth-centred perifocal reference system). Thus, varying it leads to very different orbital evolutions, as seen in Figure 4.20. Since for GTOs the initial argument of perigee has to be either 0 or 180 degrees, only those two cases have been plotted.

Finally, the orbital evolution and lifetime is less sensitive to the initial true anomaly, as seen in Figure 4.21. Changing its value only affects the position of the propagated body within the orbital plane, but does not affect the Earth-Sun-pericenter geometry significantly. In the case of a GTO, with a period of about 10.5 hours, changing the initial true anomaly may be considered equivalent to changing the initial start epoch by less

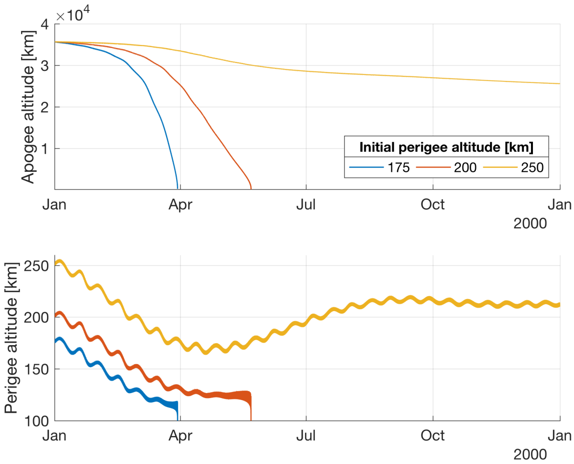

Figure 4.16: Evolution of the apogee and perigee altitudes of a GTO as a function of the initial perigee altitude.

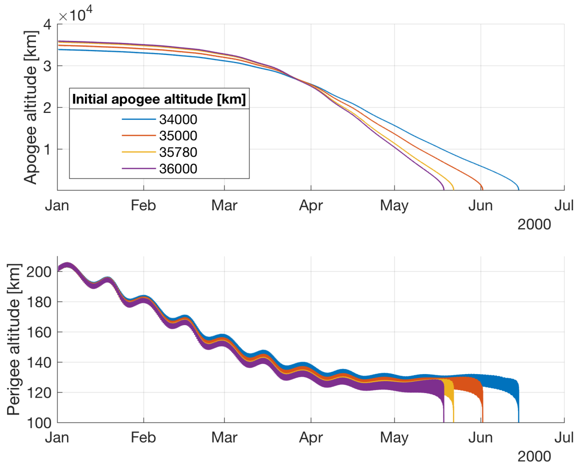

Figure 4.17: Evolution of the apogee and perigee altitudes of a GTO as a function of the initial apogee altitude.

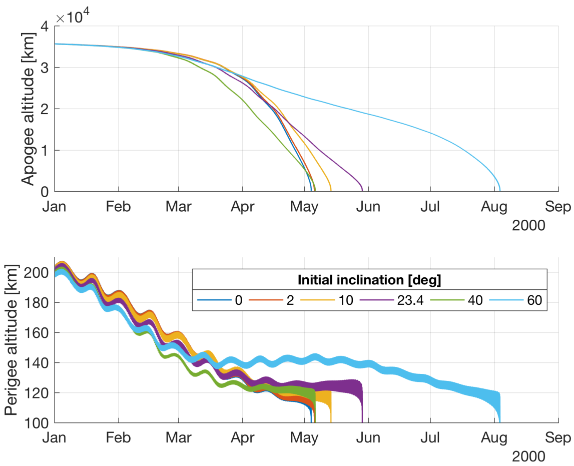

Figure 4.18: Evolution of the apogee and perigee altitudes of a GTO as a function of the initial inclination.

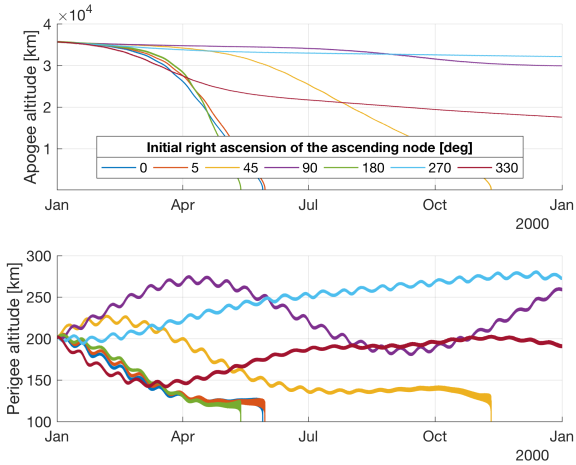

Figure 4.19: Evolution of the apogee and perigee altitudes of a GTO as a function of the initial right ascension of the ascending node.

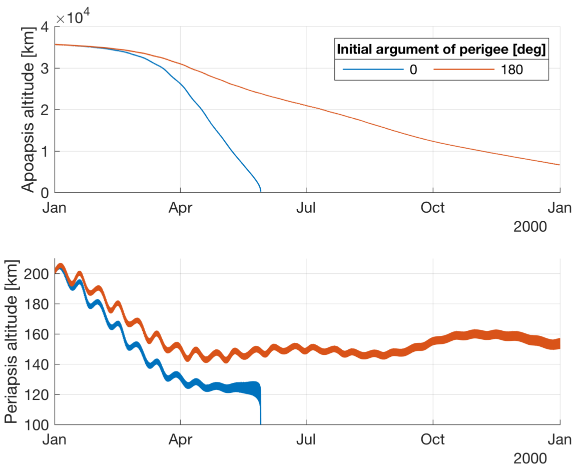

Figure 4.20: Evolution of the apogee and perigee altitudes of a GTO as a function of the initial argument of perigee.

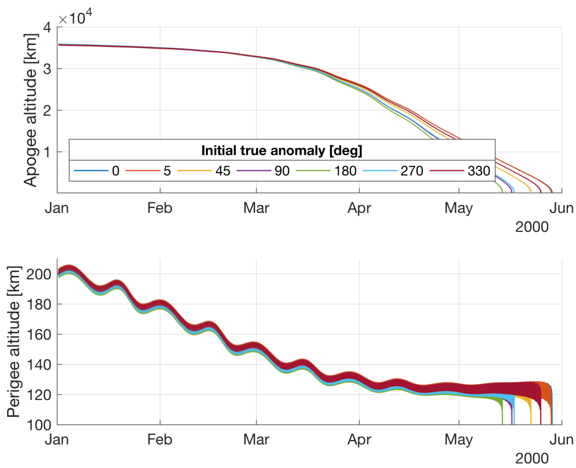

Figure 4.21: Evolution of the apogee and perigee altitudes of a GTO as a function of the initial true anomaly.

than 10.5 hours. Although this has no significant consequences during the initial part of the propagation, over long periods of time the various orbital evolutions begin to diverge slightly, eventually leading to variations in the value of the lifetime that may not be negligible (depending on the desired accuracy).

4.3. PROBLEM DEFINITION

The main research objective of this Master thesis consists in determining whether it is possible to use the effects of orbital perturbations reliably in order to make debris in GTO decay as fast as possible (or in a period shorter than a given maximum), and, if so, to find out the initial conditions leading to those optima. Previous studies have used a simple grid search to solve this problem, although they have only provided a few plots, whose resolution may not be sufficient given the Sun-synchronous resonance affecting GTOs, and limited to very specific cases, which may not be applicable to launches from places such as Kourou or Cape Canaveral.

Still, it has been decided that a grid search is the best way to approach the problem at hand. More advanced optimisation techniques exist, but usually those yield the optimum without providing much information about the surroundings and/or other (local) optima. A launch company wanting to comply with debris-mitigation guidelines will be interested to find as many launch opportunities as possible, and not only the best one, but also all other cases satisfying the guidelines.

It is necessary to study this problem in more detail if solid conclusions are to be drawn. The choice of the optimisation variables will be covered in Section 4.3.1, followed by the determination of a reasonable range of values and resolution in Section 4.3.2 leading to reliable and usable results.

4.3.1. CHOICE OF OPTIMISATION VARIABLES

From the sensitivity analyses described in Section 4.2 it is clear that the lifetime of objects in GTO is very sensitive to many parameters. Changes in the body's ballistic coefficient, the initial epoch, and all the elements of the initial state (perigee and apogee altitudes, inclination, RAAN, argument of perigee and even true anomaly) can lead to significantly different lifetimes. In many cases, a non-linear behaviour has been observed due to the existence of Sun-synchronous resonance. Thus, it is necessary to limit the number of variables so that the optimisation process can be completed in feasible times.

Limiting the number of variables entails fixing the values of some of the aforementioned parameters. Ideally, the parameters whose value should fixed are those for which the lifetime is less sensitive to and/or those that are less prone to undergoing significant changes during the phase of the mission design of a satellite launch.

BODY PROPERTIES

The ballistic coefficient of the body depends on its cross-sectional area, mass and drag coefficient. It is clear that there may be some uncertainty in its value mainly due to the fact that the body may be tumbling, leading to different cross-sectional areas that are difficult to predict. Moreover, carrying out an optimisation process in which the ballistic coefficient is chosen so as to minimise the lifetime does not seem realistic, as in general the rocket is designed attending to other aspects (such as aerodynamic efficiency, maximum payload mass, etc.) and is typically a given. Thus, it will be assumed that the ballistic coefficient is fixed and will not be considered as an optimisation variable. Since the effect of changing the radiation pressure coefficient is smaller (compare Figures 4.11 and 4.13), this parameter will also be kept constant.

INITIAL EPOCH

The lifetime of objects in GTO is very sensitive to the initial epoch, as was shown in Figure 4.15. This is mainly due to the fact that, for a given orbit, the location of the Sun will change depending on the day of the year and local time. This is the reason why the initial day of year (DoY) has been used by many authors as one of the optimisation variables [9–11].

The existence of Sun-synchronous resonances can make the orbital evolution even more sensitive. For instance, from Figure 4.22, it can be seen that, a given object in a given GTO that re-enters in less than four years, will still be in orbit (with an apogee altitude over 15 000 km) after more than 5 years if the propagation is started only one day earlier. Thus, it seems clear that the initial epoch cannot be fixed and should be taken as an optimisation variable.

It is important to recall that the initial epoch is the epoch at which the satellite is injected into GTO, which does not coincide with the launch epoch (there will be an offset of around 20 minutes between these two events for a direct ascent, cf. Section 7.1.1). In this document, the initial epoch will also be referred to as epoch of injection into GTO in some plots.

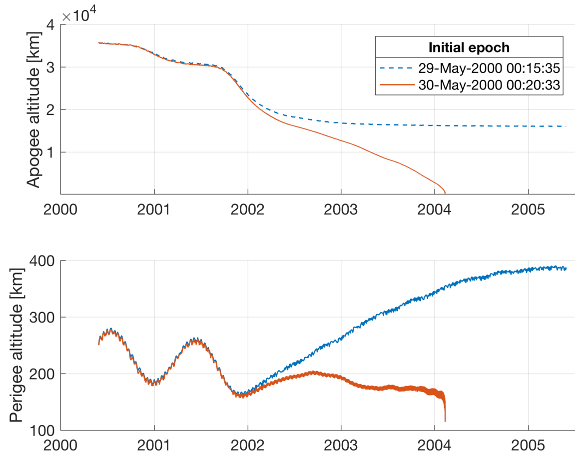

Figure 4.22: Evolution of the apogee and perigee altitudes of a GTO undergoing a solar resonance for two different initial epochs.

INITIAL STATE

The values of some of the elements of the initial state of the body can also be fixed. The most evident one is the true anomaly, which was shown to be the element that the lifetime is less sensitive to. The lifetime is not very sensitive to the apogee altitude either, and moreover the apogee altitude of GTOs is generally very close to GEO altitude (35 780 km), and thus it can also be assumed to be fixed during the last stages of mission design.

However, the lifetime was seen to be very sensitive to the initial values of other elements, namely the perigee altitude, inclination, RAAN and argument of perigee. However, given the general characteristics of missions to bring satellites into GEO, some of these can also be fixed. For instance, the inclination will be generally close to zero, as this is the inclination of GEO. It is possible that the GTO will be slightly inclined, and then the payload will be put into GEO by performing a manoeuvre at GEO altitude that circularises its orbit and turns it into equatorial ($i = 0$). However, this inclination that the GTO may have is generally small (less than 40 degrees) based on historical data from previous launches [34] (basically because the change of the orbital inclination is expensive in terms of propellant mass), so it can be assumed to be fixed at late stages of the mission design.

In order to determine whether the initial perigee altitude should be considered as an optimisation variable, it is necessary to look at the different phases of the mission, and the different ways in which a satellite may be brought to GEO. Most of the launchers generating debris in GTO are following a direct ascent to GEO, as discussed in Sections 2.2.2 and 7.1.1. In this case, the perigee altitude cannot be chosen freely (compared to the case in which a low parking orbit is used), but depends on the ascent profile, the used rocket vehicle and the mass of the payload and propellant to be used. This leads to the use of GTOs with perigee altitudes of around 200 km for the injection of objects in GEO when following a direct ascent (cf. Section 7.1.1). When another approach is followed, such as an ascent in which several burns are performed, even after injection into GTO, debris are generated in several orbits, generally having higher perigee altitudes. When these altitudes are above 400–500 km, it will take very long for natural re-entry to take place, so compliance with debris mitigation-guidelines is not possible [24]. This means that the range of interest of the perigee altitude is rather limited (150-400 km) and thus it can also be assumed to be fixed during the last stages of the mission design, so it will not be taken as optimisation variable.

As discussed previously, the argument of perigee at injection into GTO (and thus the value of the initial argument perigee to be used for the propagation) has to be either 0 or 180 degrees so that the satellite will reach GEO altitude when the orbit crosses the equatorial plane. Thus, the argument of perigee cannot be taken as an optimisation variable and will be set to 0 for all future propagations, unless otherwise specified. On the other hand, the RAAN does play a relevant role (cf. Figure 4.19), and is determined by the launch time and location, as discussed in Section 3.1.4. Thus, this will be the second optimisation parameter, since having propagated a set of orbits with different RAANs can potentially provide valuable information on what the optimum (local) times of launch are at different launch locations.

The other elements of the initial state to be analysed are the inclination and the true anomaly. The true anomaly is the one having the smallest influence on the evolution of the orbit (cf. Figure 4.21), and thus will be set to 0 in future propagations. On the other hand, the inclination does have a big influence on the evolution of the orbit, as seen in Figure 4.18. However, this parameter is usually fixed during mission planning and is chosen as small as possible in order to avoid having to perform expensive correction manoeuvres. Depending on the launch site, the minimum value will be close to e.g. 5 degrees (Kourou) or 28 degrees (Cape Canaveral), leading to different results. Thus, at some point, it will be necessary to generate different colour-map plots for different inclinations. However, this will not be chosen as optimisation variable, as having three optimisation variables (epoch of injection into GTO, RAAN and inclination) will render the problem unfeasible to solve, and additionally, it is very unlikely that any launcher would accept to use a larger inclination (and thus more propellant) in order to make the debris decay faster, if other alternatives that do not require the use of extra propellant exist. Thus, initially this variable will be set to 10 degrees, so the resulting optimisation will be applicable to launches from Koruou but not from Cape Canaveral. Later, it will be necessary to repeat the optimisation procedure for different inclinations, or at least 28 degrees if the obtained results are to be applied to launches from Cape Canaveral.

4.3.2. VARIABLES' RANGE AND RESOLUTION

In Section 4.3.1, it was concluded that the two optimisation variables would be the epoch of injection into GTO or day of year (DoY) and the initial RAAN. However, the range of interest and the required resolution, i.e. the minimum distance between consecutive steps that provides reliable results, have yet to be determined.

The DoY cannot be chosen in a completely arbitrary manner, i.e. the launcher company cannot ask the client to wait for e.g. 5 years because at that moment solar activity levels will be higher and that will lead to more favourable conditions from a debris-mitigation perspective. However, a flexibility of e.g. a few months or weeks *may* be acceptable for the satellite's operator. Given that the orbital evolutions are very similar when the start dates differ by a multiple of one year (as the position of the Sun is the same and only the Moon and the solar activity levels can play a role), most researches have limited the range of the initial DoY to one year [9–11]. The lower limit for the DoY has been generally set in the past, e.g. J2000, 1998, etc. as propagating in the future requires using predictions of the solar activity levels, which are inaccurate. However, if the results from this research are to be used in practice, the lower limit of the DoY will have to be placed eventually somewhere in the future and predictions of the solar activity levels will have to be made and used.

Although in the past most authors have used a range of one year for the initial DoY, it has been found that orbits with a DoY differing by 6 months have similar lifetimes, since the long-period effects of the Sun have a period of 6 months (cf. Section A.2.2). Thus, at least in this initial optimisation problem, the DoY range will be limited to just 0.5 years.

Regarding the launch epoch, it is reasonable to use at least a range of 12 hours (i.e. a range of 180 degrees for Ω_0), as this will include the most favourable and unfavourable locations of the Sun in the Earth-centred reference frame for the evolution of the perigee altitude, as well as two neutral locations for which it does not have any effect. However, there are more perturbations that play a role on the orbital evolution aside from the Sun's gravity. For instance, atmospheric density is maximum at around 2 PM local solar time [39]. This means that an object in GTO that reaches perigee at night will experience less drag than one that reaches perigee during the day. The slightly different position of the Moon and the Sun (they move slightly in 12 hours) can also have a small but noticeable effect over long periods of time. Thus, in principle, the range for the RAAN will be set to 360 deg. If the obtained plots contain two halves that are very similar, then the range will be limited to just 180 deg. Most authors have used a range of 24 hours (or 360 degrees) [8–11].

In the past, previous researchers have divided both the DoY and RAAN in about 50 steps each, leading to a resolution of 1 week for the DoY and 30 minutes for the launch time [11]. However, this seems insufficient when Sun-synchronous resonances take place. For instance, from Figures 4.22, it was seen that changing the epoch of injection into GTO just by one day can lead to a completely different orbital evolution. Similarly, from Figure 4.23, it can be seen that changing the initial RAAN just by 1 degree (i.e. a change of 4 minutes in the launch time) can make the object enter a Sun-synchronous resonance and increase the lifetime significantly (by a factor of almost 6 in this case). Choosing a large step-size is dangerous because certain cases affected by a Sun-synchronous resonance may be overlooked due to the use of an insufficient resolution. Thus, the step-size for the RAAN will have to be chosen small enough so that no Sun-synchronous resonance cases are overlooked. In this way, the zones close to negative Sun-synchronous resonance cases will be avoided.

Given the observations made in Figures 4.22 and 4.23, a lower limit for the resolution to use for the DoY and the RAAN can be proposed. Any optimisation carried out with a worse resolution may lead to contiguous cases whose lifetime differs drastically. Choosing resolutions of about 2 days for the DoY and 2 degrees (8 minutes) for the RAAN (launch time) or larger is insufficient. However, the actual minimum values that lead to reliable results (i.e. not overlooking any case undergoing a Sun-synchronous resonance) were not known,

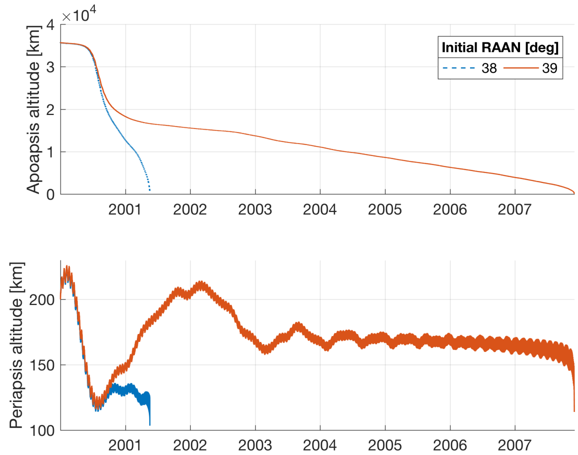

Figure 4.23: Evolution of the apogee and perigee altitudes of a GTO undergoing a solar resonance for two different initial RAANs.

so many propagations were performed using increasing resolutions until the values were found. This iterative process is shown in Figure 4.24. It can be seen that for the resolution of Figure 4.24b there are some isolated pixels with long lifetimes, and high-resonance ridges are overlooked. With the resolution from Figure 4.24c this is not the case, since the shape and location of the diagonal high-lifetime ridge can be inferred.

Based on this study, the recommended step-sizes for the DoY and RAAN are respectively 0.001 years (about 0.36 days) for the epoch of injection into GTO and 0.36 degrees for the RAAN (or about 1.5 minutes for the launch epoch). This leads to a plot in which no high-lifetime ridges (such as the one that can be inferred from Figure 4.24c and that is clearly visible in Figure 4.24d) are overlooked, and thus can provide useful information to the launch firm on which are the dangerous conditions that may lead the rocket to undergo a negative Sun-synchronous resonance.

Since the recommended range for the DoY is 0.5 years and the step-size is 0.001 years, this leads to 500 steps in the first optimisation variable. In the case of the initial RAAN, the recommended range is 360 degrees and the step 0.36 degrees, leading to 1 000 steps. Thus, the total number of cases to be tested per optimisation task amounts to 500 000.

4.3.3. Feasibility study

The propagation rate is defined as the propagation period (i.e. the difference between the final and initial integration epochs) per unit of computation time. In this report, it will be provided in units of propagated days per computation second (or simply days/s). Its value depends on many parameters, such as the (available) power of the processor on which it is being run, the used integrator and propagator, desired accuracy or perturbations included in the acceleration model.

The propagation rate on one of the cores of a dual-core 2.7 GHz Intel Core i5 was on average about 17 days/s. However, this value depends on the lifetime as well. For orbits that take short time to re-enter, most of the time is spent at low altitudes, where perturbations are larger and more variable, which renders the propagation slower, while for orbits that are propagated for several years this final part only represents a small percentage of the whole propagation, leading typically to a larger overall propagation rate.

The propagation rate on one of the cores of the Eudoxos server is slightly slower. On average, it was found to be around 13 days/s for different test cases.

Through the use of the GNU Parallel software described in Section 4.1.1, it is possible to run many propagations in parallel on computers with multiple cores. For instance, on a MacBook Pro equipped with the dual-core 2.7 GHz Intel Core i5 it is possible to run up to four propagations in parallel, as it supports hyper-threading, which consists on simulating two logical processors in a single physical core. However, it is less powerful than having four physical cores (without hyper-threading), as none of the tasks can use all the processing power of one core. It has been seen that, when four propagations are running in parallel, each of them uses about 80% of the CPU. The consequence is that the individual propagation rate decreases from about 17 days/s when only one task is being run to about 9 days/s when four tasks are being run in parallel. This means that, in practice, the aggregate propagation rate is 36 days/s. In summary, the processing power can be increased by a factor of 2.4 when using all the processing power of the MacBook Pro simultaneously.

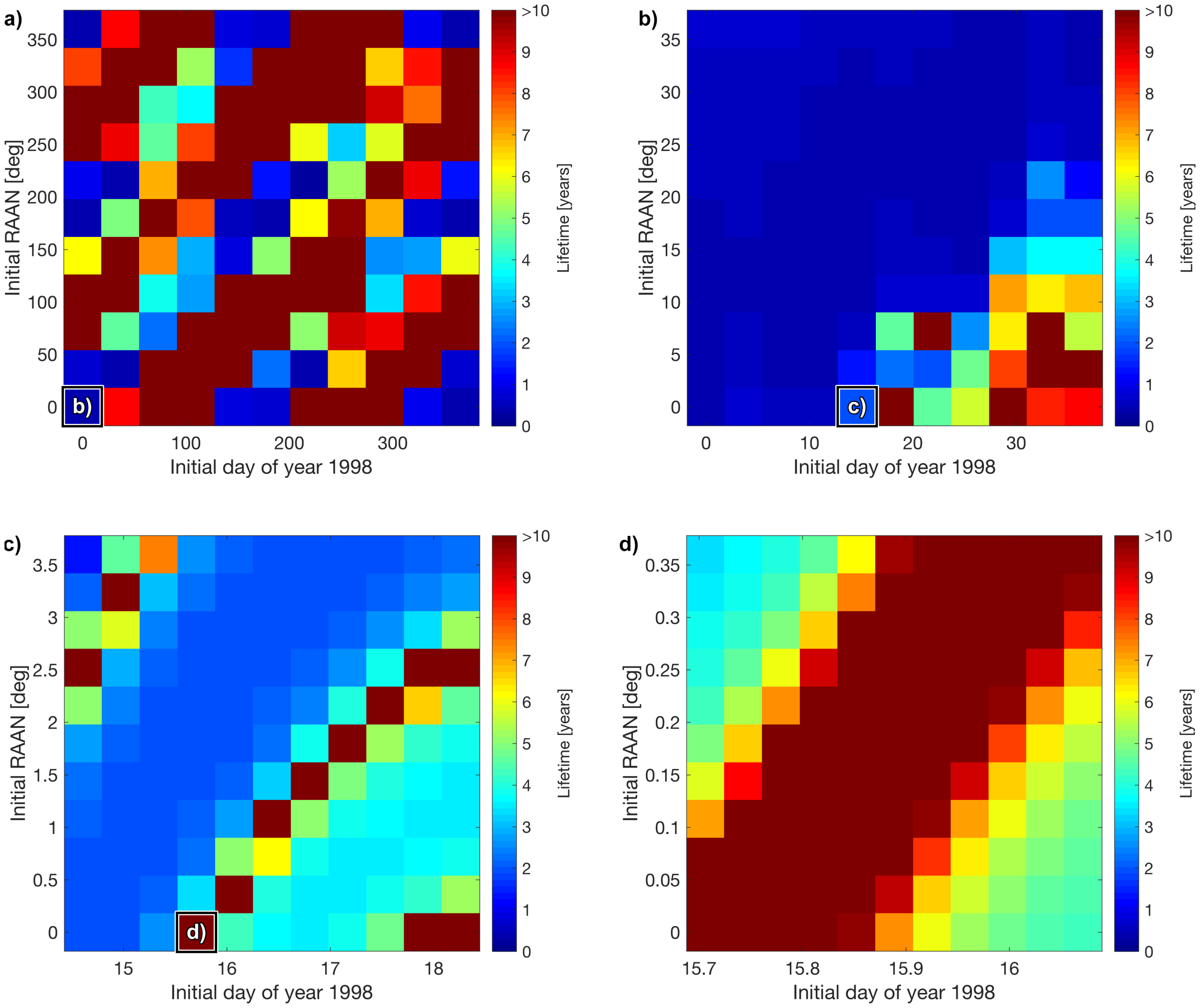

Figure 4.24: Lifetime of a GTO as a function of initial epoch and RAAN. Resolutions of **a)** 0.1 years and 36 degrees, **b)** 0.01 years and 3.6 degrees, **c)** 0.001 years and 0.36 degrees, **d)** 0.0001 years and 0.036 degrees.

Although the individual propagation rates are lower on the Eudoxos server, it is equipped with 56 cores, so the aggregate propagation rate will be larger. As previously mentioned, the total number of concurrent tasks is limited to 14. Thus, the aggregate propagation rate amounts to 180 days/s. This is almost five times faster than the MacBook Pro at full capacity.

Since the server is significantly faster and can be always on, it was decided that the optimisation tasks would be run on Eudoxos. With an aggregate propagation rate of 180 days/s, and knowing that the total number of orbits to be propagated per optimisation task is about half a million, the only thing missing in order to be able to provide an estimate of the overall computation time per optimisation task is the average propagation period of the considered orbits.

At this point, it was decided that the orbits would be propagated until the perigee altitude reached 100 km (re-entry) or the propagation period reached 10 years, whatever happened first. It was assumed that the average orbital lifetime using a low resolution would be representative of the actual mean lifetime for the domain of interest, so the average was taken from the results of the optimisation task shown in Figure 4.24**a**. The mean was 3.4 years. This means that each propagation covers on average a period of 1 240 days.

The overall number of days to be propagated per optimisation task, when the used resolution is small enough to provide reliable results, is thus about 620 million days. At the propagation rate of 180 days/s, this leads to an overall computation time of 40 days per optimisation task when the task is run on the server. On the MacBook Pro, the same task would take about 200 days.

These computation times are deemed to be unfeasible. Although a launcher company with access to computers with high processing power may have the optimisation task completed in a few weeks (which could be acceptable), quick tests could not be performed at early stages of the mission design in which many of the parameters have not been fixed yet. This kind of study may only be feasible at the end of the mission design phase, when everything except the time of launch has been fixed.

However, even though performing a single optimisation task may be feasible if enough processing power is available, the research objectives of this Master thesis cannot be reached using the available processing power and propagation techniques. Since access to more processing power is not an option, it will be necessary to use other propagation techniques, such as semi-analytical propagation, in order to increase propagation rates. Otherwise, it will not be possible to identify patterns and study how changes on other parameters (such as drag, inclination, etc.) affect the lifetime, as this will require carrying out many optimisation tasks, each of which taking weeks.

Indeed, in order to avoid having to wait for 40 days before getting the first preliminary results, the resolution was decreased for this first optimisation problem, hoping that it will still be possible to infer the location of high-lifetime ridges as in Figure 4.24c. The resolution of both the DoY and the RAAN was halved, leading to 125 000 cases to be propagated instead of 500 000, so the total estimated computation time (on the sever) was reduced to 10 days.

4.4. PRELIMINARY RESULTS

Even though reaching the research objective by following a fully-numerical approach had been deemed to be unfeasible, it was possible to obtain some preliminary results by completing one optimisation task. Using a step-size of 0.002 years for the DoY and 0.72 degrees for the initial RAAN, a colour-map plot was obtained. In this case, the RAAN was varied between 0 and 360, which would help determine whether studying the full range is necessary or it can be limited to just 180 degrees. The range for the initial epoch was just 0.5 years, as recommended after the discussion presented in Section 4.3.2, although it may be extended to one year or longer in future optimisation tasks if the process becomes more efficient.

The results of this optimisation task, which took 13 days to complete, are provided in Figure 4.25.

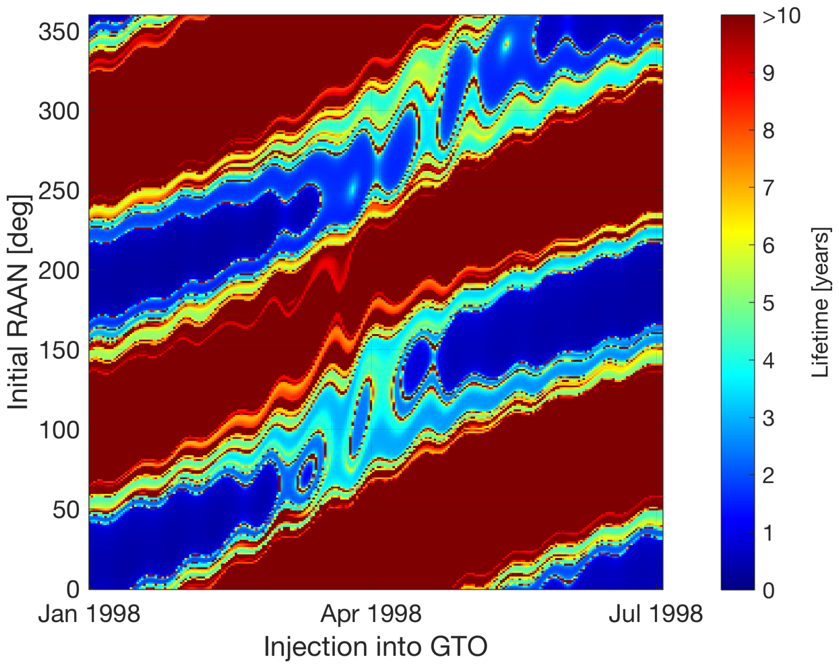

Figure 4.25: Lifetime of a satellite as a function of epoch of injection into GTO and initial RAAN.

The characteristics of the propagated body and initial orbit were exactly the same as those mentioned at the beginning of Section 4.1.2, with the exception of the initial epoch and RAAN, which were variable.

A few remarks can be made about Figure 4.25:

- There are many narrow high-lifetime ridges.
- No narrow low-lifetime valleys were found.

- The lifetime does not change smoothly from low-lifetime regions to high-lifetime regions, but presents increases in finite amounts, leading to several plateaus with relatively homogeneous lifetimes within them that are generally separated by high-lifetime ridges.

- Although the patterns found in the region $\Omega < 180$ degrees are similar to those found for $\Omega > 180$ degrees, the differences are significant (e.g. for the month of April), so the range of the initial RAAN (or launch time) cannot be reduced to just 180 degrees (12 hours).

- Two significant high-lifetime peaks are seen in the region $\Omega > 180$ degrees.

- Many low-lifetime basins are observed in the low-lifetime regions.

Note that the texture of Figure 4.25 is clearly sharper than that of other similar plots obtained in previous studies, such as the ones leading to the plots provided in Figures 3.4 or 3.9. In this case, a larger resolution has been used, leading to the appearance of large gradients near zones of solar resonance that cannot be easily observed in Figure 3.9, where the resolutions for the epoch of injection into GTO and launch time were, respectively, 5 and 10 times coarser, and interpolation was used to obtain a smooth plot. In the case of Figures 3.4a, atmospheric drag was not included in the acceleration model, and a lower resolution was used and the results interpolated, leading to a smoother plot.

In this case, the individual results have not been interpolated, as the high-lifetime ridges are not yet properly interpolated at this resolution. However, it has to be recalled that some authors have approached this problem from a statistical perspective, propagating many cases with slightly different conditions for each combination of DoY–RAAN. High-lifetime cases associated to solar resonance are very sensitive to initial conditions, so it is possible that the results for cases near resonance ridges are not always representative of the most likely orbital evolution. To address this issue, the statistical approach described in Section 3.3.3 has to be followed. However, this would require carrying out a much larger number of propagations (depending on the number of cases to be considered for each combination of DoY and RAAN). For instance, if this number were set to 100, the optimisation task would not taken 12 days, but 3 years, which is deemed to be completely unfeasible. Thus, this problem cannot be approached in a statistical way when using fully numerical propagation, as already suggested in previous studies [34].

The largest gradients in the horizontal direction for Figure 4.25 are close to 12 years per day, i.e. the lifetime changes by 12 years if the epoch of injection into GTO is varied by one day. These high gradients are found near the high-lifetime ridges, as seen in Figure 4.26 (left). Regarding the vertical gradients, the maximum values are close to 2 years/min, i.e. a change of the lifetime by 2 years when the launch time is varied by one minute, as shown in Figure 4.26 (right). Note that the gradients could not be computed for all cases, as the lifetime for the dark-red regions of Figure 4.25 are unknown (they are only known to be more than 10 years). For the narrow high-lifetime ridges, a lower limit for the value of the lifetime gradient was obtained when there was no more than one adjacent unknown-lifetime pixel. When two adjacent pixels have unknown lifetimes, nothing can be said about the (minimum) gradient between them. This means that the maximum lifetimes will be even larger than the aforementioned values, as the lifetimes of the resonance ridges extend beyond the limit of 10 years.

It is obvious that, if a launch company chooses a point close to a resonance ridge, the actual lifetime may be anywhere from a few months to several decades, as there are some sources of uncertainty, mainly related to the computation of atmospheric drag, which will introduce significant errors, especially near resonance-affected cases. Thus, launch firms should focus on the regions of low gradients, mainly the dark-blue regions of Figure 4.25.

To sum up, from this preliminary optimisation task it has been concluded that launch companies should avoid launching near resonance-affected regions because of the extreme sensitivity to initial conditions and uncertain parameters and, instead, should focus on finding safe areas in which both the lifetime and the lifetime gradient are small. However, the obtained plot is only valid for a certain body (with fixed mass, cross-sectional area, C_D and C_R) and for a specific initial orbit with perigee altitude of 200 km and inclination of 10 degrees. If other cases want to be studied, the optimisation task would have to be performed again after changing those parameters. Additionally, a statistical approach will have to be followed to determine whether the high-lifetime ridges corresponding to cases affected by resonances that can be observed in Figure 4.25 have to be definitely avoided by launch companies or whether they can be accounted into the 10% group of cases that would not fulfil the requirement of re-entry in less than 25 years with a 90% probability. Taking into account that generating these plots can take weeks (or years when following the statistical approach), even

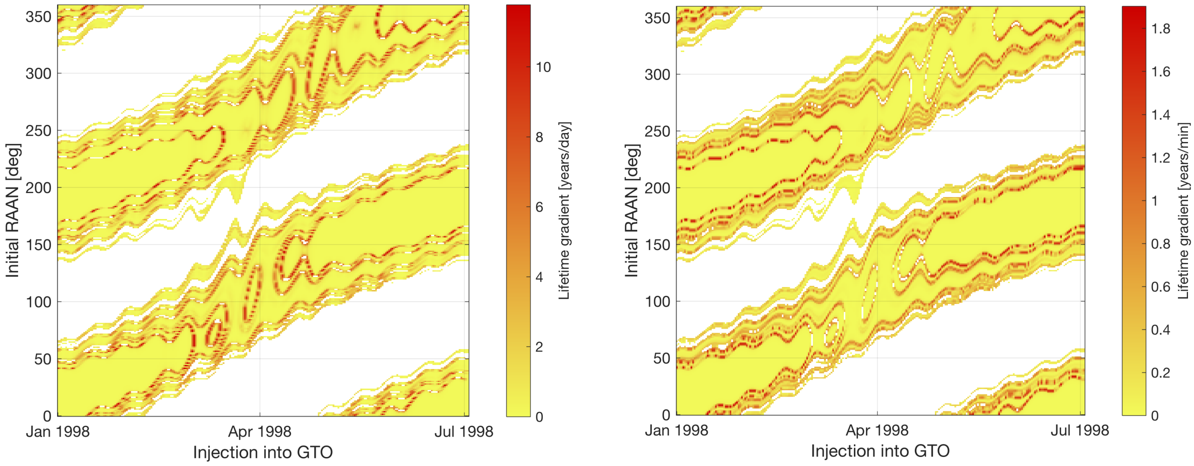

Figure 4.26: Lifetime gradient in the horizontal (left) and vertical (right) directions given per unit of change of the day of injection into GTO (left) and launch epoch (right). White colour represents unknown gradients.

when using 14 cores non-stop, it seems obvious that other techniques should be used in order to obtain practical results in feasible times. In the next chapter, a semi-analytical approach that can reduce computation times significantly is introduced.

5

Semi-analytical approach

Given the large number of propagations that will have to be carried out, it was found that the research objective cannot be reached using a fully numerical approach in which the state of the orbiting body has to be calculated several times for every orbital revolution, as this would lead to unfeasible computation times, as discussed in Sections 4.3.3 and 4.4.

One of the potential solutions to this issue, identified in previous studies [34], is the use of semi-analytical techniques, in which the mean elements are propagated in place of the osculating elements. Since these parameters vary much more slowly than e.g. the Cartesian position and velocity vectors, it is possible to use much larger step-sizes, in the order of one day for GTOs [14], leading to feasible computation times, while still keeping proper levels of accuracy. In this chapter, the theoretical basis of semi-analytical satellite theory will be introduced in Section 5.1. Then, in Section 5.2, the use of this theory in the implementation of a new propagator in Tudat will be discussed, followed by a verification and validation process using data from the Cowell numerical propagator and satellite-tracking data as reference. Finally, in Section 5.3, the procedure to reach the research objective will be redefined and an updated feasibility study will be provided based on the performance of the new semi-analytical propagator. Results will be presented in Chapter 6.

5.1. Semi-analytical satellite theory

The use of Keplerian elements instead of Cartesian components when solving the equations of motion (Eq. (3.9)) has several advantages. Firstly, it provides more insight about the temporal evolution of the orbit. Secondly, it enables the identification of perturbations with different periods and amplitudes, which can be treated independently using different techniques in order to optimise the integration process. However, this comes at a price, since generally the disturbing potentials and accelerations in Eq. (3.9) are given in Cartesian components (or in terms of longitude and latitude in the case of the geopotential), meaning that these functions have to be reformulated in terms of the orbital elements that are being used. Keplerian elements present singularities for near-circular and near-equatorial orbits, and thus it is typical to use other sets of parameters during integration, such as the equinoctial elements defined in Eq. (3.2).

Despite their higher complexity, semi-analytical techniques can reduce the computation times of orbital propagations over several decades by several orders of magnitude [14]. In this section, the Semi-analytical Satellite Theory (SST) reviewed in [14] will be presented after a short introduction to the basics of averaging techniques.

5.1.1. Fundamentals of averaging

In Figure 5.1, the temporal evolution of a generic orbital element that experiences three types of variations can be seen. Variations that steadily develop from the initial value are called secular variations. Long-period variations are superimposed on the secular variation and are oscillatory, with a period in the order of the period with which other slow-varying orbital elements (such as ω, Ω, or i) change. Finally, short-period variations are superimposed on top of long-period variations and have lower amplitude and shorter period, in the order of the period with which the fast-varying orbital parameter (such as M, f or u) changes, i.e. in the order of one orbital period [39]. By obtaining analytical expressions for the disturbing potentials and accelerations as a function of the orbital elements, the different terms causing these three different variations can be

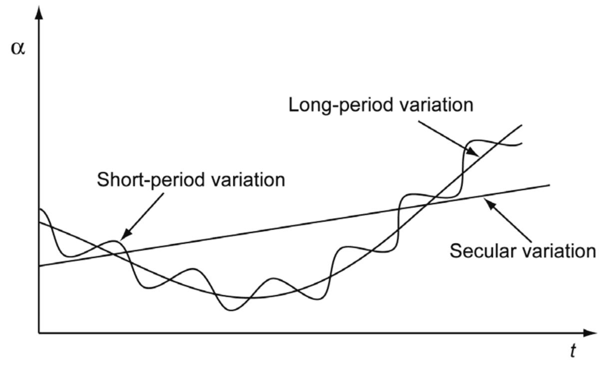

Figure 5.1: Secular, long-period and short-period variations of a generic orbital element [39].

identified and isolated. This is the basis of semi-analytical techniques, in which short-period variations are removed, enabling the use of a larger step-size and thus a much faster integration. This process is known as averaging.

To illustrate the basis of the averaging process, the disturbing potential due to the J_2-term of the geopotential can be used [39]:

$$\tilde{R} = \frac{3}{2} J_2 \frac{\mu R^2}{a^3} \left(\frac{a}{r}\right)^3 \left[\frac{1}{3} - \frac{1}{2}\sin^2 i + \frac{1}{2}\sin^2 i \cos 2(\omega + f)\right] \tag{5.1}$$

Since Eq. (5.1) has been expressed in terms of Keplerian elements, it is possible to readily identify different terms causing different types of variations. The J_2-term only produces secular variations in ω and Ω (cf. Table 3.1), and thus, when only this perturbation is considered, the only term of the part between square brackets on the right-hand side of Eq. (5.1) that is not constant is the last one. The two first terms in the bracket are constant and thus associated with secular variations. The third term depends on the true anomaly, and thus corresponds to short-period variations. There is no term depending on ω but not on f, which would correspond to long-period variations.

When only the secular variations and long-period variations of the orbital elements are of interest, short-period variations are averaged out by taking the mean value of $\tilde{R}$ with respect to M, after using Eqs. (A.6) and (A.7) to replace f by M. The mean value of a function $f(\boldsymbol{x}, y)$ with respect to y is defined as [67]:

$$\langle f \rangle (\boldsymbol{x}) = \frac{1}{2\pi} \int_{-\pi}^{\pi} f(\boldsymbol{x}, y)\, \mathrm{d}y \tag{5.2}$$

where $f(\boldsymbol{x}, y)$ is periodic in y of period 2π, $\boldsymbol{x}$ represents the slow variables and y is a fast variable.

A review of the basics of averaging techniques is presented in [67]. There these techniques are used, in combination with satellite-tracking data, in order to extract geodynamic parameters from the long-term and secular variations of mean elements, but it is also mentioned that they can be used for long-term trajectory propagations. However, this application is not treated in detail in the article. The theory presented there is given in generic terms, using generic x (slow) and y (fast) variables and generic functions. As a result, the application of this theory is not limited exclusively to the study of orbital perturbations. By using Eq. (5.2), the initial value problem

$$\begin{aligned} \dot{x} &= \varepsilon f(x, y) \\ \dot{y} &= h(x) + \varepsilon g(x, y) \\ x(t_0) = x_0, &\quad y(t_0) = y_0 \end{aligned} \tag{5.3}$$

where ε has a small value, can be transformed into

$$\begin{aligned} \dot{\overline{x}} &= \varepsilon \langle f \rangle (\overline{x}) \\ \dot{\overline{y}} &= h(\overline{x}) + \varepsilon \langle g \rangle (\overline{x}) \end{aligned} \tag{5.4}$$

where the dependency on the fast variable y has been removed from the right-hand side of the differential equations, and where the over-line on $\overline{x}$ and $\overline{y}$ denotes that the solution obtained from this system will correspond to the mean (or averaged) values of the variables. Thus, in astrodynamics, the averaged potential can be used to find the so-called averaged or mean orbital elements. If the disturbing potential is averaged again, but with respect to a slow variable, such as ω, then the resulting potential can be used to derive the so-called doubly-averaged or mean-mean orbital elements, in which only secular variations remain.

The perturbations due to the irregular Earth gravity field, third-body attraction, atmospheric drag and solar radiation pressure, which are the ones that have to be considered for the propagation of objects in GTO, can be single-averaged [14]. Then, analytical expressions (typically truncated series) for the short-period terms can be obtained, while the long-period and secular terms are integrated numerically, using a step-size several orders of magnitude larger than when no averaging is applied. In this reference, the equinoctial elements defined in Eq. (3.2) are used. The authors provide an exhaustive analysis in which not only the results that may be relevant for the implementation of semi-analytical techniques in a propagator are given, but also the intermediate derivations are included in most cases, for verification purposes. In the following subsections, the fundamentals of this theory are reported.

5.1.2. EQUATIONS OF AVERAGING

Eq. (3.9) can be written as a set of six first-order differential equations using the equinoctial orbital elements $(a_1, \ldots, a_6) = (a, h, k, p, q, \lambda)$, which leads to the so-called variation of parameters (VOP) equations of motion [14]:

$$\dot{a}_i = n\delta_{i6} + \frac{\partial a_i}{\partial \dot{\boldsymbol{r}}} \cdot \boldsymbol{q} - \sum_{j=1}^{6} (a_i, a_j) \frac{\partial \tilde{R}}{\partial a_j} \tag{5.5}$$

where $n = \sqrt{\mu / a^3}$ is the Keplerian mean motion, $\boldsymbol{q}$ is the sum of the disturbing accelerations, $\tilde{R}$ is the sum of the disturbing potentials expressed in equinoctial elements, and δ_{i6} is the Kronecker delta, which is equal to 0 for $1 \le i \le 5$ and 1 for $i = 6$. The partial derivatives of the equinoctial elements with respect to the velocity vector and the Poisson brackets (a_i, a_j) are given, respectively, in Sections 2.1.7 and 2.1.8 of [14].

From Eq. (5.5) it can be seen that the rate of change of any orbital element has three contributions: the first term on the right-hand side is the two-body part, which is different from zero only for the mean longitude; the second term is the Gaussian or non-conservative part; and the last term is the Lagrangian or conservative part.

These VOP equations of motion can be rewritten in such a way that short-period variations can be treated independently from long-period and secular variations. The first step is to assume that the osculating (i.e. non-averaged) elements contain two contributions, using the notation [14]:

$$\hat{a}_i = a_i + \eta_i(a, h, k, p, q, \lambda, t) \tag{5.6}$$

where the hat denotes osculating elements, a_i are the mean elements and η_i are small 2π-period variations. The short-periodic variations η_i can be written as [14]:

$$\eta_i = \sum_{j=1}^{\infty} \left[C_i^j \cos j\lambda + S_i^j \sin j\lambda \right] \tag{5.7}$$

which can also be written in terms of the eccentric longitude, $F = E + \omega + \Omega$, in order to avoid the infinite series. Expansions for η_i in terms of F, in terms of the true longitude, $L = f + \omega + \Omega$, and in terms of λ and θ, with θ the perturbing-body phase angle, can be found in [14]. Depending on the type of perturbation, it will be easier to express the potential or disturbing acceleration in terms of certain parameters. The terms C_i^j and S_i^j also depend on the fast parameter that is being used, and can be found in [14] as well.

When the mean elements are being propagated, Eq. (5.5) becomes:

$$\dot{a}_i = n\delta_{i6} + A_i(a_1, \ldots, a_5, t) \tag{5.8}$$

where A_i are the mean element rates. Note that the right-hand side of the equations does not depend on the fast variable $a_6 = \lambda$. This is achieved by averaging the osculating contributions over one orbital revolution:

$$A_i = \left\langle \frac{\partial a_i}{\partial \dot{\boldsymbol{r}}} \cdot \boldsymbol{q} - \sum_{j=1}^{6} (a_i, a_j) \frac{\partial \tilde{R}}{\partial a_j} \right\rangle = \frac{1}{2\pi} \int_{-\pi}^{\pi} \left(\frac{\partial a_i}{\partial \dot{\boldsymbol{r}}} \cdot \boldsymbol{q} - \sum_{j=1}^{6} (a_i, a_j) \frac{\partial \tilde{R}}{\partial a_j} \right) \mathrm{d}a_6 \tag{5.9}$$

Note that the osculating elements can be obtained from Eq. (5.6) if the mean elements and the short-period terms are known. The mean elements can be obtained by integrating Eq. (5.8) using large step-sizes if A_i is known, while the short-period terms (up to order j) can be computed directly from Eq. (5.7) if C_i^j and S_i^j are known. Expressions for A_i, C_i^j and S_i^j for the main perturbations affecting objects in GTO (zonal terms, some dedicated tesseral terms, third-body attraction, atmospheric drag and radiation pressure with or without eclipses) are provided in [14]. The equations corresponding to short-period terms are not included here, as some of them are several pages long and provide little insight on the physical description of the problem. However, a short review of the mean element rates for each of the relevant perturbations is provided in the following subsections.

ZONAL TERMS OF THE GEOPOTENTIAL

The mean element rates caused by zonal terms of the geopotential are given by [14]:

$$
\begin{aligned}
\frac{\mathrm{d}a}{\mathrm{d}t} &= 0 \\
\frac{\mathrm{d}h}{\mathrm{d}t} &= \frac{B}{A}\frac{\partial U}{\partial k} + \frac{k}{AB}\left(pU_{,\alpha\gamma} - qU_{,\beta\gamma}\right) \\
\frac{\mathrm{d}k}{\mathrm{d}t} &= -\frac{B}{A}\frac{\partial U}{\partial h} - \frac{h}{AB}\left(pU_{,\alpha\gamma} - qU_{,\beta\gamma}\right) \\
\frac{\mathrm{d}p}{\mathrm{d}t} &= -\frac{C}{2AB}U_{,\beta\gamma} \\
\frac{\mathrm{d}q}{\mathrm{d}t} &= -\frac{C}{2AB}U_{,\alpha\gamma} \\
\frac{\mathrm{d}\lambda}{\mathrm{d}t} &= -\frac{2a}{A}\frac{\partial U}{\partial a} + \frac{B}{A(1+B)}\left(h\frac{\partial U}{\partial h} + k\frac{\partial U}{\partial k}\right) + \frac{1}{AB}\left(pU_{,\alpha\gamma} - qU_{,\beta\gamma}\right)
\end{aligned}
\tag{5.10}
$$

The mean orbital equinoctial elements are used to obtain the values of [14]:

$$
\begin{aligned}
A &= \sqrt{\mu a} \\
B &= \sqrt{1 - h^2 - k^2} \\
C &= 1 + p^2 + q^2
\end{aligned}
\tag{5.11}
$$

Additionally, the cross-derivative operator is defined as [14]:

$$
U_{,\alpha\beta} = \alpha\frac{\partial U}{\partial \beta} - \beta\frac{\partial U}{\partial \alpha}
\tag{5.12}
$$

The disturbing potential U due to zonal terms is more easily expressed in terms of the direction cosines α, β and γ rather than using the orbital elements p and q. The direction cosines are obtained from [14]:

$$
\begin{aligned}
\alpha &= \boldsymbol{z_B} \cdot \boldsymbol{f} \\
\beta &= \boldsymbol{z_B} \cdot \boldsymbol{g} \\
\gamma &= \boldsymbol{z_B} \cdot \boldsymbol{w}
\end{aligned}
\tag{5.13}
$$

where $\boldsymbol{z_B}$ is the unit vector from the satellite to the disturbing body for perturbations caused by third bodies, or the unit vector from the centre of mass to the geographic pole of the disturbing body for perturbations caused by the central body, such as that due to zonal terms. The vector basis of the equinoctial reference frame $(\boldsymbol{f}, \boldsymbol{g}, \boldsymbol{w})$ has been introduced in Section 3.1.3 and is given in terms of p and q in Eq. (A.18).

The derivatives of the disturbing potential caused by zonal terms are given by [14]:

$$
\begin{aligned}
\frac{\partial U}{\partial a} &= \frac{\mu}{a^2}\sum_{s=0}^{N-2}\sum_{n=s+2}^{N}(2-\delta_{0s})(n+1)\left(\frac{R}{a}\right)^n J_n V_{ns} K_0^{-n-1,s} Q_{ns} G_s \\
\frac{\partial U}{\partial h} &= -\frac{\mu}{a}\sum_{s=0}^{N-2}\sum_{n=s+2}^{N}(2-\delta_{0s})\left(\frac{R}{a}\right)^n J_n V_{ns} Q_{ns}\left(K_0^{-n-1,s}\frac{\partial G_s}{\partial h}+h\chi^3 G_s\frac{\mathrm{d}K_0^{-n-1,s}}{\mathrm{d}\chi}\right) \\
\frac{\partial U}{\partial k} &= -\frac{\mu}{a}\sum_{s=0}^{N-2}\sum_{n=s+2}^{N}(2-\delta_{0s})\left(\frac{R}{a}\right)^n J_n V_{ns} Q_{ns}\left(K_0^{-n-1,s}\frac{\partial G_s}{\partial k}+k\chi^3 G_s\frac{\mathrm{d}K_0^{-n-1,s}}{\mathrm{d}\chi}\right) \\
\frac{\partial U}{\partial \alpha} &= -\frac{\mu}{a}\sum_{s=0}^{N-2}\sum_{n=s+2}^{N}(2-\delta_{0s})\left(\frac{R}{a}\right)^n J_n V_{ns} K_0^{-n-1,s} Q_{ns}\frac{\partial G_s}{\partial \alpha} \\
\frac{\partial U}{\partial \beta} &= -\frac{\mu}{a}\sum_{s=0}^{N-2}\sum_{n=s+2}^{N}(2-\delta_{0s})\left(\frac{R}{a}\right)^n J_n V_{ns} K_0^{-n-1,s} Q_{ns}\frac{\partial G_s}{\partial \beta} \\
\frac{\partial U}{\partial \gamma} &= -\frac{\mu}{a}\sum_{s=0}^{N-2}\sum_{n=s+2}^{N}(2-\delta_{0s})\left(\frac{R}{a}\right)^n J_n V_{ns} K_0^{-n-1,s} Q_{ns}\frac{\mathrm{d}Q_{ns}}{\mathrm{d}\gamma} G_s
\end{aligned}
\tag{5.14}
$$

where N is the maximum degree of the geopotential expansion to be considered, $J_n = -C_{n0}$ are the geopotential coefficients and R is the reference radius of the geopotential model being used. The parameter χ is defined as the reciprocal of B. All the coefficients dependent on n and/or s are given in [14], usually as recursive formulae.

THIRD-BODY ATTRACTION

The mean element rates caused by the gravitational attraction of third bodies are obtained using the same equations as for zonal terms, i.e. Eq. (5.10).

However, here the direction cosines are computed in a different way, with $\boldsymbol{z_B}$ being the unit vector from the propagated body to the disturbing body, and the disturbing potential U has a different expression, leading to slightly different equations for its partial derivatives [14]:

$$
\begin{aligned}
\frac{\partial U}{\partial a} &= \frac{\mu_3}{R_3 a}\sum_{s=0}^{N_3}\sum_{n=\max(2,s)}^{N_3}(2-\delta_{0s})\, n\left(\frac{a}{R_3}\right)^n V_{ns} K_0^{ns} Q_{ns} G_s \\
\frac{\partial U}{\partial h} &= \frac{\mu_3}{R_3}\sum_{s=0}^{N_3}\sum_{n=\max(2,s)}^{N_3}(2-\delta_{0s})\left(\frac{a}{R_3}\right)^n V_{ns} Q_{ns}\left(K_0^{ns}\frac{\partial G_s}{\partial h}+h\chi^3 G_s\frac{\mathrm{d}K_0^{ns}}{\mathrm{d}\chi}\right) \\
\frac{\partial U}{\partial k} &= \frac{\mu_3}{R_3}\sum_{s=0}^{N_3}\sum_{n=\max(2,s)}^{N_3}(2-\delta_{0s})\left(\frac{a}{R_3}\right)^n V_{ns} Q_{ns}\left(K_0^{ns}\frac{\partial G_s}{\partial k}+k\chi^3 G_s\frac{\mathrm{d}K_0^{ns}}{\mathrm{d}\chi}\right) \\
\frac{\partial U}{\partial \alpha} &= \frac{\mu_3}{R_3}\sum_{s=0}^{N_3}\sum_{n=\max(2,s)}^{N_3}(2-\delta_{0s})\left(\frac{a}{R_3}\right)^n V_{ns} K_0^{ns} Q_{ns}\frac{\partial G_s}{\partial \alpha} \\
\frac{\partial U}{\partial \beta} &= \frac{\mu_3}{R_3}\sum_{s=0}^{N_3}\sum_{n=\max(2,s)}^{N_3}(2-\delta_{0s})\left(\frac{a}{R_3}\right)^n V_{ns} K_0^{ns} Q_{ns}\frac{\partial G_s}{\partial \beta} \\
\frac{\partial U}{\partial \gamma} &= \frac{\mu_3}{R_3}\sum_{s=0}^{N_3}\sum_{n=\max(2,s)}^{N_3}(2-\delta_{0s})\left(\frac{a}{R_3}\right)^n V_{ns} K_0^{ns} Q_{ns}\frac{\mathrm{d}Q_{ns}}{\mathrm{d}\gamma} G_s
\end{aligned}
\tag{5.15}
$$

where μ_3 and R_3 are, respectively, the gravitational parameter and distance to the third body. The value of N_3 has to be chosen for each third body depending on the size of the orbit and proximity to the disturbing body. Later it will be shown that for the Sun and the Moon a value of two can provide sufficiently accurate results (cf. Section 5.2.3).

ATMOSPHERIC DRAG

Atmospheric drag cannot be expressed as a disturbing potential, and thus the disturbing acceleration $\boldsymbol{q}$ is used. The expression for this perturbing acceleration was given in Eq. (3.15) in terms of the ballistic coefficient, atmospheric density and relative velocity.

The contribution of atmospheric drag to the mean element rates is then obtained from [14]:

$$
\frac{\mathrm{d}a_i}{\mathrm{d}t} = \frac{1}{2\pi B}\int_{L_1}^{L_2}\left(\frac{r}{a}\right)^2\left(\frac{\partial a_i}{\partial \dot{\boldsymbol{r}}}\cdot\boldsymbol{q}\right)\mathrm{d}L \tag{5.16}
$$

which is known as the averaging integral of (atmospheric) drag, although Eq. (5.16) represents actually six integrals, one for each orbital element. These integrals cannot be solved analytically due to the dependence of $\boldsymbol{q}$ on the atmospheric density, which is given by an atmospheric model such as NRLMSISE-00. The partial derivatives of the mean elements a_i with respect to the velocity vector $\dot{\boldsymbol{r}}$ are given in [14].

The limits for the true anomaly in between which drag is relevant are determined by choosing an altitude limit $\overline{h}$ above which the effects of drag can be assumed to be negligible. Using this limit, it is possible to determine the critical true anomaly above which atmospheric drag can be neglected [14]:

$$\overline{f} = \arccos\left[\frac{\frac{a(1-e^2)}{R_E+\overline{h}} - 1}{e}\right] \tag{5.17}$$

and, from there, the limits for the averaging integral of drag in terms of true longitude:

$$L_1 = -\overline{f} + \omega + \Omega \qquad \text{and} \qquad L_2 = \overline{f} + \omega + \Omega \tag{5.18}$$

The values of these integrals can be estimated by using a Gaussian quadrature or through other techniques discussed in Section 5.1.3.

SOLAR RADIATION PRESSURE

The contribution of SRP to the mean element rates can be obtained using Eq. (5.16), using the value for the disturbing acceleration given by Eq. (3.19) and different limits for the integral, with L_1 and L_2 indicating the shadow exit and entry longitudes.

When eclipses are neglected (or when no eclipses are undergone during the current orbital revolution), the averaging integral of SRP can be solved analytically. In that case, the contribution of SRP to the mean element rates is obtained using the same expressions as for zonal terms and third-body attraction, i.e. Eq. (5.10). The partial derivatives of the disturbing function are identical to those for third-body attraction given by Eq. (5.15), except for the fact that the second summation starts from $\max(1,s)$ instead of $\max(2,s)$ and the factor μ_3 is replaced by $-\mathscr{T}$, where [14]:

$$\mathscr{T} = C_R \frac{W_S A}{2mc} \mathrm{AU}^2 \tag{5.19}$$

with AU the value of 1 AU in metres.

5.1.3. PRACTICAL ASPECTS

Each of the four perturbations that are relevant for the propagation of GTOs are treated independently in [14], where complex expressions for the mean rates A_i and the short-periodic terms η_i are derived. Only expressions for a few zonal and tesseral harmonics are given in [14], but expressions up to order and degree 50 can be found in [68]. The mean element rates can then be used to integrate the VOP equations of motion numerically and obtain the mean elements. Then, the short-periodic terms can be evaluated directly since they are given in closed analytical form (typically as a truncated series). Adding the short-period terms to the mean elements as in Eq. (5.6), the osculating elements can be obtained at the integration steps.

When the osculating elements are needed at some epoch for which the mean elements are not available (because the time of interest is not a multiple of the integration step-size), one has to resort to interpolation techniques. However, the goal of this project is not to predict accurately what the state of an orbiting body at a given epoch in the future will be, but to determine how long it will take for that object to reach re-entry altitude. Thus, when the integration is finished because the object has just begun to re-enter, it is pointless to use interpolation techniques or to evaluate the short-periodic terms η_i, since the expressions given in [14] are not valid for re-entry conditions. Nevertheless, if interpolation techniques are needed in future research following this thesis, a few techniques can be found in [14].

Another relevant aspect when using the theory presented in [14] for propagation of GTOs is the choice of the integration step-size to be used when solving Eq. (5.5). This parameter cannot be chosen freely: there is an upper limit imposed by the desired integration accuracy and a lower limit for ensuring convergence of the averaging equations. Calling $\tilde{T}$ the minimum period of the perturbations included in the averaged equations of motion, the recommended rough range for the integrator step-size κ is [14]:

$$\frac{\tilde{T}}{100} \leq \kappa \leq \frac{\tilde{T}}{8} \tag{5.20}$$

Since the mean element rates depend on slowly varying quantities, step-sizes of a day or more can usually be used [14], even when the orbital period of a GTO object is about 10.5 hours.

In addition to single-averaging techniques, the possibility of doubly-averaging the equation of motion to obtain mean-mean elements, in which only the secular terms remain, is also discussed in [14]. Although this can reduce computation times even further, it would also have an impact on the accuracy of the propagation and, moreover, not all the perturbations that are relevant for the propagation of GTOs can be doubly-averaged. A perturbation is said to be averagable if the application of the averaging operator (cf. Eq. (5.2)) leads to its decomposition in slowly-varying averaged rates and small short-period variations. Although the averaging operator can be applied as many times as desired, in some cases the resulting terms will have to be integrated with a very similar integration step-size, and then the perturbation is said to be non-averagable (or non-doubly-averagable if it has already been averaged once). Only central-body gravitational sectoral and tesseral harmonics and third-body perturbations caused by bodies orbiting the central body can be doubly-averaged. Thus, this is not considered further in this thesis.

Finally, although the perturbations that are relevant in GTOs can be generally averaged, under certain conditions not even the single-averaging is possible due to large second-order effects. For instance, third-body attraction becomes non-averagable when the satellite comes too close to the third body or when it leaves the sphere of influence of the central body, whilst atmospheric drag cannot be averaged during the terminal stage of reentry. GTOs will not encounter these conditions (propagation will be terminated at the beginning of re-entry), and thus the theory presented in [14] can be used for the semi-analytical propagation of GTOs under all foreseeable circumstances.

5.2. SST PROPAGATOR

A new propagator based on the theory described in Section 5.1 and making use of the equations provided in [14] was developed during this thesis. The implementation of this propagator in Tudat will be described in Section 5.2.1, not going into the details of C++ code or the interfacing with the rest of the Tudat's libraries, but focusing on the aspects that were implemented in a different way than proposed in [14]. Then, the performance of the obtained propagator will be tested against the results provided by the verified Cowell propagator in Section 5.2.2, in order to assess both its accuracy and performance.

5.2.1. IMPLEMENTATION IN TUDAT

Eqs. (5.10) and (5.16) giving the mean element rates for each of the relevant perturbations, namely zonal terms, third-body attraction, atmospheric drag and SRP, were implemented into Tudat. Those for tesseral terms were not included, as it has been found that the propagations of GTOs can be performed accurately including just zonal terms up to degree 7 (cf. Section 4.1.2). In the case of SRP, two implementations were added: one in which occultations of the satellite by Earth's shadow are considered, in which the averaging integral has to be solved numerically; and one in which occultations are neglected, which leads to a closed analytical solution for the averaging integral. Depending on whether the user chooses to include occultations in the acceleration model or not, one of the two implementations will be used.

AVERAGING INTEGRAL

Since the averaging integral of atmospheric drag and SRP when occultations are considered cannot be solved analytically, a numerical quadrature technique was implemented into Tudat in order to be able to get an estimate of the value of this integral. The chosen method was the Gaussian Quadrature, following the recommendations of [14].

A quadrature method approximates an integral by a weighed sum of the values of the integrand evaluated at different points of the integration interval, called nodes:

$$\int_{-1}^{1} f(\xi)\,d\xi \approx \sum_{i=1}^{n} w_i f(\xi_i), \qquad -1 \le \xi_1 \le \xi_2 \le \ldots \xi_n \le 1 \tag{5.21}$$

where w_i are the weight factors and ξ_i the nodes or abscissae. As the number of nodes n increases, the error made in Eq. (5.21) tends to become smaller.

Note that the integral in Eq. (5.21) must have integration limits -1 and 1, but this is not the case for the averaging integrals, which usually have limits $-\pi$ and π. However, an integral with arbitrary integration limits $[a, b]$ can be transformed into

$$\int_{a}^{b} f(x)\,dx = \frac{b-a}{2} \int_{-1}^{1} f(\xi)\,d\xi \tag{5.22}$$

by introducing a change of variable

$$\xi = \frac{2x - (a+b)}{b-a} \tag{5.23}$$

It was found that the accuracy of the quadrature for solving the averaging integral of drag is higher for odd values of n. When n is odd, the node $\xi = 0$ is included, which means that drag is evaluated at perigee, where it is largest and thus most relevant. When n is chosen even, atmospheric drag is not assessed at perigee, introducing a significant error in the estimated value, as can be seen in Figure 5.2 (left). Thus, only odd values will be used for n in the future in the case of atmospheric drag. In the case of SRP, any value (odd or even) can be used, getting more accurate results as more nodes are considered.

One of the tasks taking most of the computation time during propagation is indeed the evaluation of the integral of drag, which represents about 60-70% of the total computation time per integration step when occultations are neglected and a value of 7 or 9 is used for n. This means that finding a way to estimate the value of the averaging integral faster while maintaining accuracy could potentially reduce the overall computation times significantly. To that end, an estimation procedure which only evaluates drag at one node (perigee) was developed. This procedure is explained in the following subsection.

EVALUATION OF ATMOSPHERIC DRAG AT PERIGEE ONLY

The first step in the attempt to generate a procedure capable of estimating the average effect of atmospheric drag on the mean elements over one orbital revolution by evaluating it just at one node (perigee) consists in determining a reference (accurate) description for a representative GTO to which the new method can be compared. This has been achieved by solving the averaging integral of drag using a Gaussian quadrature with an increasing (odd) number of nodes, until convergence.

As seen in Figure 5.2 (right), convergence has not been reached yet for a number of nodes equal to 7 or 9. However, for 11, 13, 15 and 17 nodes the orbital evolution is very similar. In fact, the value for the lifetime when using 17 nodes lies between those obtained when using 13 nodes and 15 nodes. Thus, it was decided that the target orbital evolution to be replicated by the single-node technique will be that of 17 nodes.

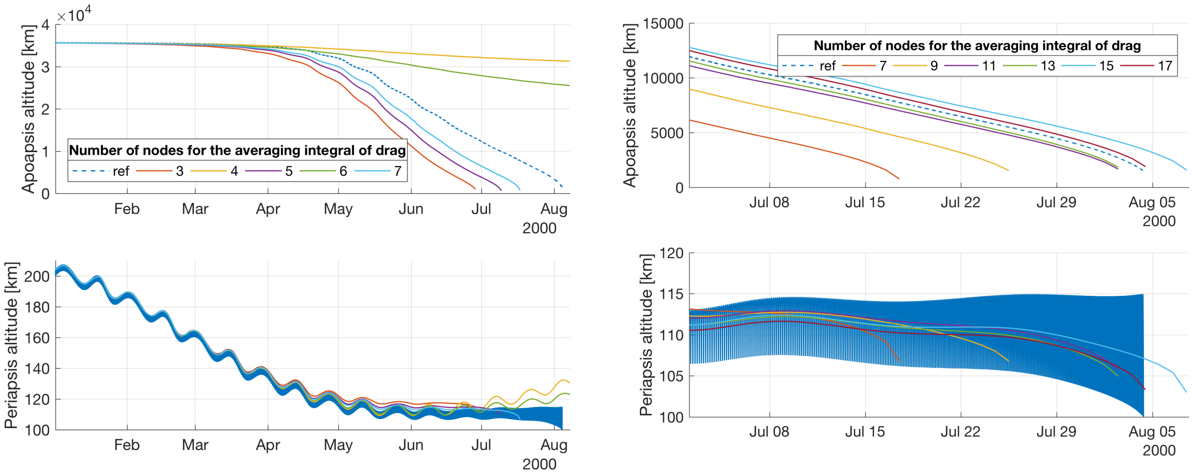

Figure 5.2: Evolution of the apogee and perigee altitudes of a GTO as a function of the number of nodes for solving the averaging integral of drag, considering both odd and even numbers (left) and only odd numbers (right). The results of the numerical approach have been included as a reference.

The next step was to determine the relationship, for every integration step, between the contribution of atmospheric drag to the mean element rates computed using 17 nodes for the Gaussian quadrature, and the value that would have been obtained if it had been assumed that atmospheric drag is constant and equal to the value at perigee during the part of the orbit in which drag cannot be neglected. In both cases, drag was assumed to be zero for altitudes above $\overline{h} = 600$ km. Using Eqs. (5.17) and (5.18), the limits for the averaging integral of drag can be obtained at each integration step throughout the propagation.

The following ratio is introduced:

$$r_{17/1} = \frac{|A_i|_{n=17}}{|A_i|_{n=1}} \tag{5.24}$$

where $|A_i|_{n=17}$ is the norm of the mean element rates vector obtained by using 17 nodes for the Gaussian quadrature and and $|A_i|_{n=1}$ is the corresponding norm when only one node (perigee) has been used. Note that, when calculating the norm of the 6-element vectors, the first element is first divided by the semi-major axis.

As expected, the value of $r_{17/1}$ is smaller than one, since for $n = 1$ drag has been assumed to have equal strength from L_1 to L_2 (maximum strength equal to that of perigee) while for $n = 17$ that value changes through L_1 to L_2. For a representative GTO propagated for 10 years, this ratio can be seen in Figure 5.3. If this signal can be easily recreated (i.e. with low computational effort), then the mean element rates given by the averaging integral of drag can be estimated to be:

$$A_i \approx r_{17/1} \times [A_i]_{n=1} \tag{5.25}$$

where $[A_i]_{n=1}$ can be computed relatively quickly (about 17 times faster than when using 17 nodes for the Gaussian quadrature).

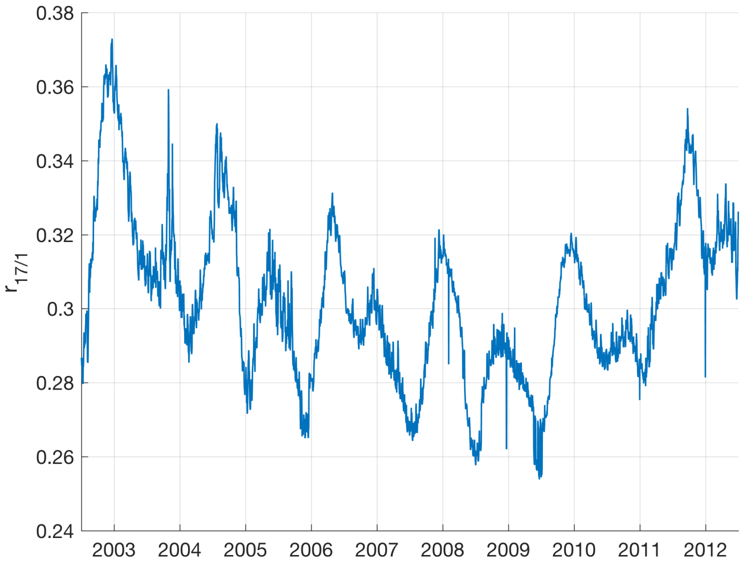

Figure 5.3: Evolution over a period of 10 years, for a representative GTO, of the ratio between the normalised mean element rates caused by atmospheric drag when using a Gaussian quadrature with 17 nodes and a single evaluation at perigee to estimate the value of the averaging integral of drag.

The problem consists thus in finding a way to recreate the signal $r_{17/1}$ without large computational effort. Looking at Figure 5.3, one can identify two signals: one with a shorter period of about 10.5 months (note the relative maxima approximately every 10–11 months) and a signal with a longer period of about a decade. It was seen that there is a significant correlation between the value of the instantaneous perigee altitude and the signal in Figure 5.3, as can be seen in Figure 5.4 (left). The location of the relative minima and maxima seems to match to some extent. Using a polynomial fit, the following relationship was obtained:

$$r_{17/1} \approx 3.73 \times 10^{-7} h_p + 0.207 \tag{5.26}$$

with the perigee altitude h_p in metres. For this orbit, this fit has an R^2 of 0.30. Although it is better than a constant fit (using just the mean value of $\overline{r}_{17/1} = 0.302$ would lead to $R^2 = 0$), it is still far from being an accurate fit, with values of R^2 close to e.g. 0.9.

The next step was to include also the value of the solar activity index $F_{10.7}$ in the fit, as this variable has a period of about 11 years, similar to the period of the long signal identified in $r_{17/1}$. The following fit was tested:

$$r_{17/1} \approx \left[\left(3.73 \times 10^{-7} h_p + 0.207 \right) (F_{10.7} - c)^d \right] A + B \tag{5.27}$$

The values A and B of the fit were computed for several combinations of the values of c and d, and the R^2 value was computed for each case, then the best one selected. It was found that the best combination was $(c, d) = (45.3, 0.07)$, which leads, after simplifying, to the following expression:

$$r_{17/1} \approx \left[\left(2.74 \times 10^{-7} h_p + 0.152 \right) (F_{10.7} - 45.3)^{0.07} \right] + 0.011 \tag{5.28}$$

which, for this orbit, leads to an R^2 value of 0.56, significantly better as can be seen in Figure 5.4 (right).

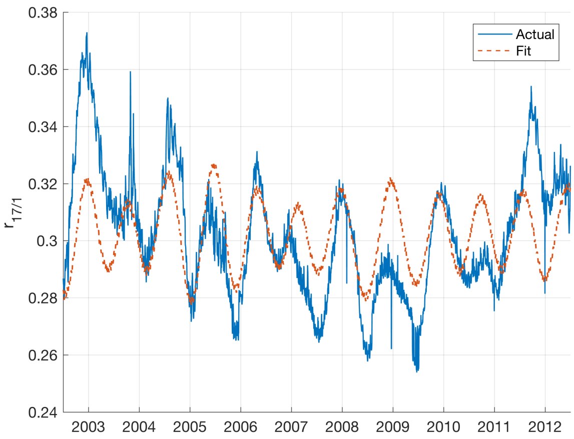

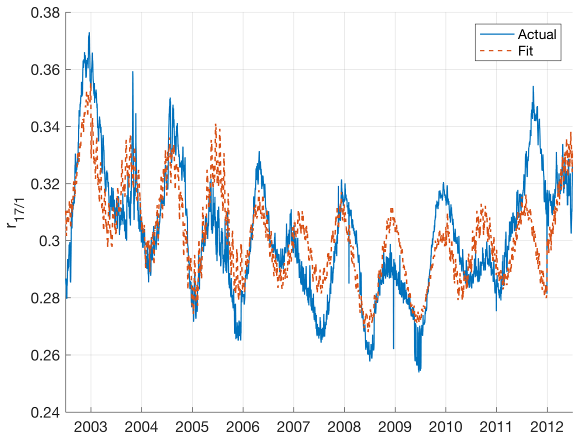

Figure 5.4: Fit of the $r_{17/1}$ signal using the instantaneous values of the perigee altitude exclusively (left) and in combination with the solar activity index $F_{10.7}$ (right).

At this point, it is still not known whether this fit is good enough. Thus, in Section 5.2.2, the new SST propagator will be tested with different settings, one of them being the use of a large number of nodes for the Gaussian quadrature or a single node together with this fit to estimate the average integral of drag. The two cases will be compared, taking into account aspects such as accuracy and computation time.

SHORT-PERIOD TERMS

It was decided that the short-period terms would not be implemented in Tudat at this point. First, the new propagator without the inclusion of short-period terms will be compared to the results of the numerical approach and, if it is deemed to already provide sufficient accuracy, the short-period terms will be left out.

However, the short-period terms are not only necessary in order to convert the mean elements obtained from the integration to osculating elements. They are also needed before starting the integration in order to transform the initial state provided by the user (typically in osculating elements) to mean elements, which are the elements that are propagated when following semi-analytical techniques. If this step is not performed, and the initial mean elements are assumed to coincide with the initial osculating elements, this relatively small initial error in the state may get bigger over time as it builds up after every integration step and lead to significant errors.

Thus, it was decided that the short-period effects caused by the zonal term J_2 would be implemented, as it is the largest contributor to the short-period terms [39]. In the current implementation of the SST propagator, those terms are only used to convert the initial elements from osculating to mean, but are not used to convert the mean elements obtained from the integration to osculating elements. Thus, the results provided by the SST propagator correspond to mean elements.

It has been confirmed that, indeed, the zonal term J_2 is the one causing the largest short-period effects. An orbit has been propagated using the SST propagator and compared to the Cowell results, both for the case in which the conversion from initial osculating to mean elements is skipped and the case in which it is performed just by using the contribution of J_2. As seen in Figure 5.5, if this conversion is not performed, the initial elements coincide for the two cases (Cowell and SST) but the orbital evolutions start to diverge, even only after one month. When the initial conversion from osculating to mean elements is performed, the mean orbital evolution follows the results of the Cowell method more accurately.

ECLIPSES

Before starting to use the SST propagator to generate results, it was necessary to study in more detail whether occultations of the satellite by Earth's shadow could be neglected during the assessment of SRP. If so, the SST propagator would be much faster, since the averaging integral to compute the mean element rates due to SRP would have an analytical solution.

In Section 4.1.2 it was found that eclipses can be neglected unless the orbit of interest is at (or near to) conditions leading to solar resonance. However, later in Section 4.4 it was concluded that the lifetime near solar resonance conditions could not be predicted accurately due to the extremely large sensitivity around those regions. Thus, it was decided that the focus would be put on the regions that are free of resonances. It is still convenient to know where the resonance ridges are approximately, but whether the lifetime will

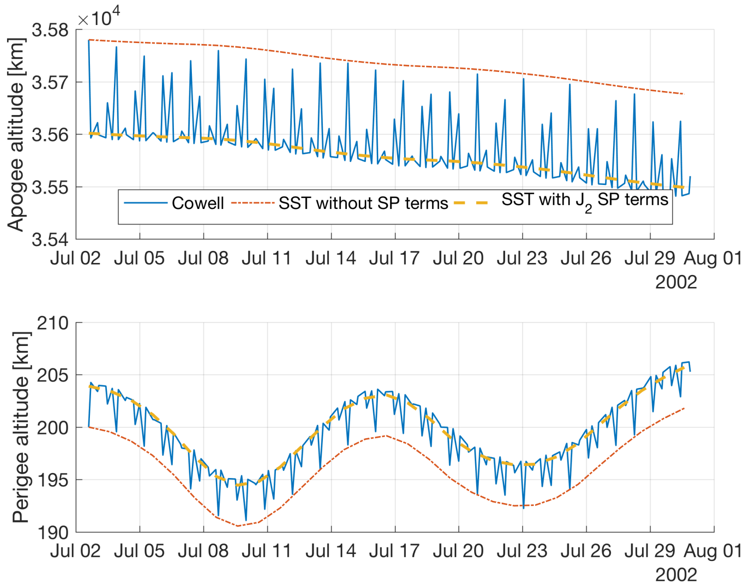

Figure 5.5: Temporal evolution of the mean apogee and perigee altitudes of a GTO propagated using the SST propagator without the use of short-period terms (dash-dotted line) and using the short-period terms due to J_2 to convert the initial elements from osculating to mean (dashed line), compared to the osculating apogee and perigee altitudes given by the Cowell propagator (solid line).

be 5 or 50 years at those regions is impossible to know due to uncertainties introduced mainly by the body cross-sectional area and the atmospheric model. Thus, further investigations were carried out in order to determine whether eclipses can be completely neglected in the acceleration model. If the location of the resonance regions does not change, then it is safe to neglect eclipses even though it will introduce some uncertainty in the value of the lifetime near resonance regions. But since these regions are to be avoided, if the model can predict their location correctly, then it would be sufficient.

Still using the Cowell propagator and the fully numerical approach, a region of the domain in Figure 4.25 was propagated again but ignoring eclipses in this case. The lifetimes for these two cases (considering and neglecting eclipses) can be found in Figure B.3. Neglecting eclipses does not change the shape of the plot or the location of the resonance ridges. Since the differences between the two plots are difficult to see with the naked eye, the relative errors introduced in the lifetime when neglecting eclipses is provided in Figure 5.6. As anticipated in Figure 4.10, the error introduced in the value of the lifetime by neglecteing eclipses near resonance regions can be close to 7%. However, in most of the plot (including all resonance-free regions) the introduced error is virtually 0%. Note that in the regions in which the lifetime was 10 years because the propagation was stopped before re-entry, the actual lifetime is not known and thus the relative errors cannot be computed. Those cases are represented with white (transparent) colour.

From the results provided here, it can be concluded that eclipses can be neglected and, consequently, all the results generated with the SST propagator (including those for verification and validation) will be obtained with the propagator configured to exclude eclipses from the acceleration model, which makes it significantly faster in terms of computation times.

5.2.2. Verification and validation

The new SST propagator has been verified by comparing the results that it generates to the ones obtained by using the Cowell propagator following the fully numerical approach described in Chapter 4. Additionally, it has been validated using external sources to ensure the validity of the generated results, by comparing the results of simulations carried out with this propagator to actual satellite-tracking data of a few representative objects resulting from GEO launches.

Verification

Initially, the errors introduced in the value of the lifetime have been studied in the whole domain (a range of 1 year for the epoch of injection into GTO and a range of 360 degrees for the initial RAAN), although previously it has been said that the focus will be put exclusively on the resonance-free regions. However, it was deemed interesting to know how accurately the SST can describe the lifetime near resonance regions, even though

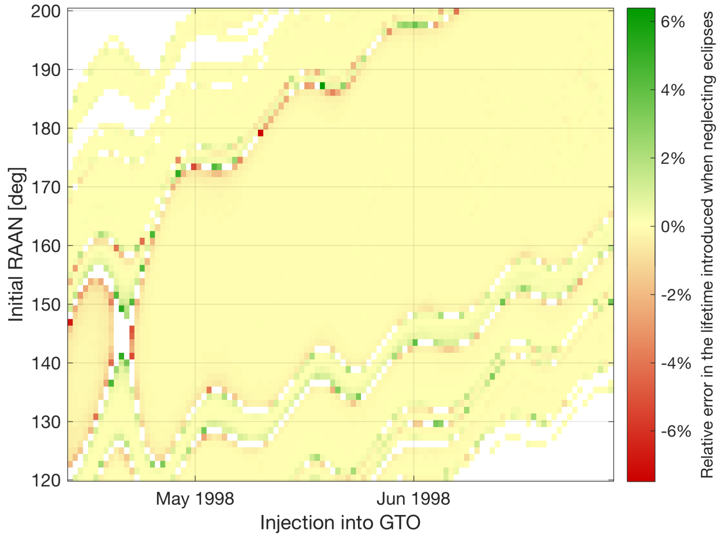

Figure 5.6: Relative errors in the lifetime of a satellite as a function of epoch of injection into GTO and initial RAAN introduced when neglecting eclipses. White colour represents unknown errors.

the important thing is whether it is able to predict the location of those regions rather than the lifetimes within them. The lifetimes for a representative GTO propagated using the Cowell and SST propagators can be found in Figure B.4. Again, since the shape of the plot does not change significantly and the resonance ridges remain in the same regions, the differences are difficult to spot with the naked eye. Thus, the relative errors are provided in Figure 5.7.

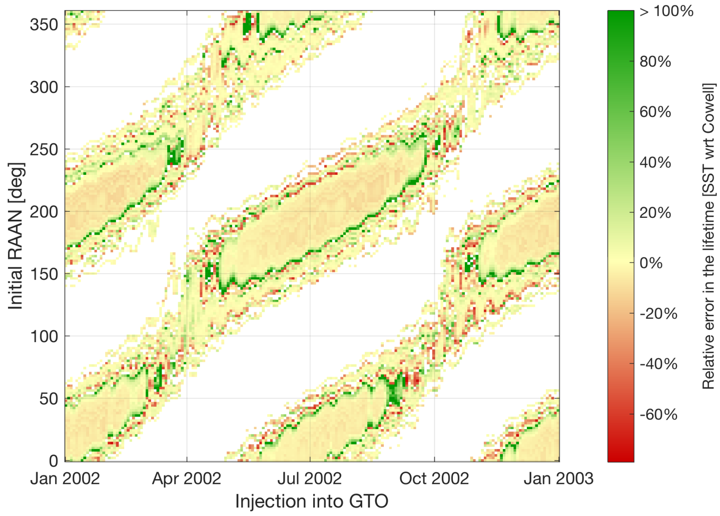

Figure 5.7: Relative errors in the lifetime of a satellite as a function of epoch of injection into GTO and initial RAAN introduced when using the SST propagator. The results of the Cowell propagator have been taken as reference. White colour represents unknown errors.

In this case, the introduced errors are much more significant, due to the fact that the mean elements, rather than the osculating elements, are being propagated, leading to slightly different orbital evolutions, which can have a big influence on the value of the lifetime for orbits undergoing solar resonance, which are very sensitive to initial conditions and to the mathematical description of the perturbation model. In some cases (represented with dark green in Figure 5.7), the lifetime predicted by the SST propagator can be more than twice the value of that predicted by the Cowell propagator, leading thus to a conservative prediction in which the actual lifetime will be probably shorter than the value given by the SST propagator. In other cases (represented with red), SST provides underestimations, so the predicted lifetime can be less than half the actual value. However, these big errors are found mostly near the resonance ridges; in the regions corresponding to the dark blue areas of Figure 4.25, i.e. the resonance-free regions, the errors are much smaller.

It is clear that the SST propagator (without the inclusion of the short-period terms) is not accurate enough to predict the lifetime of GTOs near resonance regions. However, this was also the case with the Cowell propagator, due to the high sensitivity and the existence of other sources of uncertainty, such as the body cross-sectional area and the value of the atmospheric density or the errors in the predictions for solar activity levels. Thus, from now on, the focus will be put on the resonance-free regions in order to determine whether the SST propagator can provide sufficient accuracy to predict the lifetimes therein.

The relative errors in the resonance-free regions (defined in the same way throughout this section, namely those combinations of epoch of injection into GTO and initial RAAN leading to a lifetime of less than one year and to a lifetime gradient of less than 0.25 years per pixel in all directions) can be seen in Figure 5.8. Note that, in those regions, the SST propagator provides mostly underestimations for the lifetime (as much as 12% shorter than Cowell), while as one gets closer to the resonance ridges, the propagator tends to provide overestimations (of up to 30% with respect to the Cowell results). The root mean square (RMS) error in the resonance-free regions is 6.6%. This is deemed to be acceptable, since 15% uncertainty in the atmospheric density alone can lead to uncertainties in the lifetime of about 3% in resonance-free regions, as discussed in Section 4.1.2. This holds for propagations in the past using solar activity indices obtained from measurements. When performing propagations in the future, this error will be larger as the predictions for solar activity levels can be significantly off given the variability of the solar activity maxima during the last cycles (cf. Figure 3.8). If one adds other sources of uncertainty, such as the satellite attitude (leading to different body cross-sectional areas) or initial conditions, the error of 6.6% introduced by the SST will probably be lower than the uncertainty obtained when using a very accurate propagator, such as Cowell with short integration step-sizes.

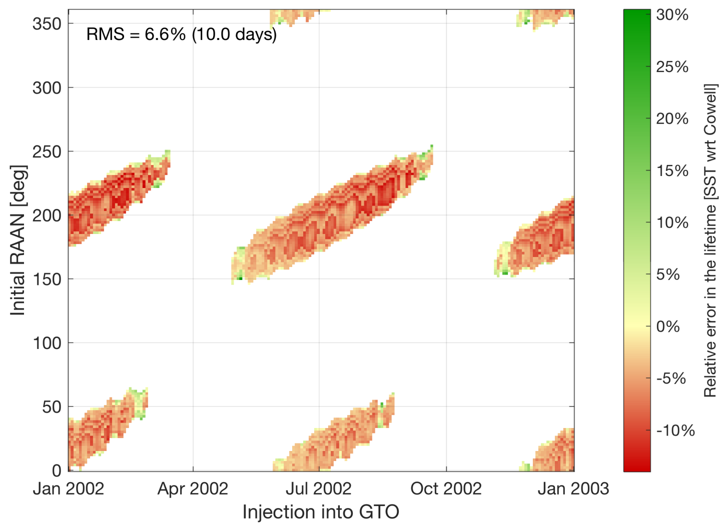

Figure 5.8: Relative errors of the SST propagator in the lifetime of a satellite for combinations of the epoch of injection into GTO and initial RAAN leading to resonance-free orbits. The results of the Cowell propagator have been taken as reference.

Another important aspect in the verification of the SST propagator is to study how accurately it can predict the optimum launch time (or equivalently initial RAAN) leading to the shortest lifetime for a given day. To do so, the local minima have been found for every day of the year (of for every two days, depending on the resolution used for the epoch of injection into GTO), and this has been done for every resonance-free region. Thus, for some days, there will be two local minima (i.e. two optimum launch epochs), while for others there will be just one or none. These optimum initial RAANs are provided in Figure 5.9 for the Cowell and SST propagators.

As can be seen from Figure 5.9, the optimum RAANs do not match exactly for the Cowell and SST propagators. However, their location is relatively similar and, from Figure 5.8, one can expect the errors in the value of the lifetime at the optima to be no larger than 12%. Given that, within the resonance-free regions, the lifetime changes smoothly and by small amounts, the error introduced by SST when predicting the conditions leading to minimum lifetime is deemed to be acceptable.

The RMS error when only the optima are considered (instead of the whole resonance-free regions) is about 7.0% for the studied orbits. The RMS error in the predicted initial RAANs leading to minimum lifetime is about 2.6 deg or, equivalently, 10.5 minutes in terms of launch time. This means that the SST propagator can

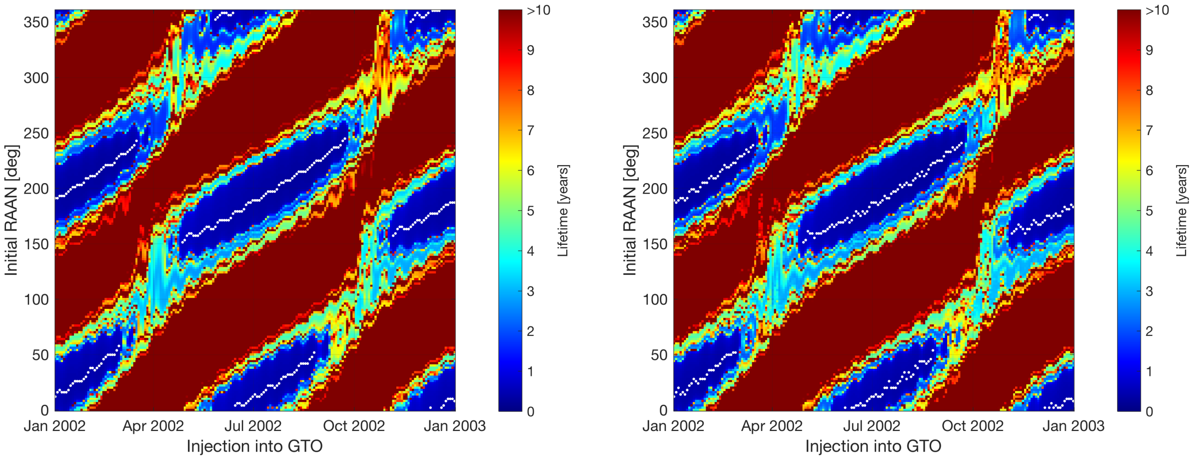

Figure 5.9: Combinations of epoch of injection into GTO and initial RAAN leading to minimum lifetime in the resonance-free regions using the Cowell propagator (left) and the SST propagator (right), indicated with white dots.

predict the optimum launch time for a given day with an accuracy of 10.5 minutes (compared to the Cowell propagator), which is deemed to be sufficient taking into account that there are other sources of uncertainty that may introduces larger errors.

Since the shape of the two plots in Figure 5.9 is not exactly the same, there are some non-matching optima. For instance, for injection into GTO on September 22nd, the Cowell propagator leads to an optimum at about 245 degrees, while the SST propagator yields no optimum for this day as all the cases fall outside resonance-free regions. This only happens for a few cases near the boundaries of resonance-free regions. The percentage of matching optima can be defined quantitatively as:

$$\%\text{ matching optima} = \frac{2 \times \text{number of matching optima}}{\text{number of optima Cowell} + \text{number of optima SST}} \times 100\% \tag{5.29}$$

For the cases studied in this subsection, the percentage of matching optima is 99.2%. For computing the RMS errors provided previously referring to optimum conditions, only the matching optima have been taken into account, since when one of the two (either the reference Cowell optimum or the SST optimum) is missing, it is not possible to compute the error.

VALIDATION

As was discussed in Chapter 2, most GTO objects are depleted rocket bodies and thus they do not carry GPS antennae for determining their location nor communication antennae for transmitting such data back to Earth. Thus, it will be necessary to resort to satellite-tracking data in order to validate the propagator used to generate the relevant results for this Master thesis.

One possibility is the use of two-line elements (TLE) data. Two-line elements is a widely used orbital data encoding format [69]. The set of orbital parameters used in this standard is $(i, \Omega, e, \omega, M, n)$. This information is provided in the second line of the data. In the first line, other information, such as identifier, international designator or the epoch for which the information holds, is given, as can be seen in Figure 5.10. In some cases, an additional line is included to specify the name of the satellite the following two lines refer to.

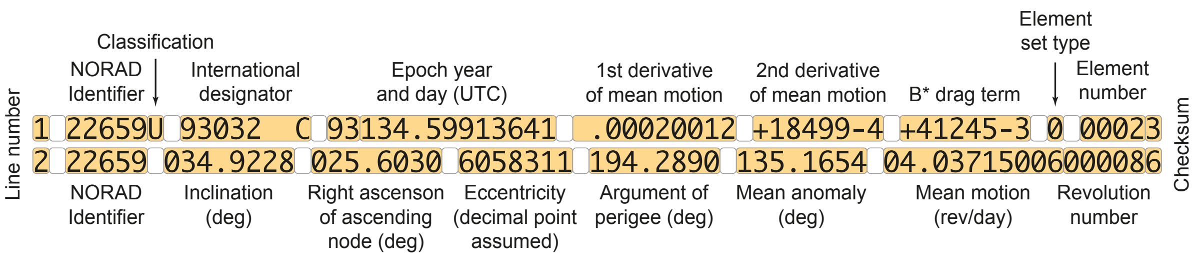

Figure 5.10: Description of the data fields of a two-line element set [70].

The US Strategic Command is the only organisation that maintains a publicly available catalog of near-Earth objects [71]. They provide an application programming interface (API) that can be freely accessed by identified users to request satellite-tracking data. Queries can be built using a graphic interface provided on their website [38], in which it is possible to specify a set of filters, sorting settings, etc. to narrow down the search results. This generates a URL that can be accessed from programming platforms such as MATLAB to download plain text data.

Using this tool, tracking data of GTO objects resulting from recent GEO launches were retrieved for validation of the SST propagator. The TLEs of the tracked objects described in Table 5.1 were obtained.

Table 5.1: Characteristics of three GTO objects resulting from GEO launches using a Falcon 9 v1.1 used for validation of the SST propagator.

Satellite	**Launch date**	**Last TLE**	**Tracked object ID**	**Initial perigee altitude**	**Initial apogee altitude**	**Reference**
Thaicom 6	6 Jan 2014	29 May 2014 (re-entered)	39501	296 km	89 636 km	[72]
AsiaSat 8	5 Aug 2014	1 Jun 2017 (still on orbit)	40108	165 km	35 723 km	[73]
TurkmenSat 1	27 Apr 2015	1 Jun 2017 (still on orbit)	40618	180 km	36 600 km	[74]

The TLEs of the objects in Table 5.1 were retrieved and used to plot the temporal evolution of the Keplerian components, as seen in Figure 5.11, where the tracking data from the object with ID 40108 is shown as a solid line. Then, an object with the same characteristics and initial state was propagated from the date of the first available TLE using the SST propagator, leading to the evolution shown as a dashed line in Figure 5.11. However, not all the data needed for the propagation could be inferred from the TLEs. Although the ballistic coefficient can be computed from the BSTAR term, the values of the mass, cross-sectional area and drag coefficient cannot be determined individually. For a propagation in which SRP is neglected, it is not necessary to know the values of each of these parameters separately. However, in the SST propagator SRP is being considered, so a cross-sectional area (of 15 m^2), drag coefficient (of 2.2) and radiation pressure coefficient (of 1.5) had to be assumed. Then, the mass of the satellite could be computed from the value of BSTAR. In the propagation using the SST propagator, the cross-sectional area is assumed to be constant, but this is not the case for a tumbling object, leading to different values of BSTAR for each TLE. Thus, a mean value was computed from the different TLEs in order to be able to determine a constant mass for the body which is compatible with the assumption that the cross-sectional area stays constant.

As can be seen, the Keplerian components obtained from the SST-based propagator follow closely those from tracking data. There are, however, some noticeable deviations, especially for the inclination, although in this case it can be seen that there is some noise in the signal retrieved from TLEs, probably due to uncertainties in the estimation process. Thus, one cannot expect the two signals to match precisely (recall that there are some sources of uncertainty in the simulation such as the satellite attitude and atmosphere model that can introduce significant errors).

The same process was repeated for the two other objects in Table 5.1. The results can be found in Figures B.5 and B.6. In the later one, an outlier TLE can be clearly identified right after the launch date, highlighting the fact that satellite-tracking data should be taken as a 100% reliable data source, although it does allow to conclude that the SST propagator is able to describe the evolution of objects in GTO with proper accuracy.

5.2.3. Tuning and benchmarking

The SST propagator can be tuned by changing the value of a few parameters, namely:

- The number of terms in the series expansion for the mean element rates caused by the Sun's gravity, by changing the value of N_{Sun}.
- The number of terms in the series expansion for the mean element rates caused by the Moon's gravity, by changing the value of N_{Moon}.

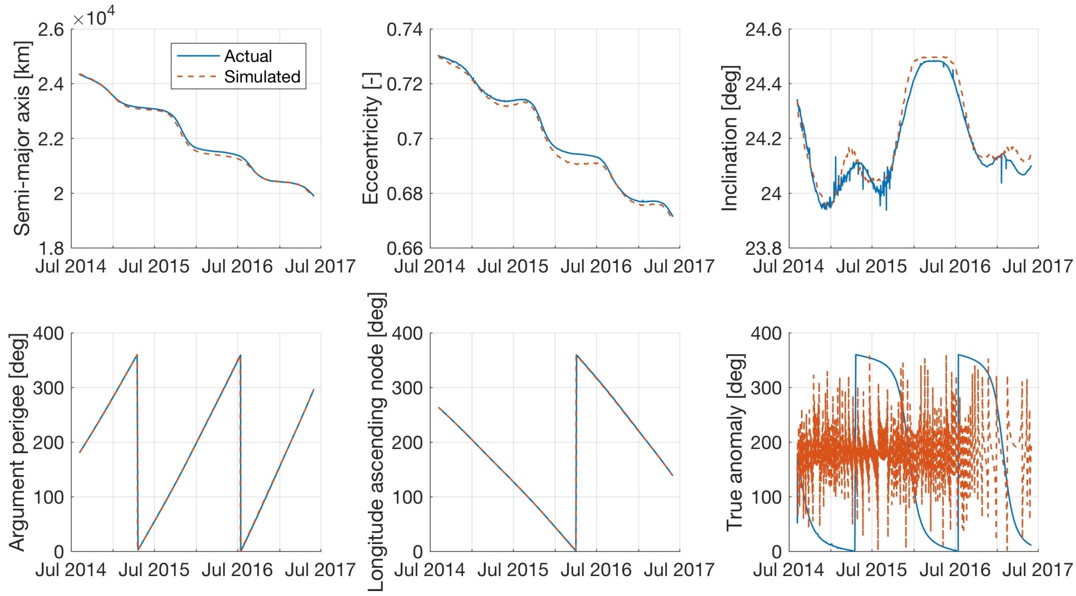

Figure 5.11: Evolution of the Keplerian components of the upper stage of the Falcon 9 rocket (CATID 40108) used to launch AsiaSat 8 obtained from tracking data [38] (solid line) and simulated using the SST propagator (dashed line).

- The number of terms in the series expansion for the mean element rates caused by SRP when eclipses are neglected, by changing the value of N_{SRP}.
- The number of nodes in the Gaussian quadrature for solving the averaging integral of drag, N_{drag}.
- Whether to use a fit based on perigee altitude exclusively or in combination with the solar activity index when the averaging integral of drag is estimated by evaluating just the perigee node (cf. Section 5.2.1).
- The altitude above which atmospheric drag is assumed to be negligible, $\overline{h}$.
- Whether short-period terms due to J_2 are used for converting the initial osculating elements to mean elements.
- The step-size of the integrator, κ.

A few sensitivity analyses were carried out in order to fix the values of some of these parameters. Namely, it was found that N_{Sun}, N_{Moon} and N_{SRP} can be set to 2. Using a value of 1 would reduce computation times but leaves out some relevant terms that cannot be neglected. Using a value larger than 2 increases computation times but the results do not change significantly.

Additionally, it was observed that $\overline{h}$ could be set anywhere above 300 km, leading to very similar results. Choosing a large value (e.g. 900 km) leads to more inaccurate results if the number of nodes in the Gaussian quadrature is not increased accordingly (i.e. neglecting drag above 900 km and using 7 nodes leads to worse results than neglecting drag above 300 km and using also 7 nodes). Basically, the ratio between the percentage of the orbit in which drag is not neglected and the number of nodes for the integral of drag has to remain roughly constant if one wants accuracy to be maintained. This means that choosing a large $\overline{h}$ requires a large number of nodes N_{drag} and thus more computation time. If was found that some combinations of $(\overline{h}, N_{drag})$ leading to virtually identical results are (500 km, 11), (600 km, 13), (700 km, 15) or (800 km, 17).

When trying to estimate the averaging integral of drag by evaluating only the central node (i.e. the conditions at perigee), a fit has to be performed before this can be achieved using the perigee altitude (and solar activity index). In this fit, the reference signal to be reproduced is obtained once (i.e. this operation does not have to be repeated for future propagations once the parameters of the fit have been obtained) by fixing the values for $\overline{h}$ and N_{drag}. The fits discussed in Section 5.2.1 were performed using propagation data obtained with $\overline{h} = 600$ km and $N_{drag} = 17$. This is not optimum in terms of computation times (13 nodes would have sufficed for that altitude limit) but yields accurate results that can be used to obtain the values of the parameters of the fit.

Since several configurations of the SST propagator were going to be tested, it was deemed reasonable to fix the value of the altitude limit at 600 km for all the configurations, since this is the value for which Eqs. (5.26) and (5.28) hold. In this way, the comparison between the different propagator settings is performed with consistent values of $\overline{h}$.

The other parameters were varied to generate different propagator configuration settings. The procedure described in Section 5.2.2 was repeated for each of these configurations, leading to different values for the RMS error for the lifetime at the resonance-free regions and for the lifetime and the RAAN at the local minima. Moreover, each of the propagator settings led to different computation times, which is a key parameter to take into account, especially for configurations leading to similar accuracies.

Regarding the integrator step-size, a value of one day was used in most cases, as recommended by previous studies [14, 34, 44]. In principle, the value must be smaller than one eighth of the period of the perturbation with the shortest period on the mean element rates (cf. Eq. (5.20)). In the case of GTOs, the perturbation with shortest period on the mean elements is the Moon, with a period of about 14 days. This leads to a maximum value for the integrator step-size of 1.75 days. Using larger values would lead to significant errors.

The possibility of using a variable step-size integrator (e.g. RK78) was also studied. However, the improvement seen when using an RK78 over an RK4 with the Cowell propagation is not seen in this case. In the numerical propagation, the state derivative is evaluated several times per orbital revolution. Given the large eccentricity, the dynamics are much faster at perigee than at apogee, so the use of a variable step-size is advantageous in that case. However, in the semi-analytical propagation, the mean element rates (instead of the osculating rates) are propagated. These rates change slowly and at a slowly-varying rate, so a simple RK4 with constant step-size can provide the same accuracy and be faster than an RK78. Thus, the results of all the propagations carried out with the SST propagator presented in this report correspond to an RK4 integrator.

After this discussion on the different parameters that can be modified to tune the SST propagator, a benchmarking of eight different configurations is provided. The results of one of these configurations (the one used to generate the results for verification and validation purposes) were already introduced in Section 5.2.2. The settings used there were: $N_{Sun} = N_{Moon} = N_{SRP} = 2$, $N_{drag} = 7$, $\overline{h} = 600$ km, short-period terms due to J_2 not used (i.e. the initial osculating elements were assumed to be mean elements) and integrator step-size $\kappa = 1$ day. In the other seven configurations, the same values for N_{Sun}, N_{Moon}, N_{SRP} and $\overline{h}$ were used. Additionally, eclipses were neglected in all cases. The other parameters were changed according to the configurations described in Table 5.2, leading to the results provided in Table 5.3 and visualised in Figure 5.12.

Table 5.2: Settings for the different tested configurations of the SST propagator.

Configuration	N_{drag}	Use of short-period terms due to J_2	Integrator step-size [days]
#1	7	No	1.0
#2	7	Yes	1.0
#3	7	Yes	1.5
#4	7	Yes	2.0
#5	7	Yes	2.5
#6	7	Yes	3.0
#7	1*	Yes	1.0
#8	1**	Yes	1.0

* The effect of drag has been estimated by evaluating it at perigee and using Eq. (5.26).
** The effect of drag has been estimated by evaluating it at perigee and using Eq. (5.28).

As can be seen in Table 5.3, computation times are much shorter when using the SST propagator than when using the Cowell propagator, as could be expected from the fact that the integrator step-size is significantly larger. For instance, the SST propagator was able to generate the results shown in Figure 5.9 (right) in about 4 hours, while the Cowell propagator took almost 4 days to solve the same problem, leading to the results shown in Figure 5.9 (left). Thus, the SST propagator is about 24 times faster when ignoring all short-period effects and using 7 nodes for the averaging integral of drag and a fixed step-size of 1 day for the RK4 integrator. According to the obtained results, the propagator becomes slightly faster when the J_2 terms are used to convert the initial elements from osculating to mean, although this should not be the case as one additional operation is being performed at the beginning of each propagation. In this case, configuration #2 should be slightly (almost unnoticeably) slower than #1. However, it is difficult to measure computation times accurately, as they depend on some uncontrolled factors, such as the availability of resources on the

Table 5.3: Results of the benchmarking on the different configurations for the SST propagator. The best-performing configuration for each column is highlighted in boldface.

Config.	RMS error of lifetime at resonance-free regions [days]	Percentage of matching optima	RMS error of lifetime at optima [days]	RMS error of launch time at optima [minutes]	Computation time [SST/Cowell]
#1	10.0 (6.6%)	**99.2%**	9.5 (7.0%)	**10.5**	1/24
#2	10.7 (6.4%)	99.4%	8.9 (**5.9%**)	11.7	1/25
#3	14.3 (9.5%)	99.6%	15.0 (10.7%)	14.5	1/33
#4	21.6 (13.7%)	98.6%	22.0 (14.7%)	19.0	1/42
#5	27.6 (17.0%)	98.6%	29.2 (18.7%)	22.0	1/48
#6	32.6 (19.5%)	98.6%	31.6 (20.4%)	25.7	**1/53**
#7	8.7 (5.9%)	99.0%	**8.4** (6.6%)	12.3	1/45
#8	**8.6 (5.8%)**	98.6%	**8.4** (6.6%)	12.3	1/44

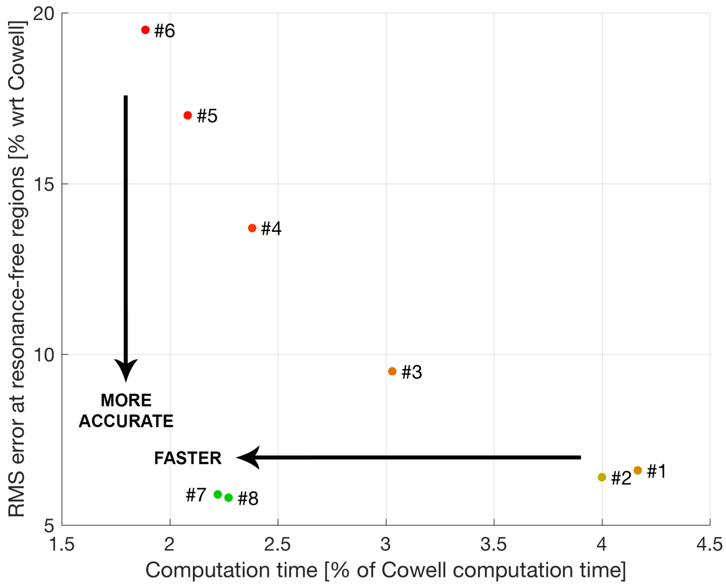

Figure 5.12: Computation times and RMS errors of the tested SST propagator configurations compared to the Cowell propagator.

computer in which the propagations are being run. Although in all cases the number of concurrent processes was limited to 14 and the server can handle up to 56 simultaneous processes at full CPU usage, it is possible that other background processes or other user's tasks would have slowed down some of the propagations carried out during configuration #1. In any case, the difference between 1/24 and 1/25 is so small that it can be considered to be non-significant.

However, the difference in computation times does become significant when the integrator's step-size is increased. When using step-sizes of 2.5 or 3 days, the propagator speed can double with respect to the case in which a value of 1 day is used. However, as the step-size increases, so does the uncertainty in the results. For instance, for step-sizes between 1.5 and 3.5 days, the RMS error of the lifetime at optima lies between 10 and 20%, while it was 6-7% for a step-size of 1 day. Thus, following the recommendations of previous studies and after observing these results, it has been decided to fix the integrator step-size at 1 day for all future propagations using the SST propagator, as it can provide proper accuracy and still be several times faster than the Cowell propagator.

Regarding the percentage of matching optima (cf. Eq. (5.29)), which can be seen as a measurement of how accurately the shape of the plot obtained by the SST propagator matches that of the Cowell propagator, all the configurations provide very similar results (between 98.5 and 99.5%), so the choice of the best propagator configuration should not be made based on this parameter.

It can be seen that configurations #7 and #8 are very similar, since the improvement in terms of RMS error is very small and the computation times are practically identical. Thus, if one of the two is to be chosen as the best configuration, which would be #8, as it is slightly more accurate when predicting the lifetime of objects in orbits at resonance-free regions.

Configuration #8 is much faster than #1 or #2. By estimating the effects of atmospheric drag using only the value at perigee and a fit based on the current perigee altitude and solar activity levels, it was possible to reduce computation times almost by 50% with respect to the case in which the averaging integral of drag is solved using a Gaussian quadrature with 7 nodes. This leads to a configuration of the SST propagator that is about 45 times faster than the Cowell propagator. However, this comes at a small decrease in accuracy. For instance, configuration #1 predicted the optima launch times with an error of 10.5 minutes, and configuration #2 predicted the lifetime of those optimum cases with a relative error of 5.9%. For configuration #8, these errors are 12.3 minutes and 6.6%, respectively. However, the absolute RMS error of the lifetime at optima is smallest for #8. The fact that a smaller absolute error can lead to a larger relative error is explained by the fact that #8 has more or less the same relative errors for all the cases (6.6%) while #2 describes short-lifetime orbits more accurately (leading to small relative errors) and long-lifetime orbits less accurately (leading to large absolute errors but still small relative errors, as the difference is compared to a long-lifetime value).

The final aspect to take into account is how accurately the different configurations can describe the lifetime at resonance-free regions. Configuration #8 is the best in this aspect; that, together with the fact that it can provide the lowest absolute error for the optimum lifetime and given that is is much faster than #1 or #2, makes it reasonable to recommend the use of this configuration in future propagations for the generation of additional results. All the plots provided in Chapters 6 and 7 have been obtained using the results generated by the SST propagator with configuration #8.

5.3. Problem redefinition

Now that the new SST propagator has been validated and tuned, and with a tool that is capable of generating results about 45 times faster than the Cowell propagator while still providing proper accuracy for the regions of interest, it is possible to re-define the tasks that have to be carried out in order to reach the research objective.

The answer to the question on whether orbital perturbations can be exploited to make debris in GTO re-enter faster has been partially obtained at this point. From Figure 4.25 obtained following the numerical approach, it was concluded that, indeed, there exist combinations of epoch of injection into GTO and RAAN (or equivalently launch time) that lead to favourable conditions. However, solar resonances cannot be exploited to optimise the lifetime of objects in GTO due to the extremely high sensitivity of the lifetime to the environment and initial conditions when a resonance is undergone, which makes predictions unreliable taking into account the various sources of uncertainty. Instead, it is convenient to identify the combinations of epoch of injection into GTO and RAAN leading to resonances in order to avoid them rather than trying to exploit them. Thus, the question that has to be answered at this point is whether the resonance-free regions observed in Figure 4.25 are also obtained for other GTOs and body properties. That plot is valid for a GTO with initial inclination of 10 degrees and initial perigee altitude of 200 km and a satellite with a ballistic coefficient of 0.011 kg/m^2, but nothing is known about the shape of the plot when the values of these parameters are changed.

Using the faster SST propagator, additional colour-map plots will be obtained for different values of the initial perigee altitude, inclination and ballistic coefficient, as these are deemed to be the most relevant parameters as found in Section 4.2. The orbital evolution is much less sensitive to changes in the true anomaly or the value of C_R. Additionally, other parameters,such as the initial apogee altitude and argument of perigee will be fixed because of mission-design-related constraints. These results will be provided in Section 6.2.

One of the research questions was how each of the orbital perturbations affects the evolution of objects in GTO. Although this was partially answered in Section 4.1.2 by propagating a GTO with different perturbations included and excluded from the acceleration model, those results hold for a single orbit, which may not always be representative of the whole picture when a large range of epochs of injection into GTO and initials RAANs are considered. Thus, making use of the powerful SST propagator, several colour-map plots will be obtained in which only certain perturbations are considered. In this way, it will be possible to know which perturbations are actually driving the evolution of objects in GTO and it should be possible to corroborate that solar resonances appear only when the effects of both zonal terms and the Sun's gravity are included in the acceleration model. These colour-map plots will be provided in Section 6.1.

Additionally, it would be interesting to study the orbital evolution of GTO for a longer period of time. Until now, all the propagations have been limited to 10 years, so the actual lifetime in the dark red regions of plots such as that in Figure 4.25 is not known. With the more powerful SST propagator, this limit can be increased to e.g. 25 years while still being able to obtain results in feasible computation times. Thus, some of the plots provided in Chapter 6 will have higher limits for the maximum propagation period.

Finally, it is necessary to study the problem of estimating the lifetime of objects in GTO by following a statistical approach, as discussed in Section 3.3.3. Space debris mitigation guidelines are often formulated in terms of probabilities, i.e. showing that the generated debris from a GEO launch will re-enter in less than 25 years with a 90% probability. This is especially convenient for orbits such as GTOs, which can undergo resonances leading to very different evolutions, even for slight divergences from the nominal conditions. In order to treat the problem from a statistical perspective, it is necessary to propagate a number of cases (e.g. 100 or 200 for each combination of epoch of injection into GTO and initial RAAN) with some of the parameters slightly deviating from the nominal values, and then studying the percentage of cases re-entering in less than a given lifetime limit. This is definitely unfeasible using the Cowell propagator, as the propagation of all the cases would take 100–200 times longer than generating the plot in Figure 4.25, i.e. 3 to 6 years. Even with the faster SST propagator this could take one to two months. Thus, it will be necessary to decrease the resolution when approaching the problem from a statistical perspective in order to be able to solve it within feasible computation times. The results corresponding to the statistical approach will be provided in Section 6.3.

6
RESULTS

In this chapter, the main results obtained following the semi-analytical approach discussed in Chapter 5 are provided. The results are discussed and analysed critically with the aim to answer the research questions and reach the research objective defined in Chapter 1.

First, the effects of each individual perturbation on the lifetime of objects in GTO will be studied separately in Section 6.1. Then, the effects of changing certain parameters, namely the body's ballistic coefficient, the initial inclination and perigee altitude of the orbit, will be discussed in Section 6.2. Finally, in Section 6.3, the results obtained by treating the problem from a statistical perspective will be provided.

All the results presented in this chapter correspond to GTOs with the following parameters, unless otherwise specified:

- Initial perigee altitude of 200 km.
- Initial apogee altitude of 35 780 km.
- Initial inclination of 10 degrees.
- Initial argument of perigee of 0 degrees.
- Initial true anomaly of 0 degrees.
- Body mass of 3 000 kg.
- Body cross-sectional area of 15 m^2.
- Body drag coefficient of 2.2.
- Body radiation pressure coefficient of 1.5.

As usual, the initial epoch (i.e. the epoch of injection into GTO) and the RAAN are taken as optimisation variables.

6.1. INDIVIDUAL EFFECTS OF ORBITAL PERTURBATIONS

Colour-map plots such as the one in Figure 4.25 will be provided in this section with some of the relevant perturbations excluded from the acceleration model. First, only one perturbation will be included, and then additional perturbations will be considered until all five (drag, Sun's gravity, zonal terms, Moon's gravity and SRP) have been included in the acceleration model.

Performing the study including no perturbations is pointless, as this would correspond to a Keplerian orbit in which all the orbital elements (except for the fast element) remain constant, and thus the lifetime could not be computed, as the perigee altitude would remain at its initial value, never reaching the re-entry altitude fixed at 100 km. Thus, the first plot to be obtained should include at least one perturbation. This perturbation has been chosen to be atmospheric drag, as this is the only perturbation causing secular variations on the value of the semi-major axis and, consequently, on the perigee altitude. If drag is not considered, is does not make sense to define a re-entry altitude or talk about lifetimes. Thus, all the plots provided in this section will include the effects of atmospheric drag.

When atmospheric drag is the only perturbation included in the acceleration model, no orbit reaches re-entry altitude (100 km) before 25 years (the limit for the propagation period set for all the plots provided in this section). Thus, the lifetime is not known for any of the propagated cases. However, the value of the final perigee altitude *is* available. As can be seen in Figure 6.1, the influence of drag on the orbital evolution of GTOs is rather limited, as the final perigee altitude of all the considered cases lies within a range of just 10 km (between 183 and 193 km), down from an initial perigee altitude of 200 km. In this case, the range for the initial epoch has been chosen to be 20 years rather than just one year, since atmospheric density is affected by solar radiation levels, which vary with a period of about 11 years, so it was deemed convenient to study, at least, a period of 11 years.

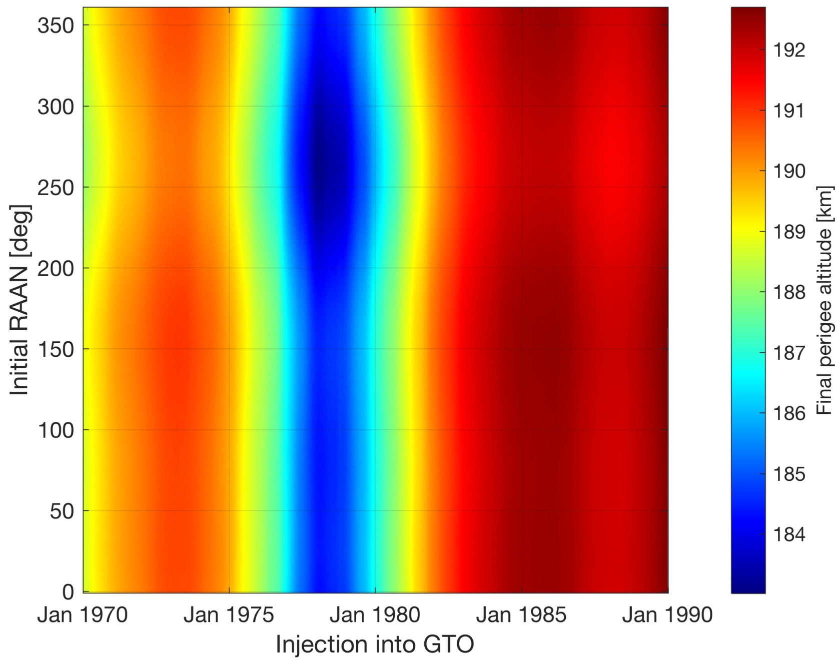

Figure 6.1: Final perigee altitude after a period of 25 years for several GTOs with initial perigee altitude of 200 km. Only perturbations caused by atmospheric drag were included in the acceleration model.

Despite the small differences, it can be seen that the orbits decay faster when the initial epoch is approximately in the year 1978. Those orbits are propagated from 1978 until 2003. From Figure 3.8 it can be observed that within those 25 years three relatively high solar maxima were reached. Orbits starting after 1985 (and propagated thus at least until 2010) include the solar maximum from year 2001 (and in some cases from 2014 as well), which were remarkably lower compared to the maxima of the previous century. This could explain the fact that those orbits decay more slowly.

The next step was to include the effects of the perturbation caused by the Sun's third-body gravity. This is considered to be one of the main perturbations driving the evolution of GTOs. Indeed, when this perturbation is included in the acceleration model, many of the studied GTOs decay in less than the maximum propagation period of 25 years, as can be seen in Figure 6.2. The shortest lifetime was 1.8 years.

From the orbits that did not re-enter in less than 25 years (those mostly in the range of RAANs from 60 to 180 degrees and from 280 to 360 degrees), many of them had final perigee altitudes much higher than the initial value of 200 km, as can be seen in Figure B.7. In fact, the orbit with the highest perigee altitude after 25 years has a perigee altitude of 1 307 km. This shows that, although the Sun's gravity cannot introduce secular effects on the value of the semi-major, it does affect the shape of the orbit, changing the eccentricity and consequently the values of the perigee and apogee altitudes significantly. It is worth highlighting the fact that the orbital evolution can change drastically depending on the initial value of the RAAN, but remains more or less constant (or at least changes much more smoothly) throughout the year.

Then, the effects of zonal terms (up to degree 7) were included in the acceleration model. Zonal terms can introduce large effects on the evolution of the RAAN, leading to the precession of the orbit that triggers the

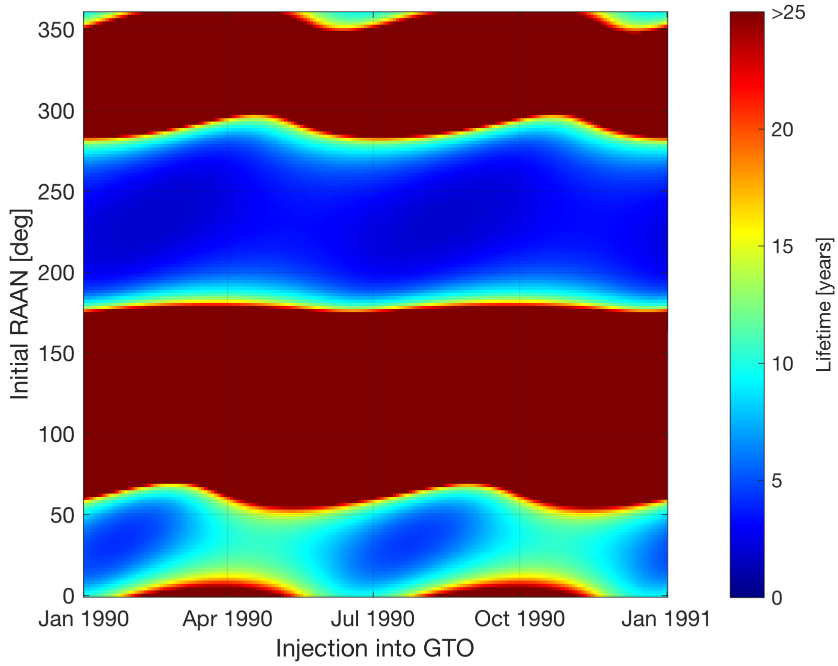

Figure 6.2: Lifetime of several GTOs as a function of initial epoch and RAAN. Only perturbations caused by atmospheric drag and the Sun's gravity were included in the acceleration model.

solar resonance described in Section 3.3.1 when the rate of precession $\dot{\Omega}+\dot{\omega}$ coincides with the rate of rotation of Earth about the Sun, i.e. about 1 deg/day. Thus, at this point, one should expect to see the appearance of cases affected by solar resonance in the colour-map plot. Indeed, when drag, the Sun's gravity and zonal terms are included in the acceleration model, resonance ridges appear for the first time, as can be seen in Figure 6.3.

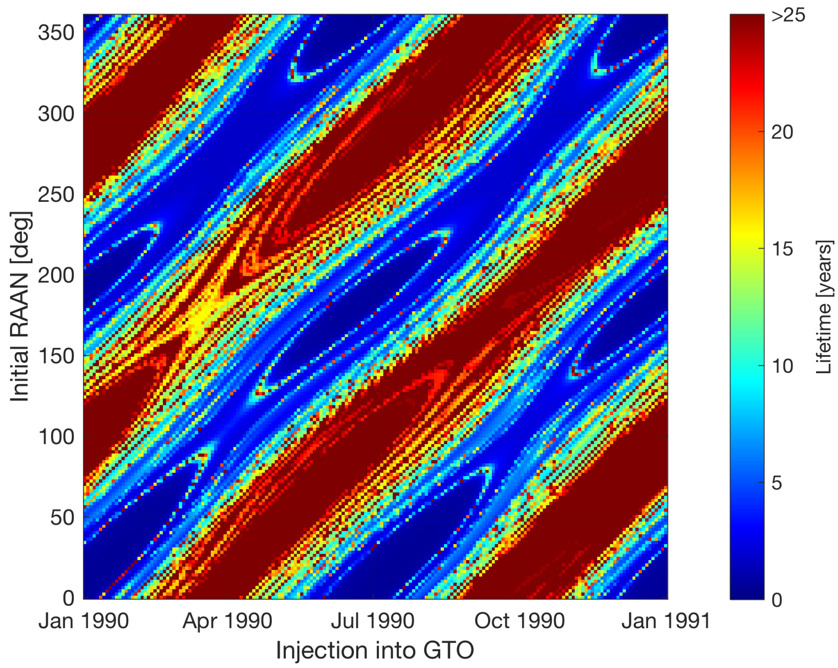

Figure 6.3: Lifetime of several GTOs as a function of initial epoch and RAAN. Only perturbations caused by atmospheric drag, the Sun's gravity and zonal terms of the geopotential were included in the acceleration model.

Note that the colour-map plots obtained in this section are starting to resemble that of Figure 4.25 obtained with all the relevant perturbations included in the acceleration model. This means that the effects of the perturbations that have not been included yet, namely the Moon's gravity and SRP, are rather limited. However, the size of the dark-blue regions (the regions of interest that are free of resonances) are still noticeably narrower in Figure 6.3 than in Figure 4.25.

The next step was to add the effects of the Moon's gravitational perturbation. As can be seen in Figure 6.4, the Moon makes the dark-blue regions wider, leading to a larger number of favourable, resonance-free conditions. At the same time, the second plateau with a slightly higher lifetime after the first resonance ridges that can be observed in Figure 6.3 has disappeared almost completely in Figure 6.4, becoming much narrower. Additionally, since the Moon introduces effects with a relatively short period, the appearance of small wiggles is observed in Figure 6.4, transforming the shape of the resonance ridges (and thus the shape of the dark-blue regions too) from almost perfect ovals to ovals with twisting boundaries.

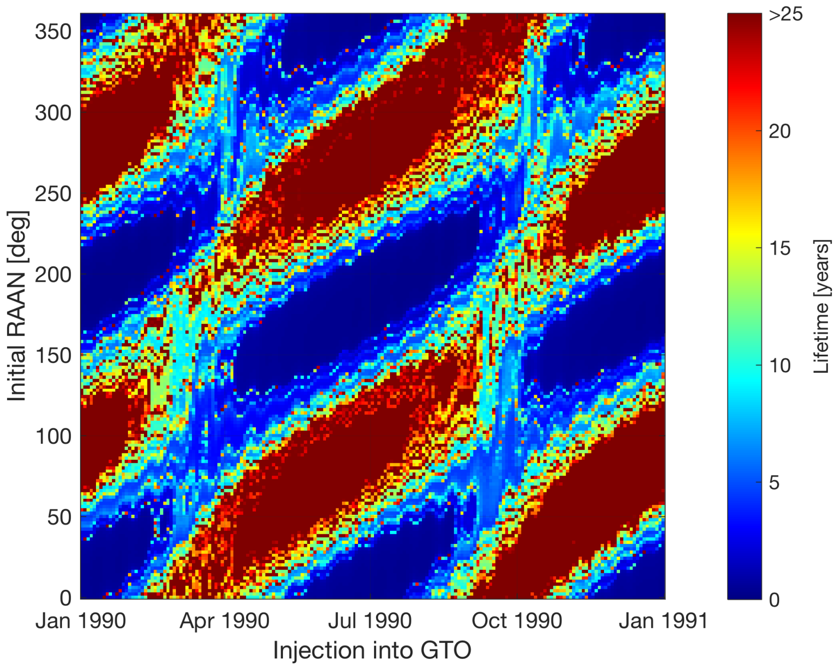

Figure 6.4: Lifetime of several GTOs as a function of initial epoch and RAAN. Only perturbations caused by atmospheric drag, the Sun's gravity, zonal terms of the geopotential and the Moon's gravity were included in the acceleration model.

Finally, when the effects of SRP (without considering occultations of the Sun by Earth's shadow) are considered, the acceleration model can be considered to be complete and the colour-map plot changes slightly from that of Figure 6.4 to the one already discussed in Chapter 5.2.2 and provided in Figure B.4 (right). Although the differences cannot be seen clearly with the naked eye (suggesting that the effects of SRP on the evolution of GTOs is limited), the shape of the resonance-free regions does change slightly, becoming wider or narrower. This can be seen in Figure B.8 (left), in which the error near the boundaries of the resonance-free regions introduced by neglecting SRP can range from −95% to +2 068%. When only the regions of interest are considered, the RMS error is only 5.5% and the individual errors range from −40% to +21%, as seen in Figure B.8 (right). Thus, SRP has a small effect on the evolution of GTOs in resonance-free regions but cannot be neglected if an accurate description is desired. The main risk of neglecting SRP is not related to the small errors introduced in the value of the lifetime prediction at the central parts of resonance-free regions, but to the slight widening or narrowing of those regions, which can lead to recommending a combination of epoch of injection into GTO-initial RAAN as a favourable case, whilst it may actually correspond to a resonance ridge.

6.2. EFFECTS OF CHANGING PARAMETERS

6.2.1. INITIAL INCLINATION

The GTO defined at the beginning of this section was propagated for several values of the initial inclination. The inclination was expected to be a relevant parameter for the evolution of GTOs, as indicated by previous studies, in which it was found that the percentage of orbits re-entering in less than a specified period of time was maximum when the initial inclination of the GTO was close to 45 degrees [34]. In Figure 6.5, it can be seen that, in fact, the size of the dark-blue, resonance-free regions increases with increasing value of the inclination. Additionally, as the inclination gets closer to 45 deg, the shape of the colour-map plots begin to ressemble that of Figure 6.2, in which only the perturbations of atmospheric drag and the Sun's gravity were included in the acceleration model. Thus, as the inclination gets closer to 45 degrees, the effect of zonal terms on the evolution of GTOs becomes less relevant.

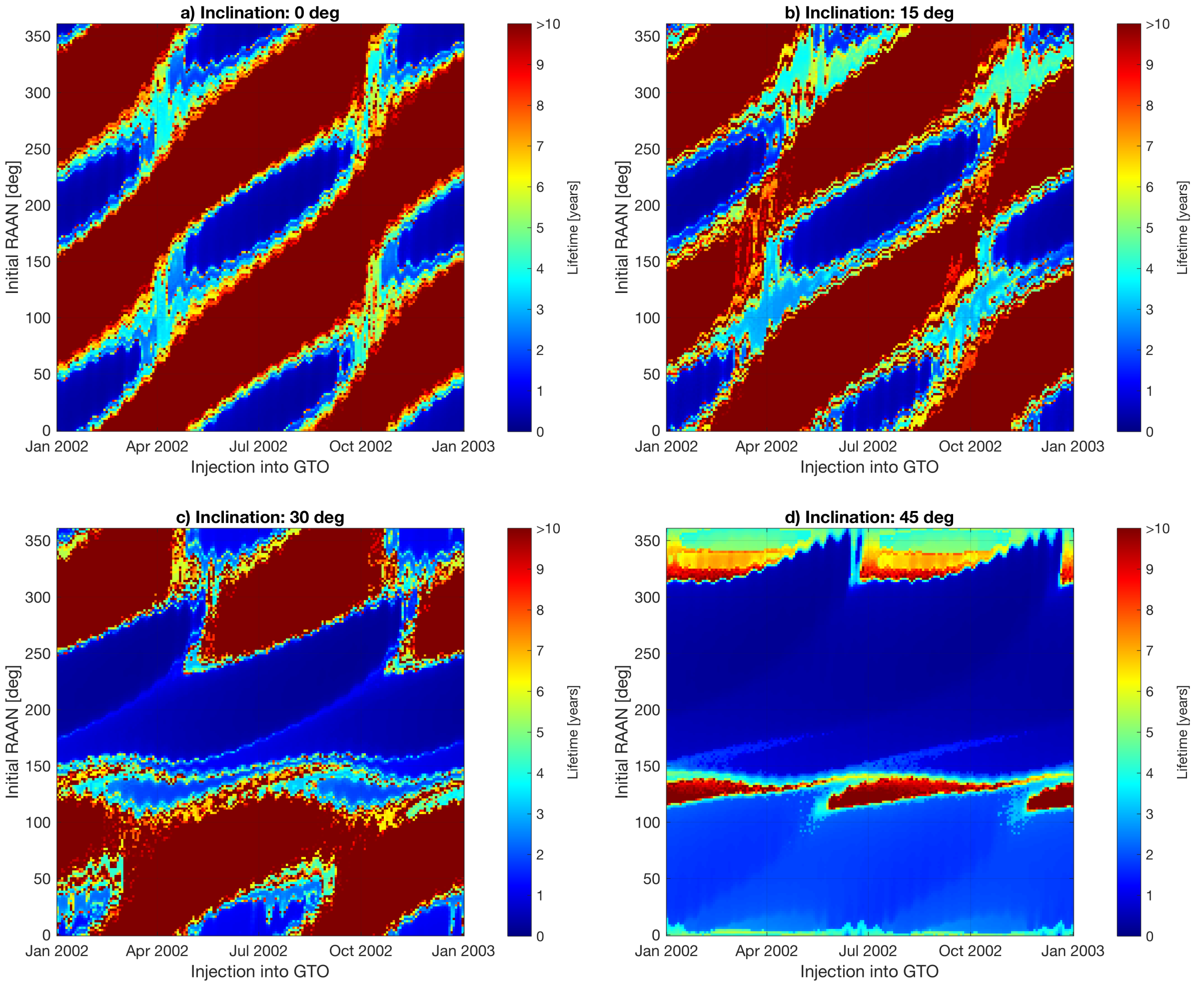

Figure 6.5: Lifetime of a satellite as a function of epoch of injection into GTO and initial RAAN for different initial inclinations: **a)** 0 degrees, **b)** 15 degrees, **c)** 30 degrees and **d)** 45 degrees.

This behaviour can be explained by studying the effects of the most relevant zonal term J_2 alone, which is also the main contributor to the mean drift of perigee, $\dot{\Omega}+\dot{\omega}$. From Eqs. (A.30) and (A.32), the contribution of J_2 to the mean drift of perigee can be obtained:

$$\dot{\Omega}+\dot{\omega} = \tilde{J}_2 n \left[-\cos i + \frac{1}{2}\left(5\cos^2 i - 1\right)\right] \tag{6.1}$$

As can be seen in Figure B.9, the contribution of J_2 to the mean drift of perigee becomes zero for $i = 46.4$ deg, while it is maximum (equal to $\tilde{J}_2 n$) when the inclination is 0 deg (considering only prograde orbits). As discussed in Section 3.3.1, the mean drift of perigee is a relevant parameter to explain the existence of solar resonances: when it becomes close to 1 deg/day, solar resonances can be triggered. However, for orbital inclinations close to 46.4 degrees, it remains close to zero, so the solar resonance is never triggered, leading to orbital evolutions such as the ones shown in Figure 6.5d, which are relatively similar to the ones in Figure 6.2 in which the effects of zonal terms had not been included in the acceleration model.

Although choosing a larger inclination can lead to a larger number of favourable launch conditions from a debris-mitigation perspective, this is obviously not convenient from a mission-design point of view. GTOs are used to bring payloads to GEO, which is equatorial and thus has an inclination of 0 degrees. If the payload reaches GEO altitude with an inclination of 45 degrees, a correction manoeuvre will have to be carried out to bring its inclination to 0 degrees, which is very expensive in terms of delta-V and propellant usage. For that reason, GEO launches are usually carried out from low latitudes (such as Kourou in French Guiana), which makes it possible for the inclination of the GTOs to be around 5 to 10 degrees. When GEO payloads are launched from higher latitudes (such as Cape Canaveral), the inclination has to be larger, at least 28 degrees, so a GTO is not always used. In some cases, the payload is brought to a super-synchronous altitude (e.g. 80 000 km) and the inclination-correction manoeuvre is carried out there, where it is less expensive in terms of delta-V [75]. Consequently, the generated debris do not stay in a GTO but in a super-synchronous orbit without crossing the LEO or GEO protected regions. This means that, although in theory a larger orbital inclination can be beneficial for debris mitigation, the actual values for inclinations of GTOs due to mission design constraints will not be chosen to be larger than 30 degrees, and in most cases will be less than 10 degrees, as shown in the inclination histogram for existing GTOs provided in Figure 2.7.

6.2.2. INITIAL PERIGEE ALTITUDE

The initial perigee altitude can also have significant effects on the evolution of GTOs. Since atmospheric drag changes exponentially with altitude, relatively small changes in the value of the perigee altitude can lead to very different lifetimes, as seen in Figure 6.6. As one could expect, choosing a higher initial perigee altitude leads the lifetimes to larger values. When the perigee altitude is chosen sufficiently small, the dark-blue, resonance-free regions widen to intersect with each other, as shown in Figure 6.6a. This means that, for an initial perigee altitude of 170 km, there exists at least two favourable launch times for every day of the year. However, if the initial perigee altitude is increased to e.g. 185 km, as seen in Figure 6.6b, the resonance-free regions are not continuous anymore, which means that, for some days of the year (mostly around April-May and October-November), there is only one launch time that will guarantee an orbital evolution free of solar resonances.

If the initial perigee altitude is increased further to 215 km, the resonance-free regions become even narrower, leading to some days of the year for which no launch time can lead to an orbit guaranteed to be free of solar resonances, as seen in Figure 6.6c. Increasing the initial perigee altitude further, to e.g. 250 km, causes the resonance-free regions to shrink to a point in which no combination of epoch of injection into GTO and initial RAAN would lead to an orbital evolution guaranteed to be free of solar resonances, as seen in Figure 6.6d.

6.2.3. BALLISTIC COEFFICIENT

The effects of changing the ballistic coefficient on the lifetime of GTOs is similar to that of changing the initial perigee altitude, as can be seen in Figure 6.7. A larger ballistic coefficient (i.e. a body with larger area and/or smaller mass) experiences more drag than a body with a small ballistic coefficient, and thus reaches re-entry conditions faster. In Figure 6.7a it can be seen that a ballistic coefficient of 0.032 m^2/kg leads to wide resonance-free regions, although there are still certain days of the year for which only one favourable launch time exists. Decreasing the ballistic coefficient by a factor of two narrows the resonance-free regions, leading to some days of the year in which no launch time can guarantee a resonance-free orbital evolution. Decreasing the value of the ballistic coefficient further can limit the number of favourable launch conditions and the size of the launch windows considerably as seen in Figures 6.7c or 6.7d. Recall that, in the study of existing objects in GTO presented in Section 2.2.3, it was found that the median of the ballistic coefficient of those objects is about 0.011 m^2/kg, with 25% of the objects having ballistic coefficients smaller than 0.0048 m^2/kg and another 25% having ballistic coefficients larger than 0.034 m^2/kg, so it can be said that the values of the ballistic coefficients for the four cases considered in Figure 6.7 are within reasonable limits that are indeed found in practice.

6.3. STATISTICAL APPROACH

As discussed in Section 3.3.3, some authors have recommended to study the problem of propagation of GTOs following a statistical approach, in which rather than determining the lifetime to be a fixed amount of time, the probability of the lifetime being smaller than a specified amount is found. This would allow launch companies to comply with guidelines of the type "re-entry in less than 25 years with a 90% probability" or "re-entry probability of at least 90% after 25 years".

In order to be able to generate these kind of results, it is necessary to propagate many orbits for each

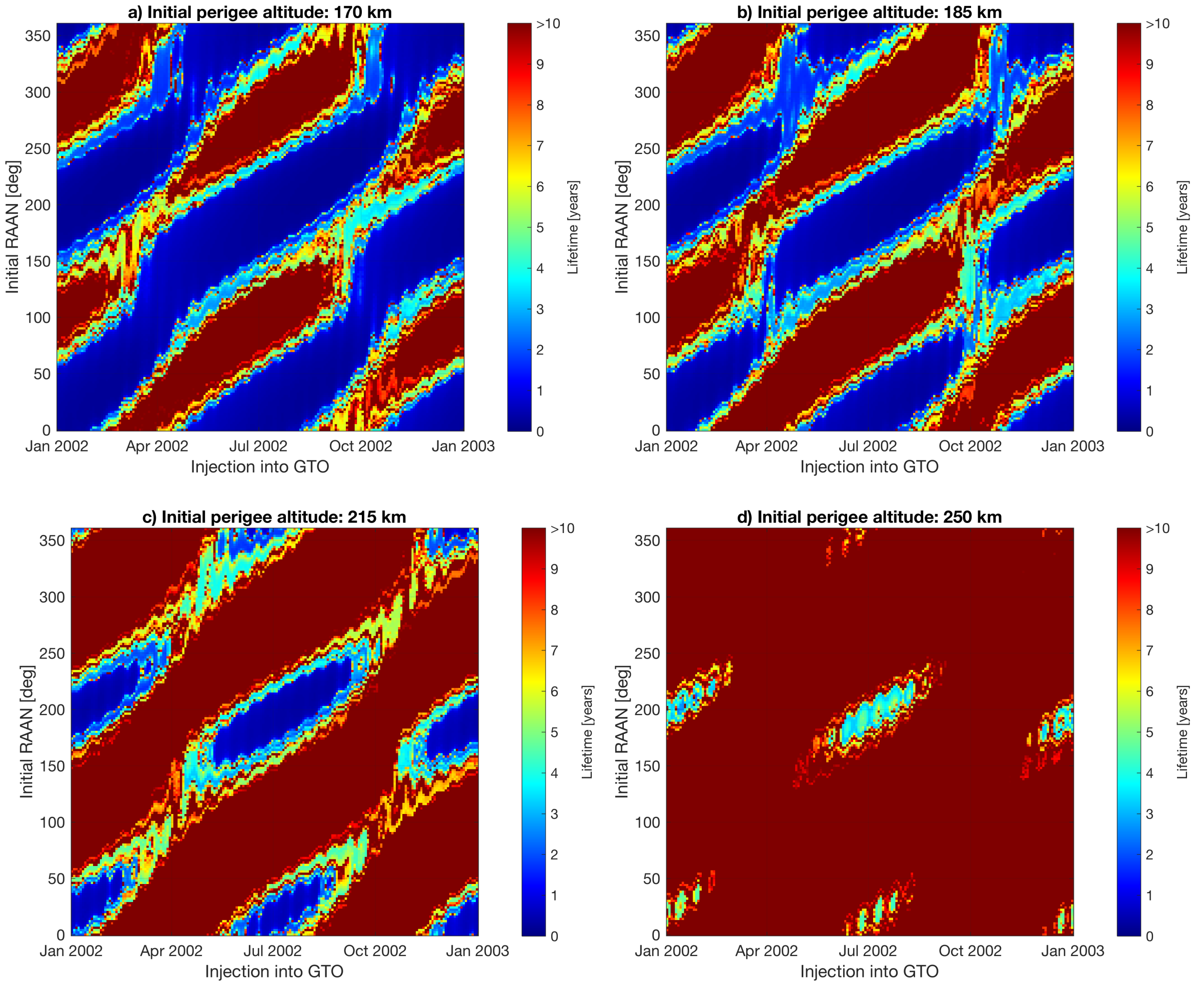

Figure 6.6: Lifetime of a satellite as a function of epoch of injection into GTO and initial RAAN for different initial perigee altitudes: **a)** 175 km, **b)** 180 km, **c)** 215 km and **d)** 250 km.

combination of epoch of injection into GTO and initial RAAN, with slightly varying values for some of the parameters affected by uncertainties. Based on the statistical study of the characteristics of existing objects in GTO presented in Section 2.2.3, the parameters in Table 6.1 have been set to vary following the normal distribution with the mean and standard deviation values specified therein. The remainder of the parameters were kept constant at the values specified at the beginning of this chapter, except for the initial epoch and RAAN, which are the optimisation variables.

Table 6.1: Mean and standard deviation of the parameters whose value is changed when approaching the propagation of GTOs from a statistical perspective.

Parameter	**Mean**	**Standard deviation**
Initial perigee altitude	200 km	2 km
Initial apogee altitude	35 650 km	1 000 km
Initial inclination	8.3 deg	0.5 deg
Body mass	3 000 kg	100 kg
Body cross-sectional area	15 m^2	5 m^2

The colour-map plots presented so far have been recreated, but instead of propagating a single orbit for each combination of epoch of injection into GTO and initial RAAN, 200 cases have been propagated, in which the values for the parameters indicated in Table 6.1 have been obtained, for each case, by generating pseudo-random numbers following a normal distribution based on the specified mean and standard deviation values

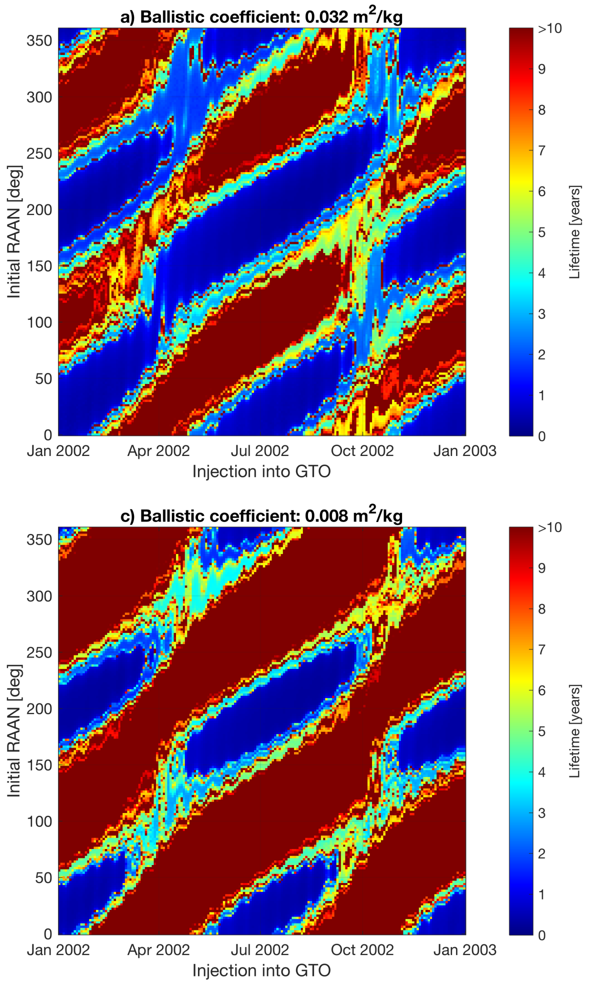

Figure 6.7: Lifetime of a satellite as a function of epoch of injection into GTO and initial RAAN for different body ballistic coefficients: **a)** 0.032 m^2/kg, **b)** 0.016 m^2/kg, **c)** 0.008 m^2/kg and **d)** 0.004 m^2/kg.

(i.e. a Monte Carlo simulation). Since it would take about 200 times longer to generate the results (compared to the deterministic approach), the resolution had to be decreased in order to be able to obtain the results of interest within feasible computation times. Namely, a step-size of 4 days was used for the epoch of injection into GTO and a step-size of 4 degrees was used for the initial RAAN. After performing the propagations, the colour-map plot provided in Figure 6.8 was obtained by computing the mean lifetime of the 200 cases propagated for each combination of epoch of injection into GTO and initial RAAN (excluding the cases with initial invalid parameters, such as a negative cross-sectional area or an inclination smaller than Kourou's latitude). Note that the propagations were stopped after 25 years if re-entry had not been achieved yet at that point, so the mean values in Figure 6.8 are actually a lower limit, since the value of 25 years has been used for orbits that, in reality, take longer to re-enter.

When comparing with Figure 6.4, the most noteworthy finding from Figure 6.8 is the disappearance of the high-lifetime ridges caused by solar resonances. This is not due to the use of a lower resolution. The colour-map plot in Figure 4.24b was obtained using a resolution (3.65 days for the epoch of injection into GTO and 3.6 degrees for the initial RAAN) similar to the one used in Figure 6.8. When a deterministic approach is followed, some cases affected by solar resonance can be spotted, in the form of isolated high-lifetime points, as seen in Figure 4.24b. On the other hand, when the statistical approach is followed, these cases affected by resonances are averaged out, since only a few of them (e.g. 5–10 out of the 200 cases) undergo resonances. The result is a much smoother plot in which the lifetime gradients are much smaller than the ones presented in Figure 4.26. The claim that the choice of a lower resolution is not causing overlooking of resonance ridges was corroborated by focusing on a small region of Figure 6.8 and propagating it with a higher resolution, obtaining still smooth variations for the value of the lifetime, as can be seen in Figure B.10.

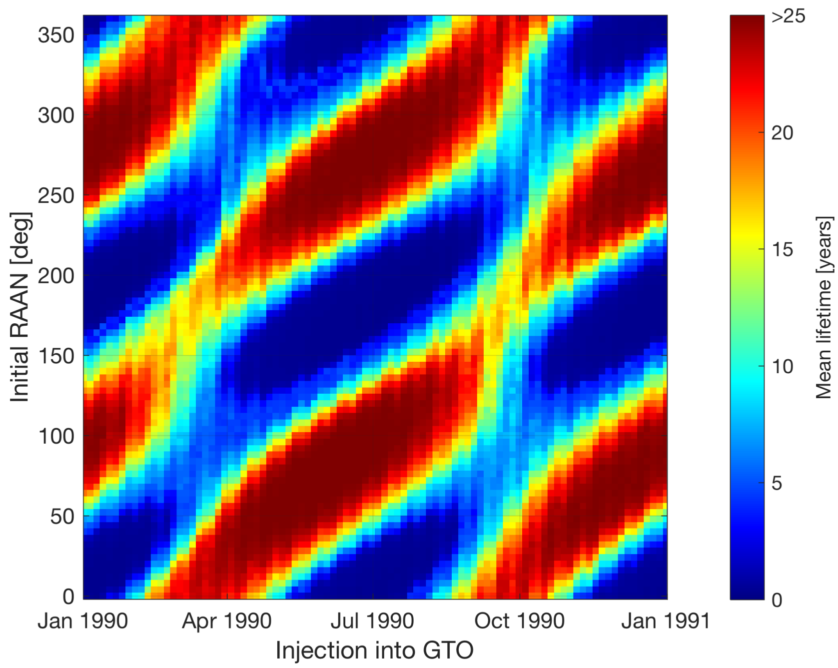

Figure 6.8: Mean lifetime for objects injected into GTO at different epochs and with different RAANs.

However, it is not recommended to use the results provided in Figure 6.8 to predict the lifetime of a given GTO. Although the mean lifetime could be e.g. 15 years for a certain combination of epoch of injection into GTO and initial RAAN, some of the orbits corresponding to that case might have much longer lifetimes of even more than 25 years. This can be observed in the histogram in Figure 6.9 (right) corresponding to an initial RAAN of 180 deg and an injection into GTO on the 24th of February. In this case, the data cannot be said to be normally distributed, so the average lifetime (14.5 years) should not be used as a representative value for this date of injection into GTO and initial RAAN. In other cases, however, the data can be said to be normally distributed, as can be seen in Figure 6.9 (left), corresponding to an initial RAAN of 180 deg and an injection into GTO on the 13th of February. In this case, the average value of 8.6 years is, to some extent, representative of the lifetime values to be expected for this combination of date of injection into GTO and initial RAAN. However, it is worth highlighting that the distribution is widely spread (the peak of the PDF is below 10%).

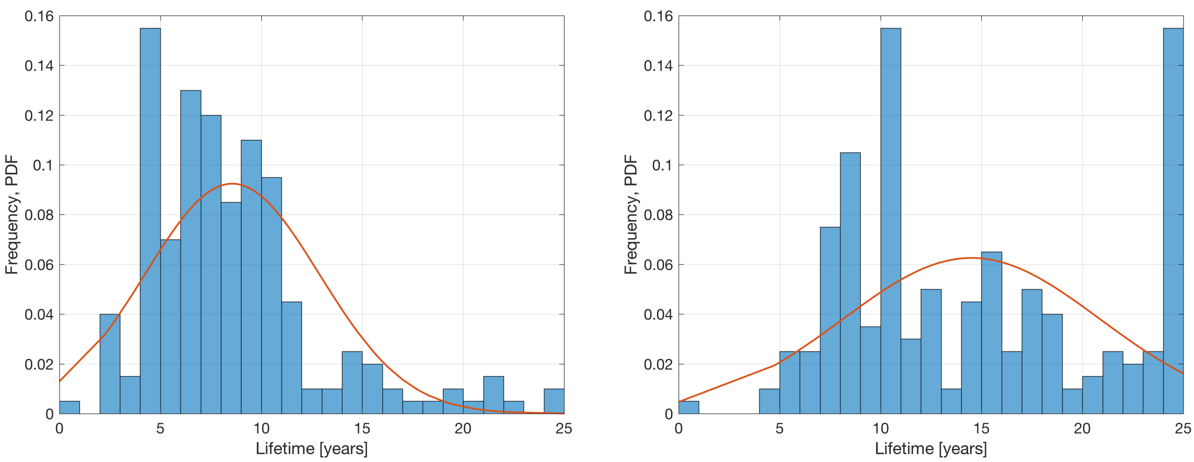

Figure 6.9: Probability distribution of the lifetime for GTOs with initial RAAN of 180 degrees and injection into GTO on the 13th of February (left) and on the 24th of February (right).

Given the fact that the lifetime is not always normally distributed, it is convenient to use the obtained results to generate plots showing the probability of re-entering in less than a specified amount of time, such as the ones in Figure 6.10. In those plots, the re-entry probability has been obtained by dividing the number of orbits re-entering in less than the specified amount of time (10 or 25 years) by the total number of studied cases (200) for each combination of epoch of injection into GTO and initial RAAN. For instance, Figure 6.10 (right) can be used to determine the launch conditions that will lead to re-entry in less than 25 years with a 90% probability for the object and initial orbit described at the beginning of this section. In Figure 6.10 (left), the range of satisfactory options is more limited, because the requirement of re-entry with a 90% probability has been set to 10 years instead of 25 years, leading to a smaller number of cases fulfilling the criterion.

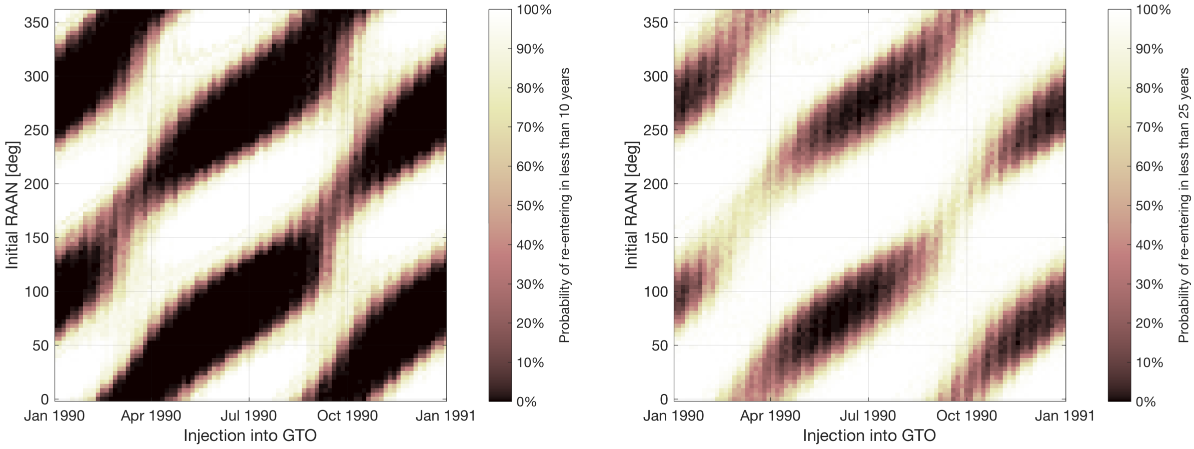

Figure 6.10: Probability of re-entry in less than 10 years (left) and in less than 25 years (right) for objects injected into GTO at different epochs and with different RAANs.

7

PRACTICAL APPLICATION

In the previous chapters, the results obtained by studying the temporal evolution of objects in GTO have been provided in terms of the initial epoch for the propagation and the initial RAAN of the orbit. However, these results cannot be applied directly to reach the research objective: although it has been shown that by changing the launch conditions the lifetime of the objects in GTO can change significantly due to the interplay between several orbital perturbations, the launch conditions leading to those optimal cases (or leading to compliance with debris-mitigation guidelines) have yet to be determined from the obtained results. This will be discussed in Section 7.1, where the conversion from RAAN to local time of launch will be done. Also in that section, some of the aspects related to mission design that need to be taken into account during the launch of satellites to GEO will be covered, and a few simplifications will be introduced in order to be able to apply the results provided in Chapter 6 to real launches. Finally, in Section 7.2, the obtained results will be applied in the analysis of a case study involving the launch of a satellite to GEO from the Euroepan spaceport in Kourou.

7.1. MISSION DESIGN

Injecting a satellite into GEO requires the use of launch vehicles capable of bringing the satellite to an altitude close to that of GEO with a relatively low orbital inclination. Then, a final manoeuvre has to be performed to inject the payload into its assigned GEO slot at precisely GEO altitude and with an orbital inclination of 0 degrees. In the past, many procedures have been followed to achieve this, including the use of several propellant burns leading to the generation of debris in several types of orbits below GEO altitude (such as LEO, MEO, GTO or close to GEO), or even in orbits above GEO where the changes of inclination can be performed using less amounts of propellant [75]. However, in most cases, at least during the last decades, GEO launches have been performed from locations close to the equator in order to achieve a low-inclined GTO, and typically debris such as upper stages and other mission-related objects (such as payload adaptors or motors used during the last phase of injection) have been left in GTOs with characteristics that are similar to those of the GTOs studied in previous chapters [34]. Leaving debris in GTO poses a risk for existing and future missions, as they cross the LEO and GEO protected regions and can take several decades to re-enter.

In the analysis of GEO missions performed in [34], it was found that the perigee altitudes of the debris generated by launches using the Ariane 5 launch vehicle, which was the major contributor to the debris population in GTO in the period 2004-2012, were in the range of 222–658 km, with the nominal perigee altitude being 250 km. Other launchers used GTOs with generally lower perigees: between 105 and 215 km for the Chinese Long March rocket family; 172–192 km for the Indian Geosynchronous Satellite Launch Vehicle; 180–263 km for launches by the Japanese H-IIA; and 110–236 km for most of the launches by the United States using the Atlas, Delta and Titan launch vehicle families. Sea Launch launched satellites using the Zenit family leading to low-perigee GTOs in some cases (132, 134 km), but it also generated debris in GTOs with perigee altitudes as large as 11 250 km. The Proton launch vehicle used by Russia generated debris in very different GTOs, with perigee altitudes ranging from 310 to 5 157 km.

From these figures, it is clear that different procedures for injecting payload into GEO are being used, and studying all of them individually is beyond the scope of this thesis. Thus, the focus will be put on the procedures followed by two launch companies that account for 87 of the 89 LEO- and GEO-crossing debris generated in the period 2004-2012: Ariane 5 (which generated 75 objects) and Zenit-3SL (which generated

12) [34], operated by Arianespace and Sea Launch, respectively.

7.1.1. ASCENT PROFILE

The ascent profile of GEO missions depends mainly on whether several burns are performed during ascent to GEO altitude, leading to debris in several GTOs with different perigee altitudes, or only one continuous burn is performed initially until the payload (and upper stages) have been injected into the final GTO. Two example ascent profiles, one for each of these approaches, are provided in Figures 7.1 and 7.2.

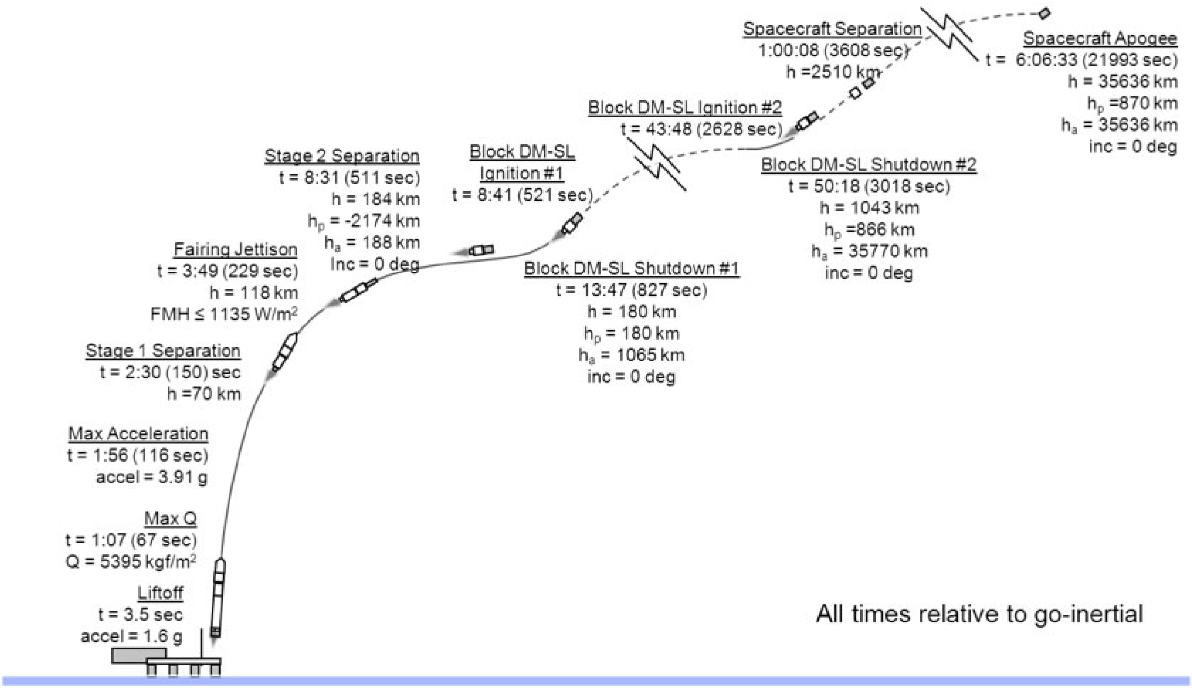

Figure 7.1: Ascent profile of Intelsat 19 launched in June 2012 using a Zenit 3SL operated by Sea Launch. [76]

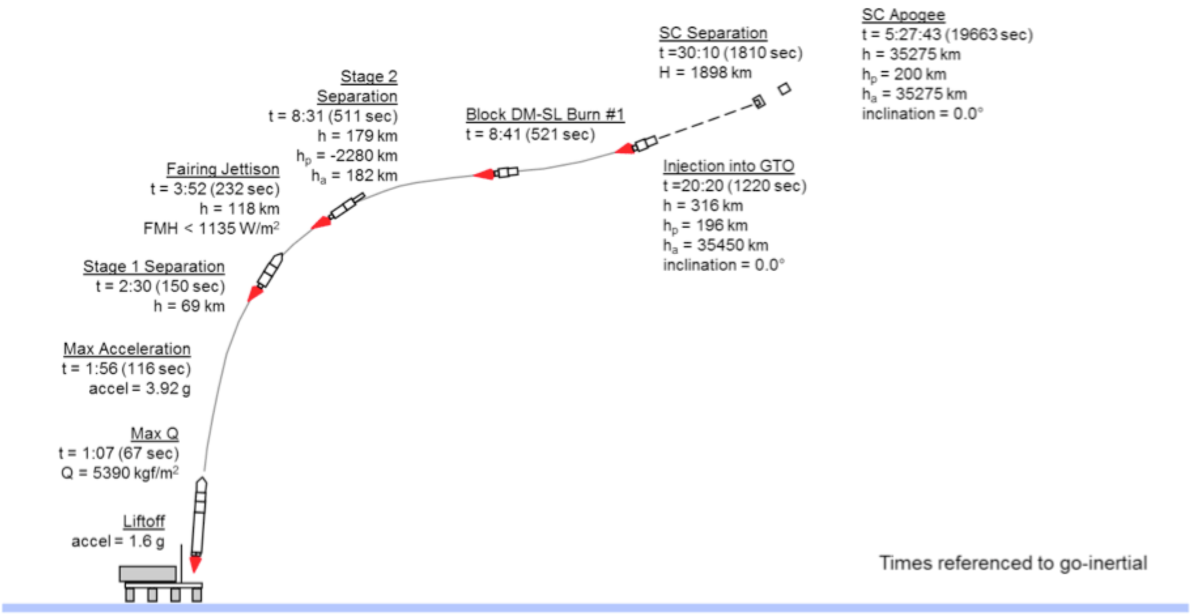

Figure 7.2: Ascent profile of Intelsat 27 launched in February 2013 using a Zenit 3SL operated by Sea Launch. [76]

Both ascent profiles include an initial flight powered by the first and second stages, up to an altitude of about 180 km. Then, in the ascent profile of Intelsat 19, provided in Figure 7.1, it can be seen that the upper stage Block DM-SL was ignited twice, with a period of unpowered flight of 30 minutes between the two ignitions. This led to a spacecraft separation at an altitude of 1 043 km, generating debris in a GTO with perigee altitude of 866 km. On the other hand, the Block DM-SL was ignited only once during the launch of Intelsat 27, as can be seen in Figure 7.2, right after separation of the second stage. This led to an injection into the final GTO at a much lower altitude (316 km), and the resulting GTO in which the debris were left had a perigee altitude of 196 km.

In both cases, the launch was performed from the Odyssey Platform in the Pacific Ocean, at 0°N 154°W. The use of different ascent profiles led to reaching GEO altitude after different periods of time: in the case of Intelsat 19, with two burns and a phase of unpowered flight, the ascent was slower, taking 6 h 6 min, while for Intelsat 27, which can be considered to be a direct ascent, GEO altitude was reached 5 h 27 min after liftoff. In any case, it is clear that this time will be at least half the orbital period of the resulting GTO. The period of a GTO with perigee altitude of 200 km and apogee altitude of 35 786 km is 10.5 hours, so the minimum time period since liftoff until arrival to GEO can be expected to be 5 h 15 min.

The ascent profile of missions in which the upper stage is ignited several times is less interesting from the point of view of studying the applicability of the results obtained in previous chapters, as the resulting debris are generated in GTOs with high perigee altitude (more than 300 km), which will not be able to comply with debris-mitigation guidelines, as can be inferred from the sensitivity analysis provided in Section 6.2.2 in which the lifetime of GTOs was studied as a function of initial perigee altitude. Little can be done to comply with debris-mitigation guidelines if the generated debris are in an orbit with a perigee altitude of e.g. 500 km. However, when the approach corresponding to Figure 7.2 is followed, the debris are generated in orbits with perigee altitudes close to 200 km (or the nominal 250 km for launches using Ariane 5), and in that case, orbital perturbations can indeed be exploited in order to comply with debris-mitigation guidelines without the use of additional propellant.

7.1.2. REACHABILITY OF GEO SLOTS

The use of different ascent profiles for injection of payloads into GEO is usually driven by the need to inject the satellite into a specific slot in the GEO ring. The mean motion of satellites in GEO coincides with the rotational speed of Earth, which means that, once injected into GEO, the satellite will be stationary in the sky with respect to an observer on Earth (small manoeuvres will have to be performed periodically to correct for the effects of orbital perturbations). Thus, if a company wants to launch a GEO satellite to provide coverage to certain regions of Earth, they will choose a fixed longitude and a certain slot in the GEO ring will be assigned to them. Consequently, there will be a constraint on the value of the longitude of the sub-satellite point (SSP) when the payload is injected into GEO.

When a direct ascent is performed, the longitude at which GEO will be reached cannot be chosen freely. In fact, the longitude that will be reached upon arrival at GEO is given by:

$$\Lambda_{GEO} = \Lambda_{GTO} + 180° - \frac{360°}{1 \text{ sidereal day}} \frac{T_{GTO}}{2} \approx \Lambda_{GTO} + 101° \tag{7.1}$$

where Λ_{GTO} is the longitude of the SSP at the GTO's perigee and T_{GTO} is the orbital period of the GTO in sidereal days. The second term, equal to 180°, is the angle swept by the GTO object during the transfer from perigee to apogee. The third term corresponds to the angle swept by the GEO ring during this transfer, which will last $T_{GTO}/2$ if a Hohmann transfer is assumed (i.e. a single impulsive shot at perigee). For direct ascents, injection into GTO will happen close to GTO's perigee and relatively soon after liftoff, so the value of Λ_{GTO} cannot be chosen by staying in a phasing orbit, as the ascent is continuously powered until injection into GTO. For instance, from Figure 7.4, it can be seen that the longitude of the sub-satellite point at injection into GTO was about 63° east of the launch site for the launch of Intelsat 27 (the longitude of the launch site was 154°W and the longitude of the satellite at injection into GTO was about 91°W).

If a slot in the GEO ring with a different longitude is to be reached, a stepped ascent can be followed, leading to an evolution of the SSP as the one shown in Figure 7.3, corresponding to the launch of Intelsat 19. The unpowered flight between the two burns of the Block DM-SL leads to reaching a different GEO slot despite having launched from the same location. However, as already discussed, this is not ideal from a debris-mitigation point of view, as debris are generated in a GTO with a high perigee, leading to very long lifetimes (several decades or even centuries). Thus, a different approach will have to be followed in order to be able to reach any slot in the GEO orbit while still following a direct ascent that will generate debris in GTOs with low perigee altitudes.

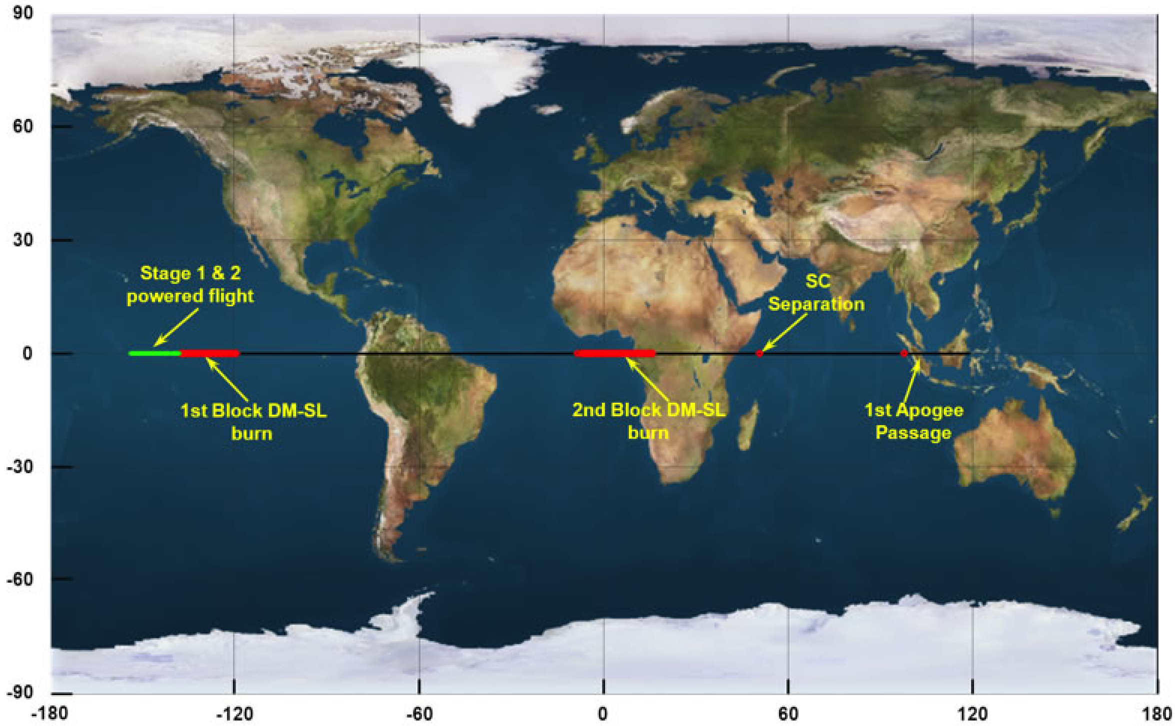

Figure 7.3: Evolution of the sub-satellite point of Intelsat 19 during its ascent to GEO. [76]

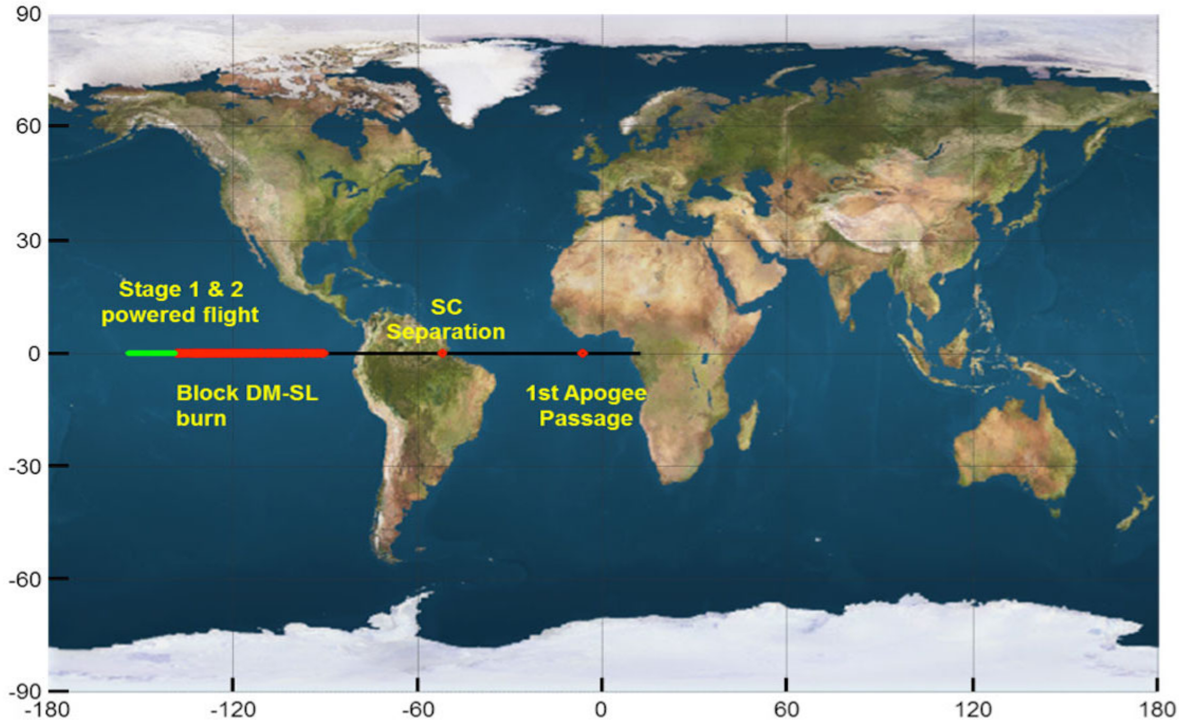

Figure 7.4: Evolution of the sub-satellite point of Intelsat 27 during its ascent to GEO. [76]

There are several approaches that can be followed in order to reach an arbitrary GEO slot when launching from a fixed location on Earth. Usually these approaches entail the use of (temporary) phasing orbits with an orbital period different from that of GEO. For instance, the payload and upper stage can wait in a LEO until the right phasing angle is achieved. At that point, an impulsive shot injects the payload into GTO to reach

GEO at the right slot about 5 h 15 min later. For a LEO of 200 km altitude, the maximum waiting period in the worst case scenario (if the desired GEO slot is almost 360° ahead of the slot that would be reached when no phasing orbit is used) would be about 94 minutes. However, this procedure can generate debris in the LEO orbit, which has to be avoided given the high density of spacecraft in this region, and drag is large for an circulat orbit at 200 km. For that reason, a direct ascent to an altitude slightly lower than that of GEO, followed by a phasing orbit at that altitude, is preferable. This is also the approach followed by most launch companies [34]. However, waiting periods in the phasing orbit are longer in this case, since an orbit with an altitude close to that of GEO has also a similar mean motion. In Figure 7.5 it can be seen that the waiting period can range from a few days to several months in the worst-case scenario, i.e. when the required phasing angle is 180°. When the required phasing angle is larger than 180°, then a higher altitude would be chosen for the phasing orbit.

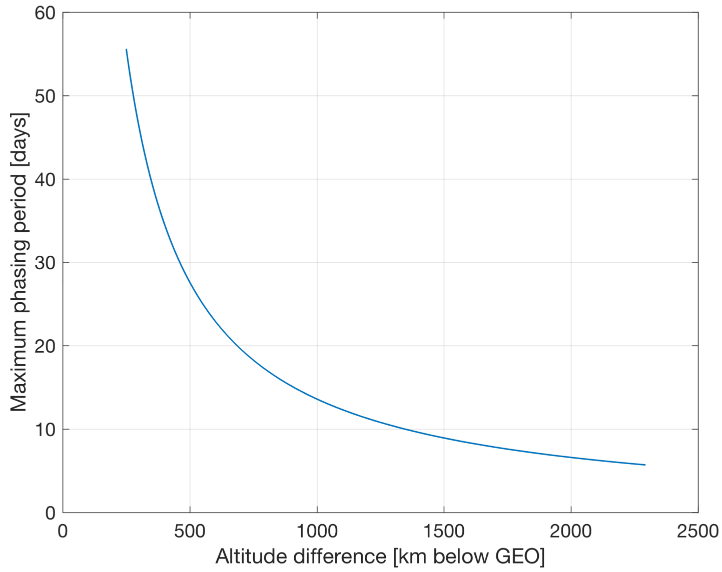

Figure 7.5: Maximum waiting period in a circular orbit slightly below GEO necessary to reach any arbitrary slot in the GEO ring, as a function of the altitude difference between GEO and the phasing orbit.

In order to determine the required delta-V for going from this phasing orbit slightly below GEO to the final GEO, the following equation can be used if a Hohmann transfer is followed [77]:

$$\Delta v = \sqrt{\frac{\mu_E}{r_{phasing}}}\left(\sqrt{\frac{2r_{GEO}}{r_{phasing}+r_{GEO}}}-1\right)+\sqrt{\frac{\mu_E}{r_{GEO}}}\left(1-\sqrt{\frac{2r_{phasing}}{r_{phasing}+r_{GEO}}}\right) \tag{7.2}$$

where $r_{phasing}$ and r_{GEO} are the radii of the phasing orbit and GEO, respectively. This leads to a required delta-V between 3.7 and 75.6 m/s for altitude differences between the GEO and phasing orbit ranging from 100 to 2 000 km. This is extremely small when compared to the delta-V budget for a launch from Earth's equator to GEO (more than 13 km/s) and in the same order of magnitude as the yearly delta-V required for stationkeeping in GEO (about 50 m/s) [78].

7.1.3. LOCAL TIME OF LAUNCH

In the previous subsection it was shown that the choice of the time of launch does not necessarily determine the GEO slot that will be reached. Instead, this is given by the longitude of the launch site and the followed ascent profile (the duration of the period powered by the first and second stages, the use of phasing orbits, etc.). However, this does not mean that the time of launch is completely irrelevant, as the results provided in previous chapters showed that the choice of the initial RAAN (which translates to a given local time of launch) can lead to orbital evolutions with very different lifetimes, which is attractive from a debris-mitigation point of view. In this section, the implementation of the equations provided in Section 3.1.4 to convert between initial RAAN and local time of launch, and the consequences that this conversion has for the lifetime colour-map plots, will be discussed.

As discussed in Section 3.1.4, in order to convert the initial RAAN to local time of launch it is necessary to follow an iterative procedure making use of Eq. (3.7), in which several local times are tested until the one leading to the target RAAN is found. By repeating this procedure for the different days of the year, the plots provided in previous chapters can be expressed as a function of local time of launch for any given launch site on Earth. For instance, the plot in Figure 6.10 (right) can be converted to Kourou local time, leading to the plot in Figure 7.6. The used coordinates for the Euroepan spaceport in Kourou are 5.36°N 52.76°W, and Kourou's time zone is GMT-3.

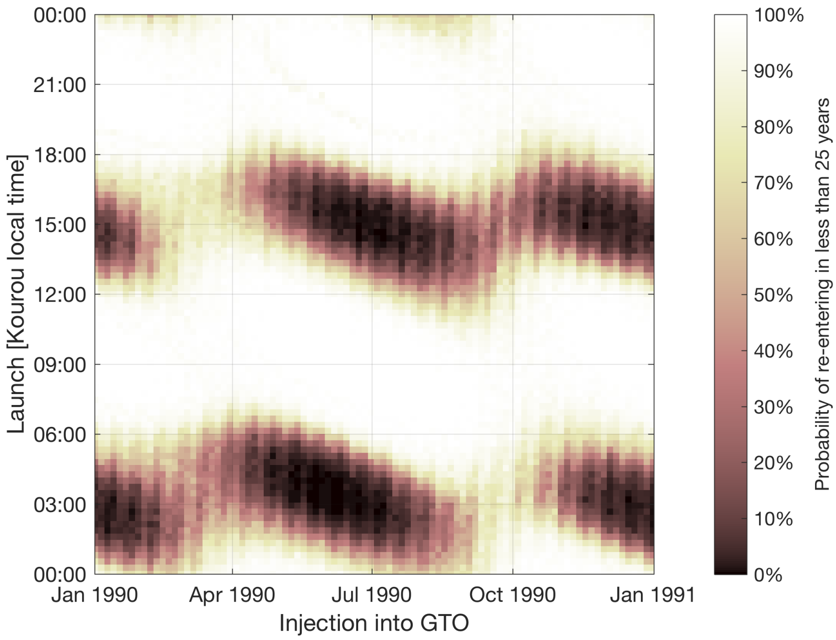

Figure 7.6: Probability of re-entry in less than 25 years for objects launched from Kourou at different local times and injected into GTO at different epochs of the year.

The first noteworthy aspect from Figure 7.6, when compared with Figure 6.10 (right), is the change of the shape of the plot when converting from initial RAAN to local time of launch. If one looks at the re-entry probabilities for a given day, such as the 1st of January of 1990, it can be seen that an offset is introduced. However, this offset is not constant throughout the year, which leads from a plot in which the unfavourable conditions follow a diagonal pattern when represented as a function of RAAN to a plot in which these patters are more or less horizontal, meaning that the optimum launch conditions are not strongly dependent on the day of launch. For instance, for launches from Kourou, launches are unfavourable (from a debris-mitigation point of view) for local times approximately between 0 h and 6 h, and between 12 h and 18 h, regardless of the day of the year.

This change in the shape of the lifetime plots, and the fact that the favourable launch time remains constant throughout the year, can be explained by the change of the longitude of the vernal equinox throughout the year, which causes the offset between the local time of launch and the RAAN to vary accordingly on a yearly basis. When the same plot is obtained for a different launch location, the shape of the plot remains the same as that in Figure 7.6, the only difference being a constant offset in the value of the local time of launch, as seen in Figure B.11 (i.e., the contents of the plot move vertically).

However, the fact that the optimum launch times do not depend strongly on the epoch of year does not hold for cases in which a higher inclination is used. For instance, if the initial inclination of the GTO is 30 degrees, the patterns are rather horizontal when represented as a function of RAAN, as was shown in Figure 6.5c, and become rather diagonal when represented as a function of the local time of launch, as seen in Figure B.11.

7.1.4. LIFETIME PREDICTIONS

So far, all the propagations that have been carried out to generate the provided results have started in the past and have run until as far as June 2017. This means that the value for the lifetimes provided in previous sections are not predictions but estimations. However, if the work presented in this Master thesis is to be applied to real missions in the future, it will be necessary to obtain the same kind of results by propagating orbits in the future.

The main difference between performing propagations in the past or in the future resides in the availability of space weather data used for the estimation of the atmospheric density. The other perturbations can be predicted with high accuracy, since Earth's rotational state and the position of the Sun and the Moon are available for future epochs. The main additional source of uncertainty when performing predictions instead of estimations is related to solar activity levels, which affect atmospheric density as discussed in Section 3.2.3. Historically, the value of the solar activity index $F_{10.7}$ has oscillated with a period of roughly 11 years between values of 50 and 250 sfu, with peak values close to 400 for specific dates. However, the value of $F_{10.7}$ cannot be predicted accurately, since the maximum values vary from cycle to cycle. For instance, in the last cycle, the maximum was about 150 sfu, while during 1975-2000, the value of $F_{10.7}$ went above 250 sfu several times.

Thus, it is convenient to have an estimate of the error introduced in the values of the lifetime predictions when the $F_{10.7}$ deviates from the nominal (predicted) conditions. In order to estimate how the actual lifetime would differ from the predicted lifetime when the measured value of $F_{10.7}$ is e.g. twice or half the predicted value used for the simulations, some of the propagations performed to generate the results in previous chapters have been repeated, but the value of $F_{10.7}$ has been artificially modified to simulate the introduction of uncertainty.

Historically predictions for the value of $F_{10.7}$ have not been off by more than −50% or +100%, so the propagations carried out to generate the colour-map plot in Figure 5.9 (right) were run again but with the measured value of $F_{10.7}$ artificially multiplied by 0.5 and 2, leading to slightly different lifetimes. The errors introduced in the value of the lifetime when compared to the case in which the measured value of $F_{10.7}$ is used unmodified are provided in Figure 7.7. As can be seen, large errors in the value of the solar activity index of −50% and +100% are scaled down, respectively, to RMS errors of only 3.7% and 7.0% in the value of the lifetime for resonance-free orbits. This can be explained by the relatively small influence of atmospheric drag in the evolution of GTOs. This was shown in Section 6.1, where the effects of each of the relevant perturbations were analysed separately.

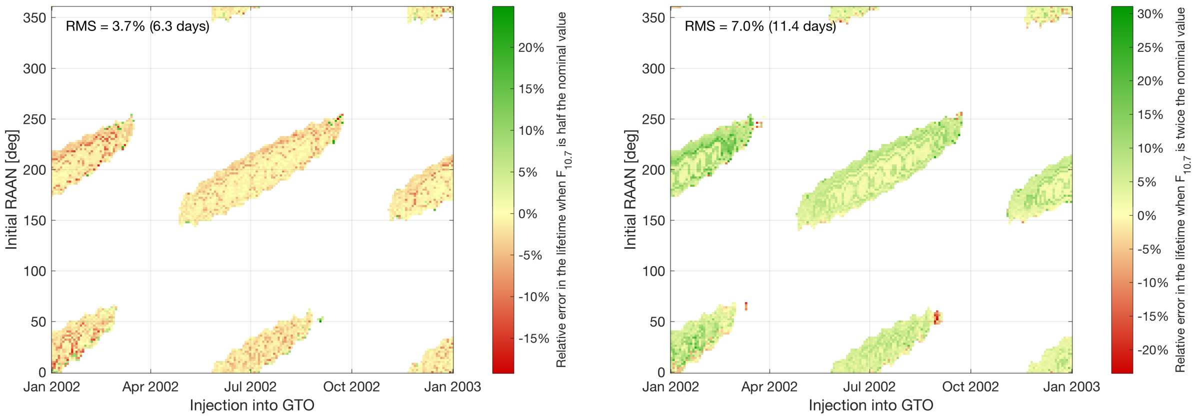

Figure 7.7: Relative errors introduced in the value of the lifetime of a satellite when artificially multiplying the value of $F_{10.7}$ by 0.5 (left) and by 2 (right), as a function of epoch of injection into GTO and initial RAAN, for orbits in resonance-free regions.

The uncertainties in the estimates of the lifetime are similar to (or even smaller than) the ones introduced by the use of the SST propagator when compared to the more accurate Cowell propagator (cf. Section 5.2.2). Additionally, the uncertainties in the NRLMSISE-00 atmosphere model, even when propagations are performed in the past using data from actual measurements, introduces an error of a mere 2.5-3% for resonance-free orbits, as discussed in Section 4.1.2. Thus, it can be concluded that the procedure presented in this Master thesis, in which propagations in the past have been carried out, is also valid for propagations in the future used to obtain lifetime predictions, with the introduction of an additional error that, in the worst-case scenario, will be similar to the error introduced by the use of a propagator based on semi-analytical techniques or by the use of an atmospheric model such as NRLMSISE-00.

7.2. CASE STUDY: LAUNCH FROM THE EUROPEAN SPACEPORT

Now that all the issues that could arise when applying to the obtained results to actual launches to GEO have been addressed, it is possible to provide an example to illustrate how the generated results can be used to recommend launch times complying both with debris-mitigation guidelines and mission-design constraints.

In this section, a case study involving the launch of a satellite to GEO from the European spaceport in Kourou is provided. For this case study, the following assumptions and constraints hold:

- The coordinates of the launch site are 5.36°N 52.76°W.
- The payload will be ready for launch on February 1st, 1990.
- The payload will have to be injected into GEO before the end of February 1990.
- A direct ascent to GEO will be followed.
- There will be a single period of powered flight starting at liftoff and lasting 20 minutes, leading to injection into GTO.
- The satellite is assumed to be at perigee at the moment of injection into GTO.
- The sub-satellite point is assumed to be 120 degrees east of the launch site at injection into GTO.
- The GTO will have an altitude of 200 ± 2 km and an orbital inclination of 8.3 ± 0.5 deg.
- The upper stage, with a mass of $3\,000 \pm 100$ kg and a cross-sectional area of 15 ± 5 m^2, will remain in GTO. The drag and radiation pressure coefficients are assumed to be constant and equal to 2.2 and 1.5, respectively.
- The payload will be injected into a circular phasing orbit slightly below GEO altitude before final injection into GEO.
- The payload has to be injected in a slot in GEO corresponding to a longitude of 200°E.
- To comply with debris-mitigation guidelines, it will have to be shown that the debris left in GTO will re-enter in less than 25 years with a 90% probability. The debris can be assumed to have re-entered when the perigee altitude reaches a value of 100 km.

Then, the question to be answered is:

What are the launch conditions (day and local time of launch) and the altitude of the phasing orbit leading to compliance with all the requirements?

The first step is to determine the longitude of the SSP when the satellite reaches apogee for the first time. Using Eq. (7.1), it is found that:

$$\Lambda_{GEO} \approx \Lambda_{Kourou} + 120° + 101° \approx 168°\text{E} \tag{7.3}$$

The longitude of the assigned slot is 200°E, so the phasing angle is $\Delta\Lambda \approx [200 - 168]_{mod180} = 32$ deg. From here, it is possible to obtain the wait period in the phasing orbit near GEO altitude:

$$T_{wait} = \frac{\frac{\Delta\Lambda}{360°}}{\frac{1}{T} - 1} \tag{7.4}$$

where T is the orbital period of the chosen orbit in sidereal days, and the wait period is also given in sidereal days.

Since the launch has to take place in February, and the slot in GEO has to be reached before the end of February, the maximum wait period is 28 days (or 28.08 sidereal days), leading to a maximum orbital period for the phasing orbit of $T \approx 0.9968$ sidereal days, which corresponds to a maximum altitude of 35 697 km for the phasing orbit, or about 89 km below GEO altitude. Choosing this phasing orbit limits the launch opportunities to just February 1 0:00 AM. Thus, a slightly lower phasing orbit will have to be chosen to have a wider range of launch possibilities. For instance, in order to increase this range to 6 days (which decreases the maximum wait period to 21 days), the phasing orbit has to have an altitude of at least 112 km below GEO. The same can be done for a different range of possible launch days, leading to the plot in Figure 7.8.

Using Figure 7.8, it is possible to fix the altitude of the phasing orbit (and thus the apogee altitude of the GTO) by choosing a launch window. In case that something were to go wrong during the preparations, the launch may have to be delayed. Moreover, the larger the launch window, the larger the probability of finding launch conditions complying with debris-mitigation guidelines. Thus, it has been decided to set the launch

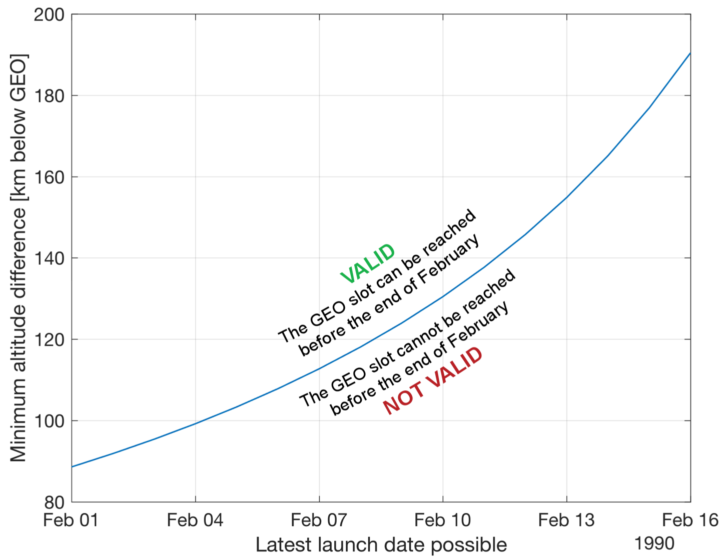

Figure 7.8: Combinations of launch days and altitudes of the phasing orbit leading to reaching the assigned GEO slot before the end of February 1990.

window to 6 days, i.e. the launch will take place between the 1st and the 6th of February (both included). This means that, choosing an altitude for the phasing orbit 112 km below LEO will always lead to reaching the right GEO slot before the end of February, as can be deduced from Figure 7.8. In conclusion, the apogee altitude of the GTO will be 35 674 km and the launch opportunities to be studied will range from February 1st to February 6th.

The next step consists in generating a plot similar to the one provided in Figure 7.6, but only for the first six days of February. Many cases (e.g. 100–200) have to be propagated for each combination of day of injection into GTO (assumed to coincide with the day of launch) and the local time of launch (or initial RAAN), in order to account for deviations in the orbital parameters and body characteristics from the nominal values. The characteristics of the orbit and debris have been chosen to coincide with those used to generate Figure 7.6, so that the information therein can be used for this case study. The only differing parameter is the apogee altitude, which in that case was nominally 35 650 km, and in this case it is 35 674 km. Given the small difference and the fact that the effect of changing the value of the apogee altitude has little influence on the evolution of GTOs (cf. Section 4.2.2), the results from those propagations can be used for this case study as well.

The same results used to generate the plot in Figure 7.6 can be used to obtain a different plot, provided in Figure 7.9, in which the parameter $T_L^{(90\%)}$ introduced in Section 2.2.3 has been represented. This parameter is defined as the period of time since injection into GTO necessary for debris to re-enter with a 90% probability. For instance, a $T_L^{(90\%)}$ of 10 years means that the debris launched under those nominal conditions will have re-entered in 90% of the cases after 10 years, while there is a 10% probability of the debris still being in orbit after that period of time.

Figure 7.9 can be used to immediately discard all combinations of epoch of injection into GTO and local time of launch that would not comply with debris-mitigation guidelines, i.e. those with $T_L^{(90\%)}$ longer than 25 years. Those cases are represented as dark-red pixels in Figure 7.9. All the other cases would comply with debris-mitigation guidelines, although some are more favourable because their $T_L^{(90\%)}$ is shorter.

Also from Figure 7.9 it is possible to provide a rough estimate of the recommended launch times in the first days of February that would lead to compliance with debris-mitigation guidelines. It can be seen that launches from approximately 23:30 to 6:00 and from 11:30 to 17:30 have to be avoided, as the resulting $T_L^{(90\%)}$ would be longer than 25 years. Launches at 9 AM/PM are ideal, as they have some of the lowest $T_L^{(90\%)}$ and correspond to regions in which the lifetime gradient is small, so deviations from the nominal conditions would not lead to significant changes in the value of the lifetime (unless these deviations are very large).

The results from the propagations can be used to generate a plot for each possible launch day in which the probability of re-entry in less than 25 years is provided, such as the one in Figure 7.10 (left) for the 2nd of February.

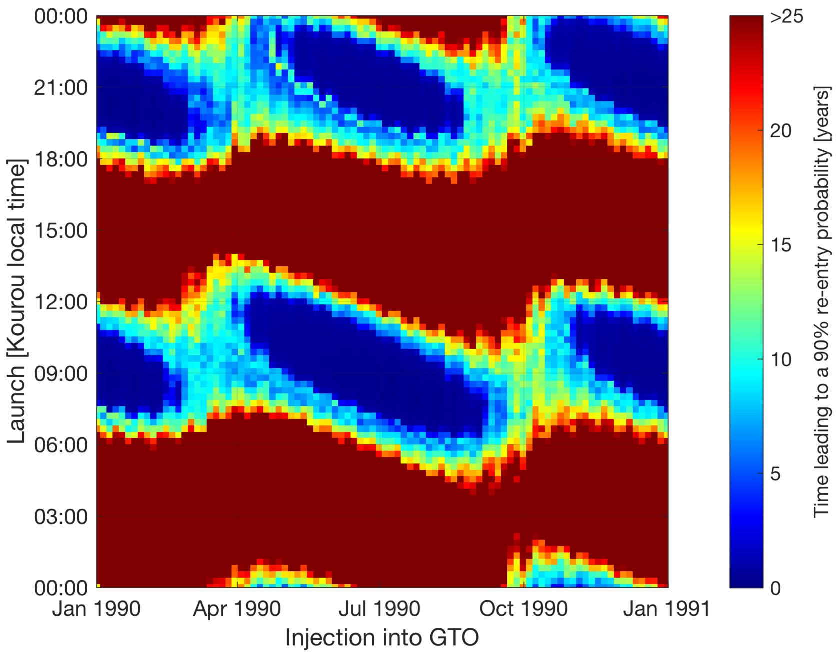

Figure 7.9: Period of time since injection into GTO leading to re-entry with a 90% probability for launches from Kourou at different epochs of year 1990.

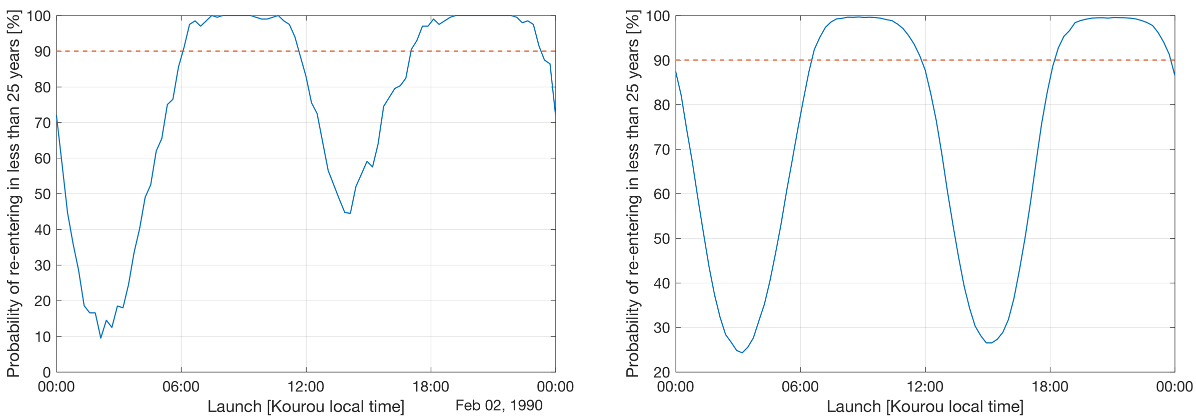

Figure 7.10: Probability of re-entering in less than 25 years as a function of Kourou's local time of launch for objects injected into GTO on 2 February 1990 (left) and yearly mean of 1990 (right). Cases above the 90% dashed lines comply with debris-mitigation guidelines.

Since the lifetimes are not strongly dependent on the day of the year, it is possible to provide an estimate of the probability of complying with debris-mitigation guidelines as a function of Kourou's local time of launch independent from the day of the year. Although for a specific mission a thorough study like the one presented in this section should be carried out, the information provided in Figure 7.10 (right) illustrates that the compliance with debris-mitigation guidelines is highly dependent on the time of launch, and that there are certain moments in the day during which the launch is clearly more favourable.

As already mentioned, for launches from Kourou, the ideal launch time is around 9 AM/PM regardless of the time of the year. For launches to GEO performed using Ariane 5 launcher vehicles in the period 2004-2012 (recall that GEO launches with Ariane 5 were the major contributors to the LEO- and GEO-crossing debris population in GTO generated in the period 2004-2012, accounting for 84% of the total [34]), in 90% of the cases the launch took place after noon [79]. The mean launch time for the afternoon launches was 18:35 local time, with some 78% launches after 18 h. Although these launch times would lead to complying with debris mitigation guidelines for a GTO object with the initial perigee altitude and ballistic coefficient used in this section, the favourable launch window can become narrower for different values of these parameters, so postponing the customary launch time from 18:35 to 21:00 can increase the probability of compliance with debris-mitigation guidelines, regardless of the orbital and body characteristics and the day of the year. If the favourable launch window is wide (e.g. 6 hours), it would be preferable to schedule the launch for the moment at which the window opens (e.g. 18:00), so that if anything were to go wrong, more time would be available for implementing a fix before the window closes.

8

CONCLUSIONS AND RECOMMENDATIONS

In this chapter, the most relevant findings of the Master thesis and recommendations for future research are provided. In Section 8.1, the main conclusions will be provided in the form of answers to the research questions introduced in Section 1.1. Then, in Section 8.2, recommendations for future steps to be taken in order to further research the problem will be given.

8.1. CONCLUSIONS

The research questions outlined in Section 1.1 have been answered during the development of this Master thesis. Those questions are repeated here together with their respective answers.

1. *How can the orbital evolution and lifetime of GTO objects be reliably predicted?*
   (a) *What is the best way to model orbital perturbations to enable fast, yet accurate, long-term propagations?*
   The propagation of GTOs following a numerical approach involves the integration of the equations of motion expressed in Cartesian components representing the osculating state of the satellite. This requires the use of small integration step-sizes (in the order of seconds or minutes) that lead to long computation times when many cases have to be propagated. Obtaining the results discussed in this report following this approach would have taken several years of CPU time. Thus, it is more convenient to approach this problem using semi-analytical techniques, in which equations depending on the mean (equinoctial) elements are integrated instead. In this way, larger integrator step-sizes (generally 1 day for GTOs) can be used, leading to much faster propagations (45 times faster than the numerical approach on average while maintaining proper accuracy). Additionally, given the high sensitivity of the lifetime to initial conditions and body characteristics, a statistical approach has to be followed in order to obtain reliable predictions.
   (b) *What is the accuracy of the lifetime predictions for GTO objects?*
   The accuracy of lifetimes predictions has been assessed for resonance-free orbits, as these are the cases of interest for launcher companies that want to minimise the lifetime of their debris in GTO. The largest uncertainties are related to the computation of atmospheric drag. The main sources are thus the used atmospheric model, the cross-sectional area and the solar activity levels. The NRLMSISE-00 atmosphere model introduces an error of 2.5–3% in the lifetime predictions of resonance-free GTOs, while errors in the solar activity levels predictions are expected to introduce errors no larger than 7%. The error introduced because of the uncertainty in the cross-sectional area of the body will depend on the shape of the body. For a spherical body, the cross-sectional area will be constant, so this parameter will be known precisely. For an elongated body, this parameter can introduce a large error, although using a mean area is accurate if the body is tumbling relatively quickly. In general, it can be said that errors in the atmospheric density or the cross-sectional area are scaled down by a factor of 5 to 6 for lifetime predictions, so in the worst-case scenario, when the body is not tumbling and its cross-sectional area is off by 50% from the mean value used in the propagation, the error introduced in the lifetime would not be larger than 10%. These uncertainties exist both for the numerical and semi-analytical approach. For the latter there

are additional sources of uncertainty, related to the use of mean elements without including the short-period terms. It was found that these errors are around 6–7% for resonance-free GTOs.

2. *How do orbital perturbations affect the evolution of GTO objects?*

   (a) *Which are the most relevant perturbations and which can be neglected?*
   An accurate description of the temporal evolution of objects in GTO over long periods of time (in the order of decades) can be obtained by including the perturbations caused by the zonal terms of the geopotential up to degree 7, the Sun's and the Moon's point-mass gravitational attraction, drag caused by Earth's atmosphere and solar radiation pressure in the acceleration model. Other perturbations, such as those caused by higher-degree or tesseral terms of the geopotential, third bodies other than the Sun or the Moon, Earth's tides or relativistic effects can be neglected without introducing significant errors in the lifetime predictions.

   (b) *How can these perturbations affect the lifetime of GTO objects?*
   The interplay between the relevant orbital perturbations, mainly the Sun's gravity, zonal terms and atmospheric drag, can influence the evolution of objects in GTO drastically, causing changes in the value of the lifetime of several orders of magnitude for the same object and orbit. This is due to the existence of a solar resonance that can be triggered for orbits with a semi-major axis of roughly 15 000 km. Since the semi-major axis of GTOs decreases from 25 000 km until re-entry, GTO objects are susceptible to undergoing this resonance. Whether this resonance will be triggered and how strong its effects will be depends on the relative positions of Earth, the Sun and the orbit itself (inclination and location of the perigee) during the period in which the value of the semi-major axis is close 15 000 km.

   (c) *What is the influence of initial launch conditions, body characteristics and environment-related parameters on the orbital evolution of objects in GTO?*
   The evolution of objects in GTO is very sensitive to initial launch conditions, namely the launch epoch and initial orbital state. For the same object and orbital parameters, the lifetime of an object can change by several orders of magnitude by varying the initial epoch. This evolution is also very sensitive to the initial perigee altitude, inclination, RAAN and argument of perigee of the GTO. On the other hand, the sensitivity to changes in the values of the apogee altitude and true anomaly is much more limited. The body characteristics and environment-related parameters have an influence on the effect that drag and SRP have on the orbital evolution. Since these perturbations have a relatively small influence on the orbital evolution, sensitivity to changes in the values of the body mass, cross-sectional area, C_D, C_R or solar radiation levels is relatively small (when compared to other parameters such as initial epoch). However, these changes are generally not negligible.

   (d) *What are the main sources of uncertainty in the lifetime predictions?*
   Earth's rotational state and the position of the Sun and the Moon are known very accurately for future epochs, so the perturbations caused by zonal terms of the geopotential and third-body attraction do not introduce significant uncertainties in lifetime predictions. The main source of uncertainty is related to the estimation of the atmospheric density for the computation of drag and to the cross-sectional area of the orbiting body, as this will depend on its attitude, which in general is difficult (or impossible) to predict, having to rely on the use of a mean area. Even the most accurate atmospheric models, such as NRLMSISE-00, provide values for the atmospheric density with uncertainties of around 15%, when running propagations in the past using data from actual measurements. When propagations have to be carried out in the future, in order to obtain lifetime predictions, this uncertainty increases due mainly to the inaccuracy of the solar activity index predictions, which affects the value of the atmospheric density.

   (e) *What are the launch conditions that lead to the shortest lifetimes?*
   As could be expected, bodies with larger ballistic coefficients (larger area and/or smaller mass), larger C_D, or in orbits with lower initial perigee altitude, have generally shorter lifetimes. However, this only holds for orbits that do not undergo solar resonance. For orbits affected by solar resonance, counter-intuitive effects are observed, so an object with e.g. a larger C_D can take longer to re-enter than an object with a smaller C_D launched under the same conditions into the same orbit. The sensitivity to initial conditions is so high that it is not possible to reliably predict the lifetime of objects in GTO following a deterministic approach; instead, several cases with parameters slightly deviating from nominal conditions have to be propagated and then it is possible to

find the lifetime leading to re-entry with e.g. a 90% probability. When this is done, the optimal launch conditions from a debris-mitigation point of view depend on the launch site and launch time (day of the year and local time). For launches from the Centre Spatial Guaynais' launch site in Kourou, the shortest lifetimes are achieved for launches around 9 AM/PM local time, with slight variations undergone throughout the year and very strong variations undergone throughout the day.

After having answered all the subquestions laid out in Section 1.1, it is possible to provide an answer to the main research question:

How can orbital perturbations be used to comply with debris-mitigation guidelines for future geostationary transfer orbit objects?

In this Master thesis, it has been found that the lifetimes of objects in GTO can only be predicted reliably when they do not undergo solar resonance; otherwise, their lifetime is very sensitive to initial conditions, body characteristic and environment-related parameters. Small deviations in these parameters from the nominal values used in the propagation can be scaled up by several orders of magnitude for GTOs undergoing solar resonance, leading in some cases to counter-intuitive effects, such as the fact that an actual atmospheric drag larger than the one predicted in the propagations can lead to a slower decay.

Although a solar resonance can introduce a quasi-secular decrease of the perigee altitude, leading to a fast re-entry, the extremely large sensitivity to initial conditions makes it impossible to exploit it reliably, i.e. launching under conditions prone to leading to undergoing solar resonance will result in a lifetime that can range from months to decades, and the actual lifetime cannot be predicted given the several sources of uncertainty in the model. Consequently, cases experiencing solar resonance should be avoided and the focus should be put on cases whose lifetime is less sensitive to initial conditions and body and environment characteristics. Accordingly, when following a deterministic approach, the study was limited to resonance-free cases in order to obtain reliable predictions about the lifetime of objects in GTO. For launches from Kourou using a GTO with perigee altitude of 200 km, it was found that the launch has to take place around 9 AM/PM and the months of March, April, September and October should be avoided, for a representative GTO object with a ballistic coefficient of 0.011 m^2/kg. Under those conditions, the lifetimes are generally shorter than one year and the lifetime gradients are small, so deviations from the nominal conditions do not lead to lifetimes differing significantly from the predicted values.

Debris-mitigation guidelines specify a limit of 25 years for the lifetime with a 90% probability, i.e. the launch company should be able to prove that the generated debris will re-enter Earth's atmosphere in less than 25 years in 90% of the propagated cases in which the values of the relevant parameters are modelled to account for the existence of expectable uncertainties. Thus, restricting the launch options to orbits that will never undergo resonance and that will have lifetimes shorter than one year may result in narrow launch windows from which cases that would actually comply with debris-mitigation guidelines are excluded. For that reason, the problem had to be studied following a statistical approach that can provide reliable information even for cases affected by solar resonance. Using the results of thousands of orbital perturbations, it was shown that for launches from Kourou using a GTO with a nominal perigee altitude of 200 km, it will not be possible to comply with debris-mitigation guidelines for objects with a ballistic coefficient of 0.011 m^2/kg when launching from 0 to 6 h or from 12 to 18 h local time. These are just approximate figures that change slightly throughout the year; the exact numbers can be inferred from the colour-map plot provided in Figure 7.9 for year 1990, and the same approach can be followed for future launches with different orbital and body characteristics. It was found that the most favourable conditions are found approximately at the middle of the intervals, i.e. around 9 AM/PM local time, and that changing the initial perigee altitude and/or ballistic coefficient affects the width of the launch window complying with debris-mitigation guidelines but has little influence on the optimal launch time. Thus, regardless of the orbital and body characteristics, it will always be more advantageous to launch at around 9 AM/PM. However, from a logistical point of view, it will be preferable to schedule the launch for the moment at which the window opens, so that if anything were to go wrong, more time would be available in order to implement a fix before the window closes.

To sum up, the elements necessary to provide proof of compliance with debris-mitigation guidelines for objects in GTO within feasible computation times are:

- A perturbation model including at least:
  - Zonal terms of the geopotential up to degree 7.

  - The Sun's and the Moon's point-mass gravitational attraction.
  - Earth's atmospheric drag using the NRLMSISE-00 model.
  - Solar radiation pressure (eclipses can be neglected).

- A propagator based on semi-analytical techniques in which the mean equinoctial elements are integrated with large step-sizes, in the order of one day.

- A statistical approach in which many cases slightly deviating from the nominal conditions are propagated in order to be able to obtain the probability of re-entry in less than a specified amount of time.

8.2. RECOMMENDATIONS AND FUTURE STEPS

One of the main tasks to be carried out in future research is the enhancement of the developed SST propagator by introducing all the short-period terms. Then, the consequences of including short-period terms for the accuracy of the lifetime predictions and computation times should be assessed. If, when compared to the SST propagator without short-period terms, the introduced error (taking as a reference the results of the numerical approach) can be significantly reduced while still maintaining competitive computation times, future studies should be carried out with this improved propagator.

Another important aspect is to assess the accuracy of the SST propagator (compared to the Cowell propagator) when following the statistical approach. In this Master thesis, this assessment has been performed only for the deterministic approach, leading to the conclusion that the lifetime predictions are reliable only for resonance-free orbits. However, it is not known if the SST propagator is reliable for the other cases when the statistical approach is followed. The main limitation when carrying out this assessment is the time required to obtain the reference data to which the SST propagator has to be compared to. Obtaining a colour-map plot like the one in Figure 6.8 but with the Cowell propagator would have taken almost one year (when using 14 CPUs on the Eudoxos server continuously).

In this Master thesis, the results have been applied to launches from Kourou with Ariane rockets using a direct ascent to GEO. However, there are many other possible ascent profiles and launch sites. In the future, it may be interesting to study whether the results obtained in this thesis can be used to minimise the lifetime of debris generated by other launchers that follow a different ascent strategy. Additionally, it will be necessary to obtain and use predictions for the solar activity index if propagations have to be run for future epochs. During this thesis, all the propagations were stopped before June 2017 because no information on solar activity index predictions was available in Tudat.

There is another possible approach when performing propagations in the future, as discussed in [49]. This method is based on determining an equivalent $F_{10.7}$ valid for a period of interest (e.g. the 25 years during which the propagation will take place) computed using values from solar activity data predictions. Then, this equivalent $F_{10.7}$ can be used as a constant solar activity index for all the propagations performed in that period. The equivalent $F_{10.7}$ would be obtained following an iterative procedure in which several values are tested until one of them leads to the same lifetime prediction than the use of the variable $F_{10.7}$ for a representative GTO in the period of interest. In the future it will be interesting to study whether this approach can be useful for performing propagations in future epochs more efficiently.

Furthermore, it may be interesting to study whether it is possible to reduce the lifetime of debris in GTO (and thus widen the launch opportunities complying with debris-mitigation guidelines) by using e.g. a solar sail or choosing lower perigee altitudes for the GTO used to bring the payload to GEO. It will be necessary to assess the consequences that this would have from a mission-design point of view.

Finally, generating plots for launches in the next e.g. 5 years for different initial inclinations, initial perigee altitudes and ballistic coefficients may be useful, as they could be readily used by launch companies at early stages of mission design in order to discard combinations of parameters and launch epochs that would lead to the generation of debris in non-compliant orbits. As this would be computationally expensive, the following approach could be followed:

1. Study a single launch location, which will result in a fixed value for the initial inclination (e.g. for Kourou an inclination of about 6-7 degrees could be used).

2. Generate (for each year of interest) a low-resolution plot in which the percentage of time for which compliance with debris mitigation guidelines can be achieved, is mapped as a function of perigee altitude and ballistic coefficient, to be used at early stages of mission design. For instance, the colour-map

plot in Figure 7.9, valid for h_p = 200 km and B = 0.011 m^2/kg, would translate into a single value (52.5%, i.e. the percentage of cases having an $L_T^{(90\%)}$ shorter than 25 years). A lower resolution could be used at this point, as only a yearly value, and not the lifetime for each case, would be used.

3. Generate higher-resolution plots, in which the range of studied initial perigee altitudes and ballistic coefficients is reduced (and the grid-size increased) for the relevant month(s). These plots could be used at later stages of design when the launch date (requested by the customer) has been narrowed down to just a few weeks. These plots would be used to ensure that the selected values for h_p and B will not lead to a percentage of launch options complying with debris mitigation guidelines that is too low, which would mean in practice very narrow launch windows (for instance, when the yearly or monthly compliance is 50%, the favourable launch windows have a width of about 6 hours each).

4. Once all the parameters and day of launch have been fixed, it will be possible to determine the ideal launch time and width of the launch window by performing a full analysis similar to the one presented in Section 7.2. At this point, a finer resolution can be used for the initial RAAN (or local time of launch), and also for the day of launch if there are still several candidate days for the launch.

Although steps 3 and 4 are mission-specific, the results generated in step 2 would be of high scientific relevance, as they could be used in order to perform quick studies at early stages of mission design for future GEO launches, without the need to perform computationally expensive tasks for each and every mission.

Bibliography

[1] International Astronomical Union, *Resolution B2 on the re-definition of the astronomical unit of length,* International Astronomical Union, ed. (31 August 2012) (2012).

[2] Penrose, R., *The Road to Reality: A Complete Guide to the Laws of the Universe,* Vintage Books (2004).

[3] US National Institute of Standards and Technology, *CODATA Value: Newtonian constant of gravitation,* The NIST Reference on Constants, Units, and Uncertainty (2014).

[4] USNOUKHO, *2016 Selected Astronomical Constants,* The Astronomical Almanac Online (2016).

[5] Wikipedia, *Standard gravitational parameter,* Available online: https://en.wikipedia.org/wiki/Standard_gravitational_parameter (), accessed 20 June 2017.

[6] National Research Council, *Orbital Debris: A Technical Assessment* (The National Academies Press, Washington, DC, 1995).

[7] M. Mutyalarao and R. K. Sharma, *On prediction of re-entry time of an upper stage from GTO,* Advances in Space Research **47**, 1877 (2011).

[8] R. Sharma, P. Bandyopadhyay, and V. Adimurthy, *Consideration of lifetime limitation for spent stages in GTO,* Advances in Space Research **34**, 1227 (2004).

[9] A. Lamy, C. L. Fevre, and B. Sarli, *Analysis of geostationary transfer orbit long term evolution and lifetime,* Journal of Aerospace Engineering, Sciences and Applications **IV**, 12 (2012).

[10] P. Srongprapa, *Mapping the Effects of Earth's Gravity Field on the Orbit Propagation of GTO Spacecraft. A study within the context of passive de-orbiting through the use of perturbations,* Master's thesis, Delft University of Technology (2015).

[11] V. Morand, C. L. Fèvre, A. Lamy, H. Fraysse, and F. Deleflie, *Dynamical properties of Geostationary Transfer Orbits over long time scales: consequences for mission analysis and lifetime estimation,* AIAA/AAS Astrodynamics Specialist Conference, Guidance, Navigation, and Control and Co-located Conferences (2012).

[12] C. Colombo, *Long-Term Evolution of Highly-Elliptical Orbits: Luni-solar perturbation effects for stability and re-entry,* 25th AAS/AIAA Space Flight Mechanics Meeting (2015).

[13] CNES, *STELA User's Guide,* Available online: https://logiciels.cnes.fr/sites/default/files/Stela-User-Manual_3.pdf (Version 3.0, November 2015), accessed 18 May 2016.

[14] D. A. Danielson, C. P. Sagovac, B. Neta, and L. W. Early, *Semianalytic Satellite Theory* (Mathematics Department of the Naval Postgraduate School, Monterey, CA, 1995).

[15] P. A. Slann, *Space debris and the need for space traffic control,* Space Policy **30**, 40 (2014).

[16] ESA, *About space debris,* Available online: http://www.esa.int/Our_Activities/Operations/Space_Debris/About_space_debris (2013), accessed 11 May 2016.

[17] Space Debris Subcommittee of the International Academy of Astronautics, *Position paper on orbital debris,* Available online: https://iaaweb.org/iaa/Studies/orbitaldebris.pdf (1999), accessed 11 May 2016.

[18] NASA, *Orbital Debris FAQs,* Available online: http://orbitaldebris.jsc.nasa.gov/faqs.html#8 (2012), accessed 11 May 2016.

[19] D. J. Kessler and B. G. Cour-Palais, *Collision frequency of artificial satellites: The creation of a debris belt,* Journal of Geophysical Research: Space Physics **83**, 2637 (1978).

[20] M. Shan, J. Guo, and E. Gill, *Review and comparison of active space debris capturing and removal methods,* Progress in Aerospace Sciences **80**, 18 (2016).

[21] ESA, *SP-1301 Position paper on space debris mitigation,* Available online: http://www.esa.int/esapub/sp/sp1301/sp1301.pdf (2005), accessed 11 May 2016.

[22] US Government, *Orbital debris mitigation standard practices,* Available online: http://orbitaldebris.jsc.nasa.gov/library/usg_od_standard_practices.pdf, accessed 11 May 2016.

[23] United Nations Office for Outer Space Affairs, *Space debris mitigation guidelines of the Comitee on the Peaceful Uses of Outer Space,* Available online: http://orbitaldebris.jsc.nasa.gov/library/Space%20Debris%20Mitigation%20Guidelines_COPUOS.pdf (2010), accessed 11 May 2016.

[24] Inter-Agency Space Debris Coordination Committee, *Space debris mitigation guidelines,* Available online: http://www.unoosa.org/documents/pdf/spacelaw/sd/IADC-2002-01-IADC-Space_Debris-Guidelines-Revision1.pdf (2007), accessed 11 May 2016.

[25] J.-C. Liou and N. L. Johnson, *Risks in space from orbiting debris,* Science **311**, 340 (2006).

[26] Center for Space Standards & Innovation, *Satcat boxscore,* Available online: http://www.celestrak.com/satcat/boxscore.asp, accessed 11 May 2016.

[27] ESA, *Analysis and prediction of space debris,* Available online: http://www.esa.int/Our_Activities/Operations/Space_Debris/Analysis_and_prediction (2013), accessed 11 May 2016.

[28] L. Anselmo, A. Rossi, and C. Pardini, *Updated results on the long-term evolution of the space debris environment,* Advances in Space Research **23**, 201 (1999).

[29] Wikipedia, *Highly elliptical orbit,* Available online: https://en.wikipedia.org/wiki/Highly_elliptical_orbit (2016), accessed 12 May 2016.

[30] R. Armellin, J. F. San-Juan, and M. Lara, *End-of-life disposal of high elliptical orbit missions: The case of INTEGRAL,* Advances in Space Research **56**, 479 (2015), Advances in Asteroid and Space Debris Science and Technology.

[31] Union of Concerned Scientists, *UCS Satellite Database,* Available online: http://www.ucsusa.org/nuclear-weapons/space-weapons/satellite-database#.VzSOeWPUmRt, accessed 12 May 2016.

[32] D. Ilcev, *Highly elliptical orbits (HEO),* Available online: http://www.ee.co.za/article/is-marine-144-08-highly-elliptical-orbits-heo.html, accessed 12 May 2016.

[33] J. R. Wertz, *Orbit & Constellation Design & Management* (Space Technology Library, 2009).

[34] S. Fisher and E. David, *Debris creation in geostationary transfer orbits: A review of launch practices 2004-2012,* Accessed 12 May 2016.

[35] C. Colombo, E. M. Alessi, W. van der Weg, S. Soldini, F. Letizia, M. Vetrisano, M. Vasile, A. Rossi, and M. Landgraf, *End-of-life disposal concepts for libration point orbit and highly elliptical orbit missions,* Acta Astronautica **110**, 298 (2015), Dynamics and Control of Space Systems.

[36] E. Alessi, A. Rossi, G. Valsecchi, L. Anselmo, C. Pardini, C. Colombo, H. Lewis, J. Daquin, F. Deleflie, M. Vasile, F. Zuiani, and K. Merz, *Effectiveness of GNSS disposal strategies,* Acta Astronautica **99**, 292 (2014).

[37] ESA, *Requirements on space debris mitigation for ESA projects,* Available online: http://www.iadc-online.org/References/Docu/ESA%20Requirements%20for%20Space%20Debris%20Mitigation.pdf (2009), accessed 12 May 2016.

[38] Space-Track.org, *Satellite-tracking data,* Available online: https://www.space-track.org/, accessed 8 June 2017.

[39] K. F. Wakker, *Fundamentals of Astrodynamics* (Faculty of Aerospace Engineering, Delft University of Technology, 2015).

[40] Wikipedia, *Cartesian coordinate system,* Available online: https://en.wikipedia.org/wiki/Cartesian_coordinate_system (2016), accessed 15 May 2016.

[41] Wikipedia, *Orbital elements,* Available online: https://en.wikipedia.org/wiki/Orbital_elements (2016), accessed 15 May 2016.

[42] O. Montenbruck and E. Gill, *Satellite Orbits. Models, Methods and Applications* (Springer-Verlag Berlin Heidelberg, 2000).

[43] T. Narumi and T. Hanada, *New orbit propagator to be used in orbital debris evolutionary models,* Memoirs of the Faculty of Engineering, Kyushu University **67**, 235 (2007).

[44] V. Morand, A. Caubet, F. Deleflie, J. Daquin, and H. Fraysse, *Semi analytical implementation of tesseral harmonics perturbations for high eccentricity orbits,* CNES Conference Papers (2016).

[45] B. Tapley, J. Ries, S. Bettadpur, D. Chambers, M. Cheng, F. Condi, B. Gunter, Z. Kang, P. Nagel, R. Pastor, T. Pekker, S. Poole, and F. Wang, *GGM02 – An improved Earth gravity field model from GRACE,* Journal of Geodesy **79**, 467 (2005).

[46] Physical Oceanography Distributed Active Archive Center, *UT/CSR weekly 5x5 gravity harmonics from November 1992 to May 2011,* Available online: http://go.nasa.gov/28XpSVU, accessed 18 May 2016.

[47] C. Jekeli, *Potential Theory and Static Gravity Field of the Earth* (Elsevier B.V., 2007).

[48] J. Vinti, G. Der, and A. Bonavito, *Progress in Astronautics and Aeronautics* (American Institute of Aeronautics and Astronautics, 1998).

[49] C. Le Fevre, V. Morand, H. Fraysse, F. Deleflie, P. Mercier, A. Lamy, and C. Cazaux, *Long term orbit propagation techniques developed in the frame of the French Space Act,* Proceedings of the 5th IAASS Conference A Safer Space for Safer World (2012).

[50] Community Coordinated Modeling Center, *NRLMSISE-00 Atmosphere Model,* Available online: http://ccmc.gsfc.nasa.gov/modelweb/models/nrlmsise00.php (2016), accessed 26 May 2016.

[51] Community Coordinated Modeling Center, *International Reference Ionosphere – IRI-2007 ,* Available online: http://ccmc.gsfc.nasa.gov/modelweb/models/iri_vitmo.php (2016), accessed 26 May 2016.

[52] NASA, *Solar Cycle Prediction,* Available online: http://solarscience.msfc.nasa.gov/predict.shtml, accessed 17 June 2016.

[53] P. Fortescue, J. Stark, and G. Swinerd, *Spacecraft Systems Engineering* (Wiley, 1995).

[54] Y. Kozai, *Effects of the tidal deformation of the earth on the motion of close earth satellites,* Publications of the Astronomical Society of Japan **17**, 395 (1965).

[55] D. P. McKinley, *Long term mean local time of the ascending node prediction,* NASA Technical Documents (2007).

[56] TU Delft, *Tudat Wiki,* Available online: http://tudat.tudelft.nl/projects/tudat/wiki, accessed 22 June 2016.

[57] MathWorks, *MATLAB – The Language of Technical Computing,* Available online: http://nl.mathworks.com/products/matlab/ (2016), accessed 22 June 2016.

[58] O. Tange, *GNU Parallel – The Command-Line Power Tool,* The USENIX Magazine , 42 (2011).

[59] Wikipedia, *Geostationary orbit,* Available online: https://en.wikipedia.org/wiki/Geostationary_orbit (), accessed 12 June 2017.

[60] Royal Belgian Institute for Space Aeronomy, *Atmosphere model uncertainties and limitations,* Available online: https://www.spenvis.oma.be/ecss/e_st_10_04c/ecss_18_05_00.htm, accessed 1 February 2017.

[61] R. Noomen, *AE4-878 Mission Geometry & Orbit Design Lecture Notes: Integrators,* Available online on Blackboard (2015), version 4-7, accessed 17 June 2016.

[62] Wikipedia, *Euler method,* Available online: https://en.wikipedia.org/wiki/Euler_method (2016), accessed 17 June 2016.

[63] Wikipedia, *List of Runge-Kutta methods,* Available online: https://en.wikipedia.org/wiki/List_of_Runge-Kutta_methods (2016), accessed 24 June 2016.

[64] M. Salih, *Goeken-Johnson sixth-order Runge-Kutta method,* J. Edu. & Sci. **24** (2011).

[65] M. van Kints, *Optimization of Super-Geostationary Disposal Orbits*, Master's thesis, Delft University of Technology (2005).

[66] J. Dormand and P. Prince, *A family of embedded Runge-Kutta formulae,* Journal of Computational and Applied Mathematics **6**, 19 (1980).

[67] C. Velez and A. Fuchs, *A review of averaging techniques and their application to orbit determination systems,* 12th Aerospace Sciences Meeting, Aerospace Sciences Meetings (1974).

[68] D. J. Fonte, *Implementing a 50x50 gravity field model in an orbit determination system,* Department of Aeronautics and Astronautics, Massachussets Institute of Technology (1993).

[69] Wikipedia, *Two-line element set,* Available online: https://en.wikipedia.org/wiki/Two-line_element_set (2016), accessed 16 May 2016.

[70] E. Doornbos and K. Cowan, *AE4-874-II Astrodynamics II Lecture Notes,* Available online on Blackboard (2016), accessed 26 June 2016.

[71] C. Früh and T. Schildknecht, *Accuracy of two-line-element data for geostationary and high-eccentricity orbits,* Journal of Guidance, Control, and Dynamics **35** (2012).

[72] Wikipedia, *Thaicom 6,* Available online: https://en.wikipedia.org/wiki/Thaicom_6 (), accessed 9 June 2017.

[73] Wikipedia, *AsiaSat 8,* Available online: https://en.wikipedia.org/wiki/AsiaSat_8 (), accessed 9 June 2017.

[74] Wikipedia, *TurkmenSat 1,* Available online: https://en.wikipedia.org/wiki/TurkmenSat_1 (), accessed 9 June 2017.

[75] R. Frost, *Quora: How does one launch satellites into a geostationary orbit?* Available online: https://www.quora.com/How-does-one-launch-satellites-into-a-geostationary-orbit, accessed 13 January 2017.

[76] P. Blau, *Intelsat Launch Updates – Sea Launch,* Available online: http://www.spaceflight101.net/intelsat-19-launch-updates.html, http://www.spaceflight101.net/intelsat-27-launch-updates.html (), accessed 9 June 2017.

[77] Wikipedia, *Hohmann transfer orbit,* Available online: https://en.wikipedia.org/wiki/Hohmann_transfer_orbit (), accessed 28 June 2017.

[78] Wikipedia, *Delta-v budget,* Available online: https://en.wikipedia.org/wiki/Delta-v_budget (), accessed 28 June 2017.

[79] P. Blau, *List of Ariane launches since 2000,* Available online: https://en.wikipedia.org/wiki/List_of_Ariane_launches_(20102019), https://en.wikipedia.org/wiki/List_of_Ariane_launches_(20002009) (), accessed 13 June 2017.

[80] Wikipedia, *Rotation matrix,* Available online: https://en.wikipedia.org/wiki/Rotation_matrix#In_three_dimensions (2016), accessed 13 June 2016.

[81] N. A. Eismont, A. V. Ditrikh, G. Janin, V. K. Karrask, K. Clausen, A. I. Medvedchikov, S. V. Kulik, N. A. Vtorushin, and N. I. Yakushin, *Orbit design for launching INTEGRAL on the Proton/Block-DM launcher,* Astronomy & Astrophysics **411**, L37 (2003).

[82] Wikipedia, *Bessel function,* Available online: https://en.wikipedia.org/wiki/Bessel_function (2016), accessed 27 May 2016.

[83] Wikipedia, *Gamma function,* Available online: https://en.wikipedia.org/wiki/Gamma_function (2016), accessed 27 May 2016.

A

Astrodynamics

A.1. Frame transformations

A.1.1. Rotation matrices

The rotation matrices that rotate a vector an angle α about the X, Y and Z axes are given by [80]:

$$R_X(\alpha) = \begin{bmatrix} 1 & 0 & 0 \\ 0 & \cos\alpha & -\sin\alpha \\ 0 & \sin\alpha & \cos\alpha \end{bmatrix} \tag{A.1}$$

$$R_Y(\alpha) = \begin{bmatrix} \cos\alpha & 0 & \sin\alpha \\ 0 & 1 & 0 \\ -\sin\alpha & 0 & \cos\alpha \end{bmatrix} \tag{A.2}$$

$$R_Z(\alpha) = \begin{bmatrix} \cos\alpha & -\sin\alpha & 0 \\ \sin\alpha & \cos\alpha & 0 \\ 0 & 0 & 1 \end{bmatrix} \tag{A.3}$$

A.1.2. Cartesian components and Keplerian elements

The procedures and equations presented in this section have been obtained from [33].

Transformation from Cartesian components to Keplerian elements

First, the following parameters have to be determined:

$$\begin{aligned} &\boldsymbol{r} = [x, y, z]^T; \quad r = \|\boldsymbol{r}\| \\ &\boldsymbol{V} = [v_x, v_y, v_z]^T; \quad V = \|\boldsymbol{V}\| \\ &\boldsymbol{w} = \boldsymbol{r} \times \boldsymbol{V} = [w_x, w_y, w_z]^T; \quad w = \|\boldsymbol{w}\| \\ &\boldsymbol{N} = [0, 0, 1]^T \times \boldsymbol{w} = [N_x, N_y, N_z]^T; \quad N_{xy} = \sqrt{N_x^2 + N_y^2} \end{aligned} \tag{A.4}$$

with $\boldsymbol{V}$ the velocity vector of the orbiting body with respect to the central body and $\boldsymbol{w}$ the specific relative angular momentum vector.

Then, the Keplerian elements can be obtained from:

$$
\begin{aligned}
a &= \frac{1}{\frac{2}{r} - \frac{V^2}{\mu}} \\
\boldsymbol{e} &= \frac{\boldsymbol{V} \times \boldsymbol{w}}{\mu} - \hat{\boldsymbol{r}}; \quad e = \|\boldsymbol{e}\| \\
i &= \arccos \frac{w_z}{w} \\
\Omega &= \operatorname{atan2}\left(\frac{N_y}{N_{xy}}, \frac{N_x}{N_{xy}}\right) \\
\omega &= \operatorname{sign}\left((\hat{\boldsymbol{N}} \times \boldsymbol{e}) \cdot \boldsymbol{w}\right) \arccos\left(\hat{\boldsymbol{e}} \cdot \hat{\boldsymbol{N}}\right) \\
f &= \operatorname{sign}\left((\boldsymbol{e} \times \boldsymbol{r}) \cdot \boldsymbol{w}\right) \arccos\left(\hat{\boldsymbol{r}} \cdot \hat{\boldsymbol{e}}\right)
\end{aligned}
\tag{A.5}
$$

where the notation $\hat{\boldsymbol{r}} = \frac{\boldsymbol{r}}{r}$ is used to denote normalised vectors.

Finally, if one is interested in the values of the eccentric anomaly or the mean anomaly, those can be obtained from:

$$
E = 2\arctan\left(\sqrt{\frac{1-e}{1+e}} \tan\frac{f}{2}\right) \tag{A.6}
$$

$$
M = E - e\sin E \tag{A.7}
$$

TRANSFORMATION FROM KEPLERIAN ELEMENTS TO CARTESIAN COMPONENTS

The first step is to compute the following parameters:

$$
\begin{aligned}
l_1 &= \cos\Omega\cos\omega - \sin\Omega\sin\omega\cos i \\
l_2 &= -\cos\Omega\sin\omega - \sin\Omega\cos\omega\cos i \\
m_1 &= \sin\Omega\cos\omega + \cos\Omega\sin\omega\cos i \\
m_2 &= -\sin\Omega\sin\omega + \cos\Omega\cos\omega\cos i \\
n_1 &= \sin\omega\sin i \\
n_2 &= \cos\omega\sin i \\
H &= \sqrt{\mu a(1-e^2)} \\
r &= \frac{a(1-e^2)}{1+e\cos f}
\end{aligned}
\tag{A.8}
$$

where H is the magnitude of the specific relative angular momentum and r is the radial distance from the centre of mass of the central body to the orbiting body.

Finally, the following matrix equations can be used in order to obtain the position $(x, y, z)^T$ and the velocity $(v_x, v_y, v_z)^T$:

$$
\begin{pmatrix} x \\ y \\ z \end{pmatrix} = \begin{pmatrix} l_1 & l_2 \\ m_1 & m_2 \\ n_1 & n_2 \end{pmatrix} \begin{pmatrix} r\cos f \\ r\sin f \end{pmatrix} \tag{A.9}
$$

$$
\begin{pmatrix} v_x \\ v_y \\ v_z \end{pmatrix} = \frac{\mu}{H} \begin{pmatrix} l_1 & l_2 \\ m_1 & m_2 \\ n_1 & n_2 \end{pmatrix} \begin{pmatrix} -\sin f \\ e+\cos f \end{pmatrix} \tag{A.10}
$$

A.1.3. CARTESIAN COMPONENTS AND EQUINOCTIAL ELEMENTS

The procedures and equations presented in this section have been obtained from [14].

TRANSFORMATION FROM CARTESIAN COMPONENTS TO EQUINOCTIAL ELEMENTS

The first step is to compute the angular momentum vector from Eq. (A.4-3) and using it to determine the parameters p and q from:

$$
\begin{aligned}
p &= \frac{w_x}{1+w_z} \\
q &= -\frac{w_y}{1+w_z}
\end{aligned}
\tag{A.11}
$$

which are then used to determine the reference frame basis vectors $\boldsymbol{f}$ and $\boldsymbol{g}$ from Eq. (A.18-1) and Eq. (A.18-2).

Next, after obtaining the eccentricity vector from Eq. (A.5-2), the parameters h and k can be found:

$$\begin{aligned} h &= \boldsymbol{e}\cdot\boldsymbol{g} \\ k &= \boldsymbol{e}\cdot\boldsymbol{f} \end{aligned} \tag{A.12}$$

Then, the following two parameters are introduced:

$$X = \boldsymbol{r}\cdot\boldsymbol{f} \tag{A.13}$$

$$Y = \boldsymbol{r}\cdot\boldsymbol{g} \tag{A.14}$$

The following step is to compute the eccentric longitude from:

$$\begin{aligned} \sin F &= h + \frac{(1-h^2 b)Y - hkbX}{a\sqrt{1-h^2-k^2}} \\ \cos F &= k + \frac{(1-k^2 b)X - hkbY}{a\sqrt{1-h^2-k^2}} \end{aligned} \tag{A.15}$$

where

$$b = \frac{1}{1+\sqrt{1-h^2-k^2}} \tag{A.16}$$

Finally, a is obtained from Eq. (A.5-1) and the mean longitude from the equinoctial form of Kepler's equation:

$$\lambda = F + h\cos F - k\sin F \tag{A.17}$$

TRANSFORMATION FROM EQUINOCTIAL ELEMENTS TO CARTESIAN COMPONENTS

The first step is to compute the equinoctial reference frame basis vectors ($\boldsymbol{f}$, $\boldsymbol{g}$, $\boldsymbol{w}$), whose components in (x, y, z) are given by:

$$\begin{aligned} \boldsymbol{f} &= \frac{1}{1+p^2+q^2}\begin{pmatrix} 1-p^2+q^2 \\ 2pq \\ -2p \end{pmatrix} \\ \boldsymbol{g} &= \frac{1}{1+p^2+q^2}\begin{pmatrix} 2pq \\ 1+p^2-q^2 \\ 2q \end{pmatrix} \\ \boldsymbol{w} &= \frac{1}{1+p^2+q^2}\begin{pmatrix} 2p \\ -2q \\ 1-p^2-q^2 \end{pmatrix} \end{aligned} \tag{A.18}$$

Next, the eccentric and true longitudes, F and L, have to be found. The eccentric longitude is obtained by solving Eq. (A.17). Then, the true longitude is computed from:

$$\begin{aligned} \sin L &= \frac{(1-k^2 b)\sin F + hkb\cos F - h}{1 - h\sin F - k\cos F} \\ \cos L &= \frac{(1-h^2 b)\cos F + hkb\sin F - k}{1 - h\sin F - k\cos F} \end{aligned} \tag{A.19}$$

where b is given by Eq. (A.16).

The radial distance is found from:

$$r = a(1 - h\sin F - k\cos F) \tag{A.20}$$

and then used to determine the quantities:

$$\begin{aligned} X &= r\cos L \\ Y &= r\sin L \\ \dot{X} &= -\frac{na(h+\sin L)}{\sqrt{1-h^2-k^2}} \\ \dot{Y} &= \frac{na(k+\cos L)}{\sqrt{1-h^2-k^2}} \end{aligned} \tag{A.21}$$

Finally, the position and velocity vectors can be found from:

$$\begin{aligned} \boldsymbol{r} &= X\boldsymbol{f} + Y\boldsymbol{g} \\ \boldsymbol{V} &= \dot{X}\boldsymbol{f} + \dot{Y}\boldsymbol{g} \end{aligned} \tag{A.22}$$

A.1.4. KEPLERIAN ELEMENTS AND EQUINOCTIAL ELEMENTS

The procedures and equations presented in this section have been obtained from [14].

TRANSFORMATION FROM KEPLERIAN TO EQUINOCTIAL ELEMENTS

The transformation is directly obtained from the definition of equinoctial elements:

$$\begin{aligned} a &= a \\ h &= e\sin(\omega + \Omega) \\ k &= e\cos(\omega + \Omega) \\ p &= \tan i/2\,\sin\Omega \\ q &= \tan i/2\,\cos\Omega \\ \lambda &= M + \omega + \Omega \end{aligned} \tag{A.23}$$

The eccentric longitude, F, and the true longitude, L, are given by:

$$F = E + \omega + \Omega \tag{A.24}$$

$$L = f + \omega + \Omega \tag{A.25}$$

TRANSFORMATION FROM EQUINOCTIAL TO KEPLERIAN ELEMENTS

The first step is to compute the auxiliary angle ζ, defined by:

$$\begin{aligned} \sin\zeta &= \frac{h}{\sqrt{h^2 + k^2}} \\ \cos\zeta &= \frac{k}{\sqrt{h^2 + k^2}} \end{aligned} \tag{A.26}$$

Then, the Keplerian elements can be found from:

$$\begin{aligned} a &= a \\ e &= \sqrt{h^2 + k^2} \\ i &= 2\arctan\sqrt{p^2 + q^2} \\ \sin\Omega &= \frac{p}{\sqrt{p^2 + q^2}} \\ \cos\Omega &= \frac{q}{\sqrt{p^2 + q^2}} \\ \omega &= \zeta - \Omega \\ M &= \lambda - \zeta \end{aligned} \tag{A.27}$$

The eccentric anomaly and the true anomaly can be obtained from:

$$E = F - \zeta \tag{A.28}$$

$$f = L - \zeta \tag{A.29}$$

A.2. ORBITAL PERTURBATIONS

A.2.1. GEOPOTENTIAL

EFFECTS OF J_2

The J_2-term does not cause secular or long-period variations on a, e or i. However, Ω does experience a secular variation known as *regression of the nodes* [39]. The rate of change of the right ascension of the ascending node is given by [48]:

$$\dot{\Omega} = -\tilde{J}_2 n \cos i \tag{A.30}$$

where the term

$$\widetilde{J}_2 = \frac{3}{2}\frac{J_2 R^2}{p^2} \tag{A.31}$$

is always positive, since $J_2 = 1.0826357 \times 10^{-3}$ [45], leading to negative values of $\dot{\Omega}$ for prograde orbits ($i < 90$ degrees). Here R denotes Earth's equatorial radius and $p = a(1-e^2)$ the semi-latus rectum. Also note that for polar orbits ($i = 90$ degrees), Ω remains constant. This is a logical result, as the J_2-term is a zonal harmonic and thus one should not expect the orbital plane to rotate about the polar axis, since the deviations described by zonal terms are independent of longitude (cf. Figure 3.5 left). The rate of change of Ω is maximum for equatorial orbits ($i = 0$), but in this case this parameter is undefined.

The argument of perigee can also experience secular variations due to the J_2-term and, in addition, long-period variations too. Its temporal rate of change is given by [39]:

$$\dot{\omega} = \frac{\widetilde{J}_2}{2} n(5\cos^2 i - 1) \tag{A.32}$$

which leads to the definition of a *critical inclination* for which J_2 has no effect on ω. This value corresponds to $i = 63.435$ degrees.

EFFECTS OF J_3

The J_3-term has no secular or long-period effects on the semi-major axis; however, the other orbital elements can experience these effects. The corresponding expressions can be found in [43]. For polar orbits, the inclination remains constant at 90 degrees. For equatorial orbits, the eccentricity does not experience long-term or secular variations, and $\dot{\Omega}$ tends to infinity, although Ω is not defined if $i = 0$. When the argument of perigee $\omega = 0$, neither Ω nor ω change.

Changes in the eccentricity will have an influence on the perigee altitude, as the semi-major axis remains constant. This will have an impact on the lifetime of the orbit due to the atmospheric density changing with altitude. Thus, the rate of change of the eccentricity due to the J_3-term is deemed to be of high relevance for GTOs and is provided here [43]:

$$\dot{e} = \frac{\widetilde{J}_3}{4} n(1-e^2)(5\cos^2 i - 1)\sin i \cos\omega \tag{A.33}$$

with the coefficient

$$\widetilde{J}_3 = \frac{3}{2}\frac{J_3 R^3}{p^3} \tag{A.34}$$

always negative, since $J_3 = -2.5324737 \times 10^{-6}$ [45] and $R > 0$, $l > 0$. The term $5\cos^2 i - 1$ is positive for $i < 63.435$ degrees, which holds for most GTOs. Thus, it can be said that, in general, the rate of change of the eccentricity has opposite sign than $\cos\omega$. Using Eq. (3.1) it can be shown that $r_p = a(1-e)$, from which it is possible to deduce that the sign of the rate of change of the perigee altitude due to J_3 coincides with that of $\cos\omega$.

EFFECTS OF J_4

The J_4-term has no secular or long-period effects on the semi-major axis or the inclination; however, the other orbital elements are affected. The corresponding expressions can be found in [43]. The eccentricity is not affected when $i = 0$, $i = 67.79$ degrees or $\omega = 0$. Moreover, for polar orbits, or when $i = 49.11$ degrees and $\omega = 45$ degrees, Ω remains constant. In this case, the rate of change of the eccentricity is also deemed to be relevant and is reported here [43]:

$$\dot{e} = \widetilde{J}_4 n e(1-e^2)(1-7\cos^2 i)\sin^2 i \sin 2\omega \tag{A.35}$$

with the coefficient

$$\widetilde{J}_4 = \frac{15}{32}\frac{J_4 R^4}{p^4} \tag{A.36}$$

always negative, since since $J_4 = -1.6199743 \times 10^{-6}$. This means that, for GTOs (with $i < 67.79$ degrees), the sign of $\dot{e}$ will coincide with that of $\sin 2\omega$, or equivalently, the rate of change of the perigee altitude and $\sin 2\omega$ will have opposite signs. It can be shown that the effects of the J_3- and J_4-terms on the eccentricity (and thus on the perigee altitude) have opposite signs for $\omega < 180$ degrees, while for $\omega > 180$ the two effects add up.

EFFECTS OF $J_{2,2}$

The $J_{2,2}$-term has no secular or long-period effects on the semi-major axis or the eccentricity; however, the other orbital elements are affected. The corresponding expressions can be found in [39], where the terms of order e^2 have been neglected, which may not be valid for HEOs. For equatorial orbits, the inclination remains constant at $i = 0$ degrees. For polar orbits, Ω remains constant in the long-term, and so does ω if $i = 39.23$ degrees.

A.2.2. THIRD-BODY ATTRACTION

The secular and long-period variations over one orbital revolution due to a third body's gravity in terms of orbital elements are [81]:

$$\begin{aligned}
\Delta_{2\pi} a &= 0 \\
\Delta_{2\pi} e &= \frac{5}{2}\eta e\sqrt{1-e^2}\sin^2 i \sin 2\omega \\
\Delta_{2\pi} i &= -\frac{5}{4}\eta\frac{e^2}{\sqrt{1-e^2}}\sin 2i \sin 2\omega \\
\Delta_{2\pi}\Omega &= -\eta\frac{\cos i}{\sqrt{1-e^2}}(1-e^2+5e^2\sin^2\omega) \\
\Delta_{2\pi}\omega &= \eta\frac{1}{\sqrt{1-e^2}}\left[5\cos^2 i \sin^2\omega + (1-e^2)(2-5\sin^2\omega)\right]
\end{aligned} \tag{A.37}$$

where

$$\eta = \frac{3}{2}\pi\frac{\mu_d}{\mu_E}\left(\frac{a}{r_d}\right)^3 \tag{A.38}$$

Moreover, since the semi-major axis remains constant, an expression for the change in perigee altitude can be obtained [81]:

$$\Delta_{2\pi} h_p = -a\Delta_{2\pi} e \tag{A.39}$$

which leads to the conclusion that the perigee altitude will rise due to third-body perturbations when $90° < \omega < 180°$ or $270° < \omega < 360°$.

A.2.3. ATMOSPHERIC DRAG

The following expressions give the secular variation of the semi-major axis and the eccentricity due to atmospheric drag over one orbital revolution [33]:

$$\begin{aligned}
\Delta_{2\pi} a &= -2\pi\frac{C_D A}{m}a^2\rho_p e^{-c}[I_0 + 2eI_1] \\
\Delta_{2\pi} e &= -2\pi\frac{C_D A}{m}a\rho_p e^{-c}\left[I_1 + e\frac{I_0+I_2}{2}\right]
\end{aligned} \tag{A.40}$$

where ρ_p is the atmospheric density at perigee, $c \equiv ae/H_0$ and I_j are modified Bessel functions of order j and argument c. The modified Bessel function is given by [82]:

$$I_j(c) = \sum_{m=0}^{\infty}\frac{1}{m!\Gamma(m+j+1)}\left(\frac{c}{2}\right)^{2m+j} \tag{A.41}$$

For circular orbits, Eq. (A.40) can be simplified significantly [33], but this is not the case for GTOs. However, even in their full form they can be used to deduce that the effect of atmospheric drag on the semi-major axis and eccentricity is always a secular decrease, since the modified Bessel functions are always positive, given that $j \geq 0$, $c \geq 0$ and $\Gamma(x) > 0$ for $x > 0$ [83].

Similar expressions are provided in [43], where the terms of order e^2 and e^3 are also included. Expressions for the other orbital elements are also provided there. However, these expressions are rather complex, and thus it is not possible to determine whether the rates of change are positive or negative just by visual inspection, so they have been left out of this report.

A.2.4. SOLAR RADIATION PRESSURE

The following expressions provide a first-order approximation of the rate of change of the orbital elements due to solar radiation pressure [43]:

$$
\begin{aligned}
\dot{a} &= 0 \\
\dot{e} &= -\frac{3}{2}\frac{f_S}{r_S^2}\frac{\sqrt{1-e^2}}{na}y_S \\
\dot{i} &= \frac{3}{2}\frac{f_S}{r_S^2}\frac{e\cos\omega}{na\sqrt{1-e^2}}z_S \\
\dot{\Omega} &= \frac{3}{2}\frac{f_S}{r_S^2}\frac{e\sin\omega}{na\sqrt{1-e^2}\sin i}z_S \\
\dot{\omega} &= \frac{3}{2}\frac{f_S}{r_S^2}\frac{\sqrt{1-e^2}}{nae}x_S - \dot{\Omega}\cos i
\end{aligned}
\tag{A.42}
$$

where r_S is the distance from Earth to the Sun, x_S, y_S and z_S are the coordinates of the Sun in the Earth-centred perifocal reference frame introduced in Section 3.3.1, and

$$f_S = |\boldsymbol{a_{SRP}}| = C_R\frac{W_S A}{mc} \tag{A.43}$$

B

ADDITIONAL PLOTS

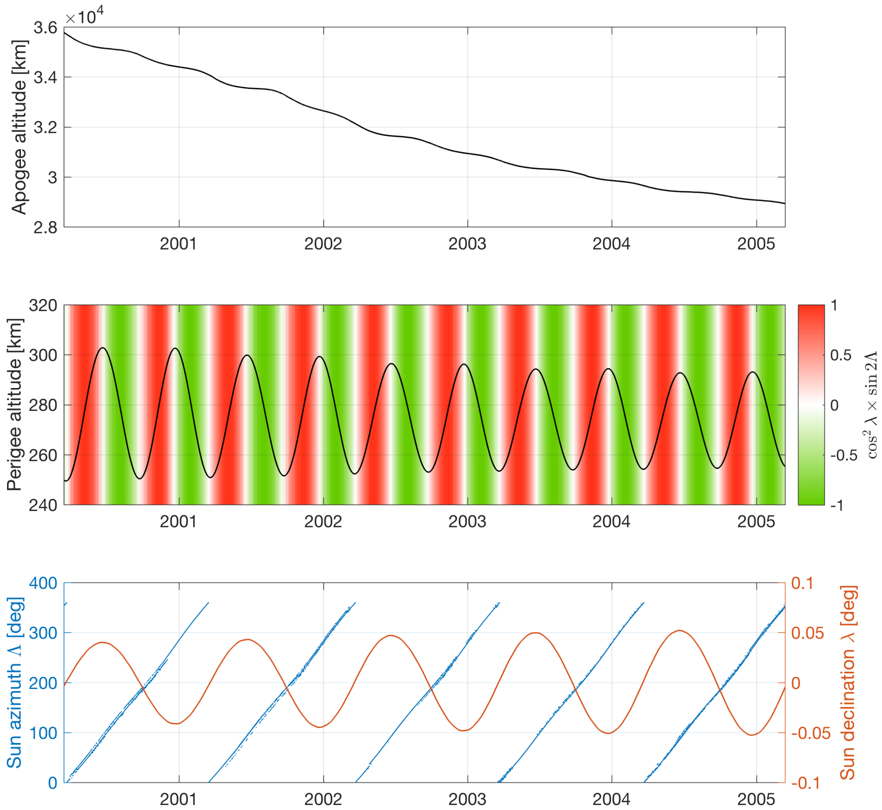

Figure B.1: Temporal evolution of the perigee and apogee altitudes and Sun azimuth and declination angles for a representative GTO, neglecting all perturbations except Sun's gravity.

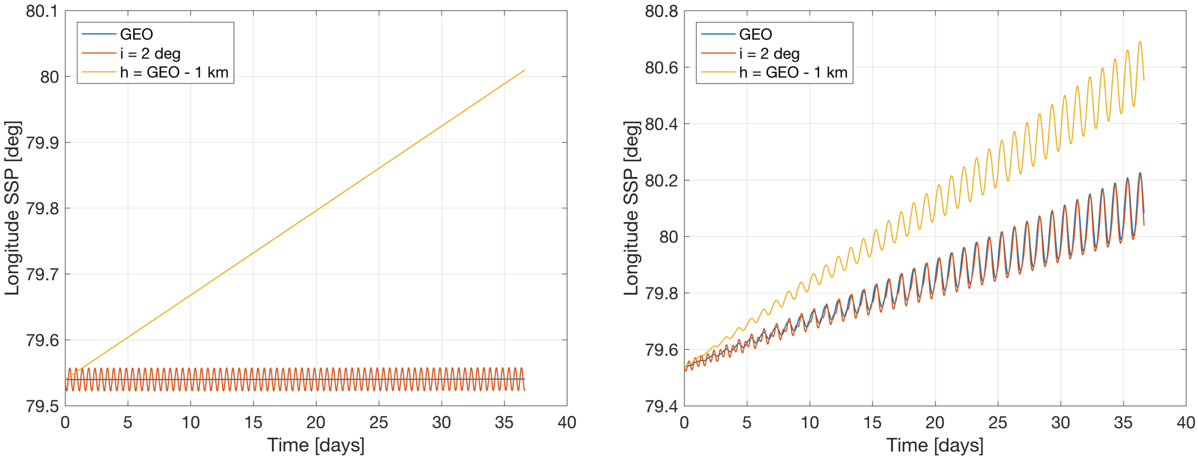

Figure B.2: Temporal evolution of the longitude of the sub-satellite point of a geostationary satellite; a satellite in a circular orbit at GEO altitude with an inclination of 2 deg; and a satellite in a circular equatorial orbit 100 km below GEO altitude, when all orbital perturbations are neglected (left) and when the effects of zonal terms up to degree 7, Sun's and Moon's gravity, drag and SRP are considered (right).

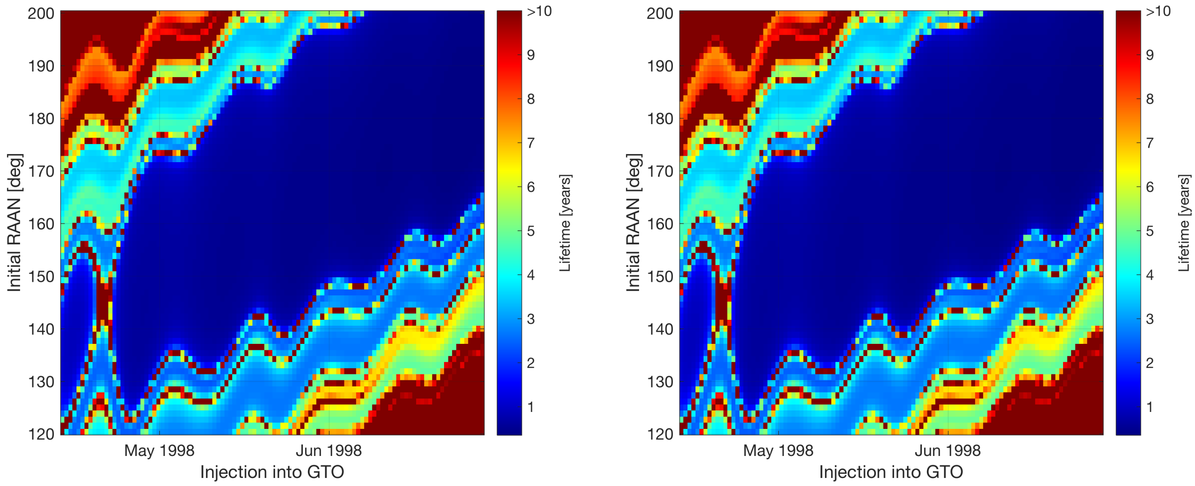

Figure B.3: Lifetime of a satellite as a function of epoch of injection into GTO and initial RAAN when eclipses are included in the acceleration model (left) and neglected (right).

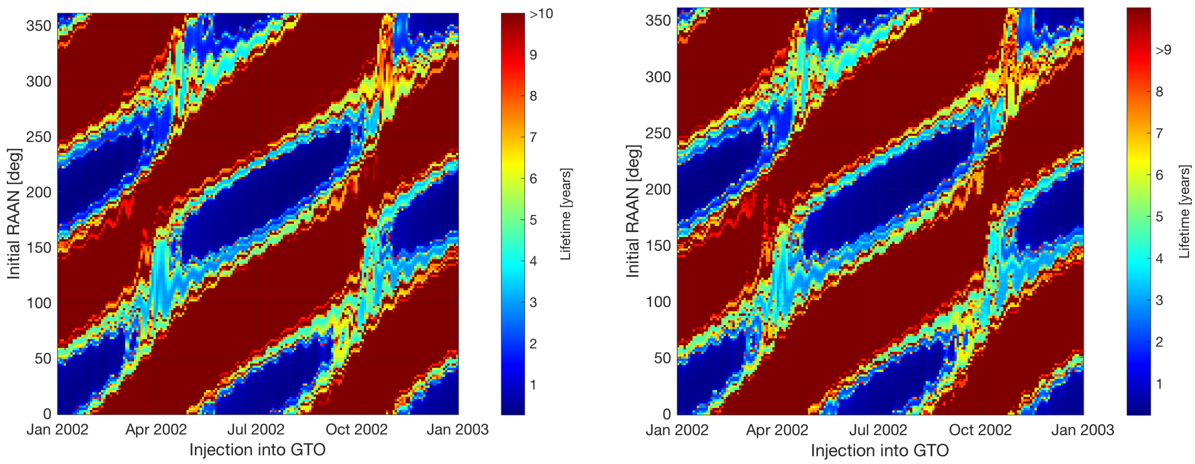

Figure B.4: Lifetime of a satellite as a function of epoch of injection into GTO and initial RAAN using the Cowell (left) and SST (right) propagators.

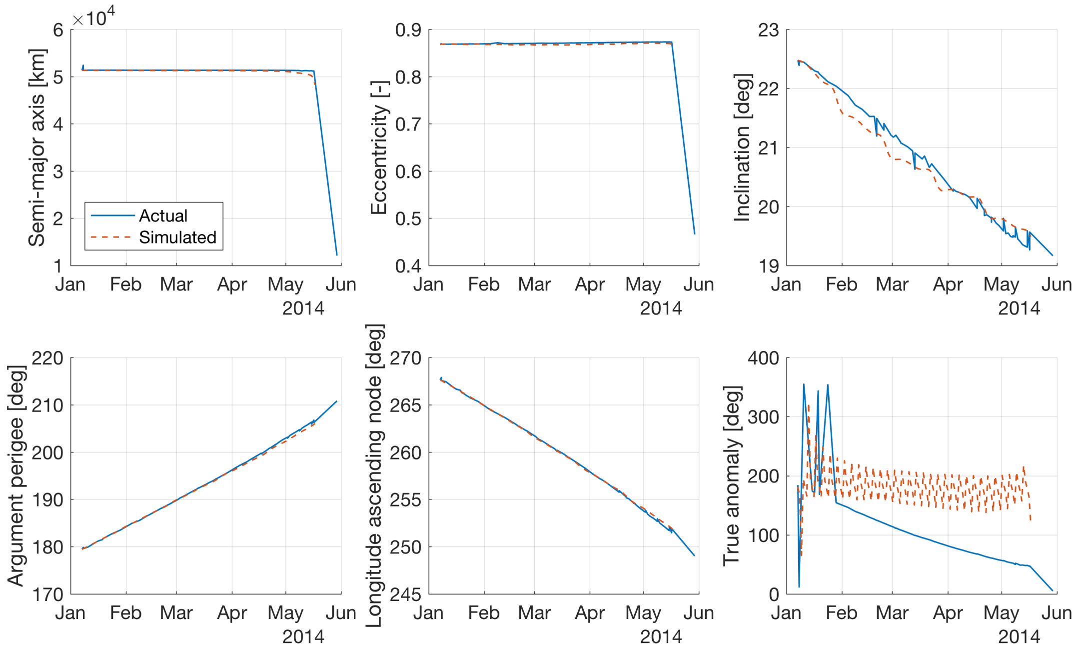

Figure B.5: Evolution of the Keplerian components of the upper stage of the Falcon 9 rocket (CATID 39501) used to launch Thaicom 6 obtained from tracking data [38] (solid line) and simulated using the SST propagator (dashed line).

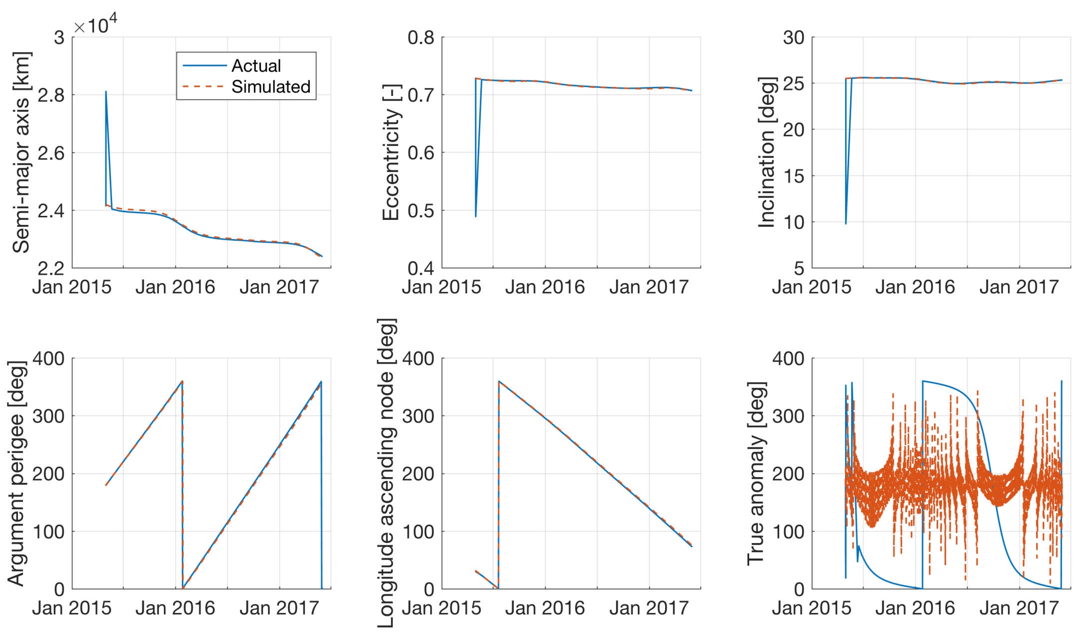

Figure B.6: Evolution of the Keplerian components of the upper stage of the Falcon 9 rocket (CATID 40618) used to launch TurkmenSat 1 obtained from tracking data [38] (solid line) and simulated using the SST propagator (dashed line).

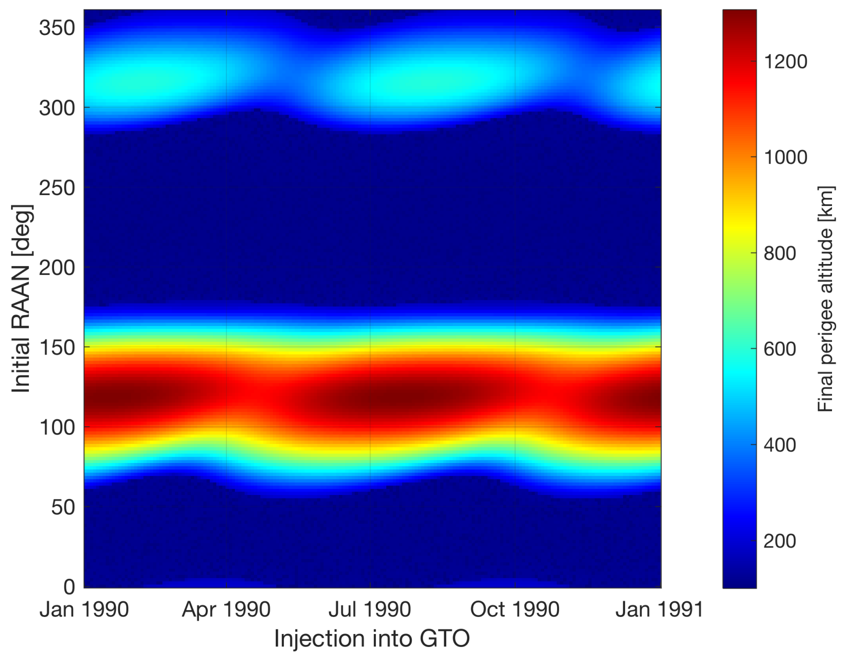

Figure B.7: Final perigee altitude after a period of 25 years for several GTOs with initial perigee altitude of 200 km. Only perturbations caused by atmospheric drag and the Sun's gravity were included in the acceleration model.

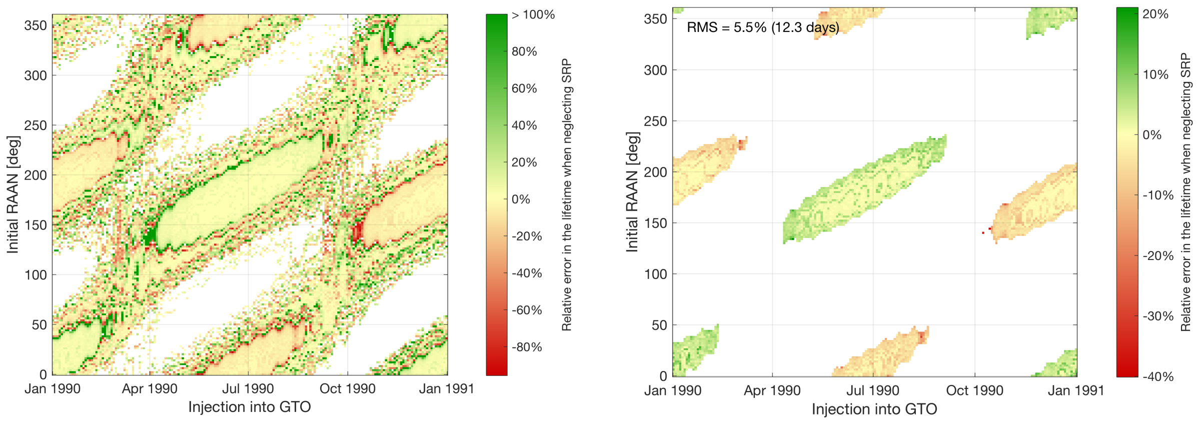

Figure B.8: Relative errors introduced in the value of the lifetime of a satellite when neglecting the effects of SRP as a function of epoch of injection into GTO and initial RAAN, for orbits with a lifetime with less than 25 years (left) and for orbits in resonance-free regions only (right).

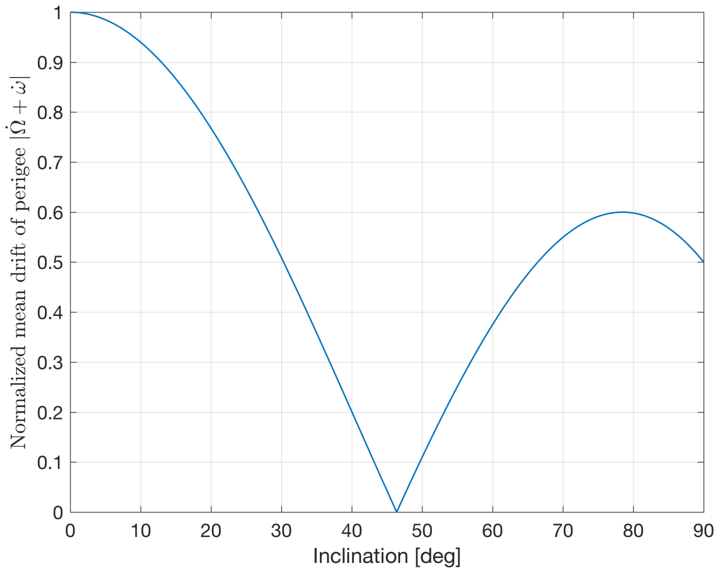

Figure B.9: Contribution of the J_2 term to the mean drift of perigee as a function of orbital inclination (cf. Eq. (6.1)).

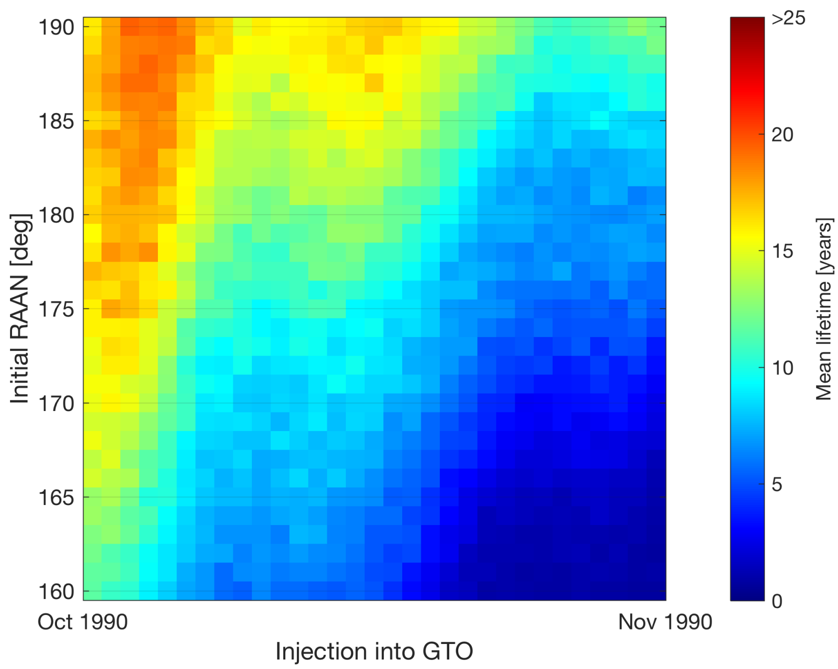

Figure B.10: Zoom-in around a region of Figure 6.8 with a higher resolution for both the epoch of injection into GTO and the initial RAAN.

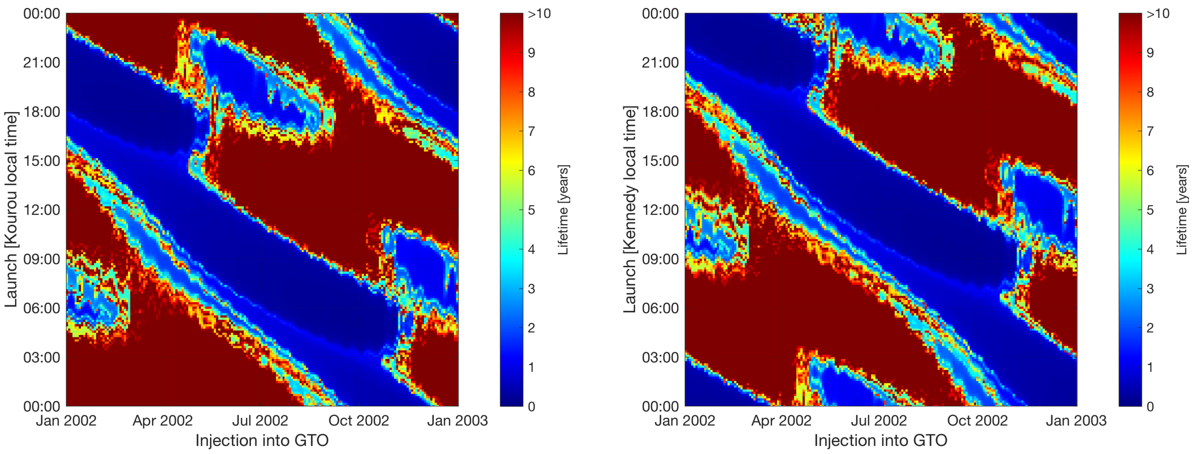

Figure B.11: Lifetimes of objects in a GTO with an initial inclination of 30 degrees as a function of epoch of injection into GTO and local time of launch from the Euroepan spaceport in Kourou (left) and from Kennedy Space Center's launch site in Cape Canaveral (right).